Critical Phenomena in Topologically Disordered Systems

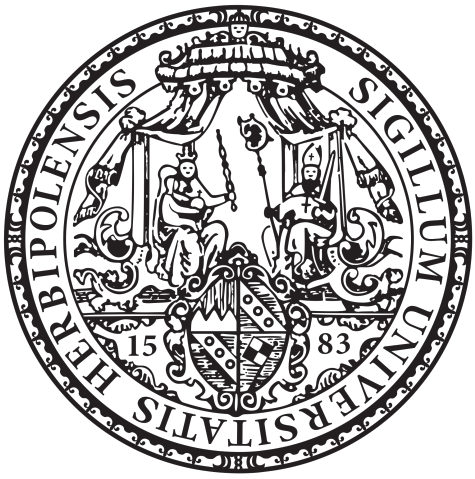

Dissertation zur Erlangung des naturwissenschaftlichen Doktorgrades
an der Fakultät für Physik und Astronomie
der Julius-Maximilians-Universität Würzburg

vorgelegt

von

Manuel Schrauth

aus Schweinfurt

Würzburg, im Januar 2020

Eingereicht am: 30.01.2020

bei der Fakultät für Physik und Astronomie

1. Gutachter: Prof. Dr. Haye Hinrichsen

2. Gutachter: Prof. Dr. Fakher Assaad

3. Gutachter: Prof. Dr. Jens Pflaum

der Dissertation

Vorsitzende: Prof. Dr. Ewelina M. Hankiewicz

1. Prüfer: Prof. Dr. Haye Hinrichsen

2. Prüfer: Prof. Dr. Fakher Assaad

3. Prüfer: Prof. Dr. Jens Pflaum

im Promotionkolloquium

Tag des Promotionskolloquiums: 23.09.2020

Doktorurkunde ausgehändigt am: .....

To my parents

"Maybe it meant something. Maybe not, in the long run, but no explanation, no mix of words or music or memories can touch that sense of knowing that you were there and alive in that corner of time and the world. Whatever it meant."

– Hunter S. Thompson (Fear and Loathing in Las Vegas)

"In this house, we obey the laws of thermodynamics!"

– Homer Simpson

"In an isolated system, entropy can only increase."

– Muse (The 2nd Law)

Abstract

Clearly, in nature, but also in technological applications, complex systems built in an entirely ordered and regular fashion are the exception rather than the rule. In this thesis we explore how critical phenomena are influenced by quenched spatial randomness. Specifically, we consider physical systems undergoing a continuous phase transition in the presence of topological disorder, where the underlying structure, on which the system evolves, is given by a non-regular, discrete lattice. We therefore endeavour to achieve a thorough understanding of the interplay between collective dynamics and quenched randomness.

According to the intriguing concept of universality, certain laws emerge from collectively behaving many-body systems at criticality, almost regardless of the precise microscopic realization of interactions in those systems. As a consequence, vastly different phenomena show striking similarities at their respective phase transitions. In this dissertation we pursue the question of whether the universal properties of critical phenomena are preserved when the system is subjected to topological perturbations. For this purpose, we perform numerical simulations of several prototypical systems of statistical physics which show a continuous phase transition. In particular, the equilibrium spin-1/2 Ising model and its generalizations represent – among other applications – fairly natural approaches to model magnetism in solids, whereas the non-equilibrium contact process serves as a toy model for percolation in porous media and epidemic spreading. Finally, the Manna sandpile model is strongly related to the concept of self-organized criticality, where a complex dynamic system reaches a critical state without fine-tuning of external variables.

Our results reveal that the prevailing understanding of the influence of topological randomness on critical phenomena is insufficient. In particular, by considering very specific and newly developed lattice structures, we are able to show that – contrary to the popular opinion – spatial correlations in the number of interacting neighbours are not a key measure for predicting whether disorder ultimately alters the behaviour of a given critical system.

Zusammenfassung

Ohne Zweifel stellen vollständig regelmäßig aufgebaute komplexe Systeme sowohl in der Natur als auch in technischen Anwendungen eher die Ausnahme als die Regel dar. In dieser Arbeit erforschen wir, wie sogenannte kritische Phänomene durch eingefrorene räumliche Unordnung beeinflusst werden. Konkret untersuchen wir physikalische Systeme, welche einen kontinuierlichen Phasenübergang aufweisen, in Gegenwart von topologischer Unordnung. Die räumliche Struktur, auf der sich das dynamische System entwickelt, ist in diesem Fall durch ein unregelmäßiges diskretes Gitter gegeben. Die Erlangung eines tiefergehenden Verständnisses des Zusammenspiels von physikalischer Dynamik und räumlicher Unordnung kann daher als das Hauptziel unserer Unternehmung angesehen werden.

Ein gleichermaßen faszinierendes wie zentrales Konzept in der statistischen Physik stellt die sogenannte Universalität dar, gemäß welcher das kollektive Verhalten von Vielkörpersystemen im kritischen Bereich nahezu unabhängig von der spezifischen mikroskopischen Realisierung der Wechselwirkungen ist. Als Konsequenz sind selbst in völlig unterschiedlichen Systemen bemerkenswerte Ähnlichkeiten an den jeweiligen Phasenübergängen beobachtbar. Diese Dissertation geht nun der Frage nach, inwieweit diese universalen Eigenschaften erhalten bleiben, wenn das System topologischen Störungen ausgesetzt wird. Zu diesem Zweck werden umfangreiche numerische Monte-Carlo-Simulationen von einigen prototypischen Systemen, welche einen kontinuierlichen Phasenübergang aufweisen, durchgeführt. Ein prominentes Beispiel für ein System im thermodynamischen Gleichgewicht stellt dabei das Spin-1/2 Ising-Modell dar, welches unter anderem magnetische Eigenschaften von Festkörpern modelliert. Zusätzlich werden auch Systeme fernab des Gleichgewichts behandelt, wie etwa der Kontaktprozess, welcher ein vereinfachtes Modell für Perkolationsprozesse in porösen Stoffen oder auch für die Ausbreitung von Epidemien darstellt, sowie spezielle Modelle, welche in engem Zusammenhang mit selbstorganisiertem kritischen Verhalten stehen.

Unsere Ergebnisse demonstrieren, dass der Einfluss von topologischen Störungen auf kritische Phänomene derzeit noch unzureichend verstanden ist. Insbesondere gelingt es uns mittels spezieller eigens entwickelter Gitterkonstruktionen zu zeigen, dass lokale räumliche Korrelationen in der Anzahl von wechselwirkenden Nachbarn, entgegen weitläufiger Meinung, kein adäquates Maß sind, um den Einfluss von Unordnung auf das Verhalten eines kritischen Systems vorhersagen zu können.

Contents

List of Figures

List of Tables

List of Acronyms

APT	Absorbing Phase Transition
BD	regular lattice with random Bond Dilutions
CC	Constant Coordination
CCx	Constant Coordination lattice with x neighbours
CLG	Conserved Lattice Gas
CP	Contact Process
CSSM	Conserved Stochastic Sandpile Model
CTTP	Conserved Threshold Transfer Process
DP	Directed Percolation
DT	Delaunay Triangulation
DT^+	Delaunay Triangulation with additional bonds
FSS	Finite-Size Scaling
GG	Gabriel Graph
HBV	Harris-Barghathi-Vojta
HPC	High Performance Computing
LGW	Landau-Ginzburg-Wilson
MC	Monte Carlo
MF(T)	Mean Field (Theory)
MSE	Micro-Scale Equivalence
NN	Nearest Neighbour
RFIM	Random Field Ising Model

RG	Renormalization Group
RGG	Random Geometric Graph
RNG	Relative Neighbourhood Graph
SA	Simulated Annealing
SD	regular lattice with random Site Dilutions
SOC	Self-Organized Criticality
QS	Quasi-Stationary
VG	Voronoi Graph

List of Symbols

ν, $\nu_\perp$	critical exponent of the correlation length
$\nu_\parallel$	critical exponent of the autocorrelation time
β	critical exponent of the order parameter
	also: inverse temperature
α	critical exponent of the specific heat
γ	critical exponent of the susceptibility
z	dynamic exponent
τ, Δ	distance from the critical point
ξ , $\xi_\perp$	correlation length
ρ	density of active states
L	linear system size
N_a	number of active sites
P_s	survival probability
ω	correction-to-scaling exponent
	also: geometric wandering exponent
T_c, β_c, p_c	critical point
q	coordination number (of a lattice site)
ϕ	generic symbol for the order parameter
$\phi(x)$	order parameter field
Ψ, $\tilde{m}$, $\tilde{\chi}$, f_O, ...	scaling functions
ℓ	bond/link length

F, f	free energy
χ	susceptibility
C	specific heat
$\mathcal{H}$	Hamiltonian
Z	partition function
$G(x - x')$	generic symbol for spatial two-point correlator
$C(x)$	spatial correlator of lattice coordination numbers
λ	infection rate
	also: RG scale factor
a	disorder decay exponent
$d(\cdot, \cdot)$	(Euclidean) distance
$U_2, U_4, \ldots, m$	cumulant (Binder) ratios of the order parameter
$\mathcal{F}$	Fourier transform
$M, (m)$	magnetization (per site)
$E, (e)$	internal energy (per site)
h	external magnetic field
R	RG invariant quantity (phenomenological coupling)

Chapter 1

Introduction

"Aber die existierenden wissenschaftlichen Begriffe passen jeweils nur zu einem sehr begrenzten Teil der Wirklichkeit, und der andere Teil, der noch nicht verstanden ist, bleibt unendlich."

– Werner Heisenberg

Exactly 100 years ago, Wilhelm Lenz devised a simple model of an "Umklappmagnet" [1] which would go on to drive the development of an entire field of physics. In the century since its introduction, the *Ising model* set the stage for the development of numerous analytical and numerical techniques – and is still intensely researched today. Named after Ernst Ising, who provided the exact solution for the one dimensional case in 1925 [2], this model has thus played a pre-eminent role in establishing what we call today the physics of *critical phenomena*. Its remarkable relevance derives to a large degree from the fact that, although originally proposed as a model for ferromagnetism, it qualitatively (and also quantitatively) describes collective long-range behaviour of many microscopic degrees of freedom of systems from vastly different areas, also beyond the natural sciences. Leo P. Kadanoff, one of the pioneers of modern statistical physics, described the impact, writing [3]:

> *Starting around 1925, a change occurred: With the work of Ernst Ising and Wilhelm Lenz, statistical mechanics began to be used to describe the behaviour of many particles at once.*

In their work, Lenz and Ising considered spins placed at discrete lattice positions, which can take

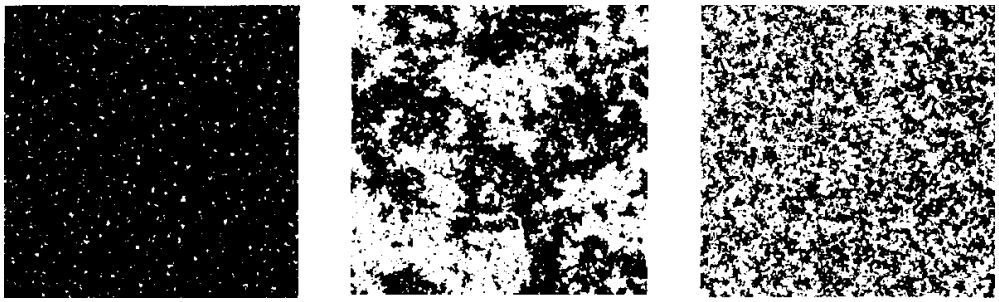

(a) (b) (c)

Figure 1.1 | Typical configurations of the two-dimensional Ising model. Colours black and white represent up and down spins, respectively. (a) Ordered state below the critical temperature. (b) Self-similar, scale-invariant clusters exactly at criticality. (c) High-temperature disordered phase.

on two configurations, +1 or -1. Figuratively speaking, they correspond to magnetic moments of atoms, pointing upwards or downwards. Individual spins interact with their immediate neighbours in a way which energetically favours parallel orientation. At the same time this ordering mechanism is countered by random fluctuations, driven by a finite temperature of the system. As a result, at a specific temperature, one observes a transition from a globally ordered phase of high symmetry to a disordered phase of low symmetry, which correctly describes the phenomenology of the ferromagnetic/paramagnetic transition, discovered by Pierre Curie in 1895 [4]. Above the so-called *Curie temperature* (about 768°C for iron, for instance), the material loses its spontaneous magnetization, which it recovers, however, when cooled down again.

In general, *phase transitions* are characterized by an *abrupt* change of macroscopic properties when certain system parameters are *smoothly* varied. In terms of the thermodynamic free energy, used to describe systems obeying the Boltzmann statistics, this corresponds to a non-analytic point in phase space. As a consequence, certain observable quantities which can be directly derived from the free energy, such as the magnetic susceptibility or the specific heat, typically diverge at the transition. If already the first derivative of the free energy presents a discontinuity one speaks of a first-order or discontinuous transition, whereas a *continuous phase transition* takes place if the first derivative is continuous, and only higher derivatives diverge. In the latter case, the degree of these (usually algebraic) singularities is characterized by so-called *critical exponents*. The emergence of a power-law behaviour at the criticality is no coincidence. Mathematically it reflects the system's *scale invariance*, one of the hallmarks of criticality [5] – at the critical point, clusters of equal spin orientation become fractal and self-similar as can be seen in Figure 1.1. Whereas the low- and high-temperature phases exhibit typical length scales, at criticality clusters of *any* size can be found in the system, ranging from the system dimensions all the way down to the lattice discretization. The typical length scale of correlations becomes infinite at a continuous transition.

What is it that makes specifically the Ising model so significant? In his historic review of the model [6], Stephen G. Brush writes:

> *In constructing a theory to interpret a complex physical phenomenon, a scientist frequently has to choose between two approaches. On the one hand, he may want to make his theory [...] as*

> *"realistic" as possible. But this approach usually leads to formulations that are mathematically so complicated that the consequences of the hypotheses cannot be deduced from the theory without gross approximations [...] On the other hand, one may intentionally sacrifice some of the more realistic features of a model in order to obtain a simpler model that is exactly soluble.*

At a first glance, the Ising model clearly falls into the second category. Attempting to model magnetic behaviour while neglecting the details of the electronic structure of the material almost entirely and reducing the individual atoms in the lattice to "arrows" that are moreover restricted to only two orientations, seems to be a rather crude approximation. In addition to that, any quantum mechanical effects are ignored, even though they are certainly expected to be relevant in describing microscopic interactions in solids, which was already known at the time when Lenz proposed the model. Astonishingly, however, the Ising model in fact *does* provide a quantitatively correct description of the magnetic phase transitions in certain real materials. For instance, Back et al. [7] measured the equation of state of a ferromagnetic atomic monolayer on a non-magnetic substrate and found a striking data collapse over 18 orders of magnitude, and experimental estimates of the corresponding critical exponents were in agreement with those of the two-dimensional Ising model.

Surprisingly, critical exponents of the Ising model were found in experiments with systems entirely unrelated to magnets [8–10], most notably at the so-called critical point of certain fluids where properties of the liquid and vapour phases become indistinguishable. It is notable that already Pierre Curie [4] was aware of an ...

> *...analogy between the way in which the intensity of magnetization of a magnetic body increases under the influence of temperature and the intensity of the field, and the way in which the density of a fluid increases under the influence of temperature and of the pressure.*

The observation that entirely different systems at their continuous phase transition appear to behave in a *quantitatively* similar fashion can not be regarded as a mere artefact. It rather suggests that these systems share certain "universal" properties. In other words, the microscopic nature of the system should become irrelevant on macroscopic scales. During the course of the last century experimental physicists found an increasing number of examples of rather distinct systems featuring strikingly similar behaviour at criticality, most notably the study of coexistence curves of simple fluids by Edward Guggenheim [11] supporting the so-called *universality hypothesis*.

On the theoretical side, the understanding of phase transitions was also progressing during this time. An early substantial advance is due to Lev D. Landau, who in 1937 introduced the concept of an *order parameter* and recognized the crucial role of its symmetries under the change of external variables [12]. About this concept, Michael Fisher, one of the pioneers of modern statistical physics, writes [13]:

> *To assert that there exists an order parameter in essence says: "I may not understand the microscopic phenomena at all, but I recognize that there is a microscopic level and I believe it should have certain general, overall properties especially as regards locality and symmetry: those then serve to govern the most characteristic behaviour on scales greater than atomic."*

Although Landau's theory successfully explained the phenomenology of critical behaviour from a mesoscopic perspective, it was only in the early 1970's that scale invariance and universality could eventually be motivated from a more rigorous mathematical point of view. Inspired by Kadanoff's block spin idea [14], Kenneth G. Wilson put forward the celebrated *renormalization group* (RG) framework [15, 16] establishing one of the cornerstones of modern statistical physics and quantum field theory [17]. In 1982, Wilson was awarded the Nobel price for his groundbreaking contributions to the theoretical understanding of critical phenomena. Steven Weinberg, a Nobel laureate himself (for his contributions to the electro-weak unification), wrote:[1]

> *Ken Wilson was one of a very small number of physicists who changed the way we all think, not just about specific phenomena, but about a vast range of different phenomena.*

It needs to be emphasized that the theoretical frameworks of both Landau and Wilson, in general do not provide exact solutions. Landau's theory is based upon the crucial approximation that local order parameter fluctuations can be regarded as "small" and hence represents what today is known as an *effective mean-field theory*. In the renormalization group framework significant approximations are involved as well, however in a considerably more elaborate and technical fashion. Results, such as critical exponents, can usually only be computed as appropriate (however oftentimes not even convergent) series expansions in which tackling higher-order terms becomes increasingly cumbersome. As a consequence, exactly solvable systems are of inestimable value. One can imagine that mathematically rigorous solutions of (even heavily simplified) models of interacting many body systems represent the absolute exception rather than the rule. It is hence not surprising that being exactly solvable on a regular two-dimensional lattice eventually cemented the Ising model's reputation as one of the most influential physical models of the 20th century. As Michael Fisher puts it [13] ...

> *... in 1944 a bombshell struck! Lars Onsager [...] computed exactly the partition function and thermodynamic properties of the simplest model of a ferromagnet or a fluid.*

The impact was immediate. Not only did Onsager's solution provide an extremely deep theoretical understanding of the problem (involving quaternion algebras), but his mathematical brilliance caused nothing less then a paradigm shift, as it convincingly demonstrated that standard thermodynamics was capable of describing critical phenomena in the first place, which was doubted at the time. Unfortunately, however, Onsager's methods, as well as other techniques reproducing his solution in later years [18–22] can not be generalized to three dimensions, rendering the three-dimensional Ising model a still unsolved problem.

[1] published in New York Times, June 21, 2013

1.1 Universality

Broadly speaking, the critical behaviour at continuous phase transitions is governed by symmetry, dimensionality and locality alone. For instance, the Ising model features short-ranged interactions and *binary* variables (up or down, on or off, active or passive, occupied or empty, plus or minus), hence the macroscopic properties remain unchanged under a global change of signs. In technical terms, one speaks of an invariance under $\mathbb{Z}_2$ group operations, which arguably represents a very simple and likewise fundamental symmetry group – and reflects precisely the reason why Lenz and Ising had not only formulated a model for ferromagnetism but (unknowingly) discovered one of the most prototypical classes of critical systems. As a consequence of the $\mathbb{Z}_2$ symmetry, below the transition (in the ordered phase) the system actually features two energetically equivalent configurations, associated to positive and negative magnetization. When cooled down from a disordered high-temperature configuration of zero net magnetization, the system will spontaneously select one of the two low-temperature solutions. This behaviour is known as *spontaneous symmetry breaking*. In fact, continuous phase transitions are quite commonly accompanied by a spontaneous breaking of certain symmetries below the transition.

As mentioned earlier, the Ising model also describes the liquid-vapour transitions of certain fluids. In this case, the binary degrees of freedom are mapped to regions featuring a density higher or lower than the average in the medium [23, 24]. A comprehensive overview of other systems described by the critical behaviour of the Ising model is given in the review article [25]. Rather than listing all of these applications, we select three other, fairly unusual ones which were studied in recent years:

- *Traffic control.* Inspired by the grid pattern of roads in major cities, Suzuki et al. [26] modelled the traffic by assigning traffic signals to each intersection, which feature two states (red and green) and are controlled in a decentralised way depending on the local traffic flow. The authors were able to show that their model undergoes a two-dimensional ferromagnetic phase transition, where the coupling strengths between signals acts as a temperature-like control variable.
- *Pistachio trees*. Studying a five year dataset of the nut production in a pistachio orchard, Noble et al. [27] found large-scale, self-similar spatial and temporal correlations, decaying as power-laws consistent with the critical behaviour of the two-dimensional Ising model. According to the authors, this suggests that short-ranged interactions between individual plants could be taking place through root grafting.
- *Stock markets.* The Ising model can serve as a toy model for financial markets, if the binary variable is interpreted as the individual agent's opinions (buy or sell) [28]. In this case, imitation serves as the effective interaction between traders whereas private information or idiosyncratic behaviour mimics the effect of a finite temperature. Moreover, external news can be interpreted as a fluctuating ambient magnetic field, leading to spontaneous symmetry breaking between buyers and sellers under equilibrium conditions.

All three examples, although seemingly unrelated to long-range collective behaviour at a first glance, in fact show Ising-like critical dynamics, hinting at the conceptual beauty of universality in general and illustrating the continuing significance of the Ising model in particular.

Systems out of equilibrium

Most systems mentioned so far are defined in terms of thermodynamic equilibrium, which means that on the microscopic level, the system reaches a state where there is no net flow of matter or energy. However, universal long-range correlations can also be found in critical systems which are generically *out of equilibrium*, i. e. which feature explicit temporal dynamics. The conceptually simplest class of transitions is found in the so-called *directed percolation* (DP) process. Originally, this process was intended to mimic filtering through porous media in a gravitational field [29]. Interpreting the dynamics as a spreading process, it furthermore can be used as a toy model for epidemics [30], where a lattice site represents an agent which can be either healthy or infected. The dynamics comprises spontaneous healing and random infection of immediate neighbours. Somewhat related, the model has also been used to describe the dynamics of forest fires spreading under the influence of wind [31]. These applications already hint at the rich variety of systems that exhibit DP behaviour. In fact, due to its simple dynamic rules, it can be regarded as the prototypical class of non-equilibrium systems, analogously to the Ising model in the equilibrium case. Consequently, since its introduction it has received considerable attention and has been investigated through numerous theoretical, numerical and more recently also experimental realizations [32–34]. Specifically, on a discrete lattice, DP behaviour is typically realized by the *contact process* (CP), comprising a number of local reaction-diffusion processes (self-destruction, diffusion, coagulation and offspring production) and their corresponding rates. Systems in the DP class exhibit a phase transition, which in the case of porous media separates the permeable from the impermeable regimes. In the epidemic language, the two phases correspond to a disease either being able to spread throughout the system or becoming extinct eventually. Note that in both descriptions the latter phase is characterized by an *absorbing state*, from which the system can not escape.

It turns out that just as for the equilibrium case, also non-equilibrium critical phenomena can be categorized into universality classes, as they are governed by long-range collective behaviour at the transition and accordingly exhibit power-law behaviour of observables with universal critical exponents. Apart from DP, another important non-equilibrium universality class which will be considered in this thesis, is the so-called *Manna sandpile model*. Its discovery was inspired by the concept of self-organized critical (SOC) systems, which had been introduced by Per Bak, Chao Tang and Kurt Wiesenfeld (BTW) in 1987 [35, 36] and describes systems reaching a critical configuration through their own dynamics, without the need for a fine-tuning of external parameters (such as the temperature or the infection probability). In particular, BTW considered a system where each lattice site harbours a number of grains. Driven by a random external injection of new grains, the sites build up piles which eventually topple and redistribute the grains to their neighbours. This can trigger whole cascades of events, so-called avalanches, which obey well-defined power-law distributions, resulting in a scale-invariant appearance of the system [37]. Only few years later, Subhrangshu S. Manna presented a variation of the original BTW model with stochastic rather then deterministic toppling rules [38], establishing the Manna universality class. We consider a conserved version of the model, the so-called *conserved stochastic sandpile model* (CSSM), where the external dropping mechanism is removed, but accounted for by a change of boundary conditions from open to periodic ones. As a result, the system shows a highly fluctuating behaviour and a phase transition into multiple absorbing states, given by configurations which prohibit further toppling events.

1.2 Disorder

Traditionally, the models introduced above are studied on a regular structure (such as a square lattice in two dimensions). Paired with periodic boundary conditions, this renders the system translationally invariant, a property which can be heavily exploited in analytical calculations and simplifies numerical studies as well. However, is this a faithful description of real systems? In the case of magnetic models, the discrete lattice naturally corresponds to the regular crystal lattice in a solid. Even though most atomic lattices can be considered as somewhat regular, in general they contain defects, such as impurities or vacancies [39, 40], which might even be intentionally introduced (e. g., doping of semiconductors). Moreover, crystalline solids may exhibit dislocations or deformations on an atomic scale [41], possibly appearing during the growth process or caused by external (mechanical) forces. Finally, there are materials with intrinsically disordered atomic structure, so-called amorphous materials [42], which also comprise certain metallic glasses [43, 44], some of which show magnetic behaviour [45]. It is hence clear that perfectly regular lattices in general can only be regarded as an approximation to real solids, which are naturally imperfect. Turning to non-equilibrium phenomena, a similar picture emerges, as a perfectly regular distribution of spreading agents in an epidemic or of trees in a forest can certainly not be regarded as very realistic. It is therefore crucial to study complex systems on *disordered geometries* as well, in order to obtain a more complete picture of their behaviour in real systems.

Investigating the influence of disorder requires a very important distinction. So-called *quenched disorder* is characterized by that fact that it remains static (frozen) on the relevant time scales of the physical system, whereas *annealed disorder* evolves dynamically. In the latter case, disorder degrees of freedom (such as the positions of impurities) can be interpreted as fluctuating together with the thermodynamic variables. Hence both can be treated on equal footing, which makes annealed disorder considerably simpler to deal with in terms of analytical and numerical methods. In this work, however, we exclusively focus on quenched randomness, which, despite calling for more sophisticated techniques, is typically a more realistic model of real disorder (at least for the systems considered here) and furthermore presents a rich phenomenology related to critical phenomena. In practice, there is a variety of different ways in which quenched disorder can be implemented. When modelling lattice imperfections, one would typically resort to diluted structures, where starting from a regular lattice, a fraction of sites or bonds is randomly removed, as illustrated in the left panel of Figure 1.2, where the individual nodes end up with a varying number of neighbours. In a related construction, one could also have random interaction strengths among neighbours instead of spatially uniform ones. In both cases, certain regions of the system interact more tightly than others, and as a consequence, might respond differently to changes of external variables.

Besides disordered structures originating from regular ones by, for instance, random dilutions or deformations, one might go one step further and place the nodes randomly in space. Connecting the cloud of points according to given geometric rules then gives rise to what is called *topological disorder*. If, moreover, interactions are solely local, i. e. only short-ranged links between nodes exist, one speaks of *proximity graphs*. One such construction is the *random geometric graph*, where each node is connected to all nodes within a given fixed distance, as can be seen in Figure 1.2. However, the possibilities are essentially endless here. Linking rules

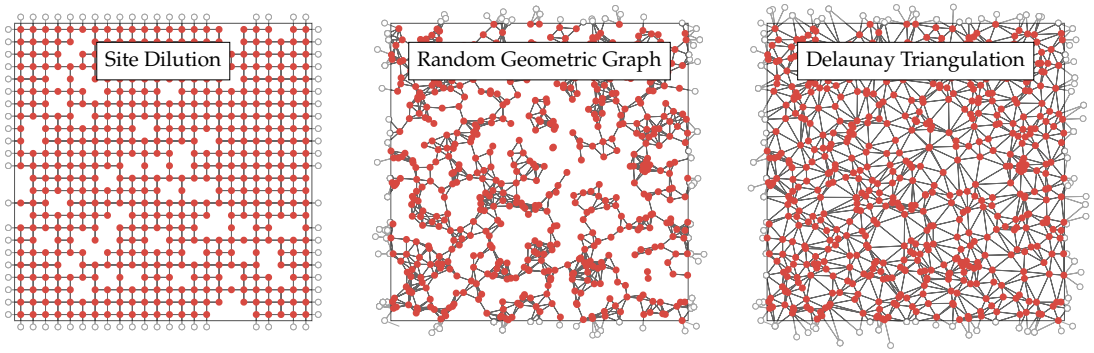

Figure 1.2 | Disordered lattices. The left panel represents a regular square lattice, where a number of sites have randomly been removed. The middle and right panel illustrate realizations of topological disorder, where the positions of the points are randomly chosen.

might, for instance, attempt to model certain real materials, or mimic their growth processes or, still, simply display a theoretically interesting property. From a more abstract, theoretical point of view, the exact realization of the disorder might however only play a secondary role. One is more interested in identifying the overarching characteristics which influence the physical model, instead of focusing on individual specifics. In the context of critical phenomena, the central question, and also the key subject of this work, can be stated as follows:

Under the influence of quenched disorder, will the universal properties of a continuous phase transition be altered or do they remain unaffected by this perturbation?

In fact, the study of critical phenomena on random geometries has a considerably long history, essentially dating back to 1974 when Arthur Brooks Harris put forward his celebrated relevance criterion, which successfully explains the influence of spatially *uncorrelated* disorder (e. g. random dilution) [46, 47]. His criterion states that the critical behaviour of a physical model is stable against quenched spatial disorder whenever

$$d\nu > 2,$$

where ν is the critical exponent of the correlation length of the model and d denotes its dimensionality. Although originally derived from heuristic arguments, the criterion can be motivated by explicit dimensional analysis of the corresponding field-theoretic setup. Driven by an increasing interest in the physics of spin glasses starting in the late 1970s [48, 49] and the discovery of the *replica trick* at the same time, uncorrelated quenched randomness could soon be handled by analytical techniques, such as the renormalization group framework. Consequently, the physics of complex systems on diluted regular structures is fairly well understood today.

In contrast, only little is known about the influence of topological disorder. Due to the significant increase in computing power over the last decades, numerical simulations on random lattices have been feasible since the early 1990's [50, 51]. Simulations particularly benefited from significant improvements in the field of numerical Monte Carlo sampling techniques discovered only a few years earlier, such as efficient cluster algorithms and histogram reweighting methods [52–56]. Consequently, since this time, a considerable number of basic models of statistical

physics, most notably the ferromagnetic Ising model and its generalizations (Potts, XY, Blume-Capel model, etc.) [50, 57–63], spin glasses [64], as well as non-equilibrium phenomena [65, 66], have been simulated on topologically disordered structures. The large majority of these studies concentrated on the so-called random *Delaunay triangulations* (illustrated in the right panel of Figure 1.2), strongly related to the well-established partition of space into Voronoi cells.

Most of these studies provided valuable information and could, for the specific model they were considering, answer the question raised above on the relevance of disorder on the phase transition. However, a general understanding was still lacking, until in 2014 Barghathi and Vojta [67] made a significant step towards a general relevance criterion for disordered structures, when they, motivated by earlier contributions of Luck [68], put forth what we will call the Harris-Barghathi-Vojta (HBV) criterion. According to their line of reasoning, the decay of spatial fluctuations of the local coordination numbers on different length scales governs the stability of the critical point. More precisely, they found disorder to be irrelevant when

$$a\nu > 1,$$

where a denotes a dimension-dependent geometric exponent of the lattice. The HBV criterion successfully explained all existing numerical results known at the time. Consequently, from a phenomenological point of view, with topological disorder not within the reach of analytical methods, at this point the topic seemed to be settled.

1.3 Results

In this work we seek to further advance the understanding of critical phenomena on topologically disordered structures. This is done by systematic numerical Monte Carlo studies of a number of physical models on specifically designed geometries. A specific goal is to shed light on the role of coordination number fluctuations which are believed to constitute the main relevant variable encoding the randomness of disordered graphs in the context of critical behaviour [67–69]. Surprisingly our results raise *considerable doubt* whether this assumption is indeed correct and suggest that geometric properties *beyond coordination numbers* need to be considered. Furthermore we are able to explicitly construct a setup which even *violates all existing relevance criteria*. Overall, the results of the present thesis reveal substantial shortcomings in the current understanding of critical phenomena on topologically disordered structures and suggest that the quest for a better understanding needs to be continued.

As already indicated, all major conclusions of this work primarily rely on results of specifically tailored numerical studies. Due to the necessary averaging over disorder configurations, as well as the demand for large system sizes in order to reduce finite-size effects, the corresponding simulations inevitably require high-performance computing (HPC) resources. These were provided by the *JULIA* and *ITPA* clusters, both located at Würzburg University, as well as by the Leibniz Supercomputing Centre through the *GCS Supercomputer SuperMUC*. In total, numerical calculations took about five million core hours, equivalent to a modern Intel CPU.

Even though all activities of the present work share the common goal of advancing the understanding of critical phenomena on topologically disordered structures, the results can be separated into five major parts, which will be summarized in the following:

Violation of the Harris-Barghathi-Vojta criterion

Physical Review Letters ***121****, 100601 (2018) [P1],*
in collaboration with J. S. E. Portela and F. Goth

As mentioned earlier in the introduction, in 1974, Harris proposed his celebrated criterion: Continuous phase transitions in d-dimensional systems are stable against quenched spatial randomness whenever $d\nu > 2$, where ν is the clean critical exponent of the correlation length. Forty years later, motivated by violations of the Harris criterion for certain lattices such as Voronoi-Delaunay triangulations of random point clouds and inspired by earlier works of Luck [68], Barghathi and Vojta [67] put forth a modified criterion for topologically disordered systems, $a\nu > 1$, where a is the disorder decay exponent, which measures how fast coordination number fluctuations decay with increasing length scale (HBV criterion).

We present a topologically disordered lattice with coordination number fluctuations that decay comparably slow (similar to those of conventional uncorrelated randomness), but for which the clean universal behaviour is preserved, hence violating even the modified criterion. Specifically, we define the DT^+ lattice: a Delaunay triangulation of a Poissonian point cloud, furnished with additional local bonds. This lattice is constructed from a usual DT triangulation to which a number of bonds between next-nearest neighbours are randomly added. We find the aforementioned disorder decay exponent for the DT^+ to be $a = 1$, which follows from the additional bonds being a source of uncorrelated disorder, which decays more slowly than the coordination number fluctuations of the original DT lattice. The HBV criterion therefore predicts that our construction should not display clean universal behaviour for any universality class with $\nu < 1$, such as directed percolation (DP), where $\nu \approx 0.73$. In order to verify this prediction, we perform extensive numerical simulations of the contact process on the DT^+ lattice and find strong indication of unchanged clean universal behaviour, hence clearly contradicting the predictions of HBV and Luck.

The Constant Coordination lattice

Physical Review E ***97****, 022144 (2018) [P2],*
Physical Review Research ***1****, 033061 (2019) [P3],*
in collaboration with J. Richter and J. S. E. Portela

We develop a stochastic algorithm for constructing a topologically disordered (i. e. non-regular) spatial lattice with nodes of constant coordination number, the *CC lattice*, presenting a novel type of connectivity disorder. Among other applications, physical systems such as certain amorphous materials with low concentration of coordination defects are an important example of disordered, constant-coordination structures in nature. In a first publication [P2], we perform large scale Monte Carlo simulations of the equilibrium spin-1/2 Ising model on a two-dimensional realization of this lattice, and using finite-size scaling techniques, find disorder-dependent effective critical exponents, similar to diluted 2D Ising systems, showing thus no clear universal behaviour. As our original CC algorithm presented an unfavourable computational complexity of $\mathcal{O}(N^2)$, where N denotes the number of sites the lattice is constructed from, as well as some inconvenient tuning parameters related to the applicability of finite-size scaling

methods, we dramatically improve the construction procedure of the CC lattice in a follow-up publication [P3]. The improved algorithm reduces the algorithmic complexity to $\mathcal{O}(N)$ and eliminates any issues related to finite-size properties entirely. As a result, the CC lattice presents an alternative to traditional proximity graphs which, especially in higher dimensions, is significantly faster to build. As an application, we characterize the criticality of the 3D Ising model on the CC lattice. We find that its phase transition belongs to the clean Ising universality class, establishing that the disorder present in the 3D CC lattice constitutes a non-relevant perturbation for this model in the sense of renormalization group theory.

Since all existing relevance criteria for topological disorder [67, 68] rely on coordination number fluctuations, they cannot be applied to our CC lattice. This raises the question, for which classes of transitions this type of disorder can be a relevant perturbation. Hence, in addition to the extensive studies of the two- and three-dimensional Ising model, reported above, we investigate also the non-equilibrium phase transition of the two-dimensional contact process on the two-dimensional CC lattice, in order to cast even more light on this quest. Our results suggest, that in this case, the disorder is relevant, as the dynamical scaling behaviour turns out non-conventional, which rules out the directed percolation universality class.

Continuous phase transitions on random Voronoi graphs

Physical Review E ***100****, 062118 (2019) [P4],*
in collaboration with J. S. E. Portela

The Voronoi construction is ubiquitous across the natural sciences and engineering. In statistical mechanics, however, only its dual, the Delaunay triangulation, has been considered in the investigation of critical phenomena. We set to fill this gap by studying the Ising model, the contact process, and the conserved stochastic sandpile model on two-dimensional random Voronoi graphs. Particular motivation comes from the fact that these graphs have vertices of constant coordination number, making it possible to isolate topological effects of quenched disorder from node-intrinsic coordination number disorder. Using large-scale numerical simulations and finite-size-scaling techniques, we are able to demonstrate that all three systems belong to their respective clean universality classes. Therefore, quenched disorder introduced by the randomness of the lattice is irrelevant and does not influence the character of the phase transitions. We report the critical points to considerable precision and, for the Ising model, also the first correction-to-scaling exponent.

Dual Tessellation

submitted for publication in Scientific Reports (preprint: arXiv:1907.05809),
in collaboration with J. S. E. Portela and F. Goth

Combining our previous findings, it becomes clear that existing criteria predicting the relevance of disorder on continuous phase transitions, although successful for a wide range of system can not be applied to some structures and even result in incorrect predictions on others. As a result, an area of research which was already settled is effectively re-opened, since the quest for a general criterion must continue. In particular, our numerical results strongly suggest that

coordination number fluctuations might only be a manifestation of a more general variable, describing the spatial structure of disorder. We strive to take a couple of first steps towards a more general description, by investigating the connectivity properties of the lattice in detail.

We design two analysis tools that seem to succeed in qualitatively distinguishing relevant from non-relevant topological disorders. The so-called *dual tessellation* generalizes the graph-theoretical concept of *duality* from planar to non-planar graphs. Specifically, we devise an algorithm which decomposes the lattice into generalized faces, so-called polygons with weights, which characterize the connectivity of the lattice locally. Then, a HBV-type coarse-graining analysis is performed on this set of polygons, which can be related to the correlation length divergence at the critical point. As a second approach we replace all links in the lattice by Hookean springs and let the system relax. It becomes clear that some graphs be will strongly distorted under this transformation, whereas others present themselves essentially stable, i. e. structurally invariant. It turns out that the stability of a graph in this setup can be somewhat related to its influence on critical systems, even though we can not provide a rigorous relation.

MARQOV framework

to be released; in collaboration with F. Goth, M. Döring, J. Richter

All numerical simulations of equilibrium models have been carried out using the MARQOV (MASSIVELY PARALLEL QUENCHED DISORDER ON VARIABLE GEOMETRIES) code framework, which was developed as a part of the present work and has recently been granted funding from the Bavarian Competence Network for Technical and Scientific High Performance Computing (KONWIHR). The project currently is in the state of a working prototype and offers a convenient, HPC-optimized workflow for the simulation of disordered canonical spin systems, using state-of-the-art numerical techniques and algorithms. All performance critical parts are written in C++14, whereas the data analysis is carried out in Jupyter notebook templates, written in Python 3. A comprehensive overview over the current features will be given in Section 4.2.

1.4 Outline

This thesis consists of five major parts, given by the chapters 2-6. The structure is schematically illustrated in Figure 1.3, where arrows denote the dominant dependencies among the corresponding chapters. A detailed outline is given in the following:

- Chapter 2 lays the necessary theoretical groundwork. We introduce the phenomenology of phase transitions as well as their classification scheme. Focussing on continuous transitions, we discuss the important concepts of universality and scaling. Then, the equilibrium spin-1/2 Ising model and its generalizations to higher symmetries, as well as the non-equilibrium contact process and Manna sandpile model are introduced. Later in this chapter, we explain how the scaling behaviour at criticality is modified in the presence of a finite geometry, establishing the finite-size scaling theory. Finally, we demonstrate how quenched randomness can be implemented and elaborate on the current state of research regarding the stability of continuous phase transitions on this type of disorder.

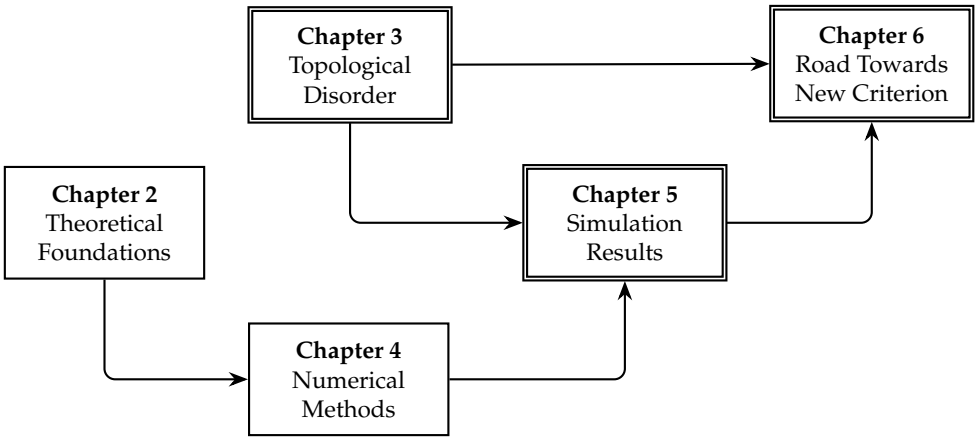

Figure 1.3 | Schematic structure of this thesis. Blocks denote individual chapters and arrows indicate the dependencies. Double framed blocks represent own results. Introduction and conclusion are omitted.

- In Chapter 3, a comprehensive overview over the relevant disordered structures considered in this work, is provided. After a brief summary of established proximity graph constructions, the larger part of this chapter concentrates on the *constant coordination lattice*, which was newly developed during the project. We elaborate on the basic idea of this construction before presenting the explicit algorithmic details. Also, relevant properties such as the computational complexity, dimensionality and possible generalizations are discussed. The chapter is concluded with an analysis of coordination number fluctuations for all random lattices considered.
- In Chapter 4, we introduce the necessary computational techniques for the simulation of classical equilibrium spin models. After a brief exposition on the essential aspects of Monte Carlo sampling, the implementation of update algorithms and histogram reweighting methods is presented. Furthermore, we define observables and expand on the specific finite-size scaling relations used later in the analysis. Also, detailed attention is given to the analysis of statistical errors. In a similar manner, numerical algorithms for non-equilibrium systems are presented in the second part of this chapter, including dynamical simulations, starting from a single seed or a fully occupied lattice, as well as methods probing the so-called quasi-stationary state. In this context, we review both static and dynamic scaling properties of non-equilibrium phenomena in detail and discuss how they are affected in the presence of disorder.
- Chapter 5 presents the detailed results of our numerical Monte Carlo simulations.
- In Chapter 6, we give a brief summary of the numerical results and their immediate implications. Motivated by the apparent shortcomings in the current understanding of critical phenomena on topologically disordered graphs, we introduce two conceptually new ways to categorize disordered structures, the dual tessellation and elastic relaxation.
- Chapter 7, concludes this thesis. The numerical results, and their implications are summarized in detail, before, in the Outlook, Chapter 8, several further interesting research directions, based on the findings of this thesis, are suggested.

Chapter 2

Theoretical Foundations

"Es ist das schönste Los einer physikalischen Theorie, wenn sie selbst zur Aufstellung einer umfassenden Theorie den Weg weist, in welcher sie als Grenzfall weiterlebt."

– Albert Einstein

2.1 Fundamentals of phase transitions

This section gives a brief introduction on the phenomenology of phase transitions. In particular, after presenting their modern classification scheme, we concentrate on continuous transitions and introduce the important concepts of universality and scaling. The scope of this chapter is chosen as to provide the necessary groundwork for this thesis. More comprehensive reviews can be found in standard textbooks on critical phenomena [70–75], which are here the implicit references.

Phase transitions are part of our everyday life. The most immediate example are the three phases of water, namely solid (ice), liquid and gas (vapour) and the respective transitions between them, most notably melting, freezing, boiling and condensation. However, phase transitions can also occur away from states of matter and thermodynamic equilibrium, such as jamming transitions on a road. If the density of cars exceeds a critical value, smooth flow becomes unstable and changes phase into a traffic jam, representing a (non-equilibrium) transition [76]. Generally speaking, a phase transition is characterized by a *drastic* change of macroscopic properties when

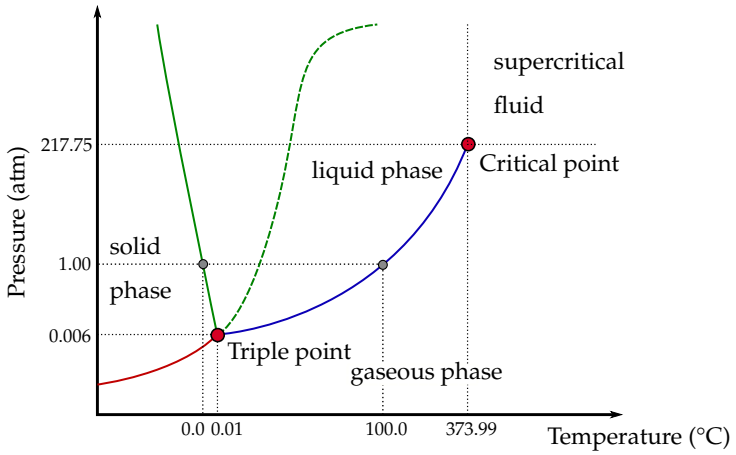

Figure 2.1 | Phase diagram of water. The sublimation curve is drawn in red, the evaporation curve in blue and the melting curve in green. Specifically, the solid green line represents the melting/freezing transition of water, which is *anomalous* compared to most other substances (dashed green line). Grey dots mark the normal freezing and boiling points of water.

certain system parameters are *smoothly* varied. The qualitatively distinct states of the system on either site of the transition are called *phases*. They can typically be characterized by a small number of macroscopic observables. Returning to the example of water, it is clear that the three phases comprise entirely different microscope structures. In the solid state, water molecules are rigidly packed close together and form a crystalline lattice whereas in the liquid phase weaker intermolecular forces allow for a movement of individual particles. Hence, they are no longer regularly arranged and can even slide past each other, although their mean separation is still small. Finally, in the gaseous phase, individual molecules are effectively unbound and the typical distance is much greater then the molecule size. Figure 2.1 shows the phase diagram of water as a function of the external parameters temperature and pressure, where the transitions are marked by solid lines.

The physical origin of phase transitions in classical thermodynamic equilibrium can be understood as an interplay between the internal energy E and the entropy S of a system, both contributing to the *Helmholtz free energy*, defined as

$$F = E - TS. \tag{2.1}$$

Whereas the internal energy favours an ordering of individual degrees of freedom[2], entropy naturally privileges disorder. As the system seeks to minimize F, it is clear that for decreasing temperature T, the entropy term becomes less dominant. At the point where its contribution remains too weak to effectively counter the energy term, the system falls into an ordered state. In this case, the temperature is called the *control parameter* as it drives the transition. Quantum phase transitions on the other hand are driven by quantum fluctuations at zero temperature, rather than by thermal fluctuations [77, 78]. Notice, however, that in the present work only classical phase transitions will be considered.

[2] In the case of water molecules, the arrangement of individual atoms generates an effective dipole moment. The lower the temperature, the stronger the individual dipoles tend to align with their neighbours.

Table 2.1 | Phase transitions and their order parameters. Examples adopted from [73].

System	Transition	Order parameter
H_2O, ^4He, Fe	liquid–solid	shear modulus
Xe, Ne, N_2, H_2O	liquid–gas	density difference
Fe, Ni	ferromagnet–paramagnet	magnetization
$RbMnF_2$, La_2CuO_4	antiferromagnet–paramagnet	staggered magnetization
^4He, ^3He	superfluid–normal liquid	superfluid density
Al, Pb, $YBa_2Cu_3O_{6.97}$	superconductor–metal	superfluid density
Li, Rb, H	Bose–Einstein condensation	condensate

In the theory of critical phenomena, the central property of the system is represented by the *order parameter* which distinguishes between the different phases on either side of the transition. This parameter is not necessarily macroscopic, as can be seen in Table 2.1, where order parameters for a number of different systems are listed. Usually, in the ordered phase, it has a finite positive value and vanishes to zero in the disordered phase.[3] However, order parameters are not restricted to being scalar quantities, but may be more elaborated objects, such as an n-component vector or a elements of a group.

From a more technical point of view, the abrupt change of macroscopic system properties at the transitions is reflected in the thermodynamic potential used to describe the system (in our case the free energy) becoming non-analytic at a specific point in phase space. As a result, thermodynamic quantities, which can be written as derivatives of the free energy, may become discontinuous. This observation was the basis for a historic classification scheme by Paul Ehrenfest [79]. Concretely, phase transitions were categorized according to the first derivative of the free energy which presented discontinuous behaviour, resulting in first-order, second-order and higher-order transitions. In a more modern classification only the first derivatives of the free energy are considered and one distinguishes between *continuous* and *discontinuous* phase transitions. Phenomenologically, discontinuous phase transitions are characterized by the emergence of a *latent heat* and a co-existence of phases at the critical point. This is often accompanied by hysteresis or memory effects due to the macroscopically long time the system requires to relax from metastable states of the old phase after crossing the transition. The *correlation length*, which denotes the spatial length scale over which individual microscopic degrees of freedom are correlated with each other, in general remains finite. Examples for discontinuous phase transitions include melting of three-dimensional solids and gas-to-liquid transition (condensation).

Continuous transition are characterized by all first-order derivatives of the associated free energy being continuous. A special type are so-called infinite-order transitions, arising, for instance, in the presence of topological constraints (such as the Kosterlitz-Thouless transition of the two-dimensional XY model [80]) or from quantum fluctuations. A key property of continuous transitions is that, at the critical point, fluctuations on all length scales become equally

[3] Ordering does not necessarily refer to real space coordinates or orientations, but can also take place in more abstract spaces, such as the momentum space, in the case of superfluid helium.

important, resulting in a scale invariant appearance of the system. Consequently, as correlations over all distances are present, the correlation length becomes effectively infinite at the transition[4] and physical quantities behave non-analytically. The degree of these singularities is described by so-called *critical exponents*. In a system undergoing a paramagnetic-to-ferromagnetic phase transition[5], a convenient choice for the control parameter is given by the *reduced temperature*, defined as

$$\tau \equiv \frac{T - T_c}{T_c}, \tag{2.2}$$

measuring the distance from the critical point T_c. The divergence of the correlation length can hence be written as

$$\xi \sim \tau^{-\nu} \tag{2.3}$$

which defines the associated critical exponent ν. Moreover, the magnetization per spin, acting as the order parameter of the transition, diverges as

$$m = -\frac{1}{V}\left(\frac{\partial F}{\partial h}\right)_T \sim (-\tau)^{\beta} \qquad \text{for} \qquad T \leq T_c \tag{2.4}$$

at vanishing external field h, where V denotes the number of spins in the system. Similar relations hold for the susceptibility and the specific heat, given by

$$\chi = -\frac{1}{V}\left(\frac{\partial^2 F}{\partial h^2}\right)_T = \left(\frac{\partial m}{\partial h}\right)_T \sim |\tau|^{-\gamma} \tag{2.5}$$

and

$$C = -\frac{T}{V}\left(\frac{\partial^2 F}{\partial T^2}\right)_h \sim |\tau|^{-\alpha} \tag{2.6}$$

respectively, where γ and α denote the corresponding critical exponents.

It has been found experimentally that various physical systems obey power laws near their critical point, already before an appropriate theoretical framework was available. In a celebrated article [11], Edward A. Guggenheim showed in 1945 that in a suitably rescaled temperature-density plot (see Figure 2.2), data points of several different liquid-gas systems collapse onto one single curve. The order parameter exponent, in this case given by the relation $(\rho - \rho_c) \sim (-\tau)^{\beta}$, was found to be remarkably close to $1/3$. Strikingly, the same exponent was found in magnetic phase transitions [81], providing strong experimental evidence that the character of continuous transitions is only determined by few fundamental (global) system properties, regardless of the details of the atomic interactions. As a matter of fact, experimentally determined critical exponents are invaluable in verifying the accuracy of theoretical predictions, which oftentimes

[4] Experimentally, this gives rise to the phenomenon of *critical opalescence* at the critical point of fluids (endpoint of the vaporization curve in the phase diagram Figure 2.1), where liquid and gaseous phase become indistinguishable. The typical size of density fluctuations becomes comparable to the wavelength of light and hence drastically changes the optical appearance of the medium at criticality.

[5] For the sake of simplicity we stick to the magnetic language in this section. A generalization to other types of transitions is straightforward.

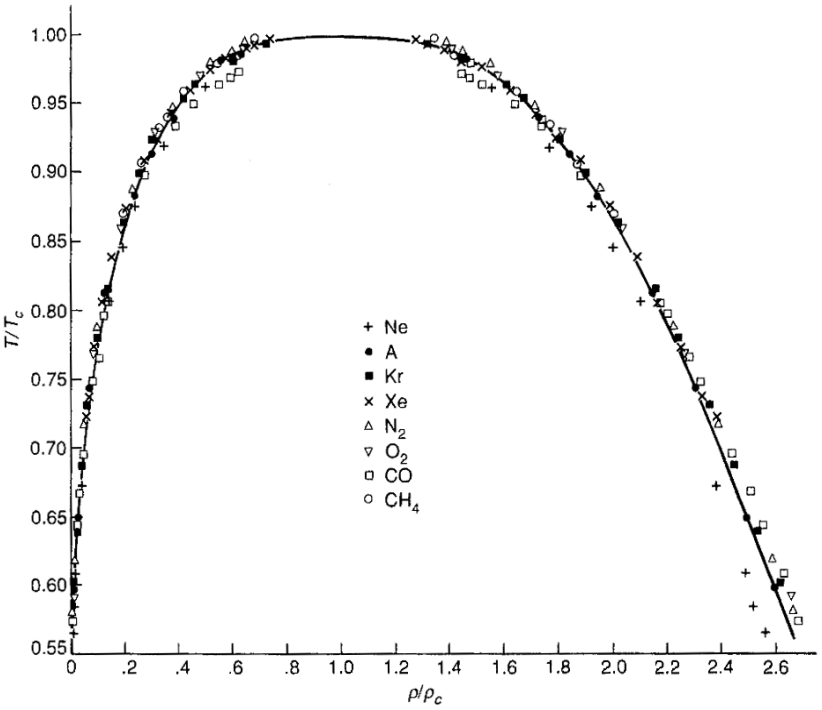

Figure 2.2 | Experimental universality. Data collapse of liquid-gas coexistence curves of several fluids, as presented in Reference [11], indicating a strikingly similar critical behaviour. The solid black line represent a power-law fit with an exponent $\beta = 1/3$ (see text).

are only available as perturbation series expansions of associated field-theoretical models or from numerical Monte Carlo simulations. To this date, the most precise measurement of any critical exponent was performed for the specific heat at the superfluid transition of ^{4}He in micro-gravity aboard the space shuttle "Columbia", where a value of $\alpha = -0.0127 \pm 0.0003$ was found [82, 83]. Interestingly, these results represent a noticeable discrepancy (about 8σ) compared to the most precise numerical estimates from Monte Carlo simulations of the three-dimensional XY model [84, 85], which might eventually be resolved through very accurate estimates recently provided by conformal bootstrap techniques [86, 87].

As already mentioned, at continuous transitions, due to the diverging correlation length, microscopic details are washed out. This gives rise to the important concept of *universality*, according to which the microscopic details of the system are largely irrelevant. The character of the phase transition (encoded in the values of the critical exponents), depends *only* on the dimensionality of the system, the symmetry of its order parameter and the range of interactions. As as consequence, surprisingly different systems fall into the same *universality class* and hence show the same exponents, such as the transition of liquid helium and the magnetic XY model, as was already pointed out above. Moreover, the emergence of self-similar behaviour at the critical point gave rise to the *scaling hypothesis* originally introduced in the 1960s by Widom [88, 89] with contributions of other authors (compare, e. g. [14, 90–93]). Sticking to magnetic language, the free energy density depends on the reduced temperature τ and the external field

h and can be written as the sum of a regular and a singular part

$$f(\tau, h) = f_{\text{reg}}(\tau, h) + f_{\text{sing}}(\tau, h), \tag{2.7}$$

where the latter is a generalized homogenous function, given by

$$f_{\text{sing}}(\tau, h) = \lambda^{-d} f_{\text{sing}}(\lambda^{y_\tau}\tau, \lambda^{y_h} h), \tag{2.8}$$

with λ, y_τ and y_h being scalar numbers. We take $\lambda^{y_\tau}|\tau| = 1$ and obtain

$$f_{\text{sing}}(\tau, h) = \tau^{d/y_\tau} f_{\text{sing}}(1, |\tau|^{-y_h/y_\tau} h) \equiv \tau^{d/y_\tau}\, \Psi_{\pm}(h/\tau^{\,y_h/y_\tau}). \tag{2.9}$$

As can be seen, the free energy can be expressed by a universal *scaling function* (in this case denoted by Ψ) depending only on a single argument. Note that we added an index to Ψ, in order to account for the behaviour below and above the transition. The exponent $\Delta \equiv y_\tau / y_h$ is often called *gap exponent*. Moreover, note that although Widom wrote down Equation (2.8) as an educated guess, it can be rigorously derived using renormalization group (RG) techniques [75], which will be briefly discussed later. In the RG framework, λ represents the factor under which the system is rescaled and the exponents y_t and y_h represent the scaling dimensions of the (relevant) scaling fields $u_\tau = \tau$ and $u_h = h$.

In order to obtain relations between the critical exponents introduced earlier and the scaling fields, we compute the corresponding derivatives, e. g. for the magnetization

$$m(\tau, 0) = \left.\frac{\partial f(\tau, h)}{\partial h}\right|_{h=0} \sim \tau^{(d-y_h)/y_\tau}, \tag{2.10}$$

which allows us to identify $\beta = (d - y_h)/y_\tau$. Differentiating again yields the susceptibility exponent $\gamma = (d - 2y_h)/y_\tau$. A similar relation can obtained for the specific heat

$$C(\tau, 0) = \frac{\partial f^2(\tau, h)}{\partial \tau^2} \sim \tau^{d/y_\tau - 2}, \tag{2.11}$$

yielding $\alpha = 2 - d/y_\tau$. Finally, we can obtain another exponent δ, defined on the critical isotherm as

$$m(0, h) \sim h^{1/\delta} \qquad \text{for} \qquad h \to 0 \tag{2.12}$$

by setting $\lambda^{y_h} h = 1$ in Equation (2.8) and differentiating with respect to the external field at $\tau = 0$. We find $\delta = y_h/(d - y_h)$. As already mentioned, there are only two relevant scaling fields, hence the exponents α, β, γ and δ are not independent and the knowledge of two of them fully characterizes the universality class. Using the relations we found above to eliminate y_t and y_h, one finds the following *scaling relations*

$$\alpha + 2\beta + \gamma = 2 \qquad \text{(Rushbrooke)} \tag{2.13}$$

$$\gamma = \beta(\delta - 1) \qquad \text{(Widom)}. \tag{2.14}$$

So far we have not considered the critical exponent of the correlation length ν. How is

it related to the other exponents? Answering this question requires us to consider another important quantity, the two-point correlation function, defined by

$$G(\boldsymbol{x}_1, \boldsymbol{x}_2, \tau, h) \equiv \langle \phi(\boldsymbol{x}_1)\phi(\boldsymbol{x}_2)\rangle - \langle \phi(\boldsymbol{x}_1)\rangle\langle \phi(\boldsymbol{x}_2)\rangle, \tag{2.15}$$

where $\phi(\boldsymbol{x})$ represents the local value of the order parameter at spatial position $\boldsymbol{x}$.[6] At criticality the system is scale-invariant, hence we can safely assume that G depends only on the distance. Choosing $\boldsymbol{x}_2$ as the origin this is $G(x, \tau)$ at vanishing external field, where $|\boldsymbol{x}_1| \equiv x$. Using similar scaling arguments as above (i. e. assuming that $G(x, \tau)$ is a generalized homogenous function) leads to

$$G(x, \tau) = \lambda^{2y_h - 2d} G(\lambda^{-1}x, \lambda^{y_\tau}\tau). \tag{2.16}$$

This general form allows us to extract the behaviour at criticality by setting $\tau = 0$ and $\lambda = x$, resulting in

$$G(x) \sim x^{2y_h - 2d}, \tag{2.17}$$

which means that the correlation function decays algebraically with distance at the critical point. Since the corresponding critical exponent is typically denoted by $G(x) \sim x^{-d+2-\eta}$, we obtain $\eta = d - 2y_h + 2$.

Finally, using the fact that, away from the critical point, the correlation function should decay exponentially as $\mathrm{e}^{-x/\xi}$ for large distances, by taking $\lambda^{y_\tau}\tau = 1$ we find $\nu = 1/y_\tau$, which eventually leads to the following scaling relations

$$\gamma = (2 - \eta)\nu \qquad \text{(Fisher)} \tag{2.18}$$

$$2 - \alpha = d\nu \qquad \text{(Josephson)}. \tag{2.19}$$

Due to the explicit appearance of the dimensionality of the system, the last relation is termed *hyperscaling relation*. It is only valid below the upper critical dimension, which will be introduced in the following section.

[6] In this work we consider lattice models, therefore $\phi(\boldsymbol{x}_i)$ might be thought of as spins on discrete lattice positions $\boldsymbol{x}_i$.

2.2 Equilibrium systems

In this section we concentrate on continuous phase transitions in thermodynamic equilibrium. Specifically, the Ising universality class and its generalization to higher symmetries are introduced. Moreover, we give an overview of the corresponding mean-field approximation and discuss how the phenomenological Landau theory captures the essential qualitative features of the phase transition. Also the renormalization group approach is briefly discussed.

2.2.1 Ising model

The prototypical physical system showing a continuous phase transition with individual degrees of freedom behaving collectively over long distances is the celebrated *Ising model* [2], defined by the Hamiltonian

$$\mathcal{H} = -\sum_{\langle i,j\rangle} J_{ij} s_i s_j - \sum_i h_i s_i, \qquad s_i = \pm 1, \tag{2.20}$$

where s_i are spins on discrete lattice positions. Individual spins couple only to their nearest neighbours, which is denoted by $\langle i, j\rangle$. Moreover, J_{ij} encodes the coupling strengths between sites i and j and h_i is the external field at site i. The model can be interpreted as a toy model for uniaxial magnets where the spins can only align along a preferred direction. The system is said to be *ferromagnetic* if the J_{ij} are positive, which means that a parallel alignment of neighbouring spins is preferred, as it minimizes the internal energy. Likewise, taking $J_{ij} < 0$ results in *antiferromagnetic* interactions, where spins tend to align in an anti-parallel manner. As a consequence, these systems usually feature multiple ground states of minimal energy, depending on the structure of the lattice [94], a phenomenon which is usually referred to as *geometrical frustration* [95]. Moreover, if the system contains a mixture of ferro- and antiferromagnetic interactions, it will present an even richer variety of frustration effects and is commonly referred to as a *spin glass* (see [96] and references therein). In the present work, however, we only consider non-negative couplings, i. e. purely ferromagnetic interactions.

We assume the system to be in contact with a heat bath of temperature T (or inverse temperature $\beta = 1/T$) which allows for the exchange of energy.[7] Hence, it is formally described by a canonical ensemble and the partition function can be written as

$$Z(\beta, h) = \sum_{\{s_i\}} \mathrm{e}^{-\beta\mathcal{H}}, \tag{2.21}$$

where the sum runs over all possible assignments of spin values to lattice sites. The thermal expectation value of a macroscopic observable O can be expressed as

$$\langle O\rangle = \frac{1}{Z}\sum_{\{s_i\}} O\,\mathrm{e}^{-\beta\mathcal{H}}. \tag{2.22}$$

[7] We trust the reader to distinguish between inverse temperature and order parameter exponent which are both denoted by the symbol β in the literature.

As can be seen, in the case of uniform couplings $J_{ij} = J$ and spatially homogenous external field $h_i = h$, the system properties depend on two parameters only, given by the temperature T and the strength of the external field h. At vanishing external field, $h = 0$, the model exhibits a continuous phase transition at some critical temperature T_c. Below that temperature, it features an ordered phase where the majority of spins are aligned in the same direction. Above T_c, thermal fluctuations dominate and destroy the ordering.

Although the Ising model was originally introduced as a model for magnetism, its actual realm of application reaches far beyond that area. For instance, the Hamiltonian (2.20) is mathematically equivalent to a toy model for a lattice gas. In fact, phase transitions in quite diverse systems, featuring short-ranged interactions and a scalar order parameter, have been found to belong to the Ising universality class. Besides uniaxial magnets, it describes, e. g. experimental liquid-vapour transitions [97] and binary mixtures, ionic fluids [98], certain transitions in high-energy physics (see references in [25]), voter dynamics [99] and can even be found in fairly unexpected areas, such as neuroscience [100] and, as was already mentioned in Section 1, the dynamics of traffic signals [26], pistachio trees [27] and finance markets [28].

Whereas an analytical solution for the one-dimensional Ising model can be obtained relatively easily [2], tackling the two-dimensional model already turns out to be highly non-trivial, even in the absence of an external field. The Ising model on a square lattice was solved in a much-celebrated work by Lars Onsager in 1944 [101], who obtained an explicit expression for the free energy of an infinite system [22], given by

$$-\beta f = \ln 2 + \frac{1}{8\pi^2} \int_0^{2\pi} d\theta_1 \int_0^{2\pi} d\theta_2 \ln \left[\cosh^2(2\beta J) - \sinh(2\beta J)(\cos\theta_1 + \cos\theta_2) \right], \quad (2.23)$$

from which the critical temperature (for a square lattice)

$$T_c = \frac{2}{\ln(1+\sqrt{2})} \approx 2.269185\ldots \quad (2.24)$$

and critical exponents (see Table 2.2) can be rigorously derived.[8] For a detailed historical overview, we refer the reader to the excellent reviews [6, 104], which particularly discuss the impact of Onsagers solution on the field of critical phenomena. A modern summary of analytical approaches can be found in standard textbooks, such as [105]. In three dimensions, the Ising model remains unsolved. In this case, critical exponents are only approximately known from numerical Monte Carlo simulations, high-temperature series expansions, field-theoretic methods and – very recently – from conformal bootstrap techniques [87]. We list the critical exponents for several dimensions in Table 2.2.

Mean-field theory

A constructive approach, which allows a qualitative insight into the phenomenology of the Ising model is given by a so-called *mean-field* (MF) approximation, which is discussed in the following. Although it might seem a crude approximation, it describes the properties of the phase transition correctly. One starts by replacing the neighbouring spins which influence a

[8] The exact expression for T_c was in fact already found a few years earlier by H. Kramers and G. Wannier who discovered a duality between high- and low-temperature expansions of the free energy [102, 103].

Table 2.2 | Critical exponents of the Ising model in two and three dimensions as well as in the mean-field regime. The three-dimensional values are truncated to four decimal digits. Most precise estimates include results from high-precision Monte Carlo simulations and conformal bootstrap calculations [87, 106]. The validity of the MF results is discussed in the text.

Exponent	$d = 2$	$d = 3$	MF
β	$1/8$	0.3264	$1/2$
ν	1	0.6300	$1/2$
γ	$7/4$	1.2371	1
δ	15	4.7899	3
η	$1/4$	0.0363	0
α	0 (log)	0.1101	0 (disct.)

given spin s_i by an effective mean or *molecular field*. Specifically, the spin variables are separated into their thermal average and fluctuations

$$s_i = \langle s_i \rangle + \delta s_i \approx m + \delta s_i \tag{2.25}$$

where in the second step, the mean magnetic field m was introduced, which no longer depends on the spatial position. Plugging this approximation into the Hamiltonian (2.20), we find

$$\begin{aligned} \mathcal{H}_{\mathrm{MF}} &= -J \sum_{\langle i,j \rangle} (m + \delta s_i)(m + \delta s_j) - h \sum_i s_i \\ &\approx -J m^2 N_B - J m \sum_{\langle i,j \rangle} (\delta s_i + \delta s_j) - h \sum_i s_i \\ &= -J m^2 N_B - J m \sum_i q_i \delta s_i - h \sum_i s_i, \end{aligned} \tag{2.26}$$

where, in the second step, we neglected quadratic fluctuations and introduced N_B as the total number of bonds in the system. Moreover, in the third step we used the fact that fluctuations at different sites are effectively decoupled and introduced the local coordination number q_i, which represents the number of outgoing bonds. To further simplify the mean-field Hamiltonian, we assume a constant coordination number $q_i = q$ (which holds for any regular lattice) and express the remaining fluctuations in terms of their definition (2.25), yielding

$$\begin{aligned} \mathcal{H}_{\mathrm{MF}} &= -J m^2 N_B - J m q \sum_i (s_i - m) - h \sum_i s_i \\ &= -J m^2 N_B + J m^2 q V - (J m q + h) \sum_i s_i \\ &= \frac{1}{2} J m^2 q V - (J m q + h) \sum_i s_i, \end{aligned} \tag{2.27}$$

where V denotes the total number of sites in the system and we used the fact that $N_B = qV/2$. Ignoring the additive constant, which is irrelevant as it can be absorbed by redefining the energy scale, we recognize that the Hamiltonian can be written as a sum of decoupled spins, interacting

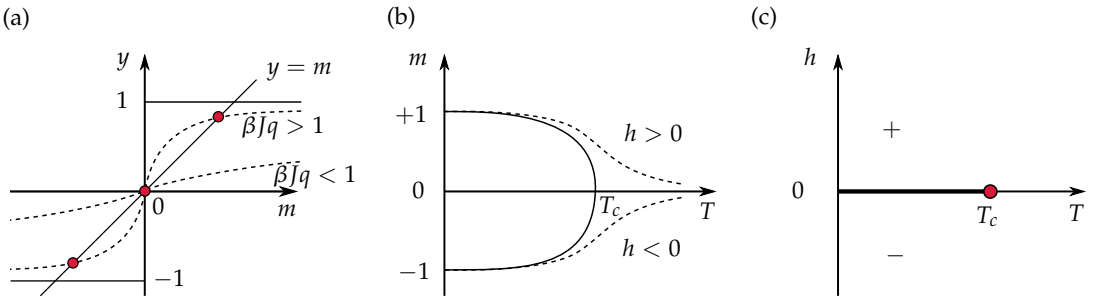

Figure 2.3 | Analytic solution of the Ising model. (a) Graphical solution of Equation (2.28) for $h = 0$ and different choices of βJq, marked as red dots. Dashed curves represent the function $\tanh(\beta Jmq)$ for $\beta Jq > 1$ (steep curve) and $\beta Jq < 1$ (flat curve). (b) Phase diagram in the magnetization/temperature plane for $h = 0$ (solid line) and $h \neq 0$ (dashed line). (c) Phase diagram in the (T, h) plane, presenting a first-order transition line (solid), ending at the critical point (red dot).

indirectly through an effective field $Jmq + h$.

As the next step, we compute an expression for the spontaneous magnetization, which is straightforward from the definition (2.22) given by

$$m \approx \langle s_i \rangle = \frac{1}{Z} \sum_{\{s_i\}} s_i \, \mathrm{e}^{-\beta \mathcal{H}_{\mathrm{MF}}} = \ldots = \tanh(\beta Jmq + \beta h), \tag{2.28}$$

resulting in a self-consistent *equation of state*. At this point it is instructive to graph our solution, as is done in Figure 2.3a, where m and $\tanh(\beta Jmq)$ are plotted for $h = 0$. When $\beta Jq < 1$, the only solution of Equation (2.28) is given by $m = 0$, whereas for $\beta Jq > 1$ we find two additional intersections at finite (positive and negative) magnetization. This implies that $T_c = Jq$ can be identified as the critical point and m acts as the order parameter. In Figure 2.3b, the solutions for m are plotted against the temperature. Note that the negative solution is also a physical one, as it reflects the $\mathbb{Z}_2$ symmetry of the system. In fact, below T_c the system selects either the positive or negative solution, whereas the solution $m = 0$ is unstable with respect to small perturbations (such as through an infinitesimal external field). Hence, in the low-temperature phase, the $\mathbb{Z}_2$ symmetry is *spontaneously broken*.

In order to obtain the mean-field value of the critical exponent of the order parameter, we expand Equation (2.28) around the critical point for $h = 0$, resulting in $m \approx \beta Jqm + (\beta Jqm)^3/3$. Solving for the magnetization yields

$$m = \pm \left(\frac{3(Jq - T)}{(\beta Jq)^2 Jq} \right)^{1/2} \sim \left(\frac{T_c - T}{T_c} \right)^{1/2} \tag{2.29}$$

and hence we obtain $\beta = 1/2$ as the corresponding exponent. Similar expansions yield also $\gamma = 1$, $\alpha = 0$ and $\delta = 3$ (see, e. g. Reference [72] for details).

So far we have not discussed the limits of our initial approximation of small fluctuations stated in Equation (2.25). In fact, the mean field approach results in a self-consistent picture only if fluctuations are indeed sufficiently small, such as we have assumed in our ansatz. In particular, considering a correlation volume ξ^d, we want the accumulated fluctuations to be

small compared to the average magnetization as the critical point is approached, in order for the MF theory to be valid [74]. Therefore, we require

$$\frac{\int_\xi \mathrm{d}^d x \, \langle \delta s_x \rangle \langle \delta s_0 \rangle}{\int_\xi \mathrm{d}^d x \, \langle s_x \rangle \langle s_0 \rangle} \to 0 \qquad \text{for} \qquad T \to T_c \qquad (\tau \to 0). \tag{2.30}$$

Using Equation (2.25), as well as the definition of the correlation function (2.15), the numerator can be computed explicitly

$$\begin{aligned} \int_\xi \mathrm{d}^d x \, \langle \delta s_x \rangle \langle \delta s_0 \rangle &= \int_\xi \mathrm{d}^d x \, \langle (s_x - \langle s_x \rangle) \rangle \langle (s_0 - \langle s_0 \rangle) \rangle & (2.31) \\ &= \int_\xi \mathrm{d}^d x \, \left(\langle s_x s_0 \rangle - \langle s_x \rangle \langle s_0 \rangle \right) & (2.32) \\ &= \int_\xi \mathrm{d}^d x \, G(x) \sim \chi, & (2.33) \end{aligned}$$

where in the last step we used the fact that the susceptibility is given by the integral of the correlation function over the whole space [74]. As the correlation function decreases exponentially fast for $|x| > \xi$, the approximation is justified. Turning to the denominator we obtain simply

$$\int_\xi \mathrm{d}^d x \, \langle s_x \rangle \langle s_0 \rangle \sim m^2 \xi^d \tag{2.34}$$

and can therefore re-express our consistency condition as

$$\frac{\chi}{m^2 \xi^d} = \frac{\tau^{-\gamma}}{\tau^{2\beta} \tau^{-\nu d}} \to 0 \qquad \text{for} \qquad \tau \to 0 \tag{2.35}$$

resulting in

$$\gamma < \nu d - 2\beta, \tag{2.36}$$

which is known as the *Ginzburg criterion*. For the MF exponents of the Ising universality class, this results in $d > 4$. Hence for dimensions larger then four, the mean-field calculations are exact, whereas for $d < 4$ the approximation is internally inconsistent. The boundary case $d_c = 4$ is called the *upper critical dimension* and shows leading MF critical behaviour with logarithmic corrections. Likewise, one can define a *lower critical dimension* d_l below which the MF approach fails even qualitatively, as there is no finite temperature phase transition. For the Ising model in one dimension no ordered phase exists, as can be explained by the lack of surface tension from magnetic domain walls [107]. Hence, no critical exponent can be defined and $d_l = 1 + \varepsilon$.[9]

[9] In fact *Van Hove's theorem* [108] states that in a one-dimensional equilibrium system with short-ranged interactions, a finite temperature phase transition can not exist. Although valid for the most prominent classes of transitions, the general range of applicability of this theorem has been questioned [109].

Landau theory

Besides the mean-field approach described above, where we performed a suitable approximation of the microscopic Hamiltonian in order to eliminate degrees of freedom, one can obtain a similar description of the critical behaviour of equilibrium systems by starting from first principles, such as symmetry considerations, and therefore without any precise knowledge of how interactions are realized in detail on a microscopic scale. In the so-called *Landau theory* one starts from a phenomenologically motivated free energy density f, which depends on the order parameter, conventionally denoted by ϕ. If we, for instance, consider an Ising-like model, the order parameter is scalar and the system is symmetric under $\mathbb{Z}_2$ transformations ($s_i \to -s_i$, $\forall i$). Therefore, we require the free energy density to be invariant under global changes of sign, $\phi \to -\phi$. We know that the order parameter vanishes at the critical point, hence we can expand f around $\phi = 0$, further assuming that it is an analytic function. This so-called *Landau free-energy expansion*[10] can be written as

$$f(\phi) = f_0 + \frac{r}{2}\phi^2 + \frac{u}{4!}\phi^4 + \frac{v}{6!}\phi^6 + \dots, \tag{2.37}$$

where f_0, r, u, and v are (in general temperature-dependent) phenomenological parameters and the numeric pre-factors are convention [75]. Note that terms of odd powers (ϕ, ϕ^3, ...) are forbidden by the symmetry constraint mentioned above. Furthermore, terms such as $|\phi|$ would violate the analyticity requirement.

What can be said about the phenomenological parameters? First, if u is positive, then the sixth-order term can be dropped, as we are only considering the vicinity of the critical point ($\phi \approx 0$) where it would result in sub-leading corrections. Moreover, we can add a term containing the external field, in a way which is compatible with our symmetry requirements[11], resulting in

$$f(\phi) = f_0 + \frac{r}{2}\phi^2 + \frac{u}{4!}\phi^4 - h\phi. \tag{2.38}$$

This already indicates how the Landau expansion, also for systems other than Ising magnets, can be obtained, namely by writing down all possible products and powers of the order parameters which respect the global symmetry requirements of the system up to the highest relevant order [107].

We know that the condition of thermodynamic equilibrium corresponds to finding the global minimum of the free energy. Hence, since we dropped the sixth-order term, necessarily $u > 0$, as otherwise an unphysical picture would arise, where $f \to -\infty$ as $\phi \to \pm\infty$. Incorporating this condition, the free energy is plotted in Figure 2.4 for three qualitatively different choices of the parameter r at zero external field. For $r > 0$ we find a global minimum at $\phi_0 = 0$, which is still there for $r = 0$, however very flat, i. e. presenting a neutral equilibrium instead of a stable one. For negative r, the minimum at $\phi_0 = 0$ becomes unstable and two new symmetric minima $\phi_\pm$ emerge, corresponding to the (spontaneously) symmetry-broken, low-temperature phase. The qualitative change of the free energy landscape at $r = 0$ suggests to identify this parameter with the distance from the critical point, which for the Ising model is given by the reduced

[10] Note that f is not the actual thermodynamic free energy, however strongly related (see, e. g. References [72, 74]).

[11] In the presence of a field, the free energy should be symmetric under simultaneous changes of signs $(\phi, h) \to (-\phi, -h)$.

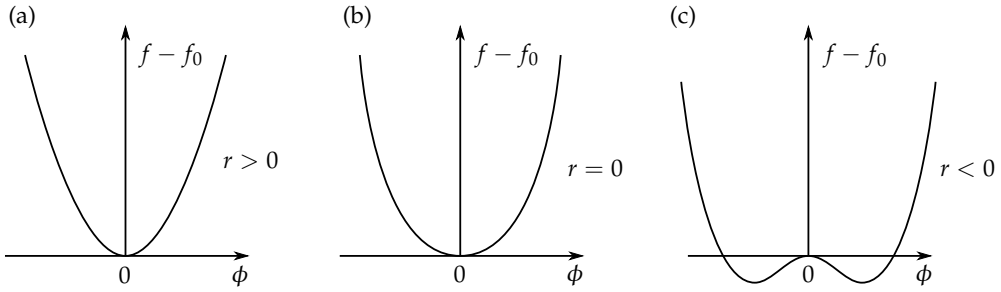

Figure 2.4 | Landau free energy. Illustration of the functional form of Equation (2.38) for positive fourth-order term, above (a), at (b) and below (c) the critical point. In the right panel, the point $\phi = 0$ has became unstable, resulting in two new minima which break the order parameter symmetry.

temperature $\tau = (T - T_c)/T_c$, therefore

$$r(\tau) = a\tau + \mathcal{O}(\tau^2) \qquad \text{with} \qquad a > 0. \tag{2.39}$$

Any dependence of higher order on the reduced temperature will not contribute to the leading behaviour at the transition. Similar arguments hold for the parameter u, which can, without loss of generality, be set to a temperature-independent constant.

The framework of Landau theory lets us easily determine critical exponents. We set $h = 0$ and consider the two regimes $\tau < 0$ and $\tau > 0$, i. e. below and above the critical point, separately. In the high-temperature phase, we already know the solution $\phi_0 = 0$, hence $f(\tau > 0) = f_0$. In the low-temperature regime we minimize f explicitly

$$\frac{\mathrm{d}f}{\mathrm{d}\phi} = a\tau\phi + \frac{u}{6}\phi^3 = 0, \tag{2.40}$$

yielding the equilibrium order parameter $\phi_\pm^2 = 6a|\tau|/u$. This allows us to read off the exponent $\beta = 1/2$, which is precisely the mean-field exponent found earlier. Keeping, instead, a non-zero external field in the minimization calculation yields the equation of state

$$h(\tau, \phi) = a\tau\phi + \frac{u}{6}\phi^3 \tag{2.41}$$

which, on the critical isotherm $\tau = 0$, allows us to read off another exponent, $\delta = 3$, as $h \sim \phi^3$. Furthermore, we can compute an expression for the inverse susceptibility of the order parameter as

$$\frac{V}{\chi} \equiv \left(\frac{\partial h}{\partial \phi}\right)_T = a\tau + \frac{u}{2}\phi^2. \tag{2.42}$$

Inserting the equilibrium solutions, $\phi_0 = 0$ for the high-temperature phase and $\phi_\pm^2 = 6a|\tau|/u$ for the low-temperature regime, we arrive at

$$\chi = aV \begin{cases} 1/\tau, & \tau > 0 \\ 1/2|\tau| & \tau < 0. \end{cases} \tag{2.43}$$

As a result, the critical exponent is given by $\gamma = 1$ on both sides of the transition, also compatible with the MF result. Moreover, we recognize that the ratio of amplitudes is exactly 2 for the susceptibility. In fact, amplitude ratios are universal and depend neither on the parameters nor on the critical temperature. Similarly, we can compute the specific heat, given by $C = VT(\partial^2 f/\partial T^2)_{h=0}$ above and below the transition and obtain

$$C = \begin{cases} 0, & \tau > 0 \\ 3VTa^2/u & \tau < 0 \end{cases} \tag{2.44}$$

which means that it exhibits a discontinuity at the phase transition, hence $\alpha = 0$.

As we have seen, the Landau ansatz for the free energy expansion correctly describes the phenomenology of a continuous phase transition if the coefficient of the fourth-order term is positive. For the case of $u < 0$, as already mentioned earlier, the sixth-order term becomes substantial and must be positive, $v > 0$, to guarantee thermodynamic stability. As a consequence, due to the interplay of the remaining parameters, r and u, metastable states can occur in the free energy landscape. In this way, Landau theory describes a *first-order* transition at $h = 0$, which we will not be discussed here, as in this work we only consider continuous phase transitions. Finally, we remark that although we wrote down the Landau free energy *ad hoc*, it can also be rigorously derived through a saddle point approximation of the corresponding field theory (see, e. g., References [74, 75] for details).

RG in a nutshell

So far, we treated the order parameter ϕ as a single scalar quantity, thereby completely neglecting any spatial structure in the system. We know however, that continuous phase transitions are characterized by rather large spatial fluctuations of the order parameter, which, in particular, leads to a breakdown of MFT in dimensions $d < d_c$, as was detailed above. Starting from the Landau free energy expansion, we can extend the theory to an effective Hamiltonian, by upgrading the order-parameter to a local, space-dependent field $\phi(\boldsymbol{x})$, which can be interpreted as a coarse-grained order-parameter density and by adding a gradient term, such as to include spatial correlations. The resulting *Landau-Ginzburg-Wilson* (LGW) Hamiltonian reads [75]

$$\mathcal{H}[\phi] = \int \mathrm{d}^d x \left[\frac{1}{2} (\nabla \phi(\boldsymbol{x}))^2 + \frac{r}{2}\phi(\boldsymbol{x})^2 + \frac{u}{4!}\phi(\boldsymbol{x})^4 - h(\boldsymbol{x})\phi(\boldsymbol{x}) \right] \tag{2.45}$$

and is usually considered an effective field-theoretical description of the Ising universality class. It can be explicitly derived from the microscopic Ising Hamiltonian through a so-called Hubbard-Stratonovich transformation [110, 111]. This Hamiltonian is usually studied by means of field-theoretical *renormalization group* (RG) analysis methods. The corresponding framework was introduced by Kenneth G. Wilson in a number of seminal articles in the early 1970s [15, 16, 112], with contributions of Leo P. Kadanoff [14] and Michael Fisher.

The central idea of the RG is to take advantage of the self-similar structure at criticality and successively eliminate correlated degrees of freedom on length scales below the correlation length ξ. This is realized by two repeatedly applied steps: First, the system is *coarse-grained*, which means that the individual degrees of freedom on the microscopic lattice scale a are

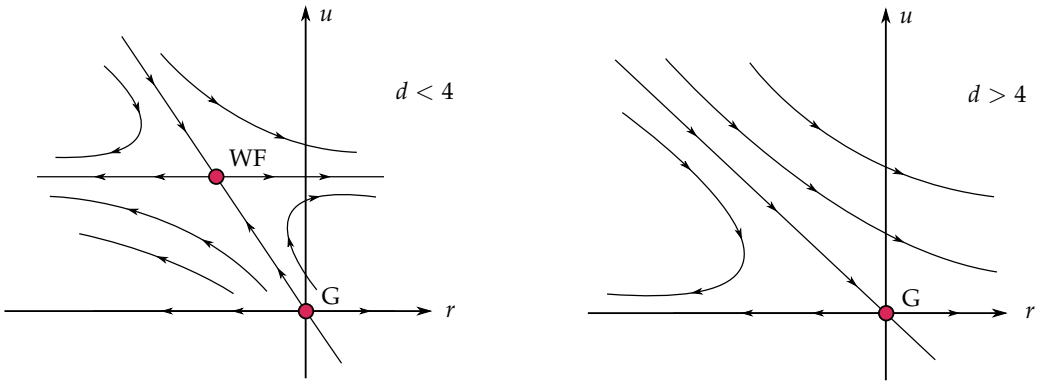

Figure 2.5 | Renormalization group flow. Schematic RG flow of the Ising field theory below (left) and above (right) the upper critical dimension in the coupling plane (u, r). G denotes the trivial Gaussian fixed point, whereas WF denotes the so-called Wilson-Fisher fixed point.

averaged (integrated out) up to a scale of λa, where $\lambda > 1$ is the so-called the coarse-graining factor. The actual realization of this procedure represents the core of the RG framework. Commonly, it is implemented in real space, e. g. by block-spin transformations, or in momentum space by integrating out high energy modes, associated to short-range correlations. Either way, it is clear that this procedure changes the scales of the system. Consequently, the Hamiltonian must be re-expressed in terms of appropriately rescaled variables. Therefore, in the second step of an RG transformation, the original scales are restored by *rescaling* all quantities, such as, for instance, the length scale $\boldsymbol{x} \mapsto \boldsymbol{x}' = \boldsymbol{x}/\lambda$ and the relative size of fluctuations $\phi(\boldsymbol{x}) \mapsto \phi'(\boldsymbol{x}')$. Accordingly, one obtains a new Hamiltonian $\mathcal{H}'(r', u', h', \ldots)$, characterized by couplings which are functions of the original ones, for instance $r' = r(\lambda, r, u, h, \ldots)$. This defines a (in general non-linear) transformation in parameter space, which can formally be denoted as $\boldsymbol{S} \mapsto \boldsymbol{R}_\lambda \boldsymbol{S}$, where $\boldsymbol{S}$ denotes the parameter vector and $\boldsymbol{R}_\lambda$ encodes the RG transformation. Since in a scale invariant system, the Hamiltonian should be identical at different scales, the critical point must be given by the fixed point of this transformation, $\boldsymbol{R}_\lambda \boldsymbol{S}^* = \boldsymbol{S}^*$. Moreover, it is clear that the mapping $\boldsymbol{R}_\lambda$ should fulfil a group property.[12] Introducing so-called *scaling fields* which are the eigenvalues of $\boldsymbol{R}_\lambda$, we can write

$$\boldsymbol{R}_\lambda \boldsymbol{R}_{\lambda'} \boldsymbol{U}_i = f_i(\lambda) f_i(\lambda') \boldsymbol{U}_i = \boldsymbol{R}_{\lambda\lambda'} \boldsymbol{U}_i = f_i(\lambda\lambda') \boldsymbol{U}_i \tag{2.46}$$

and consequently, the eigenvalues must be of the functional form $f_i(\lambda) = \lambda^{y_i}$, which is exactly what we wrote down in the phenomenological scaling ansatz, Equation (2.8). The values of the *scaling dimensions* y_i can be found by linearising the transformation around the fixed point. If, furthermore, one allows for infinitesimal transformations, i. e. $\lambda \to 0$, this eventually gives rise to a set of coupled differential equations, which determine the flow of the coupling parameters. Solving these equations for different initial conditions (corresponding to parameters of the real system), one obtains trajectories in parameter space, which are called the *renormalization group flow*. For the Ising Hamiltonian, the RG flow is illustrated in Figure 2.5. We skip the long and involved calculations here, as they can be found in standard textbooks such as [71, 75]. As can be seen, one finds a fixed point at $r = \lambda = 0$, which corresponds to the trivial, non-interacting,

[12] The renormalization group is in fact a semi-group, as the coarse-graining procedure can not be reversed.

Table 2.3 | Experimental critical exponents. Selected experimental estimates for clean and disordered Heisenberg systems (upper/middle sections, respectively, from [25]), as well as the currently most precise theoretical estimates from Monte Carlo (MC) simulations, numerical high-temperature (HT) series expansions and field theoretical (FT) methods (lower section).

Material / Method	γ	β	δ	Ref.
Ni	1.345(10)	0.395(19)	4.35(6)	[113]
$Tl_2Mn_2O_7$	1.31(5)	0.44(6)	4.65(15)	[114]
$La_{0.95}Ca_{0.05}MnO_3$	1.39(5)	0.36(7)	4.75(15)	[115]
CrO_2	1.43(1)	0.371(5)		[116]
$Fe_{16}Ni_{64}Bi_{19}Si$	1.386(14)	0.360(15)	4.86(4)	[117]
$Fe_{40}Ni_{40}P_{14}B_6$	1.385(10)	0.364(5)	4.79(5)	[118]
$Fe_{91}Zr_9$	1.383(4)	0.366(4)	4.75(5)	[119]
$Fe_{1.50}Mn_{1.50}Si$	1.274(60)	0.383(10)	4.45(19)	[120]
$MnCr_{1.8}In_{0.2}S_4$	1.39(1)	0.36(1)	4.795(10)	[121]
MC + HT	1.3960(9)	0.3689(3)	4.783(3)	[122]
FT	1.3895(50)	0.3662(25)	4.794(14)	[123]

so-called Gaussian model. In $d < 4$ this fixed point is unstable and the system flows towards another fixed point (historically named Wilson-Fisher fixed point), which constitutes the actual critical behaviour of the Ising model. In contrast, for $d > 4$ the Gaussian fixed point becomes stable and correctly describes the MF transition.

2.2.2 O(N) model

By extending the spin–1/2 Ising model to general $O(N)$ symmetric spin vectors, one obtains the XY model ($N=2$) and the Heisenberg model ($N=3$). Even higher symmetries ($N=4,5$) become relevant, for instance, in particle physics and high-temperature superconductor transitions (see [25] for a comprehensive review). Rather than being restricted to two orientations (up and down) as in the $N = 1$ case, the individual $O(N)$ spins represent N-dimensional unit vectors. The model is hence occasionally termed N-vector model. Due to its rich phenomenology and considerable range of applications, it is extensively studied, especially in two and three spatial dimensions [25, 74].

The XY model in three dimensions describes phase transitions in several physical systems, most notably the λ-transition in ^{4}He. In two dimensions, according to the Mermin-Wagner theorem [124], the continuous $O(2)$ symmetry can not be spontaneously broken at finite temperature, so that no usual second-order transition exists. Instead, a so-called Berezinskii–Kosterlitz–Thouless transition [80] can be observed (Nobel prize in 2016), where the temperature controls the binding of vortex-antivortex pairs. Turning to $N = 3$, the Heisenberg model [125] is characterized by a three-component order parameter combined with short-range interacting degrees of freedom and provides a simplified description of the critical behaviour of a number

of isotropic magnetic materials. For instance, the Curie transition in nickel, iron and certain compound materials is well described by this model, see Table 2.3. Due to the negative specific heat exponent $\alpha = -0.1336(15)$ [122], the three-dimensional Heisenberg model is stable against uncorrelated spatial disorder, as will be discussed in Section 2.5.

Extending the N-vector model to a classical lattice field theory, it can be written as, for instance

$$\mathcal{H} = -\beta \sum_{\langle i,j \rangle} \phi_i \phi_j + m \sum_i \phi_i^2 + \lambda \sum_i \left(\phi_i^2 - 1 \right)^2 , \tag{2.47}$$

where ϕ_i denotes an N-component real variable. Compared to the standard Ising Hamiltonian (2.20), also a mass term as well as a fourth-order interaction term have been added. For any positive λ, this system undergoes a continuous phase transition which lies in the universality class of the $O(N)$ model. The parameter λ can be particularly useful in a numerical analysis, as oftentimes it can be tuned such that leading scaling corrections approximately vanish. In this case one speaks of an *improved* Hamiltonian [25, 126]. For $\lambda \to \infty$ the classical XY, Heisenberg and higher-symmetry vector-models are recovered, as the field is effectively forced to unit-length $\phi_i^2 = 1$.

For completeness, we mention another generalization of the Ising model, which shows a quite rich phenomenology, the so-called q-state Potts model [127]. The spin variable can take on values $s_i = 0, 1, \ldots, q-1$ in this case. Hence, for $q = 2$ it maps exactly to the Ising model, whereas the case $q = 1$ corresponds the universality class of isotropic percolation. In two (three) dimensions, it shows a continuous transition for $q \leq 4$ ($q \leq 2$), which becomes first-order for any larger q.

2.3 Non-equilibrium systems

Whereas the previously discussed systems had been defined in terms of thermodynamic equilibrium, we now turn our attention to so-called non-equilibrium phenomena. First, some general properties of those systems are discussed. Then, we introduce two specific lattice models, the contact process and the Manna sandpile model, which both exhibit continuous phase transitions into absorbing states and elaborate on the respective universal properties.

Non-equilibrium systems are generically *out of equilibrium*, hence they do not obey detailed balance and contain the time t as an explicit coordinate.[13] As traditional methods of equilibrium thermodynamics can no longer be applied to describe these systems, one instead resorts to *phenomenological* descriptions through a *master equation* which governs the temporal evolution of the probability distributions P_t of the microstates c. In a quite general form, the master equation can be written as [5]

$$\frac{\mathrm{d}}{\mathrm{d}t} P_t(c) = \sum_{c'} w_{c' \to c} P_t(c') - \sum_{c'} w_{c \to c'} P_t(c), \tag{2.48}$$

where w denotes the set of transition rates, encoding the probability flow. Obviously, the first

[13] Recall that in equilibrium statistical mechanics there is no notion of time.

sum on the right hand site corresponds to gain terms (flow of probability into configuration c), whereas the second one accounts for loss terms (flow of probability out of c). In the case of a continuum of states, the master equation is replaced by the corresponding Fokker-Planck equation. Whereas in equilibrium statistical mechanics the probability distribution usually is given by design (e. g. the canonical Boltzmann distribution for a spin model exchanging energy with a heat bath) here one needs to solve Equation (2.48) explicitly. In fact, the set of transition rates w actually *defines* the model, similar to the energy functional in equilibrium systems. Except for some rather trivial systems, such as a simple random walk, the master equation can not be solved in a closed form. However, it can be used as a starting point to derive an associated field-theoretic action of the model and analyse it at criticality by renormalization group methods. Besides the field-theoretic treatment, also a mean-field approximation remains a possible approach to analyse non-equilibrium systems analytically. Introducing effective transition rates and neglecting any spatial information, this results in differential equations for certain coarse-grained parameters of the system (such as the density of active particles). The mean-field approach can furthermore be extended to a full *stochastic Langevin equation* by adding a suitably designed noise term. An example for such a phenomenological Langevin description, which can be rigorously derived from the corresponding master equation of the model (compare e. g. Reference [128]), will be given below. Since in this work, however, we exclusively rely on numerical simulations to study the physical models, even the mean-field approach will only be discussed briefly and we refer the reader to standard textbooks, such as [75] for more details on either theoretical approach.

2.3.1 Directed percolation

In this work we are particularly interested in non-equilibrium systems which feature a (continuous) phase transition into an *absorbing state*. Such states are characterized by certain configurations which do not allow for a further evolution of the system. In other words, once the system reaches an absorbing state, it is trapped and can not escape. The arguably most prominent reaction-diffusion-type lattice model that exhibits a non-equilibrium phase transition into an absorbing state is given by the *contact process* (CP). It was originally introduced in the context of epidemic spreading [30] and – in the community for modelling of infectious diseases – goes under the more technical notion *asynchronous susceptible-infected-susceptible (SIS) model*. On a lattice, each vertex can be in either of two states, which, in the terminology of epidemics, correspond to *infected* or *healthy* (susceptible) particles. Infected sites are also said to be *active* or *occupied*, whereas healthy ones are considered *inactive* or *empty*. Each site can only be occupied by one particle. The temporal evolution of the system comprises two fundamental stochastic processes [5]. Denoting an active site as A and empty sites as $\varnothing$, these are specifically

$$\begin{aligned} A &\to A + A && \text{offspring creation on adjacent site} \\ A &\to \varnothing && \text{on-site particle removal (death).} \end{aligned}$$

If the state of a lattice site i is encoded as $s_i(t) = 0, 1$ depending on whether it is occupied ($s_i(t) = 1$) or empty ($s_i(t) = 0$), the corresponding rates, which determine the configuration at

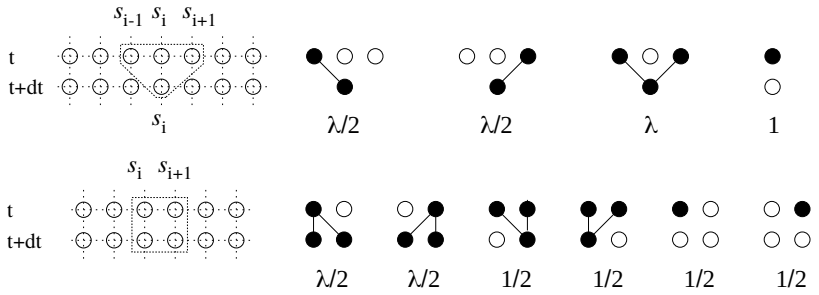

Figure 2.6 | Transition rules. Depicted are the transition rules for the (1+1)-dimensional contact process. The rates (probabilities per unit time) are indicated below. From [129].

time $t + \delta t$ are given by

$$\begin{aligned} w[0 \to 1, n] &= \lambda n/q \\ w[1 \to 0, n] &= 1, \end{aligned} \tag{2.49}$$

where the parameter λ controls the infection rate, n denotes the number of *active* nearest neighbours and q the total number of neighbours ($q = 2d$ for a d-dimensional hypercubic lattice). For the case of one spatial dimension, these rules are illustrated in the upper row of Figure 2.6. Fully equivalent, in the two-site picture (lower row of Figure 2.6), the associated transition rates are given by

$$\begin{aligned} w_{10\to 11} &= w_{01\to 11} = \lambda/2 \\ w_{10\to 00} &= w_{01\to 00} = w_{11\to 01} = w_{11\to 10} = 1/2. \end{aligned} \tag{2.50}$$

As sketched above, the CP dynamics evolves a *cluster* of active sites. The behaviour of the system is controlled by the transition rate λ, which acts as an order parameter. If offspring creation is weak (small λ), the dynamics is dominated by the annihilation process and eventually the absorbing state is reached where the whole lattice is inactive and the evolution terminates. Employing once again epidemic language, this means that the disease is extinct. In fact, as will be become important later, the existence of a *single and unique* absorbing state (the empty configuration) is a key property of the CP and related models. If, in contrast, λ is large enough, the system steadily maintains an active cluster and is said to be in the *active phase* where the disease persists indefinitely. The transition between active and absorbing phase takes place at a critical parameter λ_c whose precise value depends on the microscopic details of the lattice. At $\lambda = \lambda_c$ spatial and temporal correlation length scales, $\xi_\perp$ and $\xi_\parallel$, diverge and the emerging activity cluster becomes scale-invariant and strikingly self-similar, as can be seen in Figure 2.7.

On regular structures, the phase transition of the contact process falls into the directed percolation (DP) universality class. The name stems from an apparent relation to ordinary (isotropic) percolation. If we, in a percolating system (e. g. a regular lattice with open and closed bonds), consider one of the spatial coordinates as a temporal coordinate and furthermore interpret open bonds as creation and closed bonds as annihilation events, then the system becomes a stochastic reaction-diffusion process, evolving in time. Since, however – in the picture of water flowing through the open bonds of a lattice – only flows along a preferred direction are

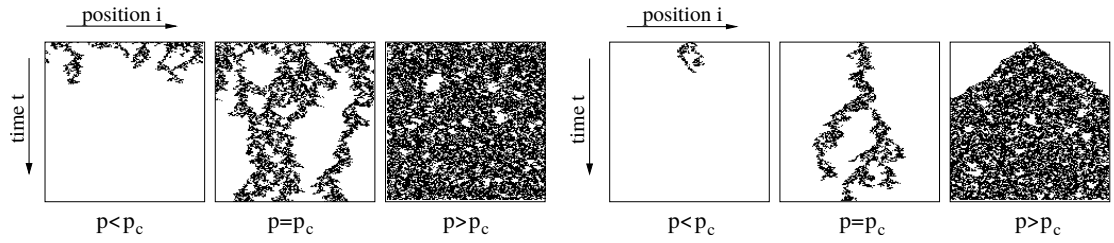

Figure 2.7 | Phenomenology of the contact process. Typical undercritical, critical and overcritical samples in 1+1 dimensions. The process is started from a fully occupied lattice in the left panels and from a single active seed in the right panels. Black regions illustrate infected particles. Adopted from [129].

allowed, the resulting behaviour is entirely different compared to ordinary percolation, as is illustrated in Figure 2.8. Due to this analogy, the DP class naturally models transport in porous media [29].

Over the last decades, DP behaviour has proven to be particularly robust. The reason stems from the fact that it can be interpreted as a reaction-diffusion process involving only very fundamental particle processes, namely

- Particle removal ($A \to \varnothing$)
- Offspring production ($A \to 2A$)
- Coalescence ($2A \to A$)
- Diffusion ($\varnothing + A \to A + \varnothing$).

In the implementation of transition rules (2.49) and (2.50), the coalescence process is contained implicitly through the requirement that an empty site can only be activated once per time step, even though more than one of its neighbours might attempt to colonize it. As a result, the maximal particle density in the system is limited. Due to its robustness, DP behaviour can be found in a large variety of different systems, such as forest fires [31], catalytic reactions [130], interface pinning [131] or turbulence [132]. In fact, according to a conjecture by Janssen and Grassberger [128, 133], any system which

- features a fluctuating phase and a unique absorbing state
- is controlled by a non-negative scalar order parameter
- includes only short-ranged interactions
- has no additional symmetries, quenched randomness or conservation laws

is expected to fall into this class. However, despite its robustness, constructing explicit experimental realizations of DP behaviour has proven to be a surprisingly challenging task [32]. The first convincing evidence has been put forth only little more than a decade ago, when Takeuchi et al. studied the phase transition between two topologically different turbulent states of electrohydrodynamic convection in nematic liquid crystals [33, 34].

From the analytical point of view, models in the DP class remain unsolved, despite considerable efforts (compare [5] and references therein), even in 1+1 dimensions. However, a coarse-grained phenomenological treatment can be obtained quite easily. Given the rates in the

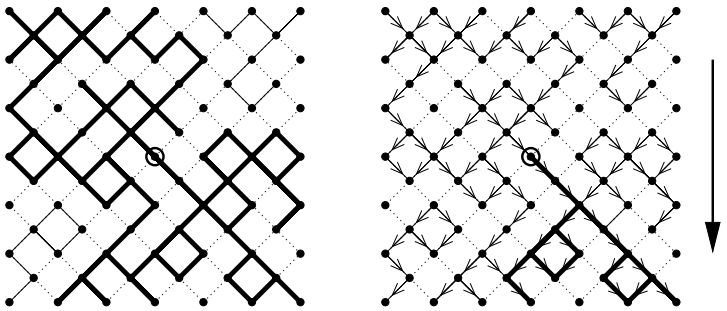

isotropic percolation directed percolation

Figure 2.8 | Isotropic and directed percolation. Interpretation of the contact process as a percolating system with the preferred direction being indicated by the arrow (right panel), compared to ordinary isotropic bond percolation (left panel). Dotted connections represent closed channels. From [129].

upper panel of Figure 2.6, we can write down a mean-field equation for the particle density $\rho(\boldsymbol{x}, t)$ as

$$\partial_t \rho(t) = \lambda\rho(t) - \lambda\rho(t)^2 - \rho(t), \tag{2.51}$$

where the first terms on the right hand side represent particle gains and the two remaining terms account for particle loss through coalescence and spontaneous removal, respectively. Note that since coalescence ($2A \to A$) represent a binary process, the corresponding gain term is non-linear, which, in fact is an essential ingredient in order to make the model non-trivial. Introducing the distance from the critical point as $\tau = \lambda - 1$, the mean field equation can be written more compactly as

$$\partial_t \rho(t) = \tau\rho(t) - g\rho(t)^2, \tag{2.52}$$

where $g = \lambda$ denotes the coupling constant of the quadratic interaction.

This simple approximation already captures some of the essential properties of the model. First and foremost, the steady-state solution $\rho = 0$ represents the absorbing state. For $\lambda > 1$ the absorbing state becomes unstable and one finds another (stable) non-vanishing stationary state $\rho = 1 - 1/\lambda$. Hence, the phase transition is located at $\lambda = \lambda_c = 1$. As this corresponds to $\tau = 0$, τ is indeed the control parameter. Given that β represents the (static) critical exponents of the order parameter, i. e.

$$\rho \sim (\lambda - \lambda_c)^\beta \sim \tau^\beta, \tag{2.53}$$

we obtain the corresponding mean field value $\beta = 1$. For non-equilibrium transitions one can also define *dynamic* critical exponents, which capture the time-dependence at criticality (more details will be given in Section 4.3). For the order parameter,

$$\rho(t) \sim t^{-\delta}, \tag{2.54}$$

we obtain $\delta = 1$, when solving Equation (2.52) for $\tau = 0$.

So far, we have neglected any spatial structure in the system. Accounting for diffusive motion by adding a term proportional to $\nabla^2\rho(\boldsymbol{x},t)$, we are able to obtain the mean-field exponents of the correlation length and correlation time, given by $\nu_\perp = 1/2$ and $\nu_\parallel = 1$, through a suitable scaling ansatz (compare Section 4.3). In fact, the mean field approximation can be extended even further by considering an effective noise term, resulting in

$$\partial_t\rho(\boldsymbol{x},t) = \tau\rho(\boldsymbol{x},t) - \lambda\rho(t)^2 + D\nabla^2\rho(\boldsymbol{x},t) + \sqrt{\rho}\,\eta(\boldsymbol{x},t) \tag{2.55}$$

which represents the phenomenological *stochastic Langevin equation* of directed percolation [128]. The noise is Gaussian and white, with the correlations

$$\langle\eta(\boldsymbol{x},t)\rangle = 0 \tag{2.56}$$

$$\langle\eta(\boldsymbol{x},t)\eta(\boldsymbol{x}',t')\rangle = \Gamma^2\delta(\boldsymbol{x}-\boldsymbol{x}')\delta(t-t'), \tag{2.57}$$

where Γ denotes a constant. Note that the noise enters through a density-dependent amplitude proportional to $\sqrt{\rho}$, which ensures a non-fluctuating absorbing state. The square-root form of the noise term can be motivated by means of local fluctuations of the coarse-grained density generated through local particle transitions and averaged according to the central limit theorem [5]. By means of a dimensional analysis of Equation (2.55) one finds that the noise is irrelevant in dimensions $d > 4$, hence $d_c = 4$ can be identified as the upper critical dimension, above which the mean-field approximation becomes exact. For dimension $d < 4$ however, a full field-theoretical RG treatment is necessary in order to study the critical behaviour of the DP. In fact, Equation (2.55) can serve as a starting point for deriving a suitable field-theoretic action for the DP class, as shown in detail in Reference [129]. For historic reasons this theory is called Reggeon field theory and – in the context of DP – has been extensively studied during the last decades (see e. g. [75, 134, 135] for comprehensive reviews).

2.3.2 Manna universality class

The second non-equilibrium system which will be considered in this work is the so-called *Manna sandpile model*. It is strongly related to the concept of *self-organized criticality* (SOC), which was put forward by Bak, Tang and Wiesenfeld in 1987 [35, 36]. In the original formulation of their model (BTW model or Abelian sandpile model), each site of a lattice harbours a number of particles, which can be interpreted as sand grains. By randomly adding new grains to the lattice, piles build up on the individual sites, which eventually topple. Specifically, as soon as a site exceeds a given threshold height, it becomes unstable and one grain is moved to each of its four neighbours, leaving the site empty after the move. In case one of the neighbours thereby exceeds the threshold it also topples and distributes its grains. In this way a whole cascade of events can be triggered, called an *avalanche*. In the BTW model the boundaries of the lattice are open, allowing particles to leave the system.

Analysing the avalanches, one recognizes that they occur in all sizes, where the size s is defined by the total number of consecutive toppling events. The distribution of s follows a well defined finite-size behaviour, exhibiting a leading power-law scaling

$$\mathcal{P}(s;L) \sim s^{-\tau_s} f_s(s/s_c) \quad \text{with} \quad s_c(L) \sim L^d, \tag{2.58}$$

where τ_s denotes a critical exponent and $f_s(x)$ represents a universal scaling function. The upper cutoff size s_c accounts for the finiteness of the lattice. Analogous relations hold for other avalanche properties as well, such as their area a (number of distinct activated sites), duration T, or the radius of gyration r, with different critical exponents τ_a, τ_T, τ_r. An excellent summary of further scaling properties is given in Reference [37].

As a consequence of the slow driving mechanism (the external injection of grains), the system reaches a critical configuration without the need for a fine-tuning of external variables. It organizes itself into a complex critical state, where, as seen above, macroscopic observables exhibit scale-free distributions. In nature, apart from granular media, self-organized criticality can be found a large variety of other applications, such as earthquakes, forest fires, neural networks, superconductors, financial markets and biological evolution to name only a few (a comprehensive review can be found in [136]). Consequently, different variations of the original BTW model have been proposed [38, 137–139] and extensively studied. It turns out that modifying the toppling rules will in general change the universality class of the model [140]. In general a distinction can be made between Abelian vs. non-Abelian[14], deterministic vs. stochastic and directed vs. undirected toppling rules [141]. A specific model which quickly became prominent as an analytic solution can be obtained under certain conditions, was introduced by Subhrangshu S. Manna in 1991. It presents a variation of the original BTW model with stochastic toppling rules and established the so-called *Manna universality class*. Due to its particularly robust and reproducible critical behaviour (see [5] and references therein), this model has been studied in great detail in numerical simulations [142].

It is known that non-equilibrium systems respond strongly to boundary conditions [143–146]. Whereas the original SOC models use open boundaries where particles can leave the system, there exists a number of models with periodic boundary conditions and no external injection of particles. Hence the total number of particles is conserved. Here, we study the conserved version of the Manna model. In this model, each site can contain an unlimited number of particles $n = 0, 1, 2, \ldots$ which is why it is considered a bosonic model (as opposed to the the fermionic contact process). As long as n is below a certain threshold N_c, a site is considered inactive, whereas it is active if $n \geq N_c$. The dynamics consists of toppling events, where a random active site distributes all of its particles to randomly chosen neighbouring sites. This so-called *conserved Manna model* (CMM) or *conserved stochastic sandpile model* (CSSM) no longer presents a self-organized critical behaviour but rather a non-equilibrium phase transition into infinitely many absorbing states (in the infinite-volume limit), controlled by the particle density p. In particular if $p > p_c$ the systems maintains a state of steady activity, whereas for $p < p_c$ an absorbing configuration is reached eventually.

The shared universal properties of the regular and conserved Manna model reveal a fundamental connection between the critical behaviour of absorbing state phase transitions (APTs) and the critical state of self-organized critical systems. In fact, as pointed out in [5] sandpile models can be considered as driven-dissipative versions of (closed) systems exhibiting absorbing phase transitions, resulting in intriguingly simple relations between corresponding critical exponents. Moreover, we remark that the conserved Manna model is closely related to the so-called conserved threshold transfer process (CTTP), the conserved counterpart of the

[14] A model is said to be Abelian if the configuration after the avalanche does not depend on the order in which the relaxation of the active sites was performed.

ordinary TTP [147]. It describes a variation of the above mentioned model, where the number of particles per site is restricted to $n \leq 2$. If during the redistribution of particles, a particular move violates the height condition (i. e. the target site already contains two particles) it is reflected and returns to its origin. In spatial dimensions $d > 1$, the CTTP belongs to the Manna universality class. Only in 1D the critical behaviour is distinct. Finally, we remark, that another well-studied model, belonging to the Manna class is the conserved lattice gas (CLG) model [148, 149], where a particle is considered active if at least one of its neighbouring sites is occupied and active particles undergo a diffusive motion.

2.4 Finite systems

We describe how the scaling behaviour at criticality derived in the previous sections is modified in the presence of a finite geometry, establishing the so-called finite-size scaling theory. In particular, our discussion covers the leading scaling behaviour as well as corrections, arising from the finite system size.

So far our discussion concerned the thermodynamic limit of infinitely-large systems. In simulations on a computer this can obviously not be realized, hence we are confined to a *finite* systems, typically characterized by a linear length scale L, the lattice dimension. As detailed earlier, in the thermodynamic limit a continuous phase transition is characterized by physical observables diverging as power-laws as the critical point is approached, such as for the correlation length and magnetic susceptibility

$$\begin{aligned} \xi &\sim |\tau|^{-\nu}, \\ \chi &\sim |\tau|^{-\gamma}. \end{aligned} \tag{2.59}$$

The origin of this divergence can be traced back to the singular behaviour of the corresponding free energy, as was detailed earlier in Section 2.1. In finite systems, however, all thermodynamic quantities are analytic. As a consequence, at the transition, they exhibit instead finite peaks which become sharper with increasing system size, diverging only for $L \to \infty$ [150]. This finite-size smoothening of the phase transition is typically unobservable in bulk experimental systems, where one has particle numbers $\sim 10^{23}$. For Monte Carlo simulations, as conducted in the present work, where the accessible particle number is heavily limited, however, the smoothening might even dominate the scaling scenario.

Combing relations (2.59), the temperature dependence can be eliminated, resulting in

$$\chi \sim \xi^{\gamma/\nu}. \tag{2.60}$$

In a finite system the correlation length is necessarily bounded by the length scale of the system L, which also cuts off the susceptibility as the critical point is approached and ξ grows. We can use the following ansatz [151]

$$\chi \sim \xi^{\gamma/\nu} \chi_0(L/\xi), \tag{2.61}$$

where χ_0 denotes a scalar, dimensionless scaling function with asymptotic limits being known

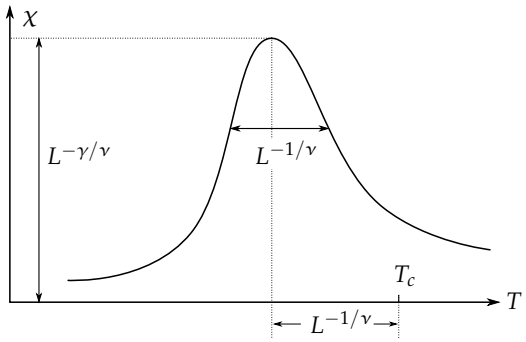

Figure 2.9 | Finite-size scaling function. Schematic illustration of the scaling function of the susceptibility in a finite system, where T_c denotes the infinite-volume critical point. Reproduced from [71].

a priori, namely [152]

$$\chi_0(x) \to 1 \qquad \text{for} \quad x \gg 1 \qquad (\xi \ll L) \tag{2.62}$$

$$\chi_0(x) \sim x^{\gamma/\nu} \qquad \text{for} \quad x \to 0 \qquad (\xi \to \infty) \qquad (\tau \to 0). \tag{2.63}$$

This means that the function $\chi_0(x)$ remains finite in the limit $x \to \infty$, yielding the correct behaviour in a finite system and exhibits a singularity which causes the function χ to behave smoothly as the critical point is approach for fixed L. Specifically

$$\lim_{x \to 0} \chi = L^{\gamma/\nu}, \tag{2.64}$$

which means that there exists a so-called pseudo-critical point given by the maximum of χ as can be seen in Figure 2.9. Notice that χ_0 does only explicitly depend on L through its function argument. In order to eliminate the explicit dependence on ξ, we rescale the scaling function

$$\tilde{\chi}(x) = x^{-\gamma} \chi_0(x^{\nu}) \tag{2.65}$$

and use again Equation (2.59) to obtain the central *finite-size scaling* (FSS) equation

$$\chi = L^{\gamma/\nu} \tilde{\chi}(L^{1/\nu} \tau), \tag{2.66}$$

where the proportionality factor from Equation (2.61) and a possible asymmetry of the scaling function below and above the transition was absorbed into the definition of $\tilde{\chi}$. The pseudo-critical point is therefore shifted away from the infinite-volume critical point by a factor of $L^{-1/\nu}$ as illustrated in Figure 2.9. The direction of this shift depends on the boundary conditions of the system and is discussed in Reference [71]. The scaling function $\tilde{\chi}$ is universal in the sense that it does not implicitly depend on the lattice size, which can be exploited in so-called scaling collapses, which will be introduced in Section 4.1.3. However, it depends on the shape of the system and on boundary conditions.

The FSS behaviour can also be obtained from the free energy (2.8), which, using the concept

of scaling fields u, introduced in Section 2.2.1, generalizes to [25, 153]

$$f_{\text{sing}}\left(u_\tau, u_h, \{u_i\}\right) = \lambda^{-d} f_{\text{sing}}\left(\lambda^{y_\tau} u_\tau, \lambda^{y_h} u_h, \{\lambda^{y_i} u_i\}\right) \tag{2.67}$$

Besides the scaling fields u_τ and u_h, which correspond to the reduced temperature and external field, respectively, $u_\tau \sim \tau$ and $u_h \sim h$, as before, we have included further operators $\{u_i\}, i \geq 3$ which are also analytic functions of the Hamiltonian parameters. Recall that the parameter λ can be motivated from the RG framework and denotes the rescaling or coarse-graining factor. For the infinite-volume Ising model, only u_τ and u_h are relevant scaling fields, whereas the remaining scaling fields $\{u_i\}, i \geq 3$ are said to be *irrelevant* due to their negative eigenvalues, $y_i < 0$, which, at criticality, lead to them becoming increasingly small and eventually vanishing. Since, as pointed out earlier, the *eigenvalues* of the relevant operators are directly related to the critical exponents, we find $y_\tau = 1/\nu$ and $y_h = (d + 2 - \eta)/2$, whereas the two leading irrelevant scaling fields are related to correction exponents, specifically $\omega \equiv y_3$ and $\omega_2 \equiv y_4$.

What about the finite size of the lattice? In fact, it can be interpreted as another scaling field. Under a scale transformation of size λ, the lattice size transforms according to $L \to L/\lambda$, which allows us to write down yet another term

$$f_{\text{sing}}\left(u_\tau, u_h, \{u_i\}, L\right) = \lambda^{-d} \mathcal{F}_{\text{sing}}\left(\lambda^{y_\tau} u_\tau, \lambda^{y_h} u_h, \{\lambda^{y_i} u_i\}, \lambda L^{-1}\right). \tag{2.68}$$

which means that L^{-1} is nothing but a relevant scaling field with eigenvalue $y_L = 1$. For solely short-ranged interactions we can safely assume that the other scaling fields do not depend on the lattice size [154]. Choosing $\lambda = L$ leads to

$$f_{\text{sing}}\left(u_\tau, u_h, \{u_i\}, L\right) = L^{-d} f_{\text{sing}}\left(L^{y_\tau} u_\tau, L^{y_h} u_h, \{L^{y_i} u_i\}, 1\right). \tag{2.69}$$

Now we compute the magnetization

$$m(L, \tau) = \left.\frac{\partial f_{\text{sing}}}{\partial h}\right|_{h=0} \sim L^{d-y_h} f'_{\text{sing}}(L^{y_\tau} u_\tau, 0) \equiv L^{\beta/\nu} \tilde{m}(L^{1/\nu} t\tau), \tag{2.70}$$

where in the last step we identified the critical exponents $\beta/\nu = d - y_h$ and used the explicit representation of the scaling field in terms of the reduced temperature, $u_\tau = \tau$. Similarly, for the susceptibility

$$\chi(L, \tau) = \left.\frac{\partial^2 f_{\text{sing}}}{\partial h^2}\right|_{h=0} \sim L^{2d-y_h} f''_{\text{sing}}(L^{y_\tau} u_\tau, 0) \equiv L^{\gamma/\nu} \tilde{\chi}(L^{1/\nu}\tau) \tag{2.71}$$

we reproduce the result of Equation (2.66).

So far we have only discussed the *leading* scaling behaviour in the finite-size regime. In general, corrections due to irrelevant scaling fields $\{u_i\}, i \geq 3$ can be expected [155], leading to correction terms proportional to $\tau^{k\theta_i}$, where $k = 1, 2, \ldots$ and $\theta, \theta_2, \ldots$ represent correction-to-scaling exponents. Additionally, scaling fields depending non-linearly on the system parameters give rise to terms of the form τ^k. For instance, for the infinite-volume susceptibility, this leads

to a general expansion of the form

$$\chi = A_\chi \tau^{-\gamma} \Big(1 + a_{0,1}\tau + a_{0,2}\tau^2 + \dots + a_{1,1}\tau^\theta + a_{1,2}\tau^{2\theta} + \dots + b_{1,1}\tau^{1+\theta} + b_{1,2}\tau^{1+2\theta} + \dots + a_{2,1}\tau^{\theta_2} + \dots\Big) \tag{2.72}$$

near criticality, where A_χ, a and b are non-universal amplitudes and we have neglected contributions from the non-singular background. Note that the terms proportional to $\tau^{2\theta}$, $\tau^{1+\theta}$, τ^2, etc. can be regarded as corrections to corrections [156] and typically have very small amplitudes.

Considering again a finite system, the corrections translate to terms depending explicitly on the lattice size. Typically, as discussed in References [154, 157], when studying system with periodic boundary conditions, one assumes that the finite-size scaling field is exactly $1/L$ (i. e. it shows no corrections of higher order) and that the coefficients of the relevant scaling fields as well as of the regular part of the free energy are independent of L. As a consequence one expects no correction terms proportional to $1/L$ and the finite-size expansion of the susceptibility reads

$$\chi = \tilde{A}_\chi L^{\gamma/\nu} \left(1 + a_{1,1}L^{-\omega} + a_{1,2}L^{-2\omega} + \dots + a_{2,1}L^{-\omega_2} + \dots\right), \tag{2.73}$$

where $\omega \equiv \theta/\nu$.

Finally, we remark that according to [158] all two-dimensional models on a square lattice exhibit a scaling correction with an exponent of exactly 2, associated to the breaking of rotational invariance.[15] Since for the two-dimensional Ising model, the operator breaking the rotational symmetry is conjectured to be the only irrelevant operator [159], $\omega = 2$ represents the leading correction for this model. For the three-dimensional Ising model on a cubic lattice the corresponding correction is not exactly integer but rather close, $2.0208(12)$ [160], and is furthermore superseded by a leading correction exponent given by $\omega = 0.8303(18)$ [161, 162].

2.5 Disorder

After a brief introduction on the phenomenology of quenched disorder, we discuss how it can be implemented in the Hamiltonian description of an equilibrium theory. Moreover, we investigate the question under which conditions disorder is expected to constitute a relevant perturbation to critical behaviour, leading to Harris' relevance criterion. We discuss several generalizations of this criterion, focusing particularly on topologically disordered structures.

In the previous sections we introduced certain models of physical system which are traditionally defined in terms of discrete degrees of freedom (spins, agents, grains, ...). The arguably simplest discrete spatial structure is given by a regular lattice. The square and cubic lattice, for instance, partition the spatial domain into equivolumetric rectangular or cuboid cells. In two dimensions each site is connected to exactly four nearest neighbours, whereas in three dimensions this number increases to six. From a technical point of view, regular structures are beneficial in so far as they exhibit homogeneously distributed sites and hence a *translational symmetry*, which can be exploited, especially in analytical calculations. It is clear however, that regular Cartesian

[15] For triangular and honeycomb lattices, the corresponding correction are $\omega = 4$ and $\omega = 3$, respectively [158] .

lattices are, in general, not rotationally symmetric.

Despite their simplicity, regular lattices present a suitable description of certain real structures. Alluding to the Ising model, one might think of the individual degrees of freedom being realized as net magnetic dipole moments of unpaired electrons, such as, for instance, can be found in iron atoms. As solid iron shows a well-defined regular atomic lattice structure, investigating the Ising model on regular lattices is plausible. However, it is clear that real solids can never be arranged perfectly periodic. They are affected by vacancies, impurities or deformations and depending on the strength of the disorder, the microscopic structure and hence the physical properties of a given material can change drastically. As a consequence, it is by no means obvious whether collectively behaving systems should – even qualitatively – show the same behaviour compared to their clean (i. e. regularly ordered) counterparts. In fact, certain physical phenomena, such as e. g. the so-called Anderson localization even require a certain degree of disorder in the medium to be observed [163].

2.5.1 Quenched randomness

An important distinction must be made between *quenched* and *annealed disorder*. The former notion describes the case, when the disorder configuration is static or frozen.[16] In the annealed case, in contrast, the disorder degrees of freedom are allowed to "move" during the evolution of the system and are hence dynamic. In terms of time scales, quenched randomness is attributed to the case when the disorder relaxation time scale is much slower then the typical time scale on which the system evolves. Vice verse, one speaks of annealed randomness if both time scales are comparable. Concrete examples include general soft matter, such as liquids or plasmas for annealed disorder and regular atomic lattices with impurities for the quenched case. As a matter of fact, in the annealed setting, the disorder degrees of freedom (e. g. the impurity distribution) can be interpreted as additional thermodynamic degrees of freedom that obey the Gibbs distribution [164]. They can in principle be traced out, resulting in a disorder-free multi-component system with modified parameters. To be more specific, let us consider a Hamiltonian, depending on thermodynamic variables ϕ (e. g. the individual spins) as well as on disorder variables ψ (e. g. random interaction strengths), where the latter are characterized by a distribution $P(\psi)$. When calculating the annealed free energy, both are treated on equal footing

$$F_{\mathrm{a}} = -\frac{1}{\beta} \log \int \mathrm{d}\psi \, P(\psi) \int \mathrm{D}\phi \, \mathrm{e}^{-\beta \mathcal{H}(\phi;\psi)} = -\frac{1}{\beta} \log \left[Z(\phi;\psi) \right]_{\mathrm{avg}} \tag{2.74}$$

and ψ is nothing but another dynamic degree of freedom in an effective potential $\sim \beta^{-1} \log P(\psi)$. Note that the latter integral runs over all thermodynamic degrees of freedom and is nothing but the continuous version of Equation (2.21). Moreover, the square brackets are used as a short notation for the disorder average.

For quenched disorder, the free energy is given by

$$F_{\mathrm{q}} = -\frac{1}{\beta} \int \mathrm{d}\psi \, P(\psi) \log \int \mathrm{D}\phi \, \mathrm{e}^{-\beta \mathcal{H}(\phi;\psi)} = -\frac{1}{\beta} \left[\log Z(\phi;\psi) \right]_{\mathrm{avg}} \tag{2.75}$$

[16] The notion of a "quench" originates from a system being cooled very rapidly such that the current distribution of random variables becomes static.

which corresponds to calculating the free energy of individual random realizations of the system and performing the disorder average *afterwards*. Obviously, this second case is much more challenging mathematically, and rather involved approximation methods, such as the replica method have to employed [48, 164], as will be detailed below. For numerical simulations, Equation (2.75) already points the way of how averages are performed. As the free energy is given by an average over the free energies of the individual disorder realizations, also the thermodynamic observables present themselves as averages over the replicas. More details about how we explicitly perform the disorder averages for the respective models considered in this work, can be found in Chapter 4.

2.5.2 Renormalization group flow

In the Landau-Ginzburg-Wilson Hamiltonian (2.45), quenched disorder can be introduced as either *random-mass disorder*, which couples to the reduced temperature of the system or *random-field disorder*, coupling to the external field. Random-field disorder locally breaks the symmetry of the order parameter, which, in a lattice realization of the Ising model, corresponds to a random external field h caused, e. g. by magnetic impurities in the material. In particular, the random-field Ising model (RFIM) has been investigated thoroughly over the last decades [see 165, and references therein]. Random-mass disorder, in contrast, leads to local fluctuations in the transition point without breaking any symmetries. For magnetic systems it is typically realized by spatial fluctuations of the bond strengths in the absence of an external field, i. e. it models for example vacancies or non-magnetic impurities in the material. If one allows for positive *and* negative random couplings, the system in general shows the behaviour of a spin glass, exhibiting highly non-trivial, random behaviour even in the ground state, which has made it a well-studied research branch on its own [96, 166, 167]. In this work, however, we will not consider spin glasses but only systems with a well-defined ferromagnetic ground state.

Using the notation $\delta\tau(\boldsymbol{x})$ and $\delta h(\boldsymbol{x})$ for the respective disorder fields, the general disordered Hamiltonian becomes for vanishing external field

$$\mathcal{H}\left[\phi|\delta\tau,\delta h\right] = \int \mathrm{d}^d x \left(\frac{1}{2}(\nabla\phi)^2 + \frac{1}{2}(r+\delta\tau(\boldsymbol{x}))\phi^2 + \frac{u}{4!}\phi^4 - \delta h(\boldsymbol{x})\phi\right), \tag{2.76}$$

where, in order to keep the notation simple, we suppress the space dependence of the spin field $\phi(\boldsymbol{x})$. Furthermore, recall that $r(\tau) = a\tau + \mathcal{O}(\tau^2)$ with $a > 0$. For now we assume both disorder fields to be characterized by zero-mean Gaussian distributions, i. e.

$$P[\delta\tau] \sim \exp\left(-\frac{1}{2\Delta_\tau}\int \mathrm{d}^d x\, \delta\tau(\boldsymbol{x})^2\right), \qquad P[\delta h] \sim \exp\left(-\frac{1}{2\Delta_h}\int \mathrm{d}^d x\, \delta h(\boldsymbol{x})^2\right), \tag{2.77}$$

which are hence fully characterized by their respective variances

$$\overline{\delta\tau(\boldsymbol{x})\delta\tau\left(\boldsymbol{x}'\right)} = \Delta_\tau\, \delta^d\left(\boldsymbol{x}-\boldsymbol{x}'\right), \qquad \overline{h_i(\boldsymbol{x})h_j\left(\boldsymbol{x}'\right)} = \Delta_h\, \delta_{ij}\delta^d\left(\boldsymbol{x}-\boldsymbol{x}'\right) \tag{2.78}$$

with the constants Δ_τ and Δ_h, respectively. As a consequence, disorder correlations are effectively short-range correlated. The implications of this assumption will become quite important later.

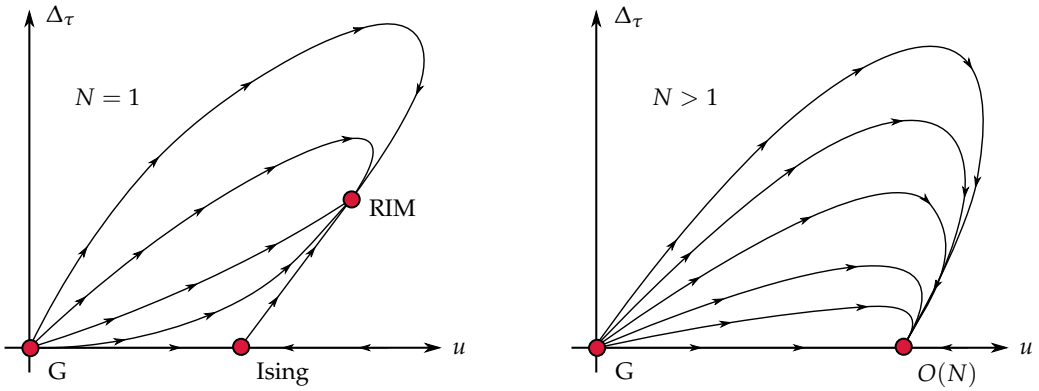

Figure 2.10 | Disordered renormalization group flow. Shown is the RG flow of the three-dimensional disordered N-vector model in the coupling plane (u, Δ_τ), for $N = 1$ (Ising model, left panel) and higher-symmetry fields (right panel). For the Ising model, the clean fixed point becomes unstable and the system flows to the random Ising model (RIM) fixed point. The trivial Gaussian fixed point is represented by G in both panels. Reproduced from [168].

Let us take a closer look at the Hamiltonian (2.76) of the N-vector field theory, coupled to quenched random-mass disorder. Moreover, we assume to have no field-randomness, which means that $\delta h = 0$. Using the replica trick

$$[\log Z]_{\text{avg}} = \lim_{n \to 0} \frac{[Z^n]_{\text{avg}} - 1}{n}, \tag{2.79}$$

one is able to replace the quenched average (2.75) by an annealed average, at the price of introducing n replicated order parameter fields ϕ_μ [48, 164]. Integrating over the disorder [169] one finds

$$\mathcal{H}\left[\{\phi\}; r, u, \Delta_\tau\right] = \int \mathrm{d}^d x \sum_{\mu=1}^{n} \left(\frac{1}{2} (\nabla \phi_\mu)^2 + \frac{r}{2} \phi_\mu^2 + \frac{u}{4!} \phi_\mu^4 \right) - \Delta_\tau \sum_{\mu,\nu=1}^{n} \phi_\mu^2 \phi_\nu^2, \tag{2.80}$$

where the explicit form of the disorder distribution given by Equation (2.77) was used. Note that because of to the last term, this Hamiltonian effectively represents a homogenous disorder-free coupled n-component theory. It can be studied using RG methods and eventually one obtains the corresponding renormalization group flow depending on the three effective couplings r, u and the disorder strength Δ_τ. In Figure 2.10 we show the results for the diluted three-dimensional N-vector model in the (u, Δ_τ) coupling plane [168]. In the right panel, where the situation for the XY, Heisenberg and higher-symmetry models ($N > 1$) is drawn, we find a Gaussian as well as a non-trivial Wilson-Fisher fixed point at finite values of the coupling parameters (compare Figure 2.5). As can be seen, the system flows towards the pure fixed point, independent of the disorder strength. It therefore stays in the clean $O(N)$ universality class, even though strong corrections to scaling can be expected [25]. Instead, for the Ising case ($N = 1$), shown in the left panel, the system runs away from the clean Ising fixed point and a new stable *disorder fixed point* emerges which attracts the system for any disorder strength. The system is hence expected to cross over to a new universality class, accompanied by critical exponents different from the clean Ising ones. For a more comprehensive discussion, see [25].

2.5.3 The Harris criterion

Under which conditions is quenched random-mass disorder expected to change the character of a phase transition? This question was answered in a seminal work by A. B. Harris in 1974. His prominent relevance criterion [46] can be deduced using a remarkably simple line of reasoning [47, 170], which will be presented in the following. For convenience, we again adopt the magnetic language, although the arguments are by no means restricted to magnetic systems.

Consider a disordered (for instance site-diluted) Ising system at a temperature T slightly above its critical point T_c. The spins are effectively organized in collective clusters whose characteristic size is determined by the correlation length ξ. Inside the clusters, the individual spins tend to be aligned in parallel due to strong couplings between them and a comparably small coupling to their surroundings. Depending on the exact realization of the randomness inside those coherence volumes ξ^d (see Figure 2.11a), the phase transition in this finite region is located at a temperature $T_{c,i}$, which is in general different from the global critical point T_c. Consequently, one obtains a distribution of local transitions temperatures in the system (see Figure 2.11b), whose root-mean-square variation will be denoted by

$$\Delta T_c = (T_{c,1}^2 + T_{c,2}^2 + \ldots)^{1/2}. \tag{2.81}$$

This width of the fluctuations is compared to the global distance from criticality $T - T_c$, which allows us to distinguish two qualitatively different regimes:

- $\Delta T_c < T - T_c$
  The fluctuations in the local transition temperatures are smaller than the global distance from criticality. As a results, all individual correlation volumes are supercritical with respect to the global phase transition, i. e. they are located on the same side of the transition, resulting in a homogeneous appearance of the system.
- $\Delta T_c > T - T_c$
  When the width of critical-temperature-fluctuations exceeds the global distance from criticality, some correlation volumes are still in the ordered phase whereas others are already in the high-temperature regime. Due to this heterogeneity, the transition will be qualitatively affected by the disorder.

Harris argued that in order for the transition to be stable, the first inequality, $\Delta T_c < T - T_c$, has to hold as the critical point is approached. At this point it is convenient to rewrite the inequality in terms of the correlation length. From Section 2.1 we know that

$$\xi \sim |T - T_c|^{-\nu} \qquad \text{as} \qquad T \to T_c, \tag{2.82}$$

where ν denotes the critical exponent of the pure system. Furthermore, employing the central limit theorem, which states that the variations in the transition temperatures of the local correlation regions scale as the square root of the block volume, we can also express ΔT_c in terms of the correlation length, namely as

$$\Delta T_c \sim \xi^{-d/2}. \tag{2.83}$$

Requiring that $\Delta T_c < T - T_c$ holds, as $\xi \to \infty$, we obtain an inequality for the exponents, called

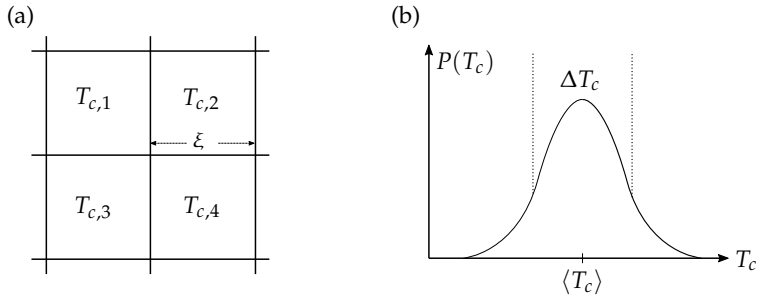

Figure 2.11 | Schematic illustration of the Harris criterion. (a) Correlation volumes of a disordered equilibrium system, exhibiting local transition temperature of individual spins which tend to fluctuate collectively inside strongly connected clusters (b) Distribution of block transition temperatures. Reproduced from [47].

the **Harris criterion**, which states that disorder is irrelevant if

$$d\nu > 2 \tag{2.84}$$

and, conversely, is expected to change the character of the transition for $d\nu < 2$. Provided that hyperscaling is in effect, the stability condition can be recast as

$$\alpha < 0 \tag{2.85}$$

using Josephson's identity (2.19), where α denotes the critical exponent of the energy fluctuations.

Despite the elegance of these heuristic arguments, the Harris criterion can also be found through a more explicit calculation, starting from the disordered Hamiltonian (2.76), where random-mass disorder is implemented as a space-dependent function for the local distance from criticality $\delta\tau(\boldsymbol{x})$. Without loss of generality, this function can again be assumed to have a zero average. The correlations are given by

$$\overline{\delta\tau(\boldsymbol{x})\delta\tau\left(\boldsymbol{x}'\right)} \equiv \Delta_\tau \, G_{\tau\tau}\left(\boldsymbol{x}-\boldsymbol{x}'\right), \tag{2.86}$$

where the constant Δ_τ controls the disorder strengths and the correlation function $G_{\tau\tau}$ depends only on the spatial distance, as the system is translationally invariant. In order to derive the stability criterion, we compare the root-mean-square fluctuations of the local perturbations of the transition temperature

$$\Delta\tau \equiv \sqrt{\sigma_\tau^2} = \sqrt{\overline{\left[\frac{1}{\xi^d}\int_\xi \mathrm{d}^d x \, \delta\tau(\boldsymbol{x})\right]^2}} \tag{2.87}$$

to the global distance from criticality, given by $|\tau|$, obtaining

$$\frac{\Delta\tau}{|\tau|} = \frac{1}{|\tau|\xi^d}\sqrt{\int_\xi \mathrm{d}^d x \int_\xi \mathrm{d}^d x' \overline{\delta\tau(\boldsymbol{x})\delta\tau\left(\boldsymbol{x}'\right)}} \tag{2.88a}$$

$$= \frac{1}{|\tau|\xi^d} \sqrt{\int_\xi \mathrm{d}^d x \int_\xi \mathrm{d}^d x' \Delta_\tau \, G_{\tau\tau}\left(\boldsymbol{x} - \boldsymbol{x}'\right)} \tag{2.88b}$$

$$= \frac{1}{|\tau|\xi^d} \sqrt{\int_\xi \mathrm{d}^d x \int_\xi \mathrm{d}^d x' \Delta_\tau \, \delta\left(\boldsymbol{x} - \boldsymbol{x}'\right)} \tag{2.88c}$$

$$= \frac{\sqrt{\Delta_\tau}}{|\tau|\xi^{d/2}} \sim |\tau|^{d\nu/2-1}, \tag{2.88d}$$

where in the third step we have explicitly used Equation (2.78), corresponding to uncorrelated or effectively short-ranged spatial disorder.[17] In order to obtain a stable critical point $\Delta\tau/|\tau|$ must vanish as $\tau \to 0$, which is only the case if $d\nu/2 - 1 > 0$ and hence $d\nu > 2$. Thus we obtain precisely the Harris inequality.

What makes Harris' criterion so elegant is the fact that it allows for a simple interpretation. If the ratio $\Delta T_c/(T - T_c)$ goes to zero as we approach the critical point, disorder becomes less and less relevant on larger length scales and eventually vanishes, leaving a homogenous critical system. Qualitatively speaking, in a clean system at criticality, if we zoom away, the appearance will not change due to the property of scale-invariance. If disorder is asymptotically irrelevant, it does not change this picture. In the opposite case, however, the strength of disorder approaches a finite value for all length scales or even becomes stronger with increasing length scale. As a consequence, the spatially non-uniform behaviour of correlation blocks is enhanced, which ultimately results in a qualitative change of the critical behaviour. Note that for the marginal case $d\nu = 2$ no predictions can be made based on the arguments above.

Adding disorder to a system (such as random lattice impurities) in general shifts the transition to lower temperatures. In the region between the clean critical point T_c^0 and the (actual) disordered critical point T_c, i. e. for temperatures in the range $T_c < T < T_c^0$, so-called *Griffiths effects* can be observed [171], as illustrated in Figure 2.12. In the thermodynamic limit arbitrary large regions devoid of impurities can be found, which effectively act as a local clean system. When the working temperature is below the clean critical point, these so-called *rare regions* tend to be locally ordered while the system is globally in the paramagnetic phase. In fact, Robert Griffiths [172] was able to show that the free energy exhibits a singular behaviour in the entire region region $T_c < T < T_c^0$, which, for this reason is called Griffiths phase [173]. The dynamics of the rare regions is very slow, as a coherent change of spins in the whole region would be required to flip them.

A classification scheme which qualitatively predicts the influence of Griffiths effects on continuous phase transition was proposed in Reference [174]. Since rare regions only occur with a probability depending exponentially on their size, their effective dimensionality d_{eff} determines whether they contribute significantly to measured observables. If d_{eff} is smaller than the lower critical dimension of the system, $d_{\mathrm{eff}} < d_l$, then the rare regions can not undergo a finite temperature phase transition on their own (compare Section 2.2.1). Hence their effects are generically weak and expected to be unobservable in experiments. The transition shows conventional power-law scaling. An example are classical equilibrium spin models with (finite, and therefore effectively zero-dimensional) random impurities, where $0 = d_{\mathrm{eff}} < d_l = 1 + \varepsilon$. In the case $d_{\mathrm{eff}} = d_l$, rare regions still can not undergo a phase transition. However, a

[17] In the heuristic derivation of the Harris criterion given earlier, this assumption enters through the use of the central limit theorem.

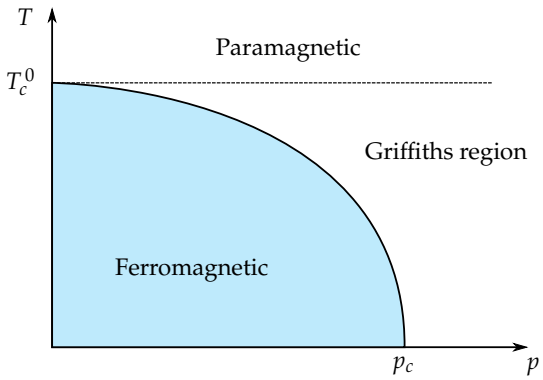

Figure 2.12 | Phase diagram of a randomly diluted Ising magnet. The x-axis shows the dilution probability, where p_c denotes the geometric percolation threshold of the lattice. The y-axis shows the temperature and the solid black line corresponds to the dilution-dependent critical temperature. Reproduced from [171].

subtle interplay between the fact that rare regions become exponentially unlikely with their volume but – in this case – individual regions contribute exponentially strong to macroscopic observables, results in strong power-law Griffiths singularities with non-universal continuously varying exponents. As also the scaling at the disordered critical point T_c is affected by rare region contributions, the conventional power-law behaviour is replaced by an exotic activated (exponential) scaling scenario. Further details will be given in Section 4.3.3, where the disordered contact process, which provides an examples for this case ($d_l = 1$, $d_{\text{eff}} = 1$, including time) is discussed. Finally, if $d_{\text{eff}} > d_l$, local regions can spontaneously undergo a transition on their own and a global phase transition is effectively destroyed by smearing [78].

2.5.4 Topological disorder

It was mentioned in the previous section that as it stands, Harris' inequality only holds for effectively (spatially) uncorrelated disorder. In fact, over the past decades, different authors employed a similar perturbative reasoning to derive relevance criteria for other types of disorder correlations as well. A specific generalization was found in 1983 by A. Weinrib and B. Halperin [175], who were the first to study long-range correlated spatial randomness, given by a disorder correlation function which decays as $G_{\tau\tau}(\boldsymbol{x}) = |\boldsymbol{x}|^{-a}$. Using this functional form to replace the δ-correlator in Equation (2.88), one arrives at a stability criterion $a\nu > 2$ for $a < d$, whereas the normal Harris inequality holds for the case $a > d$. Moreover, in 1985, W. Kinzel adapted Harris' reasoning to uncorrelated temporal disorder [176], resulting in a stable critical point, if $z\nu > 2$, where z denotes the dynamic exponent of the physical model. Another couple of years later, the first mathematically rigorous proof of Harris' original inequality was brought forward by Chayes et al. [177].

A further generalization, which is of particular importance for the present study, was put forth in 1993 by J. M. Luck [68], who investigated the influence of aperiodic structures on continuous phase transitions. This class of structures comprises smooth deformations of regular lattices, as well as quasi-periodic tilings and general random lattices. Whereas in the former case of so-called *modulated* structures, the effective disorder strength Δ_τ can be tuned arbitrarily weak,

the latter class features intrinsic topological inhomogeneities and hence the limit $\Delta_\tau \to 0$ does not exist naturally. In the absence of a regular underlying lattice, Luck resorted to fluctuations in the local coordination numbers of the lattice sites as the predominant random variable. Specifically, he considered spherical patches P of radius R, where the radius is measured based on link-distances rather then on actual spatial coordinates. To be concrete, the spherical shell of radius i around the origin site is given by all sites which can be reached from this site by travelling along exactly i links and have not already been part of the $(i-1)$-th shell. The average node coordination number of a patch is given by

$$Q(R) \equiv \frac{1}{N(R)} \sum_{i \in P} q_i \tag{2.89}$$

and fluctuates around the infinite-volume expectation value $Q_0 = \lim_{R\to\infty} Q(R)$. Moreover, $N(R)$ denotes the volume of the patch, i. e. the total number of nodes enclosed by P. Using the notation $\langle \ldots \rangle$ to average over an ensemble of graphs, for increasing patch sizes $R \to \infty$ the fluctuations decay as

$$\sigma_Q(R) \equiv \langle |Q(R) - Q_0| \rangle / Q_0 \sim \langle N(R) \rangle^{-(1-w)} \sim R^{-d(1-w)}, \tag{2.90}$$

which defines the *wandering exponent* ω. At this is point, it is important to remark that ω is a geometrical property of the considered graph, rather than a property of the physical model. For fractal structures, such as quantum gravity graphs discussed in Reference [69], d is replaced by the Hausdorff dimension.

Analogously to relation (2.88), as criticality is approached ($\xi \to \infty$, $\tau \to 0$), the corresponding fluctuations inside a correlation volume, $\sigma_Q(\xi) \sim \xi^{-d(1-w)}$, should vanish in order to guarantee stability of the critical point, i. e.

$$\sigma_Q(\xi) = \sqrt{\Delta_\tau}\, |\tau|^{d\nu(1-\omega)} \to 0 \qquad \text{as} \qquad \tau \to 0, \tag{2.91}$$

where Δ_t in this case denotes the second moment of the coordination number fluctuations, encoding the disorder strength. From Equation (2.91) we obtain a threshold value for the wandering exponent

$$\omega_c = 1 - \frac{1}{d\nu} \tag{2.92}$$

separating the regime of relevant and irrelevant fluctuations. For wandering exponents below ω_c, the regular critical behaviour persists, whereas for $\omega > \omega_c$ a new type of critical behaviour can be expected. Note that for $\omega = 1/2$ the original Harris inequality is contained as a special case. Moreover, also the criterion by Weinrib and Halperin can be recovered, since for long-range correlated disorder the wandering exponent becomes $\omega = 1 - a/2d$.

Despite the elegance of Luck's arguments, computing wandering exponents of topologically disordered structures is a non-trivial task, not free of ambiguities. In a rather elaborate study, Janke and Weigel [69] computed the wandering exponents of the two-dimensional Delaunay triangulation (DT) using two different methods, either evaluating the scaling behaviour (2.90) directly – and through an analysis of the two-point disorder correlation function. According to

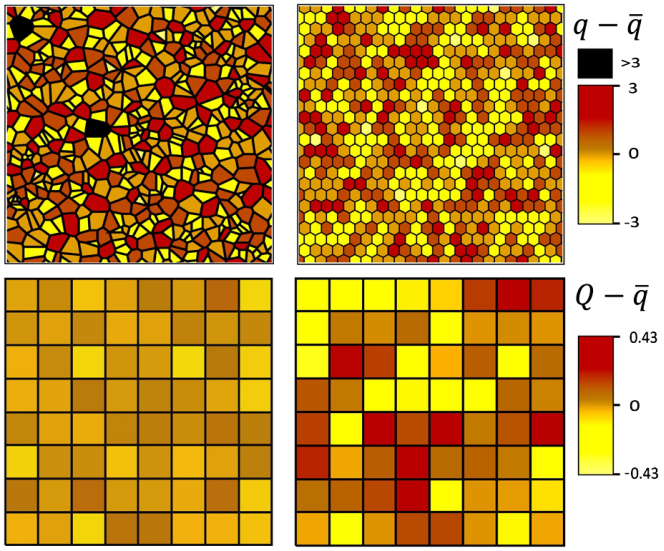

Figure 2.13 | Block-averaged coordination numbers. The top row shows the coordination numbers of a Delaunay triangulation (left) and a randomly diluted hexagonal lattice (right). In the corresponding lower panels, the coordination numbers have been averaged over spatial blocks. From [67].

their result, $\omega_{\mathrm{DT}} = 1/2$, disorder of the DT type should be as relevant as uncorrelated disorder, revealing an inconsistency to simulations of the two-dimensional Ising model on this type of disorder [50, 51, 178], where a very clear clean universal behaviour was observed with no indications of strong corrections due to a possible marginality of the system with respect to Luck's criterion. Even more striking, a study of the two-dimensional 3-state Potts model [60] on the DT reported changed critical exponents, although due to the clean correlation length exponent $\nu = 5/6$ and hence a wandering exponent threshold of $\omega_c = 2/5 < \omega_{\mathrm{DT}}$, regular universal behaviour would have been expected.

In the following years, further puzzling numerical results were found for lattice models in the DP universality class ($\nu \approx 0.733$, $\omega_c \approx 0.318$ in two dimensions) on disordered structures. Whereas the emergence of a new disorder fixed point for the contact process on randomly diluted lattices [179–181], already predicted by theory [182, 183], is fully covered by the original Harris criterion, the fact that the contact process on a two-dimensional DT shows clean universal behaviour came as a surprise. A similar discrepancy was uncovered for the three-dimensional Ising model ($\nu \approx 0.630$, $\omega_c \approx 0.471$) which features clean universal behaviour on the Delaunay lattice [58, 184], even though the Harris-Luck condition is violated.

Most of these apparent issues could be resolved in 2014 by H. Barghathi and T. Vojta [67] who presented a refinement of the previous arguments, resulting in a more convenient approach to calculate wandering exponents of a specific geometry. In particular, they were able to analytically motivate that geometrical constraints can lead to a faster decay of coordination number fluctuations and, as a consequence, the wandering exponent of the DT being actually given by $\omega_{\mathrm{DT}} = 1/4$. Specifically, the authors adapt the idea of Luck and partition the two-dimensional random lattice of size $N = L^2$ into N_b spatial blocks of size L_b^2. The average

coordination number within one block is given by

$$Q_\mu \equiv \frac{1}{N_\mu} \sum_{i=1}^{N_\mu} q_i, \tag{2.93}$$

where N_μ denotes the number of lattice sites contained in block μ and q_i is the coordination number of the lattice site i, as before. An example for the resulting block-averaged coordination numbers is shown in Figure 2.13. Moreover, one can compute the standard deviation of Q_μ, which is used to quantify coordination number fluctuations. It reads

$$\sigma_Q(L_b) \equiv \sqrt{\frac{1}{(L/L_b)^2 - 1} \sum_{\mu=1}^{(L/L_b)^2} \left(Q_\mu - \overline{q}\right)^2}, \tag{2.94}$$

where $\overline{q}$ denotes the *asymptotic* average coordination number of the lattice and we used the fact that $N_b = L^2/L_b^2$. The argument L_b already indicates that these disorder fluctuations can be evaluated on different length scales, corresponding to different patch radii in Equation (2.90). For increasing block size, the fluctuations are expected to scale according to

$$\sigma_Q(L_b) \sim L_b^{-a}, \tag{2.95}$$

which defines the dimension-dependent *disorder decay exponent*, denoted by the symbol a. If we require the fluctuations to decay sufficiently fast at criticality (compare Equation 2.91) we obtain a modified inequality which we call the **Harris-Barghathi-Vojta** (HBV) criterion. Quenched topological randomness is irrelevant and does not alter the transition if

$$a\nu > 1, \tag{2.96}$$

whereas in the converse case changed critical behaviour can be expected. Obviously, the decay exponent is strongly related to the wandering exponent, namely by

$$a = d(1 - \omega) \tag{2.97}$$

and therefore a value of $a = 1$ corresponds to uncorrelated randomness. For the DT on the other hand, Barghathi and Vojta found a different exponent, $a = 3/2$, thus rendering disorder of this type *less relevant* than generic uncorrelated randomness. Moreover, the authors were able to motivate this result from geometrical constraints, as will be detailed in the following.

Concretely, they apply the Euler equation for two-dimensional planar graphs, stating that

$$\chi = N - E + F, \tag{2.98}$$

where N, E and F denote the number of sites, edges and facets, respectively. In a triangulation, each edge is shared by two triangles and since each triangle has three edges, $3F = 2E$. As furthermore, for the case of periodic boundary conditions, the Euler number $\chi = 0$, we arrive at $E = 3N$, which means that the total coordination number does not fluctuate. In fact, every disorder realization features an average coordination number of exactly $\overline{q} = 2E/N = 6$. Applying the argument to a single block, it is obvious that only those triangles that cut the

Table 2.4 | Predictions of the HBV criterion for the two-dimensional Ising, Potts and direct percolation (DP) universality classes as well as observations from numerical, theoretical and experimental studies with respect to whether the clean universal behaviour is present (✓) or not (✗) for the respective geometry. The disorder decay exponent a is calculated in Section 3.4.

Class	ν	Lattice	a	$a\nu$	Prediction	Observation	References
Ising	1	DT	$3/2$	$3/2$	✓	✓	[50, 51, 59, 178]
Ising	1	Diluted	1	1	-	marginal	[185–200]
3-state Potts	$5/6$	DT	$3/2$	$5/4$	✓	✓	[60]
3-state Potts	$5/6$	Diluted	1	$5/6$	✗	✗	[201, 202]
4-state Potts	$2/3$	DT	$3/2$	1	-	unclear	[62, 69]
4-state Potts	$2/3$	Diluted	1	$2/3$	✗	✗	[203–206]
DP	0.733	DT	$3/2$	1.100	✓	✓	[65, 66]
DP	0.733	Diluted	1	0.733	✗	✗	[179–181]
DP	0.733	DT^+	1	0.733	✗	✓	[P1]

surface of the block can lead to coordination number fluctuations, as for the cells entirely inside the block, $3F = 2E$ holds. Assuming the surface contributions to Q_μ to be independent, we can apply the central limit theorem, resulting in $\sigma(L_b) \sim L_b^{1/2}/L_b^2 = L_b^{-3/2}$, and therefore $a = 3/2$. From Equation (2.97) it becomes clear that the correct wandering exponent of the DT is hence given by $\omega = 1/4$. The reason why Janke and Weigel obtained a spurious decay $\omega = 1/2$, is also pointed out in Reference [67]: If the patches are constructed based on link distances rather than on real-space blocks, the average coordination number inside the cluster is in general larger than the global average coordination number, i. e. $Q_0 > \bar{q}$. This bias had not been taken into account in previous studies and stems from fact that sites with more neighbours have a larger chance of being added to the cluster. Taking proper care of this bias, the result $a = 3/2$ can also be reproduced using link-distance clusters [67].

But how can the fast decay be understood? It has been shown above that for any tiling of the plane with triangles, the total number of links is constrained. As a consequence, highly connected nodes will typically be surrounded by less connected nodes and vice verse, which can be qualitatively measured using the two-point correlation function of the coordination number, as will be discussed in detail in Section 3.4, where we present numerical results for several disordered lattices. Using this measure, the authors [67] revealed strong spatial anti-correlations in the local coordination numbers for the DT, explaining the fast decay of disorder on increasing length scales. Similar holds for other constraint structures, such as quadrilateral tilings of the plane as well as certain deterministic quasi-periodic lattices. These structures are therefore expected to yield decay exponents $a > 1$ (or wandering exponent $\omega < 1/2$), resulting in an improved stability of the critical behaviour compared to uncorrelated disorder.

In fact, given the correct geometric exponent of the DT, all previous results can be explained, as detailed in Table 2.4. For the DT, the HBV criterion predicts marginal behaviour for a correlation length exponent $\nu = 2/3$, since in this case $a\nu = 1$. Interestingly, a system with this property

Table 2.5 | Timeline of disorder relevance. Listed are significant contributions towards an answer of the question under which conditions quenched disorder is relevant with respect to the stability of a continuous phase transitions. The results of Reference [P1] will be presented in detail in Section 5.3

1974	Harris	Seminal work, presenting the central argument; Uncorrelated disorder irrelevant if $d\nu > 2$	[46]
1983	Weinrib & Halperin	Extension to long-range correlated disorder	[175]
1985	Kinzel	Extension to uncorrelated temporal randomness	[176]
1989	Chayes et al.	Mathematically rigourous proof of Harris' inequality	[177]
1993	Luck	Generalization to aperiodic structures; Introduction of the geometric wandering exponent	[68]
1998	Aharony et al.	Canonical constraints on the random variables are irrelevant	[207]
2004	Janke & Weigel	First to specifically adress topological randomness; (Wrong) calculation of wandering exponent for DT	[69]
2014	Barghathi & Vojta	Correct wandering exponent for DT; Coordination number anti-correlations found to improve stability against disorder	[67]
2016	Vojta & Dickman	Generalization to diffusive disorder	[208]
2018	Schrauth et al.	Construct explicit violation for criteria of Luck and Barghathi & Vojta; Characterization of topological randomness by coordination numbers not sufficient	[P1]

does indeed exist, namely the 4-state Potts model. To our best knowledge, so far only two studies considered this model on a DT. In Reference [62] the authors – even though they indicated that their results might be inconclusive due to small lattice sizes used – found indications for changed critical exponents. In contrast, a different group of authors [69] mentioned, without explicitly presenting their results, regular critical behaviour. This discrepancy might, in the light of the HBV argument, very well be understood as an effect of corrections due the marginality of the model. However, we remark that despite the elegance of the arguments of Luck and Barghathi & Vojta, we found an explicit violation of both criteria in the present work, when we simulated the two-dimensional contact process on a specially designed variation of the DT with additional random local bonds. These results will be presented in Section 5.3.

In order to provide a better overview over the publications which significantly contributed to investigate the influence of quenched disorder on critical phenomena, we give a detailed chronological list in Table 2.5.

Chapter 3

Topological Disorder

"Ordnung ist die Verbindung des Vielen nach einer Regel."

– Immanuel Kant

As we aim at improving the understanding of critical phenomena on disordered structures, the most common types of (especially) topologically disordered lattices are reviewed in this chapter. Particular attention is given to the constant coordination *(CC) lattice and a* Delaunay triangulation with additional bonds *(DT^+), which have been newly developed in the course of the present work.*

3.1 Terminology

Besides the actual physical formulation of a problem, encoded in a Hamiltonian for equilibrium systems and in a master equation for non-equilibrium systems, also the underlying spatial structure on which the problem is placed can have crucial influence. For discrete systems, the topology of the system is usually encoded in a *lattice*, which defines neighbouring relations among individual degrees of freedom (spins, agents, grains, ...). For the number of nearest neighbours of a given site, which is the number of sites it is directly connected to, we use the terms *coordination number* and *degree* as synonyms. The usual symbol is q. Similarly, the terms *lattice* and *graph/network* can be regarded as synonyms throughout this work, even though lattice is occasionally used in a slightly more specific meaning, namely when giving emphasis to spatial graphs with predominantly local connections. Finally, also the terms *link*, *bond* and *connection* will be used interchangeably.

Topological disorder is defined by the fact that connections between lattice sites are not assembled in a regular or periodic fashion, hence lacking any translational order. As a result, in general, no local *motif* (sub-graph defined by a particular pattern of connections between vertices) will be found elsewhere in the lattice, as it is obviously the case in regular lattices but also for quasi-periodic structures [209]. Constructing a topologically disordered graph naturally starts with a random distribution of sites in the given spatial domain. The coordinates of each site are obtained through stochastic spatial point processes. Specifically, we use the *Poisson point process* with constant spatial intensity $\lambda(\boldsymbol{x}) = \lambda$ (also called homogeneous Poisson point process), which in some sense introduces the maximum amount of randomness to the system, since consecutive coordinates are drawn independently. In other words, the history of the process is irrelevant, when a new site is drawn.[18] Moreover, the name stems from the fact that the number of points in a finite region Ω obeys a Poisson distribution, i. e.

$$P(N(\Omega) = n) = \frac{(\lambda|\Omega|)^n}{n!} \exp(-\lambda|\Omega|) \tag{3.1}$$

denotes the probability of finding n points inside Ω. The resulting *spatial* distribution of sites is uniform and isotropic – hence no topological defects are introduced, which is a desirable property. More details on spatial point processes can be found in Reference [210]. In practice, the Poisson point pattern in a subspace of the Euclidean space is generated by drawing independent and identically distributed (i.i.d.) random variables in the corresponding interval from a uniform distribution for each coordinate. For the construction of our lattices we use, unless otherwise stated, periodic boundary conditions in all spatial dimensions throughout this work. Typically, the spatial domain is given by $[0, L]^d$, where the linear size L is defined by $L = N^{1/d}$ and N denotes the total number of lattice sites.

Finally, note that throughout this work, all interaction strengths are set to unity. Sites are hence influenced equally strong by all of their direct neighbours, irrespective of the actual spatial distance. This simplifies the numerical calculations and is justified in so far as it is known that coupling strengths decaying e. g. exponentially with the distance do not affect the universal properties of the phase transition [59, 60], as the interactions remain effectively short-ranged.

3.2 Proximity graphs

Given a set of discrete points in space, if connections between these points are created according to a rule defined in terms of geometrical closeness, one obtains a so-called *proximity graph*. Proximity graphs are useful in a wide range of applications, most notably mesh generation, surface modelling, pattern classification, ad-hoc networks, path planning and astrophysics [211–218]. Such graphs possess only local connections and their typical shortest path length scales as $\bar{l} \sim N^{1/d}$ on a d-dimensional set of N points, in contrast to small-world networks [219] and some scale-free networks [220], where shortcuts, provided by long-range connections, lead to logarithmic scalings $\bar{l} \sim \ln N$ and $\bar{l} \sim \ln \ln N$, respectively. On the latter, we remark that equilibrium phase transitions display pathological behaviour. For instance, the temperature of the ferromagnetic to paramagnetic crossover was found to shift with the system size and to

[18] A natural counterexample might be the hard core point process, where due to spatial interactions points can not be placed closer than a certain minimal distance (mutual repulsion).

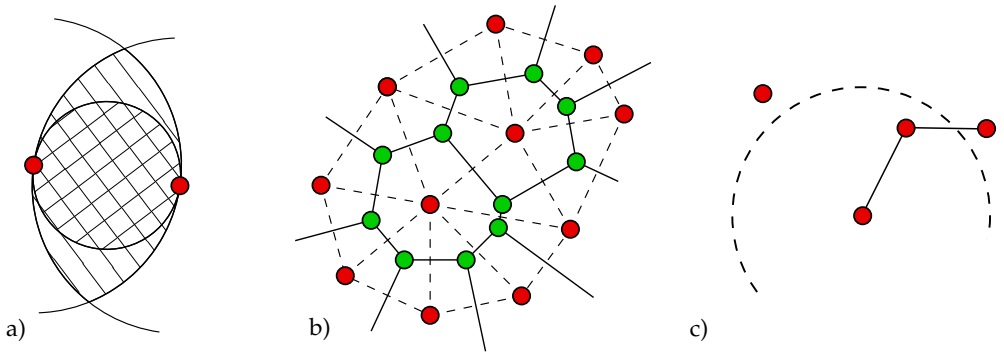

Figure 3.1 | Common proximity graphs construction rules. (a) GG (RNG) construction: the smallest circle (lune) defined by two connected sites, indicated by the cross- (single-) hatching, should contain no other sites. (b) Illustration of the VG (green) and DT (red) lattices. (c) RGG: Only those points which are closer than a certain distance (illustrated by the dashed circle, with the bottommost point as its centre) are connected.

ultimately diverge for $N \to \infty$ [221].

The outline of this section is as follows: First, we consider the *Voronoi graph* (VG) and its dual the *Delaunay triangulation* (DT), both arguably very prominent and often-used proximity graphs. Then, after a brief review of a simple distance-threshold construction (the *random geometric graph*, RGG), two further graphs will be discussed, the *relative neighbourhood graph* (RNG) and the *Gabriel graph* (GG), which represent subgraphs of the DT. Finally, lattices with constant coordination number are addressed in greater detail. We explain why constructing a topologically disordered lattice with constant local coordination number is a non-trivial task, and present our solution, the so-called *CC lattice* algorithm.

Voronoi graph and Delaunay triangulation

Many location optimization problems can be approached through area-of-influence considerations. A simple example is that of several fire stations distributed over a large city. Rather naturally, the area of responsibility attributed to a particular fire station should include those buildings which lie closer to it than to any other station. The resulting tessellation of the city map defines the so-called Voronoi graph (VG). In Figure 3.1b, which shows the construction schematically, the red dots would denote fire stations with the corresponding VG being depicted as solid black lines and green nodes. Due to its conceptual simplicity, Voronoi constructions can be found in a large number of applications, spanning all fields of physical sciences, including climate modelling [222, 223], crystal structure [224], cosmology [216, 225], microbiology [226], and growth processes [227], as well as optimization problems [228], game theory [229–231], artificial intelligence [232, 233] and, recently, also in the field of machine learning [234], among others. Moreover, numerous generalizations have been defined, such as weighted graphs, and Voronoi graphs on spherical and general curved surfaces, [235, 236], as well as for fuzzy point sets [237] or metrics other than Euclidean.[19]

Concretely, the Voronoi diagram is a partition of the plane into cells, generated by a set of

[19] In a more realistic fire station example, one might consider using the Manhattan distance rather than the standard Euclidean one.

points $P = \{p_1, p_2, \ldots, p_N\}$ such that for each cell corresponding to the point p_i, every point q in that cell is closer to p_i than to any other point p_j, i. e.,

$$d(q, p_i) < d(q, p_j) \quad \forall p_j \neq p_i. \tag{3.2}$$

The VG is defined by taking as sites the corners of the cells and, as edges, the boundaries between the cells, as shown in Figure 3.1b. Therefore, the new set of points $P' = p'_1, p'_2, \ldots, p'_{2N}$ is twice as large as the original set that defined the cells. This can be easily seen from the Euler characteristic of a finite graph, which is defined as

$$\chi = N - E + F, \tag{3.3}$$

where N, E and F are the number of vertices, edges and faces, respectively. For the periodic boundary conditions used here, $\chi = 0$ holds. In a Delaunay triangulation, which will be addressed below, $E = 3N$ as the average coordination number is exactly $\langle q \rangle = 6$ and any edge is shared by two triangles. Therefore, one ends up with $F = 2N$ faces in the triangulation and hence $2N$ points in the VG due to the duality property. The locations of the VG sites are given by the centre of the circumcircle of the corresponding triangle in the Delaunay triangulation. A sample of a periodic VG is shown in Figure 3.2. It can be easily seen that all cells have convex shape and that every site has exactly three neighbours. This latter feature, the absence of coordination number fluctuations, will be important later.

As already stated above, the dual of the VG is the so-called *Delaunay triangulation* (DT). It can be constructed by connecting points corresponding to adjacent Voronoi cells. In other words, for a set of points it is a triangulation in which the circumcircle of every triangle is empty, i. e., contains no point of the set. Such triangulations contain as a subgraph the (first) nearest-neighbour graph and guarantee that the distance along the edges between any two points is not larger than about 2.42 times their metric distance [238]. An example of such a lattice for a Poissonian point sampling is shown in Figure 3.2. As can be seen, the local number of neighbours fluctuates. In particular, the smallest possible coordination number is three (corresponding to a triangular Voronoi cell). In a periodic 2D triangulation, the average coordination number is exactly $\langle q \rangle = 6$, which can be calculated using the identity (3.3). For computing Delaunay triangulations and Voronoi graphs, we employ the Computational Geometry Algorithms Library (CGAL) [239].

The Ising model has been thoroughly studied on two- and three-dimensional Delaunay lattices (compare [50, 51, 59] and [58, 184], respectively) and found to belong to the same universality class as the corresponding clean model, both for constant as well as distance-dependent couplings. Whereas the two-dimensional Ising model represents a marginal case of the Harris criterion ($d\nu = 2$, compare Section 2.5), the unchanged universality in three dimensions was surprising, since the criterion is violated. This particular result partially motivated the study of coordination number fluctuations in [67].

Finally, we define the DT^+ lattice: a Delaunay triangulation, furnished with additional local bonds, also shown in Figure 3.2. This lattice is constructed from a DT of N sites, to which kN bonds between *next*-nearest neighbours are randomly added (we select $k = 1$), resulting in a lattice with a total coordination number of exactly $(6 + 2k)N$. This latter constraint is relevant for the applicability of the HBV criterion (compare Section 2.5.4).

Random geometric graph

In the construction of an RGG, any two points whose distance falls below a certain threshold are linked. In d dimensions, these graphs can be defined using the auxiliary variable

$$R_{\langle q \rangle} = \frac{1}{\sqrt{\pi}} \left[\langle q \rangle \, \Gamma \left(\frac{d+2}{2} \right) \right]^{1/d}, \tag{3.4}$$

which denotes the interaction radius of a random geometric graph with $\langle q \rangle$ neighbours on average. The symbol Γ denotes the gamma function with $\Gamma(2) = 1$ and $\Gamma(5/2) = 4\sqrt{\pi}/3$, for two and three dimensions, respectively. For a comprehensive review of further properties see [218]. In an RGG, correlations arise from the fact that a high degree node must be surrounded by many points close to each other, which typically implies rather high coordination numbers in its immediate surrounding as well. In other words, dense clusters are more likely than in generic random networks. This property can be observed very clearly in the example of an RGG lattice shown in Figure 3.3.

Relative neighbourhood and Gabriel graph

In a Gabriel graph (GG), also displayed in Figure 3.3, two points i and j are connected whenever

$$d(i,j)^2 \leq d(i,k)^2 + d(k,j)^2 \tag{3.5}$$

for any other point k of the graph, where $d(i,j)$ is the distance between i and j. This condition translates into requiring that the smallest circle defined by i and j contains no other points. The relative neighbourhood graph (RNG) is similarly defined by the more restrictive condition

$$d(i,j) \leq \max\left[d(i,k), d(k,j)\right] \tag{3.6}$$

and also shown in Figure 3.3. Moreover, we schematically illustrate the construction rules of both graphs in Figure 3.1a.

An interesting property, linking the majority of proximity graph constructions considered in the present section is the fact that they are subsets of each other, given by the relation

$$\mathrm{NN} \subset \mathrm{RNG} \subset \mathrm{GG} \subset \mathrm{DT} \subset \mathrm{DT}^{+} \tag{3.7}$$

where NN denotes the (first) nearest neighbour graph. Due to this property, an algorithm for constructing GGs and RNGs can be built such that starting from a DT, specific bonds, which violate the respective proximity conditions are removed. An overview of the scaling of several different algorithms in a Euclidean space is given in [212].

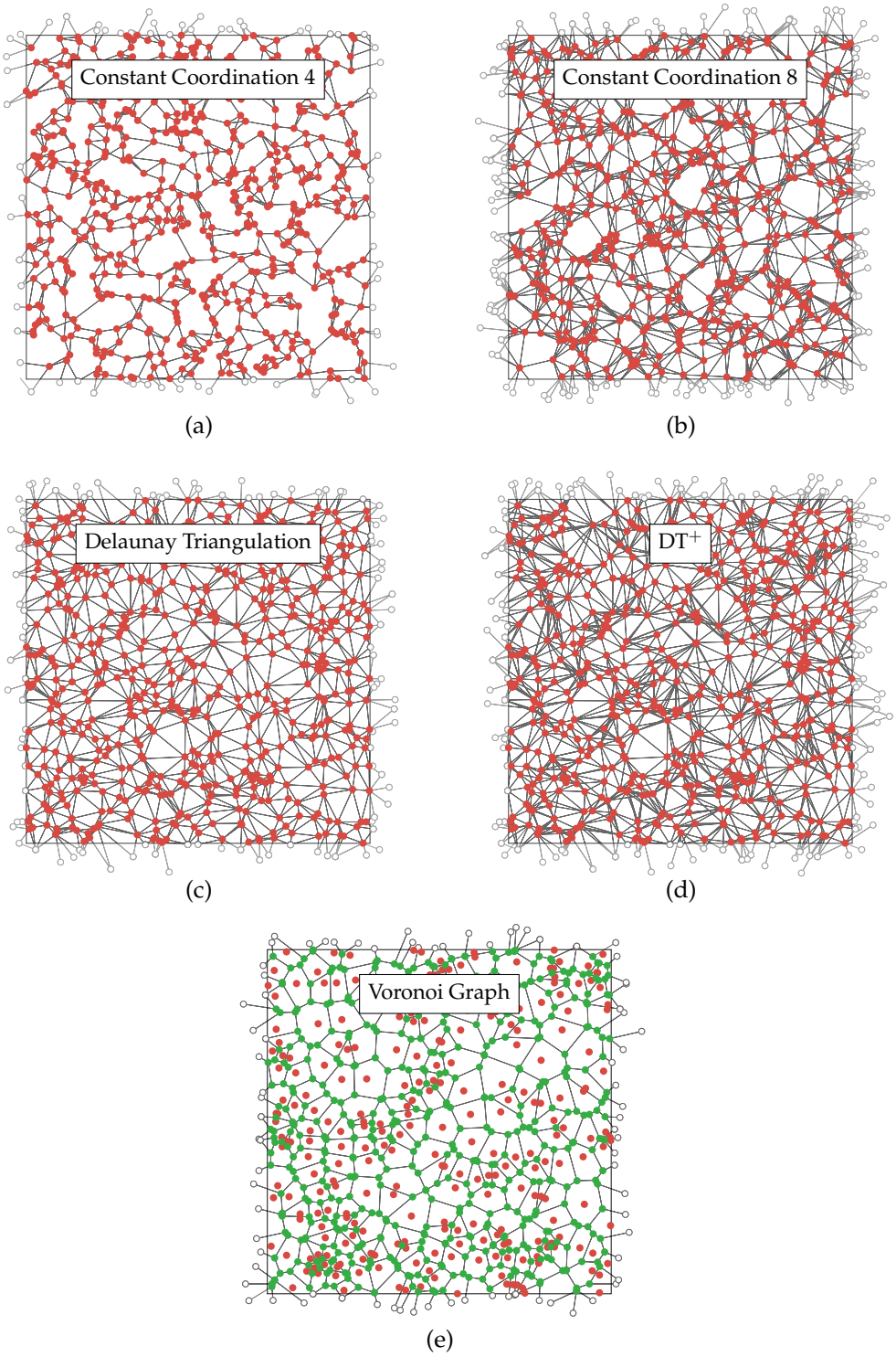

Figure 3.2 | Lattice overview – Part 1. Samples of two-dimensional lattice geometries considered in this work, generated from 24^2 points. (a) Constant coordination lattice with four neighbours, (b) CC lattice with eight neighbours, (c) Delaunay triangulation, (d) Delaunay triangulation with additional bonds, (e) Voronoi graph (green).

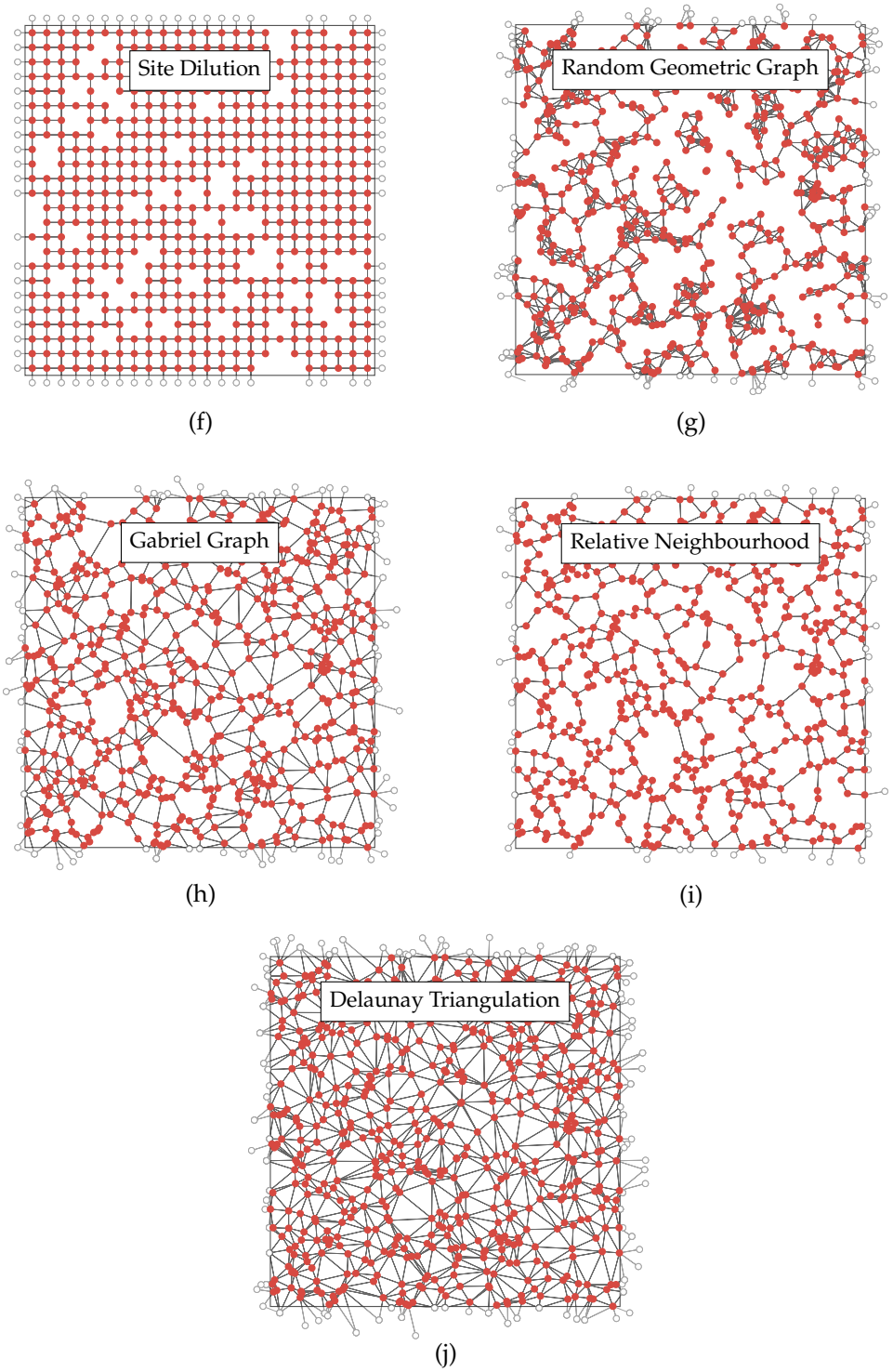

Figure 3.3 | Lattice overview – Part 2. Samples of two-dimensional lattice geometries considered in this work, generated from 24^2 points. Apart from (f), all structures are constructed form the same set of points. (f) Regular square lattice with randomly diluted sites, (g) Random geometric graph, (h) Gabriel graph, (i) Relative neighbourhood graph, (j) DT again (see Figure 3.2), for comparison.

3.3 The Constant Coordination lattice

We present an algorithm for the construction of a topologically disordered lattice with nodes of constant coordination number. Boasting a computational complexity that scales linearly with the number of points, it is significantly faster to build than other proximity graph constructions. Our algorithm performs only local operations, dividing the spatial domain into cells of small linear size compared to the lattice dimensions. This guarantees that bond lengths are bounded and allows a straightforward generalization to any number of spatial dimensions and, in principle, to different metrics and topologies. By efficiently constructing disordered graphs with a fixed number of interactions, the CC lattice could (apart from this thesis) find application in the modelling of amorphous materials such as low temperature amorphous silicon in two and three dimensions [240, 241], especially given that the most well-known lattice with constant coordination number, the Voronoi construction, is not considered a satisfactory model [242].

3.3.1 Motivation

For the majority of proximity graphs introduced above, the local number of neighbours fluctuates. In contrast, a lattice which is still disordered in the topological sense, but where coordination number fluctuations are absent, can be an interesting tool for investigating the influence of disorder on critical systems. When imposing the constraint of a *constant* coordination number of the lattice nodes, the perhaps most obvious approach would be a q-nearest neighbour lattice, where every site is linked to its q spatially closest sites. This construction is particularly simple, as no geometric information other than the point distances is required, and furthermore can be straightforwardly generalized to any dimension. However, the resulting graph in general is *directed*, since neighbourhood is not necessarily reciprocal. Therefore, only q_{out}, the out-degree of every site, will be constant, i. e. exactly q bonds emanate from each site. Since not all links are bi-directional, though, in general $q_{\text{in}} \neq \text{const}$.

In the past, it has been pointed out by several authors that equilibrium systems on directed graphs can be regarded as pathological in the sense that the detailed balance condition is violated [243]. This leads to the fact that, e. g. on a directed, scale-free Barabási-Albert graph, no spontaneous magnetization can be found for the Ising model and different update algorithms[20] lead to different results [244]. On directed small-world networks, higher-spin Ising models, as well as the Blume-Capel model, show a phase transition, which changes from second to first order if a specific critical rewiring probability is exceeded [245–247]. In the second-order regime, the aforementioned results indicate a different universality class compared to the corresponding models on a regular lattice. For a recent review article on this topic, see Reference [63]. To make matters worse, it was first pointed out in [248] that directed systems can be seen as being in a non-equilibrium stationary state rather than in conventional equilibrium. Therefore, a proper definition of the energy of the system becomes problematic [243] and hence the applicability of traditional equilibrium Monte Carlo methods can be regarded as questionable in the first place.

In order to avoid the massive complications accompanied with directedness, there are two common ways to symmetrize q-nearest neighbour constructions. One may either delete any directed links, such that only the bi-directed ones remain, or also add the reverse links to

[20] Update algorithms will be discussed in Chapter 4.

the nodes connected by directed ones. Obviously, lattice sites can be left with more than q neighbours after the latter symmetrization procedure and can have fewer than q neighbours after the former procedure. Additionally, it can easily be checked that neither symmetrization leads to a constant global coordination number Q_{tot}, which means that Q_{tot} is (slightly) different for each disorder realization. Another construction which could come to mind would be to naively link every point to some other randomly chosen points that still has fewer than q neighbours. However, this approach would result in a mean-field-like behaviour of the physical system, similar to small-world networks [249] and Erdös-Rényi graphs [250], as the mean path length is then of the same order as the system size and therefore information propagates effectively instantaneously through the lattice. We therefore must place as a particular demand on our model that the interactions are short-ranged in the sense that the bond lengths obey the relation $\ell \ll L$.

The resulting construction, incorporating the particular demands mentioned above, is called the *Constant Coordination* (CC) lattice and was introduced first in [P2]. By construction, every site is connected to exactly q other sites, without allowing for self or double connections. In this way, any perturbation on the critical behaviour of a phase transition can only originate from the implicit connectivity disorder, independent from coordination numbers. In a second paper [P3], we refined the original construction rules by proposing an improved algorithm with significantly reduced computational complexity (from quadratic to linear in the number of points). Moreover, the improved algorithm can straightforwardly be applied to dimensions larger than two and also eliminates certain shortcomings related to the applicability in finite-size scaling simulations.

The remainder of this section is organized as follows: After a presentation of the basic ideas of the CC algorithm, specific details of the improved implementation, published in [P3] will be discussed. A list of deficiencies of an earlier algorithm, published in [P2], together with detailed explanations of how they are solved in the improved one, can be found in Appendix A.1.

3.3.2 Basic concept

As typical for topologically disordered random lattices, our starting point is a cloud of randomly distributed points in a toroidal domain of linear size L with Euclidean metrics. In the first construction step, bonds between random pairs of sites are gradually introduced until each site has exactly q neighbours. The key step after that, is to subject the graph to a dynamical rewiring, by means of a simulated annealing (SA) procedure [251], in order to achieve locality, i. e. to keep connections effectively short ranged. Specifically, in the SA algorithm, two bonds $\overline{il}$ and $\overline{jk}$ are taken at random and rewired to a new configuration $\overline{ij}$ and $\overline{kl}$ whenever this leads to a decrease of the sum of the bond lengths, i. e. whenever

$$d(i,j) + d(k,l) < d(i,l) + d(j,k). \tag{3.8}$$

If, instead, the new configuration leads to an *increase* of the combined link lengths, the rewiring is accepted only with probability $\exp(-\Delta H/T)$, where

$$\Delta H \equiv [d(i,j) + d(k,l)] - [d(i,l) + d(j,k)] \tag{3.9}$$

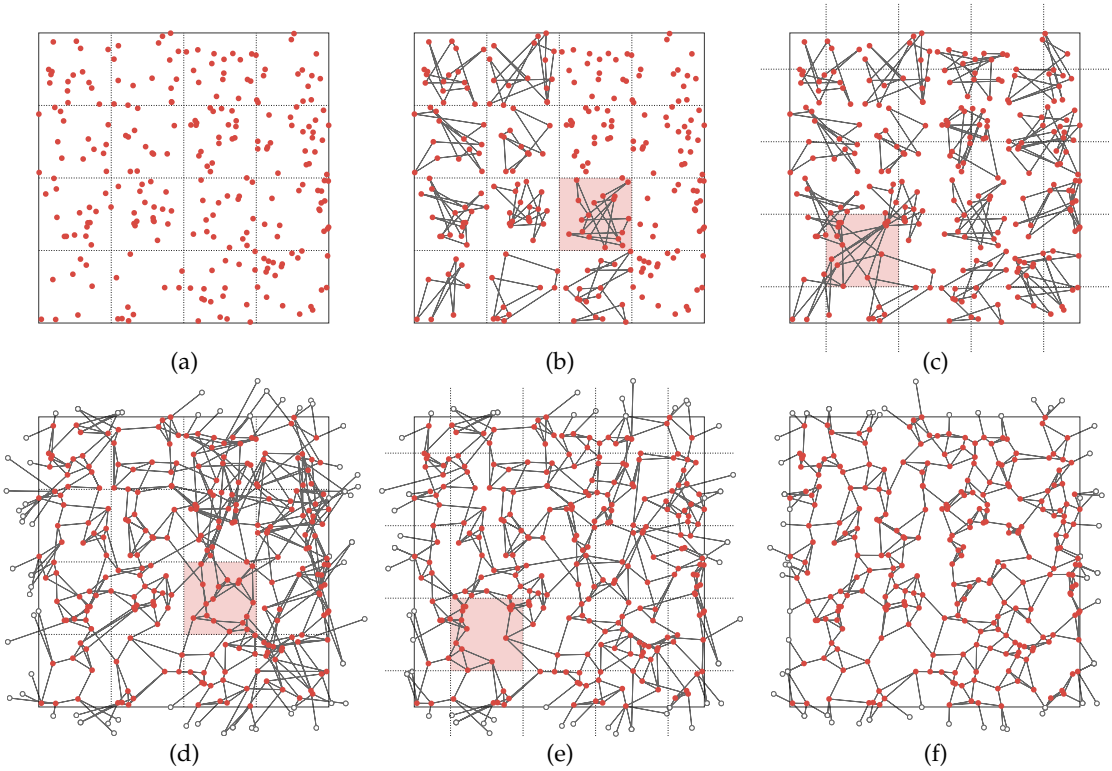

Figure 3.4 | Illustration of the construction process of a CC lattice: (a) Sites are grouped into cells and (b) each site is randomly connected to $q_1 = 2$ neighbours in its respective cell; the sites are then (c) regrouped into staggered cells and each site is connected to $q_2 = 2$ additional random neighbours in its cell; bond lengths are finally minimized by simulated annealing dynamics, performed first (d) in the original cell partition and then (e) for the staggered partition, resulting in (f) a final lattice with coordination number $q = q_1 + q_2 = 2 + 2 = 4$. Note that the shaded region marks the currently processed cell in the respective construction step.

defines the cost function. The simulated annealing temperature T has the effect of noise on the convergence to a state of low cost function. The value of T is logarithmically decreased during the simulation, such that in the beginning, non-optimal rewiring updates are accepted with moderate probability, whereas in the final stages, this probability almost vanishes and only those moves are performed where condition (3.8) strictly applies.

The first algorithm for the CC construction, put forward in the original proposal [P2], presents two central drawbacks: first, it is computationally expensive; second, it requires considerable care and the introduction of an inconvenient extra parameter in order to avoid any dependence of its geometrical characteristics on the lattice size. An improved algorithm for generating the CC lattice, which overcomes these drawbacks, can be obtained based on a simple key concept: instead of over the whole lattice, we perform the construction locally, in subgraphs delimited by grid cells of a small, fixed size. That brings the complexity from $\mathcal{O}(N^2)$ to $\mathcal{O}(N)$ by keeping fixed the size of the set to which the simulated annealing is applied and also precludes any lattice-size dependency, due to its locality.

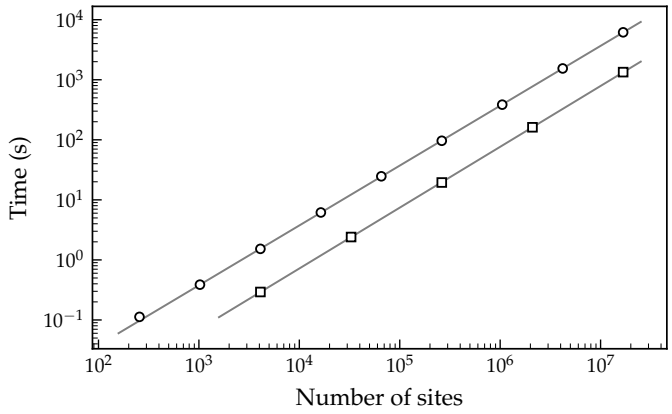

Figure 3.5 | Computing time for the CC lattice. Shown is the scaling of the construction time for CC lattices with $q = 4$ for sizes $L = 16, 32, \ldots, 4096$, in 2D (circles), and $L = 16, 32, \ldots, 256$, in 3D (squares). The straight lines are fits to the data points that return exponents 0.997 and 1.013, supporting the linear scaling behaviour. All data points are averages from at least ten realizations on an Intel Core i7-6700 CPU. The error bars are smaller than the marker sizes.

3.3.3 Algorithmic details

In this section we elaborate on the CC lattice algorithm sketched in Section 3.3.2, giving attention to its improvements over the original proposal [P2], most notably the significant reduction of computational complexity and the improved finite-size scaling properties, for which we use the term *micro-scale equivalence* (MSE). When this equivalence holds, a lattice with N sites and an arbitrary subgraph with N sites from a larger lattice, built from the same rules, are indistinguishable with respect to their connectivity properties (such as average bond length, shortest path, clustering, etc.) up to boundary effects. This property is crucial for the application of finite-size scaling methods. While it is trivially fulfilled for any geometrically constructed lattice, like regular lattices, DTs, RGGs, etc., this is not the case in the original CC algorithm, as it is explained in detail in Appendix A.1.

We impose that all the steps of the lattice construction must be local, restricted to subgraphs delimited by grid cells of a small, fixed size instead of over the whole lattice. Therefore, in the first step of the construction (Figure 3.4a), the spatial domain of linear size L is subdivided into cells $\mathcal{K}_{1,n}$ of linear size ℓ and index n. Typically, we choose $\ell \approx 8$. In the next step (Figure 3.4b), the sites in each cell are linked together, such that each of them has $q_1 < q$ neighbours. Note that building these subgraphs is always possible as long as q_1 is even[21] , a restriction imposed by the *handshaking lemma* [252]. Once this first *layer* of connections is in place, the lattice consists of $(L/\ell)^d$ disconnected subgraphs where $d = 2$ in Figure 3.4. Then, considering a second grid of cells $\mathcal{K}_{2,n}$ that is, for instance, diagonally displaced with respect to $\mathcal{K}_{1,n}$, another set of bonds is added so that each site gets q_2 additional bonds (Figure 3.4c). This staggering of layers results in a seamless, connected graph where each site has $q_1 + q_2$ neighbours. In the next step (Figure 3.4d) bond lengths are reduced by a simulated annealing procedure as described in Section 3.3.2, but now restricted to the cells $\tilde{\mathcal{K}}_{1,n}$, $\tilde{\mathcal{K}}_{2,n}$, ..., where the tilde indicates that the

[21] That we can always assign an even number q_i of neighbours to any set of sites can be easily seen by arranging the sites in a circle and connecting every site to its $q_i/2$ left (or right) neighbours.

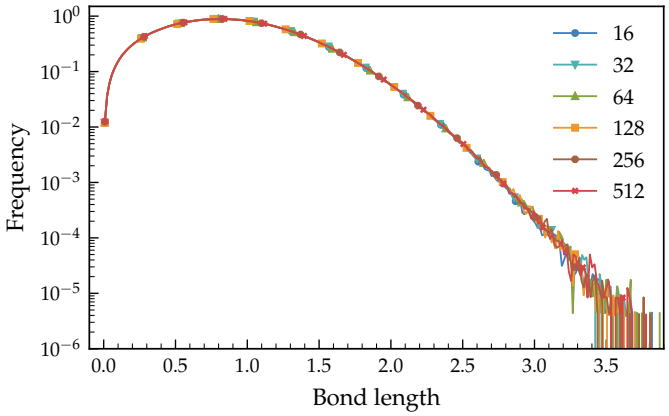

Figure 3.6 | Bond length histograms for two-dimensional CC lattices with $q = 4$ for several values of L in units of $1/L$, indicating that the high degree of locality is independent of the lattice size. Each curve is computed from a sample of 10^8 bonds, for typical parameter values.

cells are open, i. e. not only those bonds are considered which lie completely inside the cells, but also those crossing the boundaries. In contrast to the initial connection steps (b, c), the SA step may be repeated not only for diagonally staggered cells (Figure 3.4e), but also for cells displaced only horizontally or only vertically by $\ell/2$ (not shown in the figure). The rewiring is repeated until the desired degree of locality is reached, completing the construction of the CC lattice (Figure 3.4f). Note that, in order to avoid any directional bias, we switch the order in which the cells are processed (bottom left to top right in Figure 3.4) after each repetition. A detailed pseudocode for the construction procedure can be found in Figure 3.7.

The drawbacks of the earlier algorithm are eliminated in the present, improved version by restricting the most expensive construction step, namely the dynamical rewiring, to the small $\mathcal{K}$-cells. This drastically reduces the complexity of the lattice construction from $\mathcal{O}(N^2)$ to $\mathcal{O}(N)$, as shown in Figure 3.5. Moreover, the MSE property is now fulfilled by construction as long as the length ℓ is fixed for lattices of different size L in a set of finite-size scaling simulations. This can be shown (compare [P2]) by considering the distribution of bond lengths for lattices of different sizes: as the histogram of Figure 3.6 illustrates, the bond length distribution for different values of L coincides perfectly within numerical precision. The concentration of lengths around lower values seen in the figure also gives evidence of the high degree of locality of the lattice.

It should be emphasized that the link distance histogram is a sufficient condition to prove locality for our lattice construction, even though it is not a necessary one. If we, for instance, move lattice points to new randomly chosen locations while keeping all bond connections unchanged, we end up with a completely different link length profile with distances of all length scales. However, the topology of the lattice would not be different than before, as it is solely encoded in the neighbour relations. In this context, the typical shortest path length $\bar{l}$ on the graph can be used as a proper quantity to check locality. As mentioned above, for regular lattices and general proximity graphs, this distance is supposed to scale as $\bar{l} \sim N^{1/d}$, where N is the number of nodes and d denotes the dimension of the system. Since for the CC lattice, the geometric bond distances are explicitly minimized through the rewiring algorithm, this property is fulfilled by design.

Input: set G of $N = L^d$ sites in $[0, L)^d$
Parameters:

- $M_c, M_r \geq 2$ number of connection and rewiring layers
- $q = q_1 + \ldots + q_{M_c}$ coordination number ▷ $q_i \geq 2$
- $r_1, \ldots, r_{M_c+M_r} \in \mathbb{R}^d$ cell displacement vectors
- ℓ linear cell size ▷ typically $\ell \approx 8$
- s number of rewiring attempts per cell and layer
- T initial SA temperature (optional)

Complexity: $\mathcal{O}(sqM_rN)$

Phase 1 – Initial Connections

for $a = 1$ **to** M_c **do** ▷ iterate over connection layers
  subdivide spatial domain into cells $\mathcal{K}_{a,n}$
  of size ℓ^d, displaced by r_a w.r.t. the origin
  for all cells $\mathcal{K}_{a,n}$ **do**
    call CONNECT_SUBGRAPH(sites in $\mathcal{K}_{a,n}$; q_a)
  end for
end for

Phase 2 – Dynamical Rewiring

for $a = 1$ **to** M_r **do** ▷ iterate over rewiring layers
  subdivide spatial domain into cells $\mathcal{K}_{a,n}$
  of size ℓ^d, displaced by r_{a+M_c} w.r.t. the origin
  for all open cells $\tilde{\mathcal{K}}_{a,n}$ **do**
    for $b = 1$ **to** $s \cdot q$ **do** ▷ number of repetitions per cell
      $i, j \leftarrow$ two random sites $\in G$
      $l \leftarrow$ random neighbour of i
      $k \leftarrow$ random neighbour of j
      if not any duplicates in $\{i, j, k, l\}$
        and i **is not** neighbour of j
        and k **is not** neighbour of l **then**
          call REWIRING_ATTEMPT(i, j, k, l; T)
      end if
    end for
  end for
  decrease temperature (if not initially zero)
end for
repeat Phase 2 **until** desired locality is reached

Figure 3.7 | Pseudocode for the construction of the CC lattice. The subroutines CONNECT_SUBGRAPH and REWIRING_ATTEMPT are described in Figures 3.8 and 3.9.

```
procedure CONNECT_SUBGRAPH(set of sites G; q)
    SHUFFLE G
    l_G ← length of G
    for i = 1 to l_G do
        for j = 1 to q/2 do
            k ←   mod (i + j, l_G)                    ▷ cyclic connections
            Add bond from site G(i) to site G(k)
        end for
    end for
    return
end procedure
```

Figure 3.8 | Pseudocode for the subroutines (1). This function cyclically connects a set of points. Note that a call to this subroutine might produce a connection already produced by a previous call, in which case a reshuffle is necessary.

```
procedure REWIRING_ATTEMPT(sites i, j, k, l; T)
    d_A ← distance(i, l) + distance(j, k)             ▷ respecting p.b.c
    d_B ← distance(i, j) + distance(k, l)
    ΔH ← d_B − d_A                                    ▷ cost function, Equation (3.9)
    Draw random number r ∈ [0, 1)
    if r < min(1, e^{−ΔH/T}) then
        Remove bond from i to l
        Remove bond from j to k
        Add bond from i to j
        Add bond from k to l
    end if
    return
end procedure
```

Figure 3.9 | Pseudocode for the subroutines (2). This function attempts a rewiring step by choosing four sites which are mutually connected and comparing the combined bond lengths in the old and new configuration.

Table 3.1 | Examples of possible coordination number decompositions and corresponding cell displacements of the initial connection layers for the CC lattice construction in two and three dimensions.

d	q	q_i	layer displacements
2	4	2+2	$(0,0)$, $(\ell/2,\ell/2)$
2	6	2+2+2	$(0,0)$, $(\ell/3,\ell/3)$, $(2\ell/3,2\ell/3)$
2	6	4+2	$(0,0)$, $(\ell/2,\ell/2)$
2	8	4+4	$(0,0)$, $(\ell/2,\ell/2)$
2	8	2+2+2+2	$(n\ell/4,n\ell/4)$, $n=0,1,2,3$
2	8	2+2+2+2	$(0,0)$, $(\ell/2,0)$, $(0,\ell/2)$, $(\ell/2,\ell/2)$
3	4	2+2	$(0,0,0)$, $(\ell/2,\ell/2,\ell/2)$
3	6	2+2+2	$(n\ell/3,n\ell/3,n\ell/3)$, $n=0,1,2$
3	8	2+2+2+2	$(n\ell/4,n\ell/4,n\ell/4)$, $n=0,1,2,3$
3	8	2+2+2+2	$(0,0,0)$, $(\ell/2,0,0)$, $(0,\ell/2,0)$, $(0,0,\ell/2)$

We remark that some care must be taken with the set of construction parameters q_i. The handshaking lemma states that any finite graph has an even number of odd-degree nodes. As a consequence, the algorithm cannot converge for cells which end up with an odd number of nodes if q_i is also odd. Clearly, this places an important limitation on the algorithm: it should only be used for generating lattices with *even* coordination number q. Provided q_i are even, the number of layers and the amount of displacement can be seen as tunable parameters. For constructing a lattice of constant coordination number $q=6$, for instance, one could employ either $q=q_1+q_2=2+4=6$, or three layers with $q=q_1+q_2+q_3=2+2+2=6$, and displacements $\ell/3$ and $2\ell/3$. A two-layer setting $q=q_1+q_2=3+3=6$ must be avoided due to the evenness requirement from the handshaking lemma. An overview of some of the possible configurations is given in Table 3.1.

3.3.4 Higher dimensions

Whereas the $\mathcal{O}(N^2)$ scaling of the original algorithm is a significant limitation already in two dimensions, for higher dimensions it makes the construction of lattices of reasonable size prohibitively expensive. In this context, it is important to notice that the current algorithm is not only a substantial improvement over the original one, but also compares favourably with algorithms for usual proximity graphs, such as the Delaunay triangulation and its subgraphs, as well as nearest-neighbour graphs. For the latter, typical sequential algorithms are known to scale as $\mathcal{O}(N\ln N)$, through the use of spatial tree decomposition methods [253–255]. For the DT on uniformly distributed points, a $\mathcal{O}(N\ln\ln N)$ scaling is possible [256] using sophisticated divide-and-conquer techniques. In dimensions larger than two, some of those algorithms are not trivially generalized and the scaling is not maintained, such as for the RNG, where one falls back to algebraic complexity in 3D [257]. In contrast, the CC algorithm is straightforwardly

generalized to higher dimensions, as already described in Figure 3.7, while maintaining the $\mathcal{O}(N)$ scaling behaviour, as shown in Figure 3.5. Essentially, the construction remains the same, with only some parameters such as the displacement vectors having to be adjusted accordingly. In particular, the *hypercubic* grid of cells in the higher-dimensional setting admits many more layer configurations and displacement vectors than the square cells of the 2D setting (compare Table 3.1 for examples). One must only ensure that mixing in all directions takes place, such as can always be achieved by a single fully diagonal displacement, i. e.

$$r_1 = (0, 0, \ldots, 0), \quad r_2 = (\ell/2, \ell/2, \ldots, \ell/2).$$

Hence, as in 2D, the smallest possible coordination number is $q = 4$ for any dimension.

Furthermore, the CC algorithm can not only be generalized to higher dimensions, but in principle also to spaces equipped with metrics other than Euclidean, with the single necessary change being in the distance function in the algorithm's rewiring subroutine (Figure 3.9). A generalization to curved manifolds should be possible as long as a proper spatial grid can be defined, such as for the hyperbolic plane $\mathbb{H}^2$, for which a number of regular tessellations can be constructed [258]. However, due to the inherent length scale of this space (the curvature radius), the cell size is determined by geometric constraints and can not be freely chosen. Also, setting up periodic boundary conditions is non-trivial in hyperbolic spaces, although possible [259].

3.3.5 Dimensionality and connectedness

The dimensionality of the initial random point cloud does not trivially determine the dimensionality of the graphs constructed from it. We emphasize that the mere fact that we obtain excellent data collapses of the Ising model scaling functions in Section 5.5, using the known universal exponents, already provides a strong *a posteriori* verification that the lattice is of the expected dimension. Nevertheless, in this section we provide a direct verification through a cluster growth analysis.

In particular, starting from a single seed point, we count the number of sites n in the respective *shells* as the link distance i from the cluster origin grows. Averaging this quantity over different seed points and different disorder realizations, we obtain the average number of i^{th} neighbours, which allows us to determine the actual dimensionality of the graph, as this quantity should scale as $\langle n(i) \rangle \sim i^{d-1}$. In Figure 3.10 we show $\langle n(i) \rangle$ in a double logarithmic plot, averaged over 2000 realizations of two-dimensional CC4 lattices of size $L = 2048$. After an initial transient caused by the discrete nature of the network on small scales, the convergence towards the expected power law (dotted line) is very clear. For comparison we performed the same analysis for the Delaunay triangulation, representing a well-established planar two-dimensional structure. As can be seen, up to a constant offset related to the larger average coordination number ($q = 6$ for the DT), the behaviour is qualitatively the same, hence strongly supporting the fact that the CC construction indeed shows the expected dimensionality.

Besides the actual dimensionality, another important property of (spatial) graphs is their connectedness, i. e. the possibility of obtaining small isolated components, disconnected from the giant spanning cluster. As a matter of fact, the CC lattice algorithm is *not* guaranteed to produce a fully connected lattice, which means that particular realizations may feature small

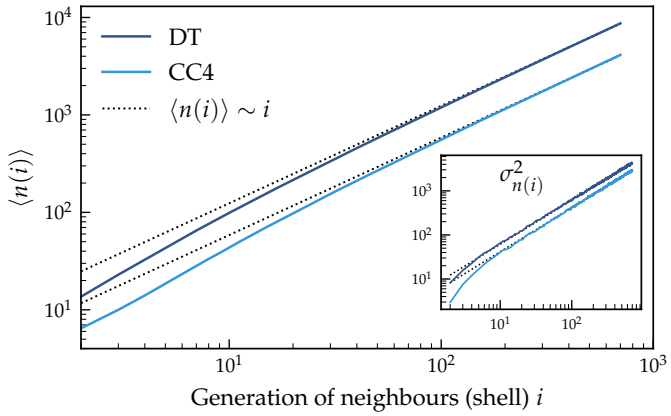

Figure 3.10 | Actual spatial dimensionality of the CC and DT graphs. Curves are computed from cluster growth of lattices of size $L = 2048$ in two dimensions. Also the variance of $\langle n(i)\rangle$, shown in the inset, scales as expected.

clusters, isolated from the giant component. For instance, in a lattice with $q = 4$, a small isolated island of five points connected only to each other might arise. However, due to its staggering mechanism, the algorithm can only construct such an island if all sites in one cell are located in the intersection region of the initial connection layer cells (a quarter of a cell in the example of Figure 3.4). This makes the occurrence of non-fully connected lattices extremely unlikely for realistic cell sizes, as estimated in the following example:

In a two-dimensional CC lattice realization of linear size $L = 512$ and cell size $\ell = 8$ there are $N_c = 4096$ cells, containing 64 sites on average. The probability of finding a cell which contains exactly k sites is approximately given by $N_c\binom{n}{k}p^k(1-p)^{n-k}$, where $n = L^2$ and $p = 1/N_c$. In order to produce an isolated cluster, all k sites need to be located in the same quarter of the cell, hence we multiply by another factor of $(1/4)^{k-1}$. Summing both contributions from $k = 5$ (minimal number of points for isolated island for $q = 4$) to $k = L^2$ (total number of points in the lattice) yields a probability of the order of 10^{-20} with the only significant contributions being those from the first few terms in k. For larger q and higher dimensions this probability is even lower.

3.4 Correlations

According to the HBV criterion, the decay of local coordination number fluctuations under spatial coarse-graining transformations determines the stability of a continuous phase transition in the presence of quenched topological disorder. As detailed in Section 2.5.4, for increasing block size L_b, the fluctuations are expected to scale according to

$$\sigma_Q(L_b) \sim L_b^{-a}, \tag{3.10}$$

where a denotes the disorder decay exponent. We perform the blocking analysis (compare Figure 2.13) for the lattices introduced in this chapter and present the results in Figure 3.11. Using the ansatz of Equation (3.10), we find decay exponents consistent with $a = 1$, corresponding

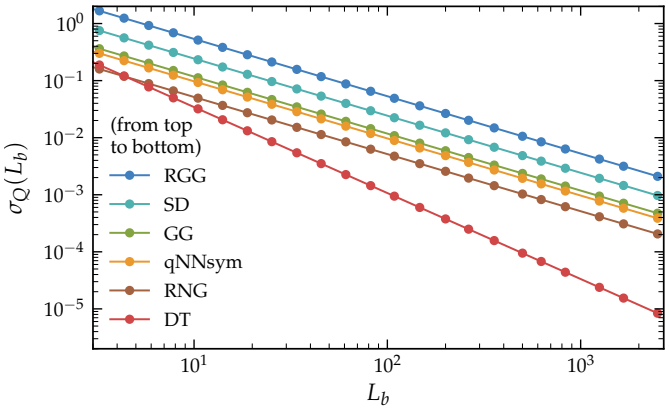

Figure 3.11 | Coordination number fluctuations on different length scales for several lattices. The curves are obtained using Equation (3.10). Measured decay exponent values: Gabriel graph (GG): $0.999(1)$, relative neighbourhood graph (RNG): $1.001(2)$, site-diluted regular square lattice (SD): $1.001(3)$, DT: $1.501(2)$, random geometric graph (RGG): $1.004(6)$ and symmetrized q-nearest neighbour graph (qNNsym) with $q \geq 6$: $1.001(2)$.

to that of conventional, uncorrelated disorder, for every lattice but the DT. For the latter, a value of $a = 3/2$ can be reproduced [67]. For the RNG and GG, however, the exponent of $a = 1$ is somewhat unexpected, especially in light of recent results from [260], which provided unambiguous evidence that the two-dimensional Ising model on those structures falls into the universality class of the regular model. Since, with respect to the HBV arguments, which predicts disorder to be irrelevant if $a\nu > 1$, both lattices behave qualitatively similar to diluted lattices (see Figure 3.11), one might expect that at least strong scaling corrections should appear for the Ising model in two dimensions, which was however not mentioned by the authors [260].

In order to shed further light on the situation, we perform the calculation of the coordination number correlation function from [67] and focus on anti-correlations in the coordination number. Specifically, we measure the *connected two-point correlation function of the coordination number*, defined as

$$C(\boldsymbol{x}) \equiv \frac{1}{N} \sum_{i,j} (q_i - \bar{q})(q_j - \bar{q}) \delta(\boldsymbol{x} - \boldsymbol{x}_{ij}). \tag{3.11}$$

Here, $\boldsymbol{x}_{ij}$ denotes the distance vector from site i to j. The results are shown in Figure 3.12a as a function of the spatial radius. As can be seen, we are able to reproduce the results for the DT from Reference [67], revealing pronounced anti-correlations for small radii, which should explain the comparably fast decay of the disorder fluctuations. The exactly opposite behaviour is given by the curve for the RGG, where correlations are entirely positive. This reflects the high clustering mentioned above, falling linearly up to the interaction radius $R_{\langle q \rangle}$, where it displays a pronounced drop before approaching zero for distances around $r = 2R_{\langle q \rangle}$. This is consistent with the fact that, for two sites with non-overlapping interaction regions, the coordination numbers are effectively uncorrelated. Turning to the GG, we find that, interestingly, the curve remains positive as well, i. e. it displays no anti-correlations at all and is thus consistent with the slow disorder decay observed above. It is remarkable that the pruning of bonds of a DT lattice in order to obtain the GG causes such a significant change with respect to the coordination

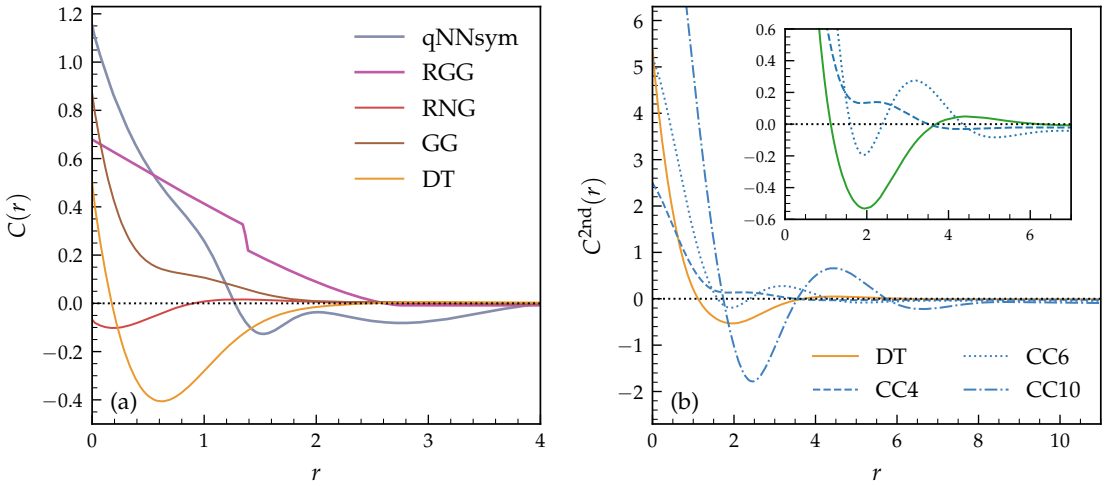

Figure 3.12 | Spatial coordination number correlation functions. (a) First-layer correlations, according to Equation (3.11), for the Delaunay triangulation, Gabriel graph, relative neighbourhood graph, random geometric graph and symmetrized q-nearest neighbour graph with $q \geq 6$, as a function of the radius. For the RGG, the radius was chosen such that the average coordination number is $\langle q \rangle = 6$ and $C(r)$ is rescaled by a factor of 0.1. (b) Second-layer coordination number correlation function (3.12) for the DT and the constant coordination models (CC4, CC6 and CC10). We show a magnification in the inset. The x-axis is in units of the lattice spacing in both figures.

number correlations. Equally surprising is the circumstance that the removal of further bonds from the GG, leading to the RNG, again considerably changes the picture and results in negative correlations for short ranges. That means that highly connected sites now tend to be linked to less connected sites and vice versa.

We remark that for the CC lattice a coarse-graining analysis of disorder fluctuations can not be performed, since the coordination number does not fluctuate per construction. Consequently, $C(\boldsymbol{x})$ is identically zero. In order to provide at least some insight into the correlation structure in those lattices, we compute the *connected two-point correlation function of the second-layer coordination number*, defined by

$$C^{\mathrm{2nd}}(\boldsymbol{x}) = \frac{1}{N} \sum_{i,j} (q_i^{\mathrm{2nd}} - \bar{q}^{\mathrm{2nd}})(q_j^{\mathrm{2nd}} - \bar{q}^{\mathrm{2nd}}) \delta(\boldsymbol{x} - \boldsymbol{x}_{ij}), \tag{3.12}$$

where q_i^{2nd} denotes the number of *next-nearest* neighbours, i. e., the number of sites that can be reached from point i by exactly two links and at the same time are not part of the set of nearest neighbours. This quantity should capture similar geometrical information as its first-layer equivalent $C(\boldsymbol{x})$. We present results for different CC lattices in Figure 3.12b, where they are compared to those of the DT. Evidently, the DT exhibits pronounced anti-correlations in the second-layer coordination number as well. The curve for CC10 is qualitatively similar, but shows significantly stronger oscillations. Comparing CC10 with CC6 and CC4, it can be noticed that the relative strength of anti-correlations decreases as q is decreased. For $q = 4$ the first minimum is hardly visible and positive values dominate (see inset of the figure).

Chapter 4

Numerical Methods

"The generation of random numbers is too important to be left to chance."

– Robert R. Coveyou

The necessary computational techniques for the simulation of equilibrium spin models are discussed in the first part of this chapter. After a brief exposition on the essential aspects of Monte Carlo sampling, the actual implementation of update algorithms is presented. We define the physical observables, develop the relevant finite-size scaling framework, discuss the analysis of statistical errors in detail and introduce the so-called histogram reweighting method, which allows a convenient extrapolation around the simulation point.

In a similar manner, numerical algorithms for non-equilibrium system are discussed in the second part of this chapter, including dynamical simulations starting from a single seed or a fully occupied lattice, as well as methods probing the quasi-stationary state. In this context we develop the static as well as the dynamic scaling properties in detail and discuss how those are affected in the presence of conventional disorder.

4.1 Equilibrium systems

In thermodynamic equilibrium, the expectation value of an observable O is given by

$$\langle O \rangle \equiv \sum_{\sigma \in S} \pi(\sigma) O(\sigma), \tag{4.1}$$

where the sum extends over the space $S = \{\sigma_1, \sigma_2, \ldots\}$ of all possible configurations of the system. In this definition, $\pi(\sigma)$ is the probability distribution of states and $O(\sigma)$ denotes the value of O in the specific configuration σ. Note that in the case of real-valued degrees of freedom (e. g. the Heisenberg model) the sum in Equation (4.1) must be replaced by an integral. In the present work, where we exclusively deal with canonical systems, π takes the form of a Boltzmann distribution, i. e.

$$\pi(\sigma) \equiv \frac{1}{Z} \exp\left(-\beta E(\sigma)\right), \tag{4.2}$$

where $\beta = 1/T$ is the inverse temperature and

$$Z \equiv \sum_{\sigma \in S} \exp\left(-\beta E(\sigma)\right) \tag{4.3}$$

defines the partition function.[22]

4.1.1 Monte Carlo sampling

Using the relations above, we are in principle able to obtain any desired quantity of the system at any temperature on a computer via direct summation. However, as the total number of states, $|S|$, grows exponentially with the system volume, the sum quickly becomes unfeasibly large. As a concrete example, even for the Ising model, where every site can only take on two values, a three-dimensional cubic system of $7 \times 7 \times 7 = 343$ spins would have $2^{343} \approx 10^{100}$ states, which is already significantly larger than the estimated number of elementary particles in the universe. As a consequence, a direct calculation is impossible and one has to rely on sampling methods in order to *approximate* the expectation value of an observable. If the sampling is performed in a stochastic fashion, one speaks of so-called *Monte Carlo* methods. A naive approach consists in picking a number of N_m states from S at random and calculate the observables from the corresponding average. Due to the random picking being ergodic, in the limit $N_m \to \infty$ this would yield the true expectation value Equation (4.1). For a realistic number of samples, however, a very poor result can be expected, since it is by no means guaranteed that the relevant region in the phase space is even hit even once by our random sampling. In fact, for the Boltzmann distribution, the overwhelming number of states have almost vanishing weights due to the exponential factor. As a consequence, the relevant region, accounting for the bulk of the sum of Equation (4.1), is extremely narrow.

To circumvent this issue one typically uses so-called *importance sampling* techniques [261] where states are not picked at random but precisely according to the distribution π. As a result, the *estimator* for the expectation value of an observable reduces to a simple sum

$$\langle O \rangle = \frac{1}{N_m} \sum_{j=1}^{N_m} O_j \tag{4.4}$$

in which N_m represents the number of measurements. Although the importance sampling

[22] The so-called Boltzmann constant k_B, oftentimes appearing in this relation, has no actual physical relevance and is therefore set to unity throughout this work.

estimator Equation (4.4) looks quite simple at the first glance, efficiently picking states according to a specific distribution is not a trivial task. Typically, one employs a so-called *Markov process*, which is a set of stochastic rules to obtain a sequence of suitable states, symbolically written as

$$\ldots \to \sigma \xrightarrow{P} \sigma' \xrightarrow{P'} \sigma'' \xrightarrow{P''} \sigma''' \ldots \tag{4.5}$$

where the P's denote the corresponding transition probabilities. The key property of such a Markov chain is the fact that a specific state in the sequence only depends on the preceding state but not on the whole history of the process. Obviously, the probabilities need to be normalized $\sum_{\sigma' \in S} P(\sigma \to \sigma') = 1$, which means that always *some* next state is generated by the Markov process. Note that it might very well occur that subsequent configurations are identical, $\sigma = \sigma'$.

In order to generate a suitable sequence of configurations obeying a specific probability distribution, the Markov process needs to fulfil two further conditions, namely *ergodicity* and *detailed balance*. Ergodicity describes the fact that starting from an arbitrary configuration every other configuration of the system must be accessible through some trajectory of states generated by the Markov chain rules. The condition of detailed balance on the other hand requires that

$$\pi(\sigma) P(\sigma \to \sigma') = \pi(\sigma') P(\sigma' \to \sigma) \qquad \forall\, \sigma, \sigma', \tag{4.6}$$

guaranteeing that there is no net flow of probability in the system. Mathematically rigorous proofs of the three necessary conditions (normalization, ergodicity, detailed balance) being fulfilled for specific update algorithms, which will be introduced in the following section, can be found in many standard textbooks, such as [151], together with a detailed exposition of how they result in a stationary sample distribution.

4.1.2 Update algorithms

Following up the last section, the main task remains in finding an appropriate set of rules for constructing a Markov chain of system configurations. In fact, there exists a large number of possibilities how an *update algorithm* resulting in a Boltzmann distribution can be implemented. The prototypical example, which can also be applied to a huge variety of other problems, is given by the *Metropolis* algorithm [262]. In fact, this algorithm sets the stage for a large spectrum of so-called *simulated annealing* methods, such as the one we used for constructing the constant coordination lattice in Section 3.3. In the case of a spin system, one site is picked at random and a flip of the corresponding spin is proposed. Let E_{old} and E_{new} denote the system energy before and after the update attempt, respectively, then the spin flip is accepted with probability

$$P(\sigma_{\text{old}} \to \sigma_{\text{new}}) = \begin{cases} 1 & E_{\text{new}} < E_{\text{old}}, \\ \mathrm{e}^{-\beta(E_{\text{new}} - E_{\text{old}})} & E_{\text{new}} \geq E_{\text{old}}, \end{cases} \tag{4.7}$$

and rejected otherwise. Hence, spin flips resulting in a less favourable configuration (higher energy) are only accepted with the probability of a Boltzmann factor depending on the energy difference $\Delta E = E_{\text{new}} - E_{\text{old}}$, thus emulating entropic contributions due to the finite temperature of the system, whereas "good" updates are always accepted. In a more compact form, the

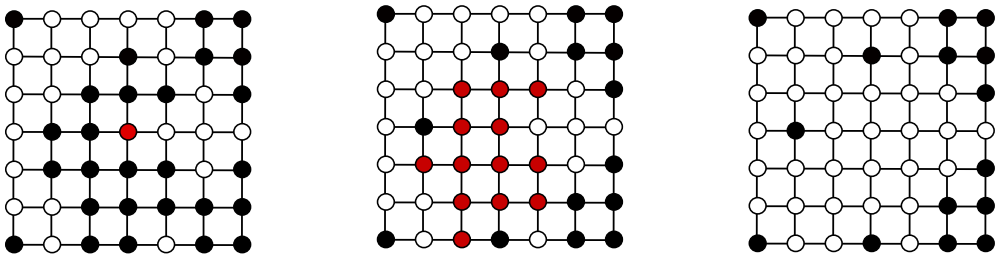

(a) (b) (c)

Figure 4.1 | Operating principle of the non-local Wolff algorithm. (a) Given the spin marked in red as the seed, the algorithm builds a cluster of equally oriented spins (b) which are eventually flipped (c).

Metropolis dynamics can be written as

$$P(\sigma_{\text{old}} \to \sigma_{\text{new}}) = \min\left(1, \mathrm{e}^{-\beta\Delta E}\right), \tag{4.8}$$

which directly follows from the general expression of the Metropolis acceptance probability

$$P(\sigma_{\text{old}} \to \sigma_{\text{new}}) = \min\left(1, \frac{\pi(\sigma_{\text{new}})}{\pi(\sigma_{\text{old}})}\right), \tag{4.9}$$

if we chose the Boltzmann distribution, defined by Equation (4.2), for π. It is obvious from the definition that the Metropolis algorithm only acts locally, since only one spin is considered at a time. There are other, similar, local update schemes, such as Heatbath or Glauber dynamics[23], which essentially only differ in the concrete realization of the transition rates. In the present work however, we use the Metropolis algorithm, due to its robustness and slightly superior performance compared to other local schemes (compare, e. g. [151, 263] for details).

Despite their wide-ranging applicability, local update algorithms are only of limited use if one studies a system close to a phase transition, as they suffer from what is called *critical slowing down*. As mentioned earlier, criticality is characterized by collective behaviour of the individual degrees of freedom over large distances. Therefore, as the critical point is approached, local, uncorrelated updates become increasingly ineffective in propagating information through the lattice. Considering, e. g. slowly changing observables, such as the magnetization, the corresponding histogram becomes very broad at criticality [264], whereas flipping spins in a local and uncorrelated manner results only in a small change of the magnetization. As a consequence, the number of update steps required in order to sample the distribution properly increases dramatically.

In order to overcome the critical slowing down, *cluster updates* have been developed, most notably the algorithms by R. Swendsen and J. Wang [52] and U. Wolff [56]. The key idea of these schemes is to grow a spatially extended cluster of connected spins and flip the entire cluster at once. As a result, even one single cluster update is able to change the system configuration substantially, which is illustrated in Figure 4.1, while still satisfying ergodicity and detailed balance [264]. Roughly speaking, the speed in which the sampling of states moves through the relevant phase space regions is dramatically increased compared to local schemes. The central

[23] For the spin-1/2 Ising model, Heatbath and Glauber dynamics are identical [263].

quantity in the Wolff algorithm is the probability of adding a site to the cluster, which is given by

$$p_{\text{add}} = 1 - \exp\left(-2\beta J_{ij}\delta_{\sigma_i\sigma_j}\right), \tag{4.10}$$

where the site with index i already belongs to the cluster and j is tested. Note that $p_{\text{add}} = 0$ if both sites do not share the same spin configuration, $\sigma_i \neq \sigma_j$. Moreover, in our case $J_{ij} = 1$ holds. One Wolff cluster update step is defined as follows:

1. Choose a random site as the cluster seed
2. Add all nearest neighbours *individually* to the cluster with probability p_{add}
3. For each site that was added, continue with its respective neighbours, i. e. repeat step 2. In this way, sites may be tested multiple times
4. The cluster is completed as soon as no further sites can be added
5. Flip the cluster

An essential aspect of what makes the Wolff algorithm so powerful, is the fact that for the specific choice of p_{add}, the update is *always* accepted. The Swendsen-Wang algorithm in contrast, decomposes the entire lattice into percolation-like clusters, but only flips some of them eventually. As a result the Wolff algorithm in general performs better, especially in higher dimensions, as shown in Table 4.1. For the sake of completeness, note that there exist a couple of further collective update schemes for Ising-like models, e. g. the invaded cluster [265–267] and worm algorithm [268], as well as conceptually different approaches to reduce the critical down, such as multigrid methods [269].

In order to allow for a quantitative comparison between the update algorithms relevant in this work, we introduce the *dynamic exponent* z defined by the relation

$$\tau \sim \xi^z \tag{4.11}$$

where the autocorrelation time τ will be addressed in detail in Section 4.1.4 and ξ denotes the correlation length of the system. A large autocorrelation time results in a large number of update steps being necessary in order to generate an effectively uncorrelated new system configuration. Moreover, as ξ tends to diverge at the critical point, but is limit by L in a finite system, the computational cost of a simulation scales as

$$\text{cost} \sim VL^z = L^{d+z}, \tag{4.12}$$

where V denotes the number of spins in the lattice. For local updates $z \approx 2$ holds, which can be motivated by a random walk in energy space where signals propagate through neighbour interactions. Cluster updates on the other hand typically have dynamic exponents $z \ll 1$, as shown in Table 4.1 and therefore dramatically outperform any local schemes in the vicinity of the critical point. In the high temperature regime $\beta \ll \beta_c$, however, the Wolff algorithm essentially reduces to a Metropolis scheme, since the clusters rarely become larger than the seed spin itself. The Metropolis dynamics even performs slightly better in this case as testing the neighbouring spins is omitted. Similar holds for the low temperature regime, where the Wolff algorithm renders effectively useless, as it flips almost the entire lattice in every update [151].

Table 4.1 | Monte Carlo update algorithms. Dynamic exponents z for several equilibrium update algorithms in $d = 2, 3$ and 4 dimensions [151].

d	Metropolis	Wolff	Swendsen-Wang
2	2.167(1)	0.25(1)	0.25(1)
3	2.02(2)	0.33(1)	0.54(2)
4	2.167(1)	0.25(1)	0.86(2)

Since in the present work, we exclusively study systems directly at, or in the vicinity of the critical point, we employ the Wolff cluster algorithm as our primary update routine. Specifically, in our simulations we perform so-called elementary Monte Carlo steps (EMCS), consisting of a number of Wolff cluster updates and a full Metropolis lattice sweep. Since the average cluster size $\langle |C| \rangle$ in a d-dimensional system at criticality scales as $L^{d-\gamma/\nu}$, where γ and ν denote critical exponents of the model, we increase the number of cluster updates with lattice size accordingly in order to keep the fraction of flipped spins approximately independent of the lattice size [58]. Moreover, even though the additional Metropolis sweeps are not necessary as the cluster updates are ergodic, they enhance the thermalization of short-wavelength modes. Also, for disordered lattices, cluster schemes might only rarely visit small, isolated components of the lattice. Additional local updates therefore ensure a proper treatment of these regions. Finally, let us emphasize that all algorithms introduced in this section are straightforwardly applicable to disordered lattices.

So far we have implicitly assumed to work with one-dimensional (Ising) spins. However, turning to the $O(N)$ model, one faces N-dimensional spin vectors and hence a continuous phase space. The Metropolis algorithm generalizes naturally to this case, as instead of a spin *flip* one simply proposes a random new direction. The Wolff cluster algorithm, however, can only be applied to systems with one-dimensional spins, as it stands. It is clear that a flip can not be generalized to a reflection for higher-dimensional spins (i. e. simply inverting the signs of all components) as this would obviously break the ergodicity of the system. Moreover, the probability (4.10) vanishes anywhere in the lattice, as no two spins are aligned perfectly in parallel. The solution is to map the higher-dimensional spins onto a one-dimensional Ising-like system. This is done by projecting all spins onto a randomly chosen direction via standard scalar products, resulting in one-dimensional spins with – due to the projection – varying lengths. The latter can be absorbed into the coupling constants in Equation (4.10). The cluster is then built according to the above algorithm. As a last step, for all spins inside the cluster, the sign of the component of the field parallel to the chosen random direction is inverted. We remark that for each cluster update, a new random direction should be chosen, in order to preserve ergodicity [56]. Other than drawing the directions at random one might also – for reasons of performance – use the Cartesian directions in a fixed sequence and occasionally globally rotate the field by a random amount [126].

Finally, turning from the $O(N)$ model to a general lattice field theory, where individual fields are not bound to unit-length, i. e. in general $|\phi_i| \neq 1$, the Wolff algorithm again does not meet ergodicity requirements, as the length is conserved by construction. Therefore, it is necessary to

perform additional Metropolis sweeps, which explicitly propose a length change of the field variables, as detailed for instance in Reference [126].

4.1.3 Observables and scaling

Unless stated otherwise, we prepare the system in a hot initial state, meaning that spin orientations are randomly chosen. The system is then thermalized using a number of EMCS, until it reaches thermodynamic equilibrium. A common check for proper thermalization is to perform simulations starting from a cold configuration as well, which must give identical results within numerical precision. After successful equilibration, we perform further EMCS and measure the magnetization and energy per spin, defined by

$$m = \frac{1}{V}\sum_i s_i, \qquad e = -\frac{1}{V}\sum_{\langle ij\rangle} s_i s_j \tag{4.13}$$

where the sums run over the lattice sites, V denotes their total number and $s_i \in \{-1, 1\}$ for the spin-1/2 Ising model. For scalar lattice field theory Hamiltonians, the corresponding definitions are used, such as, for instance, for the improved $O(N)$-symmetric ϕ^4 model

$$m = \frac{1}{V}\sum_i \phi_i, \qquad e = -\frac{1}{V}\left(\sum_{\langle ij\rangle}\phi_i\phi_j + \frac{1}{\beta}\sum_i \phi_i^2 + \frac{\lambda}{\beta}\sum_i\left(\phi_i^2 - 1\right)^2\right), \tag{4.14}$$

where ϕ_i denotes an N-component real variable. The lattice structure enters as neighbouring relations between sites which is denoted by $\langle ij\rangle$, as introduced in Section 2.2.1. Both quantities are measured after every EMCS, resulting in respective time series. From this time series the final (macroscopic) observables can be computed by performing thermal averages, denoted by angular brackets $\langle ...\rangle$.

In the investigation of disordered systems, it is necessary to average physical observables over many different, independent disorder realizations, also called *replicas* of the system. As detailed in Section 2.5, quenched averages over N_r replicas are performed at the level of (extensive) observables, rather than at the level of the partition function. Denoting quenched averages as

$$[O]_{\text{avg}} \equiv \frac{1}{N_r}\sum_{i=1}^{N_r} O_i, \tag{4.15}$$

we obtain the following definitions of magnetization, energy, susceptibility and specific heat of an ensemble of disorder replicas

$$M = [\langle|m|\rangle]_{\text{avg}}, \tag{4.16a}$$
$$E = [\langle e\rangle]_{\text{avg}}, \tag{4.16b}$$
$$\chi = V\beta[\langle m^2\rangle - \langle|m|\rangle^2]_{\text{avg}}, \tag{4.16c}$$
$$C = V\beta^2[\langle e^2\rangle - \langle e\rangle^2]_{\text{avg}}, \tag{4.16d}$$

as well as the following derivatives

$$\frac{\mathrm{d}[\langle m\rangle]_{\mathrm{avg}}}{\mathrm{d}\beta} = [\langle |m|e\rangle - \langle |m|\rangle\langle e\rangle]_{\mathrm{avg}}, \tag{4.17a}$$

$$\frac{\mathrm{d}\ln[\langle |m|\rangle]_{\mathrm{avg}}}{\mathrm{d}\beta} = \left[\frac{\langle |m|e\rangle}{\langle |m|\rangle} - \langle e\rangle\right]_{\mathrm{avg}}, \tag{4.17b}$$

$$\frac{\mathrm{d}\ln[\langle m^2\rangle]_{\mathrm{avg}}}{\mathrm{d}\beta} = \left[\frac{\langle m^2 e\rangle}{\langle m^2\rangle} - \langle e\rangle\right]_{\mathrm{avg}}, \tag{4.17c}$$

$$\frac{1}{V}\frac{\mathrm{d}[U_2]_{\mathrm{avg}}}{\mathrm{d}\beta} = \left[(1-U_2)\left(\langle e\rangle - 2\frac{\langle |m|e\rangle}{\langle |m|\rangle} + \frac{\langle m^2 e\rangle}{\langle m^2\rangle}\right)\right]_{\mathrm{avg}}, \tag{4.17d}$$

$$\frac{1}{V}\frac{\mathrm{d}[U_4]_{\mathrm{avg}}}{\mathrm{d}\beta} = \left[(1-U_4)\left(\langle e\rangle - 2\frac{\langle m^2 e\rangle}{\langle m^2\rangle} + \frac{\langle m^4 e\rangle}{\langle m^4\rangle}\right)\right]_{\mathrm{avg}}, \tag{4.17e}$$

which all exhibit singularities close to the phase transition in the thermodynamic limit. In order to keep the notation simple, averages will be omitted in the remainder of this work, hence for instance Equation (4.17c) will be denoted simply as $\mathrm{d}\ln m^2/\mathrm{d}\beta$ leaving both the thermal and replica averages implicit. In Equations (4.17d) and (4.17e), U_2 and U_4 denote the second- and fourth-order magnetic cumulants, also called Binder ratios [270], given by

$$U_2 = \left[1 - \frac{\langle m^2\rangle}{3\langle |m|\rangle^2}\right]_{\mathrm{avg}}, \tag{4.18}$$

$$U_4 = \left[1 - \frac{\langle m^4\rangle}{3\langle m^2\rangle^2}\right]_{\mathrm{avg}}. \tag{4.19}$$

Occasionally, also the sixth-order Binder ratio is used and therefore is defined by

$$U_6 = \left[\frac{\langle m^6\rangle}{\langle m^2\rangle^3}\right]_{\mathrm{avg}}. \tag{4.20}$$

Finally, in a finite lattice, a suitable definition of the second-moment correlation length [271, 272] is given by

$$\xi = \frac{1}{2\sin(k_{\min}/2)}\sqrt{\frac{[\langle |\mathcal{F}^2(\mathbf{0})|\rangle]_{\mathrm{avg}}}{[\langle |\mathcal{F}^2(\boldsymbol{k}_{\min})|\rangle]_{\mathrm{avg}}} - 1}, \tag{4.21}$$

with the Fourier transform of the magnetization being defined as

$$\mathcal{F}(\boldsymbol{k}) = \sum_j s_j \exp(i\boldsymbol{k}\boldsymbol{x}_j), \tag{4.22}$$

where $\boldsymbol{x}_j$ denotes the spatial coordinate of site j and $\boldsymbol{k}_{\min}$ corresponds to the smallest non-zero wave vector in the finite lattice. In our simulations, we measure the Fourier transform for every

direction and average the results, which, e. g. in three dimensions results in

$$\mathcal{F}^2(\boldsymbol{k}_{\min}) = \frac{1}{3}\left|\,|\mathcal{F}(2\pi/L_x,0,0)|^2 + |\mathcal{F}(0,2\pi/L_y,0)|^2 + |\mathcal{F}(0,0,2\pi/L_z)|^2\right|, \tag{4.23}$$

where in our case typically $L_x = L_y = L_z = L$. Along with m and e, the Fourier mode $\mathcal{F}^2(\boldsymbol{k}_{\min})$ is also recorded during the Monte Carlo run.

In a finite system of linear size L, it is known from Section 2.4 that near the critical point, the above quantities scale according to the following relations

$$[\langle m\rangle]_{\text{avg}} = L^{-\beta/\nu} f_m(x)(1+\ldots), \tag{4.24a}$$
$$\chi = L^{\gamma/\nu} f_\chi(x)(1+\ldots), \tag{4.24b}$$
$$C = C_0 + L^{\alpha/\nu} f_C(x)(1+\ldots), \tag{4.24c}$$
$$\frac{\mathrm{d}[\langle m\rangle]_{\text{avg}}}{\mathrm{d}\beta} = L^{(1-\beta)/\nu} f_{m'}(x)(1+\ldots), \tag{4.24d}$$
$$\frac{\mathrm{d}\ln[\langle |m|\rangle]_{\text{avg}}}{\mathrm{d}\beta} = L^{1/\nu} f_{m,1}(x)(1+\ldots), \tag{4.24e}$$
$$\frac{\mathrm{d}\ln[\langle m^2\rangle]_{\text{avg}}}{\mathrm{d}\beta} = L^{1/\nu} f_{m,2}(x)(1+\ldots), \tag{4.24f}$$
$$\frac{\mathrm{d}[U_2]_{\text{avg}}}{\mathrm{d}\beta} = L^{1/\nu} f_{U_2}(x)(1+\ldots), \tag{4.24g}$$
$$\frac{\mathrm{d}[U_4]_{\text{avg}}}{\mathrm{d}\beta} = L^{1/\nu} f_{U_4}(x)(1+\ldots), \tag{4.24h}$$

which allows to extract the critical exponents α, β, γ and ν. C_0 is the regular part of the specific heat that does not diverge at the critical point and the functions f_O are universal scaling functions with the argument x given by

$$x = (\beta - \beta_c)L^{1/\nu}, \tag{4.25}$$

where β_c denotes the infinite-volume critical point. The correlation length in units of the lattice size and the Binder ratios share the property of being scale invariant at criticality. This property is particularly useful as their curves intersect close to the critical point for different system sizes. Concretely, in the critical regime they scale according to

$$U_{2n} = f_{U_{2n}}(x)\,(1+\ldots), \tag{4.26a}$$
$$\xi/L = f_\xi(x)\,(1+\ldots). \tag{4.26b}$$

Equations (4.24) and (4.26) describe the finite-size scaling (FSS) behaviour of the considered observables to leading order. Corrections of higher order are expected to become irrelevant for large system sizes, but can have strong effects for small L, as discussed in detail in Section 2.4.

Maximum scaling

The scaling functions listed above lead the way of how critical exponents can be determined if the system is simulated for different L. However, this requires one to eliminate the dependence

on the scaling function first. Even though these functions are universal, their explicit form is usually not known. In Section 2.4 we found that observables which diverge in the infinite-volume limit exhibit pronounced maxima for finite systems at the transition. The location of these peaks tends towards the true critical point in the limit $L \to \infty$, resulting in a series of pseudo-critical points, denoted by β_c^L. Specifically, they scale according to

$$\beta_c^L = \beta_c + aL^{-1/\nu} + \dots . \tag{4.27}$$

As a consequence, when evaluated at the peaks, the scaling function reduces to a constant, as the scaling variable, defined by Equation (4.25), becomes $x = (\beta_c^L - \beta_c)L^{1/\nu} = a + \dots$. Hence, we are able to compute the exponents by taking logarithms of relations (4.24), which for instance, for the susceptibility results in $\ln \chi = \text{const} + (\gamma/\nu) \ln L$. The exponent can then be extracted by means of linear fit to $\ln L$ [263]. Let us remark that the simplicity of this so-called *maximum scaling method* originates from the fact that the peaks of the scaling functions are, so to speak, self-defined and can easily be found numerically, especially if so-called reweighting techniques are employed, which will be introduced below. One of the drawbacks of this method however is that including corrections to scaling, which are typically of the form $(1 + bL^{-\omega})$ necessarily leads to non-linear fits, which are hard to control. If the correction terms of the considered model are generically strong or one is restricted to small L, one might instead resort to other finite-size scaling methods, such as the scaling at fixed temperature, fixed phenomenological couplings (compare e. g. [273]) or the quotients method (detailed below), which all allow for a better control of scaling corrections.

Scaling collapse

This method is related to the scaling of the peak locations introduced before, as it also directly exploits the universal character of the scaling functions. The goal is to measure the observable at hand in a certain *range* of temperature in the critical region and rescale the corresponding relations (4.24) accordingly in order to extract the scaling function. Using once again the susceptibility as an example, one plots $L^{-\gamma/\nu}\chi(\beta, L)$ against the scaling variable $x = (\beta - \beta_c)L^{1/\nu}$, resulting in a collapse of curves for different L.

Even though *scaling collapses* provide a powerful and versatile tool to reveal the universal character of a transition, they present a number of immediate drawbacks. In cases where the critical exponents are known (or can be guessed), only the critical temperature needs to be tuned in order to produce a scaling collapse. However, using the method to determine exponents which are *a priori* unknown, requires three parameters to be controlled (γ, ν and β_c in the case of the susceptibility). Collapsing the curves by hand can, in this case, become very cumbersome and one might rather automatize the process using a non-linear Levenberg-Marquardt optimization procedure [274, 275]. Moreover, we remark that even though a scaling collapse over an extended region of $\tau L^{1/\nu}$ certainly represents an impressive manifestation of the universal character of a transition, it comes at the cost of requiring to simulate the system at *several* temperatures for each system size. This naturally limits the applicability of data collapses to moderate system sizes.[24]

[24] Strictly speaking, this is only the case for equilibrium or steady state properties. As we shall see, for non-equilibrium systems scaling collapses can also be performed for dynamic (i. e. time-dependent) observables. In this case, as the time evolution is naturally recorded during the simulation, scaling collapses in fact can be the method of choice for

Quotients method

A finite-size scaling method, which avoids the problems related to analytic corrections to scaling in an elegant manner, is the so-called *quotients method*. It was introduced by H. G. Ballesteros and co-workers [276, 277] motivated by earlier works [278]. The central quantities in this method are quotients of observables O, defined by

$$Q_O(\tau, L, s) \equiv \frac{\langle O \rangle(\tau, sL)}{\langle O \rangle(\tau, L)}, \tag{4.28}$$

where s represents a fixed scaling factor (typically $s = 2$). This means we consider the observable on two lattices of size L and sL. From Section 2.4, it is known that the finite-size behaviour of O is in general given by

$$\langle O \rangle(\tau, L) = L^{x_O/\nu} \left(f_O(\tau L^{1/\nu}) + L^{-\omega} g_O(\tau L^{1/\nu}) + \dots \right), \tag{4.29}$$

where f_O and g_O denote universal scaling functions, x_O is the exponent associated to the singularity of O in the infinite-volume limit and ω represents the leading correction-to-scaling exponent. Using the fact that at criticality the relation $\xi \sim \tau^{-\nu}$ holds, we can eliminate the explicit temperature dependence, writing

$$\langle O \rangle(\tau, L) = L^{x_O/\nu} \left(\tilde{f}_O(\xi/L) + L^{-\omega} \tilde{g}_O(\xi/L) + \dots \right) \tag{4.30}$$

where $\xi = \xi(\tau, L)$ represents a suitable definition of the finite-size correlation length, such as given by Equation (4.21). The quotient then becomes

$$Q_O(\tau, L, s) = s^{x_O/\nu} \frac{\tilde{f}_O(\xi(\tau, sL)/sL)}{\tilde{f}_O(\xi(\tau, L)/L)} + \mathcal{O}(L^{-\omega}). \tag{4.31}$$

If we now evaluate this equation at the temperature $\tau_c^{L,s}$ where both curves intersect, given by

$$\frac{\xi(\tau_c^{L,s}, L)}{L} = \frac{\xi(\tau_c^{L,s}, sL)}{sL}, \tag{4.32}$$

the scaling functions cancel and we find

$$Q_O|_{Q_{\xi=s}} \equiv Q_O(\tau_c^{L,s}, L, s) = s^{x_O/\nu} + aL^{-\omega} + \dots, \tag{4.33}$$

where a denotes a constant. For $L \to \infty$, the crossing points defined by Equation (4.32) approach the critical point, i. e. the critical temperature as well as the fixed point of the correlation length, denoted by $(\xi/L)^*$. Thus, the quotients method essentially can be seen as a realization of a phenomenological renormalization procedure [279]. In fact, the method is not restricted to the crossing points of the correlation length in units of the lattice size, but can rather be applied to any RG invariant quantity, such as the Binder ratios U_4, U_6, etc. In the following, we use the symbol R whenever the exact choice of these so-called *phenomenological couplings* is irrelevant.[25]

studying these system, especially for large L.

[25] Broadly, phenomenological couplings are observables which are monotonous in the critical region and become independent of the system size in the thermodynamic limit.

Equation (4.33) in principle allows us to obtain the exponent x_O/ν by means of a non-linear fit. However, we can estimate ω from the scaling behaviour of the phenomenological couplings, given by

$$R_1|_{Q_{R_2=s}} = R_1^* + A_{R_1} L^{-\omega} + \dots , \tag{4.34}$$

where A denotes a constant and $R_1, R_2 \in \{\xi/L, U_4, U_6, \dots\}$. Once ω is known, one can use a *linear* fit in order to obtain x_O/ν from Equation (4.33).

It becomes clear that one particular strength of the crossing method lies in the fact that no precise estimate of the infinite-volume critical temperature β_c is required. Since the crossing points $\beta_c^{L,s}$ effectively acts as series of pseudo-critical points (similar the peak locations in the maximum scaling method described earlier), we can – once the exponents ν and ω are known – perform linear fits according to the relation

$$\beta_c^{L,s} = \beta_c + \frac{1 - s^{-\omega}}{s^{1/\nu} - 1} L^{-\omega - 1/\nu} \tag{4.35}$$

in order to extract β_c [280].

4.1.4 Statistical analysis

As described in the last section, the calculation of observables from the importance sampling Monte Carlo "time" series of magnetization, energy and Fourier transform is straightforward. However, things become more involved when it comes to computing uncertainties of observables, as one unavoidably suffers from *auto-correlations* and *statistical bias* intrinsic to the data [281]. These important concepts will be introduced in the following.

Autocorrelations

In importance sampling Monte Carlo simulations, a naive estimator for the uncertainty of an observable (4.4) is the standard error of the mean, which can be written as [282]

$$\Delta O = \frac{\mathrm{std}(O)}{\sqrt{N_m}} = \sqrt{\frac{\langle O^2 \rangle - \langle O \rangle^2}{N_m (N_m - 1)}}. \tag{4.36}$$

The estimate (4.36) only holds for statistically independent numbers O_i, which is not a valid assumption for Markov chain Monte Carlo simulations. In fact, subsequent measurements tend to be highly correlated, especially in the critical regime, since only portions of the full system configuration are updated per EMCS. We can measure these correlations for an observable O using the autocorrelation function [283], defined as

$$C_O(t) \equiv \langle O(t_0) O(t_0 + t) \rangle - \langle O(t_0) \rangle \langle O(t_0 + t) \rangle \tag{4.37}$$

which, for large temporal separations, decays exponentially

$$\lim_{t \to \infty} C_O(t) \sim \exp(-t/\tau_{O,\mathrm{exp}}). \tag{4.38}$$

This defines the exponential autocorrelation time $\tau_{O,\text{exp}}$. However, for practical purposes one rather uses the *integrated* autocorrelation time[26], defined by

$$\tau_{O,\text{int}} \equiv \frac{1}{2} + \sum_{t=1}^{\infty} \frac{C_O(t)}{C_O(t_0)} \tag{4.39}$$

where for actual (i. e. finite) simulations, the sum should be cut off self-consistently [285] as the double summation will become expensive otherwise. Taking auto-correlations into account, Equation (4.36) can then be generalized (we omit the detailed derivation here and refer the reader to Reference [286]) and one obtains

$$(\Delta O)_{\text{corr}} = \Delta O \sqrt{2\tau_{O,\text{int}}}, \tag{4.40}$$

i. e. due to correlations in the data set the variance is enhanced by a factor of $2\tau_{O,\text{int}}$ compared to the naive estimate.

Resampling

As pointed out above, in order not to underestimate the uncertainty of an observable in Equation (4.40), monitoring the corresponding integrated auto-correlation time is crucial. However, in practice we face a couple of problems. First and foremost, calculating $\tau_{O,\text{int}}$ can become cumbersome already for the basic observables due to the double summation and noisy behaviour of $C_O(t)$ for large t [287]. Second, for combinations of observables, $f(\langle O_1\rangle, \langle O_2\rangle, \ldots)$, a proper autocorrelation analysis can not straightforwardly be defined. Moreover, it is important to note, that we cannot use standard error propagation in this case, as the different observables are measured from the same simulation and are hence trivially correlated. Ignoring those *cross correlations* (which would result in covariance terms in the error propagation analysis) could again seriously spoil the results. Finally, there are situations, where the estimator is even non-parametric, such as the location of a maximum, the intersection of two curves or fitting procedures which obtain critical exponents (compare Section 4.1.3). This rules out traditional error propagation in the first place.

The answer to all these problems lies in what is called *resampling techniques* [288], in particular *Jackknife* and *Bootstrap* [289, 290], which are nowadays considered state-of-the art techniques for statistical analysis. One particular strength is the fact that they do not rely on a parametric formulation of an underlying theoretical model and can hence be applied to a broad class of problems. The key concept is to divide the existing time series into blocks whose lengths are larger than the typical auto-correlation time of the data. These (effectively uncorrelated) blocks are then used to construct a set of new (resampled) time series and all necessary information (bias, cross-correlations, etc.) is computed from this set. It is important to note, that resampling methods do not only yield reliable estimates for the uncertainties of observables. They also allow to construct improved estimators for the actual averages, which reduce the statistical bias (it will be introduced below and is explained in greater detail in Appendix A.2) compared to a naive estimator [291], as can be seen in Figure 4.2. Both, Bootstrap and Jackknife resampling techniques are used frequently in the data analysis in this work. The technical details are therefore explained in Appendix A.3.

[26] For a purely exponential decay $\tau_{O,\text{int}} \approx \tau_{O,\text{exp}}$ holds true, whereas in general $\tau_{O,\text{int}} < \tau_{O,\text{exp}}$ [284, 285].

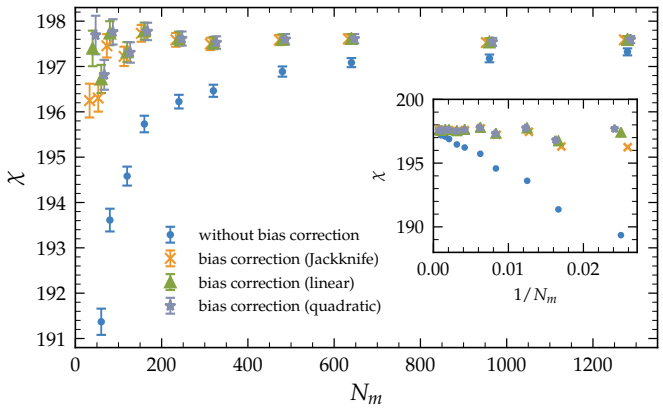

Figure 4.2 | Bias correction. Magnetic susceptibility χ of the Ising model on a three-dimensional disordered CC4 lattice with $L = 40$ near criticality as a function of the number of measurements N_m. All data points represent averages over $N_r = 10\,000$ disorder replicas and the uncertainties are computed from fluctuations among them. In the inset, χ is plotted against the inverse number of measurements, proving the expected bias to be proportional to $1/N_m$.

Statistical bias

Relying on a finite number of measurements for the calculation of observables does not only result in possibly large uncertainties, but also gives rise to a what is called *bias of an estimator* [282]. This term describes the situation when the MC estimator does not converge towards the unknown true value of an observable and comes into play as soon as we consider a function of expectation values, i. e. $f(\langle O\rangle_\infty)$. Since the function can not be defined in terms of individual measurements, a MC estimator has to be of the form

$$f^{\text{est}} = f\Big(\langle O\rangle_{N_m}\Big) = f\left(\frac{1}{N_m}\sum_{i=1}^{N_m} O_i\right). \tag{4.41}$$

For simplicity, we restrict our attention to only one observable, whereas in general, f might be a non-linear combination of several observables $\langle O_1\rangle$, $\langle O_2\rangle$, ..., compare Equation (4.17). A detailed analysis of this estimator is performed in Appendix A.2 and reveals that it actually converges to

$$f^{\text{est}} \to f\Big(\langle O\rangle_\infty\Big)\left(1 - \frac{2\tau_{O,\text{int}}}{N_m} + \mathcal{O}(N_m^{-2})\right), \tag{4.42}$$

where the latter terms in the bracket represent the *bias*. Therefore, only in the limit $N_m \to \infty$ we obtain the "true" result, whereas for a small number of measurements it might be severely underestimated.[27] It needs to be emphasized that the bias is not a consequence of auto-correlations in the data. It arises from non-linear functional dependencies between observables and can be found in completely uncorrelated measurements as well [282]. For the latter case $\tau_{O,\text{int}} = 1/2$ holds true, as can be seen from the definition in Equation (4.39), and therefore the leading bias term can be corrected by multiplying a factor $N_m/(N_m - 1)$, which is occasionally termed

[27] To be specific, the correction is negative for convex functions, such as $f(x) = x^2$, used in the definition of, e. g., the susceptibility, but positive for concave functions, according to Jensen's inequality.

Bessel's correction.[28]

As a concrete example, we measure the magnetic susceptibility of the Ising model, as defined in Equation (4.16c) on three-dimensional CC4 lattices with $L = 40$ near criticality, and show the results in Figure 4.2. The simulation is repeated for different numbers of measurements. As can be seen, especially for small N_m the biased estimator deviates quite strongly from the results for bias corrected estimators. Moreover, the inset shows the dependence on $1/N_m$ nicely. In a disordered setting, where a replica average has to be performed, one might be tempted to think that the fluctuations among the replicas exceed the individual bias and might therefore omit a correct analysis of the latter. However, as the replicas can be assumed to be statistically independent, the standard error of their fluctuations decays as $1/\sqrt{N_r}$ and therefore slower than the bias, which decays as $1/N_m$. Since, for strongly disordered systems, it is not uncommon to use as little as $N_m = 100$ measurements per replica [292–294], both terms can become comparable. This is illustrated in Figure 4.2, where 10 000 disorder replicas have been used. Even for typical values used in this work ($N_m \approx 1000$) deviations are clearly visible, which makes a proper treatment of bias crucial in order to avoid systematic errors in the entire analysis.

From the above reasoning, it becomes obvious that one should use *unbiased estimators* whenever available, even though for correlated data their proper definition in general presents a non-trivial task. Of course, one possibility is to perform a very large number of Monte Carlo update steps between two measurements, such that two subsequent configurations are effectively uncorrelated, i. e. $2\tau_{O,\text{int}} = 1$, and then multiply a proper Bessel correction term. In practice, this would require to increase the number of EMCS per update by at least one order of magnitude, which makes this approach simply too expensive from the computational point of view. Fortunately, there exist several approaches for constructing unbiased estimators for correlated data. As mentioned above, and shown in Figure 4.2, binning techniques, such as Jackknife or Bootstrap represent convenient approaches to reduce the bias of an estimator. In this work, however, we use a different method (which nevertheless lies also in the spirit of binning methods), originally introduced in [295] and generalized by [273]. This method proves equally powerful than Jackknife or Bootstrap and is computationally less expensive, as large number of re-binning calculations can be avoided. Specifically, in order to construct an unbiased estimator, the time series is split into two contiguous halves and the observable is computed by combining them according to

$$f_{\text{linear}}^{\text{est,unb}} = f^{\text{est}}\left(\langle O\rangle_{N_m}\right) - \frac{1}{2}\left[f^{\text{est}}\left(\langle O\rangle_{\frac{N_m}{2},1}\right) + f^{\text{est}}\left(\langle O\rangle_{\frac{N_m}{2},2}\right)\right]. \tag{4.43}$$

By applying Equation (4.42), it can be seen that the leading bias term vanishes. Effectively, the observable is computed for two different (finite) values of N_m and linearly (hence the subscript) extrapolated for $N_m \to \infty$. One can also perform a quadratic extrapolation, where, additionally,

[28] This factor is widely used to construct unbiased estimates of variances, i. e. $f = \langle O^2\rangle - \langle O\rangle^2$. Although commonly attributed to F. W. Bessel, it was used even earlier by C. F. Gauß (Theoria combinationis observationum erroribus minimis obnoxiae, Göttingen 1823).

the time series is split into four quarters

$$f^{\text{est,unb}}_{\text{quadratic}} = \frac{8}{3} f^{\text{est}}\Big(\langle O\rangle_{N_m}\Big) - \sum_{i=1}^{2} f^{\text{est}}\Big(\langle O\rangle_{\frac{N_m}{2},i}\Big) + \frac{1}{12}\left[\sum_{i=1}^{4} f^{\text{est}}\Big(\langle O\rangle_{\frac{N_m}{4},i}\Big)\right] \tag{4.44}$$

and which again cancels the leading bias term. Both estimators are plotted in Figure 4.2. As can be seen, the results are almost identical, proving the robustness of this approach. Finally, it should be noted that another particular advantage of the estimators (4.43) and (4.44) over the Jackknife method is that they can be used even for a very small number of measurements.

4.1.5 Reweighting

The fact that a "raw" Monte Carlo time series contains a huge amount of information motivated A. M. Ferrenberg and R. H. Swendsen to develop the celebrated *histogram reweighting* method [53]. It allows one to extrapolate observables at a temperature β', away from the actual simulation point β. This is done by *reweighting* the energy histogram by appropriately shifted Boltzmann factors. In particular, one writes

$$\langle O\rangle(\beta') = \left\langle O\mathrm{e}^{-(\beta'-\beta)E}\right\rangle_{\beta} \Big/ \left\langle \mathrm{e}^{-(\beta'-\beta)E}\right\rangle_{\beta} \tag{4.45}$$

where the subscript β represents the fact that the thermal averages have to be taken at the run temperature. This way, observables can be obtained as continuous functions of the temperature, allowing, for instance, extremal points which are used in the finite-size scaling analysis to be determined with high precision. A key requirement for this method is that the energy histograms at β and β' need to present sufficient overlap. A small overlap (i. e. an attempt to reweight at a temperature considerably far away from the simulation point) naturally results in very poor statistics and possibly systematic errors of the reweighted observables [263]. In practice, we estimate the valid reweighting range as proposed in [151]. The distance $\Delta\beta \equiv |\beta - \beta'|$ inside which one can expect a reliable extrapolation is given by

$$\left[\frac{\Delta\beta}{\beta}\right]^2 \leq \frac{1}{C(\beta)} \tag{4.46}$$

where the width of the energy histogram at the simulation temperature enters through the specific heat C. The reweighting method drastically improves both workflow and required computational effort, since observables can be computed arbitrarily smooth around the simulation point, as illustrated in Figure 4.3. Note that the reweighting method is not restricted to extrapolations in the temperature and can also be performed along other Hamiltonian parameters, such as the external field or the fourth-order coupling constant u.

If one is interested in a physical observable over an *extended* range of temperature, the single-histogram reweighting method turns out to be no longer sufficient, since the range in which one can expect reliable results is very narrow in practice and systematic errors can not be controlled outside this region. A typical example are simulations where the crossing points of RG invariant quantities need to be analysed (the quotient FSS method, introduced in Section 4.1.3). As we are interested in the crossing points of the lattice pairs $(L, 2L)$, we

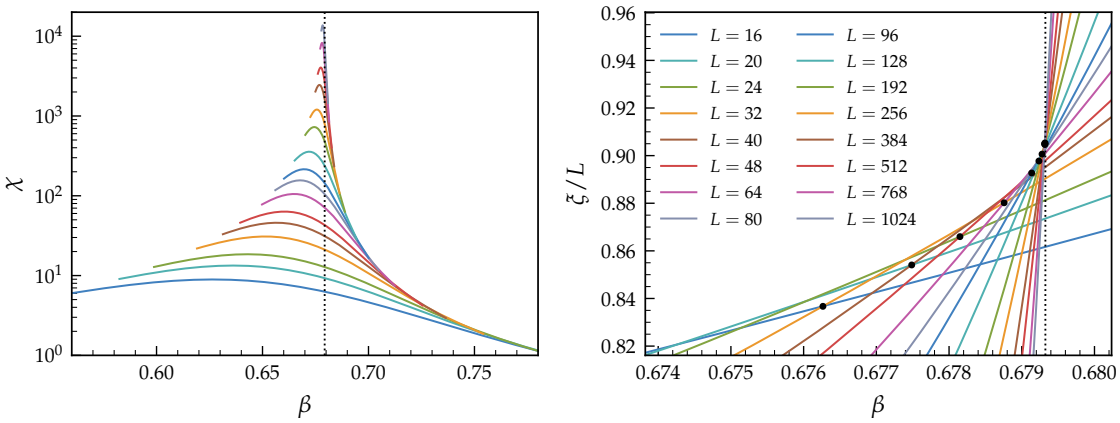

Figure 4.3 | Illustration of the single-histogram reweighting technique. Susceptibility (left) and correlation length (right) of the Ising model on a Voronoi lattice (compare Figure 3.2), reweighted from a single run at the inverse temperature indicated by the vertical dotted line. The black dots mark the maxima of the scaling function (4.24b) in the left panel and crossing points of $(L, 2L)$ lattice pairs in the right panel and can be used for extracting critical exponents. For the smaller lattices up to 10^5 disorder realizations were simulated, whereas we used at least 5000 replicas for the largest lattices.

need to know the quantity as precisely as possible at *two* temperatures.[29] Obviously, one could just perform two entirely independent simulations, which however makes the analysis cumbersome. It would therefore be convenient to combine the histogram information of several independent simulations into one reweighted curve. A clever approach how this can be done is the *multi-histogram reweighting* method, also introduced by Ferrenberg and Swendsen [54, 55]. This method is the direct precursor to a whole arsenal of so-called *weighted histogram analysis methods* (WHAM), which apart from statistical physics, quickly became very popular in molecular dynamics simulations [296–298] and are still object of current research [299]. In this work, we use a slightly modified version [300, 301], where no initial binning of the energy histogram is necessary. In particular, we define

$$f_k = -\ln \sum_{i=1}^{N_\beta} \sum_{j=1}^{N_{m,i}} P(\beta_k, E_{i,j}), \tag{4.47}$$

where $E_{i,j}$ denotes the energy of the j-th configuration at temperature β_i and

$$P(\beta, E_{i,j}) = \frac{\omega_i^{-1} \exp(\beta E_{i,j})}{\sum_{l=1}^{N_\beta} \omega_l^{-1} N_{m,l} \exp(-\beta_l E_{i,j} + f_l)}. \tag{4.48}$$

In order to account for correlations in the MC time series, additional weights $\omega = (1 + 2\tau_{E,\mathrm{int}})^{-1}$ have been added. Once the f_i are known, Equation (4.48) replaces the Boltzmann weights in the single-histogram reweighting formula (4.45). One obtains

$$\langle O \rangle(\beta) = \frac{\sum_{i,j} O(\sigma_{i,j}) P(\beta, E_{i,j})}{\sum_{k,l} P(\beta, E_{k,l})}, \tag{4.49}$$

[29] In case we are interested in the intersection points of several quantities, like U_4 and ξ/L which do not necessarily lie close, this amounts to even more points that have to be known.

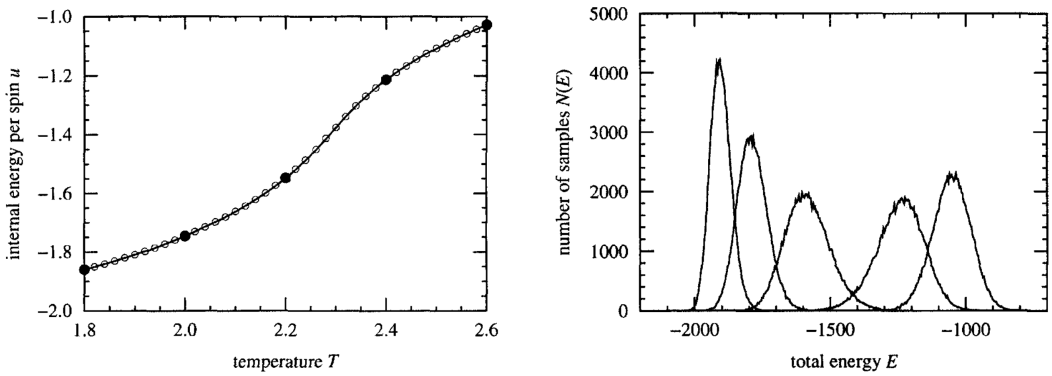

Figure 4.4 | Illustration of the multi-histogram reweighting technique. Black dots in the left panel show actual simulation temperatures, white dots show results of the MHR interpolation, which fit the analytic solution (solid line) very well over a large range of temperatures. The left panel shows the corresponding energy histograms of the five measurements. Adopted from [151].

which allows us to calculate O at temperature β using the combined information of multiple energy histograms. It needs to be emphasized that, as shown in Figure 4.4, the histograms of the individual runs need to present sufficient overlap in order for this method to work. The system of equations (4.47) is solved self-consistently using iterative multi-root finding methods, which is quite challenging, especially for disordered systems, where the replica average requires a particularly robust solver and an automatized calculation of proper initial values. In fact, optimizations and convergence properties are subject of current research [299, 302]. An illustration is depicted in Figure 4.4 which demonstrates the accuracy of the results.

4.2 The MARQOV framework

In the course of the present project we developed a code framework which incorporates the techniques mentioned in the previous section into a convenient workflow. The project currently is in the state of a prototype and goes under the working name **MARQOV** (MASSIVELY PARALLEL QUENCHED DISORDER ON VARIABLE GEOMETRIES). As this name already suggests, special focus is placed on quenched disordered systems, which are particularly demanding in terms of computational resources. Not only does the need for a large number of disorder replicas (typically 10^5–10^6 for a set of finite size simulations) require considerable computing time, but also extensive amounts of memory (due to performing simulations on multiple lattices in parallel) and permanent storage (we store the entire MC time series, in order to ensure the greatest possible flexibility when it comes to reweighting) are required. Moreover, when dealing with thousands of independent systems, parallelization and automatization aspects become particularly important. In summary, state-of-the-art MC simulations of disordered canonical spin systems clearly lie in the domain of high performance computing (HPC).

Our code framework is designed to essentially split into three parts, as can be seen in Figure 4.5. The first and most important part is the actual Monte Carlo simulation code, followed by a separate postprocessing code, performing basic statistical analysis and calculation of observables through reweighting methods mentioned above. Both codes are written in

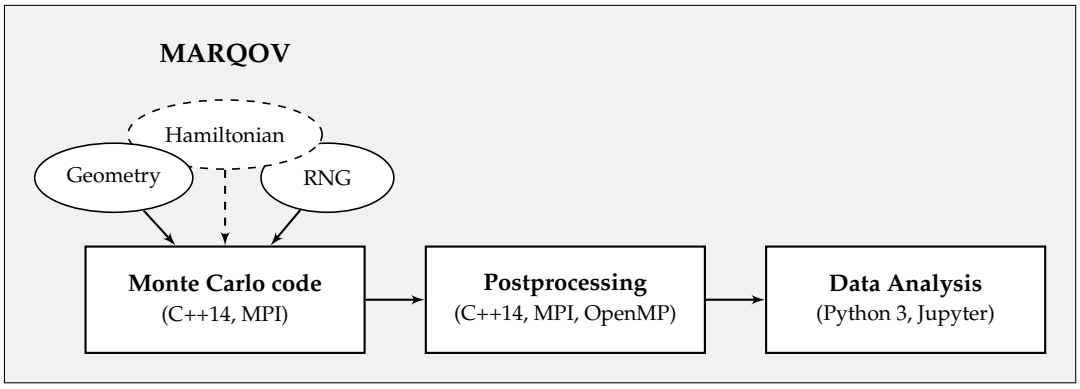

Figure 4.5 | Structure of the MARQOV framework. Ellipsis symbols denote header modules and dashed elements are not yet implemented. Arrows represent the direction of data processing.

C++14. The last stage consists of Jupyter notebook templates which perform the data analysis and are written in Python 3. All three parts of the code, as well as the header modules, are version-controlled using Git and will be briefly described in the following:

Monte Carlo code

This part of the framework performs the actual importance-sampling Monte Carlo simulation, using a combination of Wolff cluster and local Metropolis updates, as detailed in Section 4.1.2. The code is *replica-parallelized* using MPI, which means that each process runs an entirely separate disorder realization of the system. This has clear advantages over other parallelization concepts, such as domain decomposition, since in the critical regime the system shows collective behaviour over long distances, which in general would require heavy inter-process communication. Furthermore, especially in three dimensions, the cluster algorithm flips only rather small regions of the lattice, which makes proper load balancing virtually impossible. As a matter of fact, there do exist parallel implementations of the Wolff cluster algorithm [303, 304], however, the scaling of their performance with the number of processes turns out to be very poor for exactly this reason.

Our parallel implementation specifically works as follows: Upon execution, the code is given a list of run parameters (number of replicas, corresponding lattice sizes and simulation temperatures), which are scheduled to all available cores at runtime. If the number of cores is considerably smaller than the total number of replicas, this naturally results in an almost optimal scaling and load-balancing, since after the scheduling step, every process works through its individual list and no further communication is required.

Special attention is also given to the geometry of the problem, encoded in the lattice structure. We introduced a standardized container format for this purpose, which allows seamless integration of any regular and disordered lattice/network topologies as header libraries. Currently, a number of standard geometries (regular square and cubic, triangular, randomly diluted cubic, Voronoi-Delaunay and other proximity graphs) are available (compare Section 3). Moreover, also the generation of random numbers is wrapped in a header module, allowing to switch between specific generators. Currently, a Mersenne Twister 19937 generator provided by the

C++ standard library, as well as our own implementation of a generalized feedback shift-register (GFSR) random-number generator [305] are available. Finally, the implementation of an interface to include arbitrary spin Hamiltonians is planned in the future, as the ones mentioned in Section 2.2 are currently hard-coded.

Postprocessing

This part of the code uses the raw MC time series data of the previous step as an input and allows the calculation of all relevant observables at any desired temperature near the simulation point via single or multi-histogram reweighting (Section 4.1.5). It includes resampling and bias-correcting methods (Section 4.1.4). Similarly to the main code, the postprocessing is MPI parallelized using a replica scheduling system and some of the inner loops optionally support OpenMP parallelization. This presents an efficient, automatized data management solution which is crucial for both disordered systems (with possibly 10^6 or more replicas) and also for extensively long time series of regular models.

Data Analysis

We wrote a Python class which allows one to easily read and process the output of the postprocessing step. Taking advantage of the flexibility of Python's scientific libraries (numpy, scipy, pandas, matplotlib, etc.) a convenient workflow is implemented inside a Jupyter notebook template. It contains predefined functions to perform different types of FSS analyses, including plot scripts and fit procedures using Bootstrap resampling for the calculation of parameter uncertainties.

Application: O(3) model on RGG

As an application of the MARQOV framework, we simulate the $O(3)$ model (commonly referred to as the Heisenberg model and defined in Section 2.2) on a three-dimensional random geometric graph (compare Section 3.2), modelling a finite, fixed interaction radius in a disordered medium. The radius is chosen such that on average the nodes have six neighbours, representing moderate to strong disorder.[30] Due to the fact that the RGG represents effectively uncorrelated randomness (compare discussion in Section 3.4), we can apply Harris inequality, according to which disorder should be irrelevant if $d\nu > 2$. Since for the three-dimensional Heisenberg universality class, $\nu \approx 0.71$ [122, 307], the criterion predicts that one should find a clean transition in this case, similar to dilute Heisenberg systems, which have been investigated in References [308, 309] (see also Section 2.5).

As mentioned before, simulations of disordered systems are particularly demanding from the computational point of view, since on the one hand, large lattice sizes are necessary in order to reduce finite-size corrections and, on the other hand, a large number of independent disorder realizations is required. In the present case, we use linear lattice sizes $L = 8, 10, 12, \ldots$, up to 192 and simulate $N_r = 10^5$ replicas for the smaller lattices and at least $N_r = 10^4$ for the largest one. Our aim is to use the quotient FSS method, developed in Section 4.1.3, which allows us to extract the leading correction-to-scaling exponent ω to considerable precision. As this method exploits

[30] The percolation threshold of the three-dimensional RGG on a torus is located at $\langle q \rangle = 2.74(1)$ [306].

the scaling behaviour of observables at the crossing points of phenomenological couplings

$$R \in \{\xi/L, U_4, U_6, \ldots\}, \tag{4.50}$$

we chose simulation temperatures close to the crossing points of the correlation length in units of the system size, ξ/L. The precise location of the crossing points is then determined via histogram reweighting methods, introduced in Section 4.1.5.

Every replica is initially prepared in a hot (random) configuration (all spins aligned in parallel) and is thermalized using 500 elementary Monte Carlo steps. We checked for a proper thermalization by also performing simulations starting from a cold configuration, which gives identical results within numerical precision. In our update procedure, one EMCS consists of a full Metropolis lattice sweep and several Wolff cluster updates. Since the average cluster size in a d-dimensional system at criticality scales as $L^{d-\gamma/\nu} = L^{d-2+\eta}$ and $\eta \approx 0.04$ for the Heisenberg universality class, we increase the number of cluster updates linearly with the lattice size in order to keep the fraction of flipped spins approximately independent of the lattice size [58]. After the thermalization, we perform another 750 EMCS and measure magnetization, energy and Fourier transform of the magnetization after every EMCS (compare Section 4.1.3 for their definitions).

As the first step in our analysis, we determine the critical value of the RG invariant quantities as well as the leading correction-to-scaling exponent ω. This can be done without precise knowledge of the critical temperature and the correlation length exponent ν, by evaluating the scaling functions defined in Equation (4.50) at crossing points of $(L, 2L)$ pairs of the finite-volume correlation length ξ/L. The procedure is illustrated in the right panel of Figure 4.3. We use the following scaling ansatz

$$R|_{Q_\xi=2} = R^* + a_R L^{-\omega}, \tag{4.51}$$

where sub-leading corrections are neglected, R^* denotes the value of R at the infinite-volume critical point and the amplitude a_R of the leading correction term depends on the respective function used. Uncertainties for the fit parameters are obtained by a comprehensive bootstrap resampling analysis. To be specific, we construct n_B bootstrap samples (typically $n_B \approx 200$) of the full data set by averaging the observables over $N_r(L)$ randomly drawn disorder replicas rather than performing a simple average where every replica is considered exactly once. For every of those bootstrap samples the fits are performed, resulting in n_B estimates for the fit variables. Averages and standard deviations of these estimates are reported as the final fit estimates. We employ this procedure throughout the entire analysis. More details can be found in Appendix A.3.

When performing a finite size scaling analysis of crossing points of observables, it was pointed out in Reference [309] that the fact that one particular curve $R(\beta, L)$ intersects with *two* others, namely $R(\beta, 2L)$ and $R(\beta, L/2)$, introduces non-trivial correlations among the corresponding pairs of crossing points. As a consequence, using a fit method which optimizes a traditional χ^2 is no longer valid here and one rather must use a more general definition, which includes the

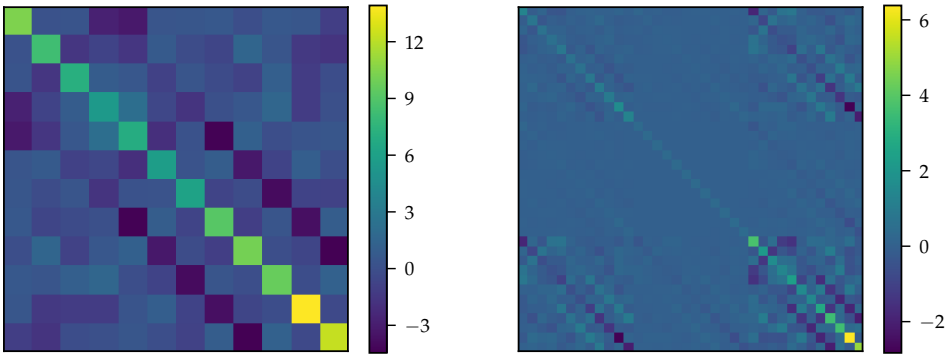

(a) (b)

Figure 4.6 | Cross-correlations. (a) Inverse covariance matrix (compare Equation 4.53) of U_4 at the crossing points of ξ/L, revealing the cross-correlation structure among the data points. (b) Cross-correlations of ξ/L, U_4 and U_6 evaluated at the crossing points of ξ/L, showing a block structure. Colour values are rescaled by a factor of 10^6 in the left and 10^7 in the right panel.

whole self-covariance of the data set, namely

$$\chi^2 = \sum_{l=1}^{N_{\text{cr}}} \sum_{m=1}^{N_{\text{cr}}} (x_l - \text{fit})\, C_{lm}^{-1}\, (x_m - \text{fit}). \tag{4.52}$$

Here, N_{cr} is the number of crossing points taken into account in the fit. Moreover, x denotes the value of the observable under consideration at the crossing point and C^{-1} is the inverse self-covariance matrix. Since, as described earlier, we perform an extensive bootstrap-replicated analysis of our simulation data, C can be straightforwardly evaluated by

$$C_{lm} = \frac{1}{n_B - 1} \sum_{i=1}^{n_B} (\tilde{x}_{l,i} - \langle x_l \rangle)(\tilde{x}_{m,i} - \langle x_m \rangle), \tag{4.53}$$

which is nothing but the definition of the general bootstrap covariance matrix [288, 289]. Recall that n_B denotes the number of bootstrap samples of the full data set. Moreover, $\tilde{x}_{l,i}$ denotes the data point corresponding to the crossing point with index l in the bootstrap sample with index i and $\langle x \rangle$ is the corresponding average over all bootstrap samples. A visual example of C^{-1} for the values of U_4 at the crossing points of ξ/L is presented in Figure 4.6a. As expected, we find a pronounced (anti)correlation structure parallel to the diagonal, representing the correlations among the data points mentioned before. Had we not performed this extensive analysis, this structure would have not been taken into account, but rather only the diagonal (simple) uncertainties, possibly resulting in systematic errors of all quantities to be extracted in the following.

When performing *individual* fits of either ξ/L , U_4 or U_6 according to Equation (4.51), the results turn out to depend quite sensitively on the precise choice of L_{min}, specifically ω fluctuates in the range 0.3 – 0.5. However, the quality of the fits (and therefore the precision of the ω estimate) can be greatly improved by performing a *simultaneous* fit of all three curves according to Equation (4.51) with joint ω. Note that our comprehensive bootstrap analysis again proves very useful here, as it allows us to take not only the cross-correlations among data points of

Table 4.2 | Results of the combined fits according to Equation (4.51), at the crossings of ξ/L (upper part) and U_4 (lower part), as a function of L_{min}. Uncertainties are computed from bootstrapping the full data set, as described in the text.

L_{min}	$(\xi/L)^*$	U_4^*	U_6^*	ω	χ^2/d.o.f
8	0.5592(11)	0.6213(2)	1.4091(16)	0.451(10)	3.45
10	0.5618(14)	0.6208(2)	1.4134(22)	0.422(13)	3.37
12	0.5615(17)	0.6207(3)	1.4142(27)	0.419(16)	2.42
16	0.5608(28)	0.6207(5)	1.4150(43)	0.419(28)	1.87
20	0.5596(36)	0.6208(6)	1.4141(58)	0.430(41)	1.87
8	0.5546(8)	0.6211(3)	1.4103(27)	0.455(13)	3.41
10	0.5571(10)	0.6204(4)	1.4167(38)	0.422(16)	1.15
12	0.5574(12)	0.6203(5)	1.4179(45)	0.416(18)	1.12
16	0.5581(21)	0.6200(8)	1.4204(75)	0.406(32)	1.28
20	0.5581(29)	0.6200(12)	1.421(11)	0.407(46)	1.60

one individual curve into account, but also the full correlations *between* the curves. Since for all three phenomenological couplings, we obtain 12 crossing points of pairs $(L, 2L)$, this amounts to a covariance matrix of size 36×36, which is calculated again by means of Equation (4.53). A typical example is shown in Figure 4.6b. As can be seen, we find considerable correlations also *between* the curves, as expected. Moreover, the self-covariance structure of the individual curves is retrieved as blocks along the diagonal. We remark that in practice, when computing the full covariance matrix of several combined observables, certain technical issues arise, which are discussed in Appendix A.4.

In the joint fits, an identical L_{min} is used for all three curves. Results are shown in the upper part of Table 5.4. Evidently, ω only fluctuates very little, as L_{min} is gradually increased. For $L_{\text{min}} > 16$, the χ^2/d.o.f of the fit does not change significantly which indicates that any sub-leading corrections to scaling become small. As our final estimate, we obtain

$$\omega = 0.42(4), \tag{4.54}$$

which includes all individual estimates for $L_{\text{min}} = 10, 12, 16, 20$ as well as their corresponding uncertainties. Obviously, this estimate is significantly smaller than the corresponding value for the pure model, $\omega \approx 0.8$ [123, 126], as well as the results found for diluted Heisenberg systems [309]. This already indicates that scaling corrections originating from the topological randomness are considerably strong and necessarily need to be taken into account in the analysis.

As a consistency check, a similar analysis at the crossing points of U_4 is shown in the lower part of the table. As can be seen the results are largely consistent with the ones in the upper part of the table, and the χ^2/d.o.f saturates already at $L_{\text{min}} = 12$. This is rather remarkable, since the simulation temperatures were located near the crossing points of ξ rather than U_4 which, when

Table 4.3 | Results of the combined fit according to Equation (4.58) as a function of L_{min}.

L_{min}	$2-\eta$	ω_2	χ^2/d.o.f
8	1.955(8)	1.68(24)	4.36
10	1.952(9)	1.91(47)	4.23
12	1.953(9)	1.98(64)	4.39
16	1.958(13)	1.95(96)	4.94
20	1.959(13)	2.1(11)	5.95

evaluating the latter, introduces systematic errors due to the reweighting step becoming less reliable as one moves farther away from the simulation point. Our final estimates for the fixed point values of the phenomenological couplings are hence given by the estimates for $L_{\text{min}} = 16$ at the crossing of ξ/L, resulting in

$$\begin{aligned} (\xi/L)^* &= 0.5608(28), \\ U_4^* &= 0.6207(5), \\ U_6^* &= 1.4150(43), \end{aligned} \tag{4.55}$$

which have to be compared to the most-precise values for the Heisenberg model on a cubic lattice, $(\xi/L)^* = 0.5644(3)$, $U_4^* = 0.6202(1)$ and $U_6^* = 1.4202(12)$ [122]. All three estimates are compatible, which, already at this stage of the analysis, strongly indicates that our model falls into the same universality class as the pure Heisenberg model. Note, however, that these quantities are only universal in a limit sense as they weakly depend on certain geometrical characteristics of the system [310–312].

Equipped with an estimate for ω, we are now able to extract critical exponents. This is done by fits to the ansatz

$$Q_O \,|_{Q_R=s} = s^{x_O/\nu} + aL^{-\omega}, \tag{4.56}$$

where x_0/ν denotes the corresponding critical exponent and the quotient is defined by

$$Q_O = \frac{\langle O\rangle(sL,T)}{\langle O\rangle(L,T)}. \tag{4.57}$$

In particular, $\partial \ln\langle m^k\rangle/\partial\beta$, where $k = 1, 2$, yields the correlation length exponent ν. Furthermore, the susceptibility χ allows us to compute $\gamma/\nu = 2-\eta$. Finally, from the magnetization $\langle m\rangle$ and its derivative $\partial\langle m\rangle/\partial\beta$, we get the exponents β/ν and $(1-\beta)/\nu$, respectively. For all fits we fix ω to the estimate (4.54), also taking into account its uncertainty. As before, the fitting procedure uses n_B independent bootstrap replicas of the full data sets. The results are shown in Figure 4.7, including the χ^2/d.o.f of the fits in the lower panels. The estimates for ν clearly approach the reference value (indicated by the solid horizontal line) for increasing L_{min} and likewise does the exponent $(1-\beta)/\nu$. In both cases, especially those fits which are – within their uncertainties – compatible with the corresponding reference values, represent the lowest

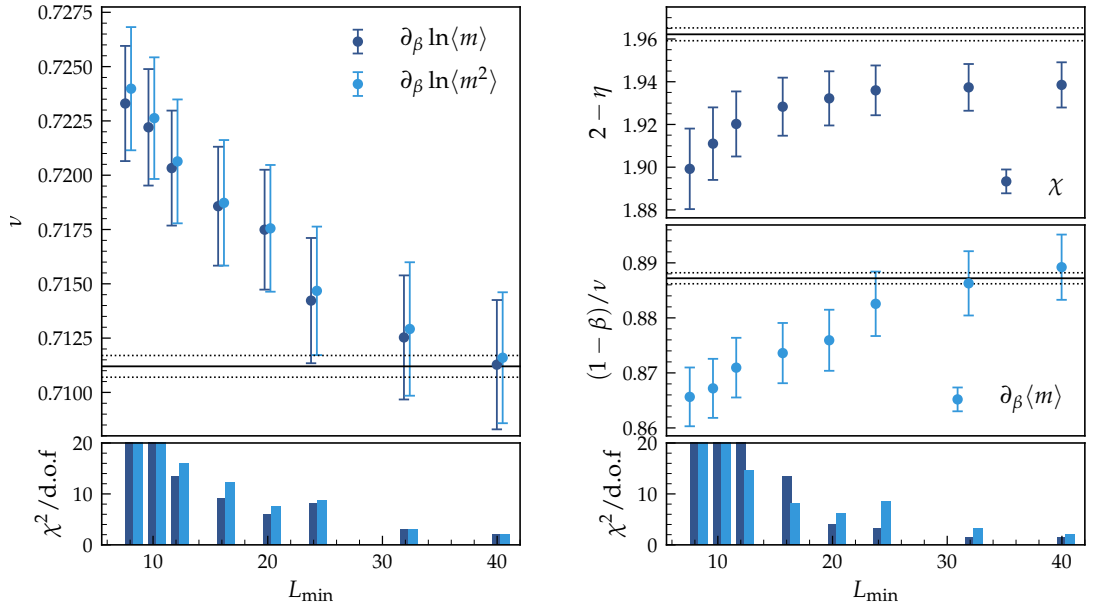

Figure 4.7 | Critical exponents of the three-dimensional O(3) model on a RGG. Results of the fits according to relation (4.56), as a function of $L_{\min}$. On the left hand side, the derivatives of $\ln\langle m\rangle$ and $\ln\langle m^2\rangle$ yield the exponent ν whereas on the right hand side the susceptibility χ yields $\gamma/\nu = 2-\eta$ and $\partial_\beta\langle m\rangle$ yields $(1-\beta)/\nu$. The χ^2/d.o.f of the fits are indicated in the lower panels on each side. Moreover, horizontal lines indicate the reference values and their uncertainties from the literature [122, 307].

χ^2/d.o.f. The exponent η, however, deviates slightly but systematically from its expected value. We hence fit the data for χ to the more general ansatz

$$Q_\chi\,|_{Q_R=s} = s^{\gamma/\nu} + aL^{-\omega} + bL^{-\omega_2}, \tag{4.58}$$

introducing an additional higher-order correction term and fixing ω as before, resulting in four free parameters. From optical inspection of the fits it becomes clear that the largest data point presents itself a considerable outlier, which could be caused the relatively low number of replicas, compared to the magnitude of the disorder. Discarding this point, we find the results listed in Table 4.3. As can be seen, the estimates are in good agreement with the reference value $2-\eta = 1.9625(5)$ [122]. Interestingly, the sub-leading correction exponent is found to be $\omega_2 \approx 2$, although showing considerably large error bars. In fact, this is a reasonable result, since the susceptibility is known to gather corrections proportional to $L^{2-\eta}$ from its regular background term [154, 313]. Furthermore, since an individual realization of the RGG is not rotationally invariant, corrections proportional to $\omega_2 \approx 2$ may arise from the breaking of the corresponding symmetry as well, as we have discussed earlier (in Section 2.4).

In summary, we find a scaling scenario consistent with the clean universal exponents of the Heisenberg universality class, which strongly indicates that the $O(3)$ symmetric model on a three-dimensional random geometric graph belongs to this class and disorder presents an irrelevant perturbation, as expected by the HBV criterion. We also find that, owed to the strength of the disorder, corrections to the leading scaling behaviour turn out to be considerably

strong ($\omega \approx 0.4$) and necessarily must be taken into account in the course of the analysis.

4.3 Non-equilibrium systems

Having discussed the required numerical methods for equilibrium spin models in detail, we now turn our attention to non-equilibrium systems. For the contact process, as detailed in Section 2.3, the time evolution of the system comprises two processes, offspring creation and spontaneous on-site removal, which evolve a *cluster* of active sites over time by means of a (continuous time) Markov process. In contrast to equilibrium systems, an algorithmic implementation of the update rules is quite straightforward. Recalling Equation (2.49), the rates of the CP are given by

$$\begin{aligned} w[0 \to 1, n] &= \lambda n/q, \\ w[1 \to 0, n] &= 1, \end{aligned} \tag{4.59}$$

where λ controls the offspring rate, n denotes the number of *active* nearest neighbours and q the total number of neighbours of the site under consideration. In a practical implementation on a computer, the rates translate to probabilities

$$p_{\text{offspring}} = \frac{\lambda n}{q(1+\lambda)} \qquad \text{and} \qquad p_{\text{removal}} = \frac{1}{1+\lambda}, \tag{4.60}$$

which control the frequency of both processes. In our simulations, we employ a random-sequential update scheme, which means that in every time step an active site is randomly chosen. With probability

$$p \equiv \frac{\lambda}{1+\lambda} = \frac{q p_{\text{offspring}}}{n} \tag{4.61}$$

the site stays active and a neighbour is randomly selected: if currently inactive, this neighbour becomes infected; if it is already infected, nothing happens. With probability $1-p$, the site recovers spontaneously, i. e. it becomes inactive but is immediately susceptible to reinfection. Either way, time is incremented by $\Delta t = 1/N_a$, where N_a is the number of active sites before the update attempt, resulting in a (pseudo)continuous time evolution, since on average all active particles are being considered once per time unit. Note that for simulations studying the dynamical (i. e. time-dependent) properties of the CP, one usually averages the results over an ensemble of several runs. Since in every realization the evolution of the cluster might evolve entirely different, the time signatures of the measurements in general do not coincide between individual runs. This problem can be circumvented by grouping the measurements into temporal bins and average the individual bins afterwards. In our simulations, we used bins with linear size for early times (typically $t < 500$) and logarithmically spaced bins for later times in order to reduce the amount of output data.

Also for the conserved Manna model, introduced in Section 2.3, a continuous-time random-sequential update scheme is employed. In particular, we use a variant of the model with unrestricted height, which means that every site can in principle carry an arbitrarily large number of particles. Sites with two or more particles are active. As for the CP, the indices of active sites are saved in a dynamic array, which allows to select one at random in each time

step. Then, all particles are transferred to randomly selected neighbouring sites and the time is incremented by $\Delta t = 1/N_a$, where N_a is the number of active sites before the redistribution.

4.3.1 Static scaling

We consider a non-equilibrium reaction-diffusion process in an infinitely large system. In the active regime, i. e. for $\Delta \equiv p - p_c > 0$, after an initial transient behaviour which depends on the chosen initial configuration, the process relaxes into a well-defined state of steady activity, where system properties take on stationary values. Particularly important is the density of active sites, given by

$$\rho(t) = \frac{1}{V} \sum_i \langle n_i(t) \rangle, \tag{4.62}$$

where V denotes the total number of sites in the lattice and each site i can either be occupied, $n_i = 1$, or empty, $n_i = 0$, at time t. As mentioned earlier, the density is typically averaged over multiple individual realizations of the Markov process, which is indicated by $\langle \ldots \rangle$. In fact, the steady state density

$$\rho_{\text{stat}} = \lim_{t \to \infty} \rho(t) \tag{4.63}$$

represents the order parameter of the non-equilibrium phase transition. Similar to equilibrium systems, at criticality, the spatial correlation length $\xi_\perp$ diverges with the (reduced) control parameter, i. e.

$$\xi_\perp \sim |\Delta|^{-\nu_\perp} \quad \text{as} \quad \Delta \to 0. \tag{4.64}$$

Analogously, for the correlation time, the relation

$$\xi_\parallel \sim |\Delta|^{-\nu_\parallel} \quad \text{as} \quad \Delta \to 0, \tag{4.65}$$

holds, where spatial and temporal correlations are related through $\nu_\perp z = \nu_\parallel$, which defines the dynamic exponent z. This enables us to write down a general scaling form of the density near the critical point [314, 315] for a finite system of linear extension L, given by

$$\rho(\Delta, t, L) = b^{-\beta/\nu_\perp} \tilde{\rho}(\Delta\, b^{1/\nu_\perp}, b^z/t, b/L), \tag{4.66}$$

where $\tilde{\rho}$ defines a scaling function with an appropriate asymptotic behaviour and b is an arbitrary scale factor. This relation allows us to extract a number of scaling relations. Taking $b = \Delta^{\nu_\perp}$ we find in the thermodynamic limit ($L \to \infty, t \to \infty$)

$$\rho_{\text{stat}} \sim \Delta^\beta, \tag{4.67}$$

where β is the critical exponent of the order parameter.

In order to obtain the dependence of ρ_{stat} on the lattice size, we evaluate the scaling form (4.66)

directly at criticality ($\Delta = 0$). Setting $b = L$ yields

$$\rho_{\text{stat}} \sim L^{-\beta/\nu_\perp}. \tag{4.68}$$

Similar relations can be obtained [314] for the susceptibility (variance of the order parameter)

$$\chi = L^d \left(\langle \rho^2 \rangle - \langle \rho \rangle^2 \right) \sim L^{-\gamma/\nu_\perp}, \tag{4.69}$$

where the following hyperscaling relation

$$\gamma = d\nu_\perp - 2\beta, \tag{4.70}$$

holds [316] and the relaxation time scale of the steady state [31] fulfils

$$\tau \sim L^z. \tag{4.71}$$

Even though the above scaling relations allow, in principle, a straightforward extraction of the critical exponents, in *finite* systems the fact that the process features (one or several) absorbing configurations brings along an issue in numerical simulations. Depending on the system size, at some point an absorbing state will be reached[32] and the system is trapped, which prohibits to probe the stationary state systematically. Actually, in a finite system, the absorbing configuration is the only true stationary state. To overcome this issue, one possibility is to apply an external field [317], which can be implemented in a way that active particles are created spontaneously [129], and analyse the scaling properties in the limit of the field tending to zero. Another possibility is to consider systems conditioned on survival, which means that one uses an ensemble of systems and $\rho(t)$ is averaged only over those which are still alive at time t [314]. Although quite different on the first glance, both methods can be derived from each other, as pointed out in Reference [318].

In this work we use a clever approach, that was suggest by R. Dickman and M. de Oliveira [319, 320] and is related to the second method mentioned above. It allows for a direct and technically convenient probing of the *quasi-stationary* (QS) regime (i. e. conditioned on survival). Specifically, the run takes place on a finite lattice and starts from a configuration where all sites are active. Every time the absorbing state is reached, the system is reset to an active configuration randomly chosen from its history. Numerically, this can be realized by saving a list of previously visited states. This list is periodically updated to assure convergence towards the QS state. At the end of the simulation, the desired observables (such as the QS density ρ_{QS}) can be obtained by a simple average over the configurations on the list. Moreover, the exponent z can be obtained by taking the mean time between successive attempts to visit the absorbing state as the relaxation time scale in Equation (4.71). As detailed in References [319, 320], this algorithm effectively samples a modified process, free of an absorbing state, but with the same QS properties as the original system. As a consequence, the QS method allows for arbitrarily

[31] There is no unique definition of a relaxation time scale in the stationary state of non-equilibrium systems with absorbing configurations. However, τ may be thought of as the time after which the stationary density decays to half of its value [314].

[32] Even in the active phase, a finite system inevitably reaches an absorbing state after a specific time scale due to random fluctuations.

long simulations while providing a good statistical sample size. Note that for certain small systems, the QS properties can even be computed analytically [321].

In a practical implementation, the QS simulation method presents two essential parameters, the size of the list of saved configurations N_c and the update probability p_r per unit time step. Typically, N_c is limited by technical constraints (memory of the computer), since storing hundreds or even thousands of configurations quickly becomes expensive for large systems. This is particularly delicate for bosonic systems, such as the Manna model, where the exact configurations needs to be stored. For the contact process in contrast, saving a list (of indices) of active sites, which in the QS regime typically turns out to be much smaller than the actual system volume, is sufficient. Note that the update probability p_r (per unit time) of the saved configurations represents important tuning parameters of the QS method. As a rule of thumb, the typical residence time of a configuration on the list, N_c/p_r, should be much larger than the QS lifetime, but small compared to the total duration of the study.[33]

4.3.2 Dynamical scaling

So far we have only considered the stationary scaling properties of non-equilibrium systems in the steady state. We now turn our attention to the so-called dynamical scaling regime, which explicitly captures the time dependence of the process. Starting from a fully occupied lattice at the critical point, we take $b = t^{1/z}$ in Equation (4.66) and, for an infinite system ($L \to \infty$), obtain

$$\rho(t) \sim t^{-\delta}, \tag{4.72}$$

where the dynamical critical exponent of the order parameter is defined as

$$\delta = \frac{\beta}{\nu_\perp z}, \tag{4.73}$$

implying that the density decays as a power law at criticality. In a finite system, the power law decay can only be observed as long as the correlation length is smaller than the linear extension of the system. As soon as spatial correlation length $\xi_\perp$ and lattice size L are comparable, the density decay becomes exponential. This time scale, representing the characteristic time after which the absorbing state is reached, is given by $\tau_{\mathrm{FSS}} \sim L^z$ [5]. Hence, in order to obtain a clean estimate of the exponent δ, one has to ensure that only the regime $t \ll \tau_{\mathrm{FSS}}$ is probed in the study. Additionally, one might also neglect the behaviour at small times due to early transient behaviour, depending on the initial configuration.

Further dynamical scaling properties can be derived if the evolution is started from a single occupied seed in an otherwise empty lattice. In these so-called *seed simulations*, typically three time-dependent quantities are measured and averaged over an ensemble of runs: the average size N_a of the evolving cluster, its mean-square radius R^2, and the survival probability P_s. We remark that the latter is typically only averaged over the surviving clusters. Furthermore, note that if there is only one absorbing state (such as for the CP), the survival probability and the density (4.66) are *dual* in the sense that they obey the same scaling behaviour [322], i. e.

[33] R. Dickman, personal communication.

$P_s(t) = \rho(t)$ in the long-time limit.[34] Guided by this identity, we are able to write down a general scaling form of the survival probability

$$P_s(\Delta, t, L) = b^{-\beta/\nu_\perp} \tilde{P}_s(\Delta\, b^{1/\nu_\perp}, b^z/t, b/L). \tag{4.74}$$

Analogous relations can be adopted for the total number of active particles and the mean-square radius of the active cluster [183], given by

$$N_a(\Delta, t, L) = b^{d-2\beta/\nu_\perp} \tilde{N}_a(\Delta\, b^{1/\nu_\perp}, b^z/t, b/L), \tag{4.75}$$

$$R^2(\Delta, t, L) = b^2 \tilde{R}^2(\Delta\, b^{1/\nu_\perp}, b^z/t, b/L). \tag{4.76}$$

At the critical point and for sufficiently large systems, this results in scaling relations

$$N_a(t) \sim t^\theta, \qquad R^2(t) \sim t^{2/z}, \qquad P_s(t) \sim t^{-\delta}, \tag{4.77}$$

where the critical exponent of the cluster volume is given by

$$\theta = \frac{d}{z} - 2\delta. \tag{4.78}$$

For systems which, due to the existence of multiple absorbing states, do not obey the symmetry mentioned above, the exponent β in Equations (4.74)–(4.76) is replaced by a different exponent β', hence P_s scales with an exponent $\delta' \neq \delta$. Also the hyperscaling relation (4.78) must be generalized in this case (see Reference [147] for details). However, since in this work only the dynamical scaling properties of the CP are considered, we will not discuss this case here.

Obviously, in numerical simulations, the relations (4.77) can only hold if the system is sufficiently large. In general, for finite systems the cluster reaches the boundaries at some point and cannot spread further. Hence, similar to the decay simulations from a fully active configuration, N_a, R^2 and P_s exhibit a well-defined finite-size cut-off after a time τ_{FSS}, which was defined above. In practice, finite-size effects can be avoided altogether by choosing the lattice sufficiently large and monitoring the cluster size during the simulation.

4.3.3 Activated scaling

For the CP, in the presence of site or bond-randomness, strong Griffiths effects emerge in the active phase [171], alongside with the transition being controlled by a new infinite-randomness fixed point. Similar to the Griffiths phase in equilibrium spin models (compare general discussion in Section 2.5.3) regions devoid of impurities are locally in the active phase, whereas the system globally is subcritical. In terms of the infection rate λ, the Griffiths region is located at $\lambda_c^0 < \lambda < \lambda_c$, where λ_c and λ_c^0 are the disordered and clean critical points, respectively. For a better overview, the phase diagram of the diluted contact process is depicted in Figure 4.8.

As already indicated in Section 2.5.3, for $\lambda > \lambda_c$ rare regions are able to maintain metastable states of activity. Even though, due to their finiteness, they eventually decay to the absorbing state, the typical lifetime scales exponentially with the distance from the clean critical point

[34] A detailed discussion of how this so-called *rapidity-reversal symmetry* arises can be found in Reference [5].

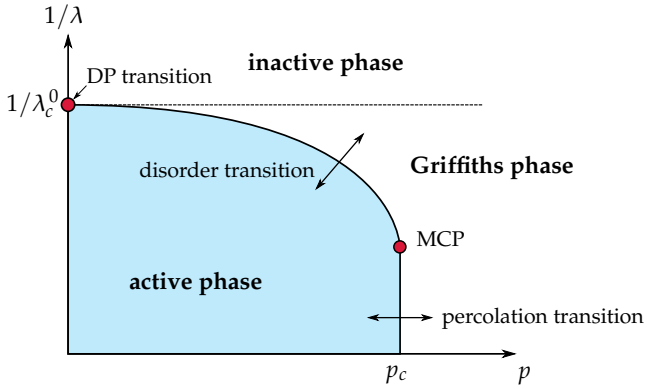

Figure 4.8 | Phase diagram of the randomly diluted contact process. The x-axis shows the dilution probability, where p_c denotes the percolation threshold of the lattice. The y-axis shows the inverse infection rate. Both transition lines (strong disorder transition with activated scaling and geometric lattice percolation transition) meet at a multi-critical point (MCP). Reproduced from [323].

(or, correspondingly the correlation length), as well as with the disorder strength. This slow decay has implications for the dynamic variables. Combined with their exponentially decaying likelihood (depending on the disorder parameter and their volume), it gives rise to power-law scaling with non-universal, continuously varying exponents in the Griffiths region $\lambda_c^0 < \lambda < \lambda_c$. In the specific case of the diluted contact process (controlled by the dilution parameter p) the asymptotic behaviour can be expressed as

$$\rho(t) \sim t^{\ln(1-p)/a} \qquad \text{with} \quad a \sim \xi^{-d} \sim (\lambda - \lambda_c^0)^{d\nu_\perp^0}, \tag{4.79}$$

where $\nu_\perp^0$ denotes the clean critical exponent of the correlation length. A more detailed discussion can be found in [181] and references therein.

At the actual critical point λ_c, the Griffiths exponents (4.79) obviously diverge, giving rise to a logarithmic scaling scenario. In fact, the critical exponents are found to be independent of the disorder strength and match those of the random transverse-field Ising model (RTFIM) universality class [324–326]. This was predicted in strong-disorder renormalization-group studies [182, 183, 327, 328] and verified in extensive numerical simulations in one, two and three spatial dimensions [179–181, 329, 330]. At this new, unconventional fixed point, the dynamics is ultraslow, which means the system evolves on a characteristic time scale proportional to $\ln t$ rather than to t itself. As a consequence, the conventional algebraic scaling laws are replaced by logarithmic counterparts, such as in the case of the density

$$\rho(\Delta, \ln t, L) = b^{-\beta/\nu_\perp} \tilde{\rho}(\Delta b^{1/\nu_\perp}, b^z / \ln t, b/L). \tag{4.80}$$

Similar relations hold for the cluster size, cluster radius and survival probability in seed simulations. The logarithmic time dependence enters in the scaling at the critical point

$$N_a(t) \sim \ln(t/t_0)^{\bar{\theta}}, \tag{4.81}$$

$$R^2(t) \sim \ln(t/t_0)^{2/\psi}, \tag{4.82}$$

$$P_s(t) \sim \ln(t/t_0)^{-\bar{\delta}}, \tag{4.83}$$

$$\rho(t) \sim \ln(t/t_0)^{-\bar{\delta}}, \tag{4.84}$$

featuring new disorder exponents, obeying scaling relations

$$\bar{\delta} = \frac{\beta}{\nu_\perp \psi} \qquad \text{and} \qquad \bar{\theta} = \frac{d}{\psi} - 2\bar{\delta}. \tag{4.85}$$

In this so-called *activated scaling* or *strong disorder scaling* scenario, where t_0 denotes a non-universal timescale, the relation between temporal and spatial correlations becomes

$$\ln(\xi_\parallel/t_0) \sim \xi_\perp^\psi, \tag{4.86}$$

rendering the dynamical exponent z formally infinite and giving rise to a new exponent ψ, called the tunnelling exponent. As a consequence, the correlation length still shows an algebraic singularity at criticality, whereas the correlation time diverges exponentially. In one spatial dimension, the disorder exponents $\bar{\delta}$, $\bar{\theta}$ and ψ can be estimated by analytical methods [182, 183], however, they can only be determined numerically in higher dimensions [181, 330, 331]. In fact, traditional Monte Carlo simulations of the CP under the influence of quenched disorder present a considerable challenge, as due to the logarithmic time-dependence, very long simulation times are necessary in order to reach the asymptotic scaling regime. Moreover, the characteristic non-universal time-scale represents an inconvenient extra parameter, significantly complicating any fitting procedures.

Finally, we note that the static scaling behaviour remains of algebraic type in the presence of quenched disorder, as can be seen in Equation (4.80), although with, in general modified values of the corresponding critical exponents, compared to the clean scaling scenario.

Chapter 5

Simulation Results

"Science is what we understand well enough to explain to a computer; art is everything else."

– Donald E. Knuth (Turing Award winner)

We review the numerical simulation results from the publications related to this work, [P1–P5], in detail and comment on the immediate conclusions. A more compact summary of these results will be provided at the beginning of Chapter 6. Note that some passages of this chapter have been quoted verbatim from the sources listed above.

The simulations have been performed on the JULIA and ITPA cluster, both located at Würzburg University, as well as on the GCS Supercomputer SuperMUC at the Leibniz Supercomputing Centre and took about five million CPU hours in total.

5.1 Ising model on two-dimensional lattices

In this section we present and discuss numerical simulations of the two-dimensional Ising model on CC lattices with different numbers of neighbours. They are analysed using the maximum finite-size scaling method. To this end, simulations on a square lattice and a DT are performed first. Having an analytical solution for the 2D Ising model available, they hence serve as a walk-through of the analysis and quantitative validation of our code (compare Section 4.2).

Square lattice benchmark

We simulate the two-dimensional Ising model on regular square lattices with linear sizes $L = 16$ up to $L = 256$ and compare the resulting critical exponents with the analytically known values. For the analysis, we exploit finite-size scaling properties of the extremal points of the scaling functions, as detailed in Section 4.1.3. All systems are simulated at temperatures close to the expected peak locations of their scaling functions, and reweighting techniques (see Section 4.1.5) are used to determine these locations with high precision. We chose one elementary Monte Carlo step (EMCS) to include 25 Wolff cluster updates and a full Metropolis lattice sweep. For each system size, a number of 10^6 EMCS is reserved to ensure proper equilibration. After that, another $2 \cdot 10^6$ EMCS are performed and magnetization and energy are evaluated after every update. Hence, in total we perform roughly 10^8 single cluster updates for each system size. Averages and corresponding uncertainties are computed using Jackknife techniques in order to properly handle autocorrelations and to reduce the bias of non-linear estimators, as was pointed out in Section 4.1.4.

In Section 2.4, we discussed that the scaling relations (4.24) generically include multiplicative correction factors, such as for the susceptibility

$$\chi = L^{\gamma/\nu} f_\chi(x)(1 + a_\chi L^{-\omega} + \dots), \tag{5.1}$$

with a correction-to-scaling exponent ω, some non-universal constant a_χ, and possibly further terms of higher order (see, e. g. [154, 157, 332] for a detailed discussion for the case of the two-dimensional Ising model). Note that ω is expected to be the same for all observables, whereas the correction amplitude is in general different. Taking into account these corrections would, however, require non-linear fitting methods with at least four parameters, which tend to be numerically unstable when maximum scaling is employed. Therefore, in order to avoid non-linear fits while still keeping track of possible systematic corrections, we adopt the following procedure [263]:

1. Determine a suitable minimum lattice size, $L_{\min}$, by discarding an increasing number of the smallest lattices and refitting, up to the point where the values of the exponents and also the goodness-of-fit parameter Q [275] cease to show a systematic trend.
2. Check the corresponding residual plot and, if necessary, increase $L_{\min}$ in order to eliminate any systematic trend still present in the remaining data points.

In order to determine the correlation length exponent ν, we use the last four scaling relations of (4.24), each of which is fitted to the seven pseudo-critical sequences of peak location (4.16c)-(4.17e), yielding a total of 28 fits. The relations could be fitted only at their own pseudo-critical temperatures with good results – however, performing the full number of fits allows for the determination of ν to the greatest possible precision. This is advantageous since this exponent is required for the determination of the infinite-volume critical temperature, as well as for the other exponents obtained from γ/ν, $(1-\beta)/\nu$ and β/ν. Nevertheless, we emphasize that taking into account all 28 fits brings about only a modest increase in precision, given that all fits are trivially correlated, as they stem from the same set of simulations.

For the regular lattice, discarding the smallest lattice size simulated, $L = 16$, we find 23 acceptable fits with goodness-of-fit values $Q \geq 0.2$. The residual plots for four of the curves

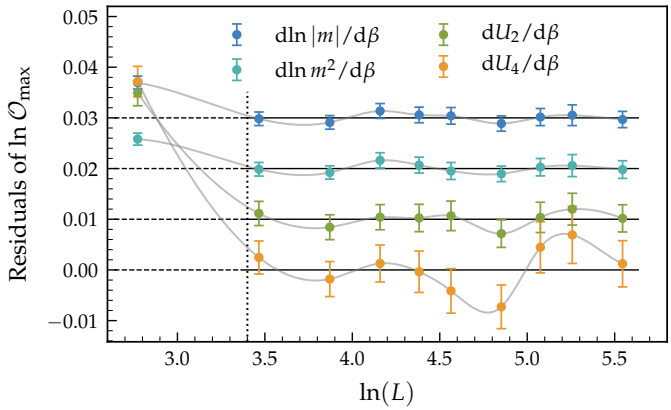

Figure 5.1 | Residuals for the exponent ν (Ising, regular). Shown are the residuals of 4 out of 28 fits, shifted vertically for convenience. The vertical dotted line separates the region that is excluded in the fits. The grey curves are guides to the eye.

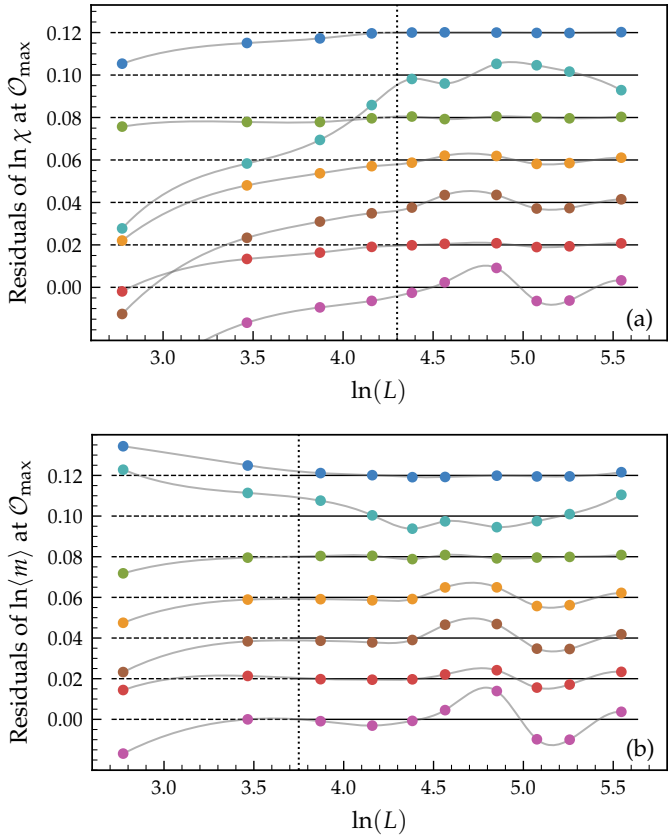

Figure 5.2 | Residuals for further exponents (Ising, regular.) Shown are the residuals for the fits of the exponents (a) γ/ν and (b) β/ν for the regular lattice. The single lines in each panel correspond to observables (4.16c) to (4.17e) from top to bottom and are shifted vertically for convenience. The vertical dotted line separates the region which is excluded from the fitting procedure and the grey curves are guides to the eye. Error bars are about the size of the markers in panel (a) and roughly two times as large in panel (b).

Table 5.1 | The seven single fits for β/ν for the two-dimensional Ising model on a regular square lattice using $L = 48$ to 256 (8 data points) as well as the average, obtained from the five values with $Q \geq 0.01$. Corresponding residuals are shown in Figure 5.2b.

β/ν	goodness-of-fit Q	at max of
0.1298 ± 0.0014	0.976	χ
0.1201 ± 0.0014	0.000	C
0.1201 ± 0.0013	0.986	$\mathrm{d}m/\mathrm{d}\beta$
0.1269 ± 0.0017	0.051	$\mathrm{d}\ln m/\mathrm{d}\beta$
0.1266 ± 0.0020	0.012	$\mathrm{d}\ln m^2/\mathrm{d}\beta$
0.1290 ± 0.0015	0.071	$\mathrm{d}U_2/\mathrm{d}\beta$
0.1343 ± 0.0021	0.000	$\mathrm{d}U_4/\mathrm{d}\beta$
0.1261 ± 0.0013	avg. $Q \geq 0.01$	

are shown in Figure 5.1. In order to obtain a final value for ν, we calculate the error-weighted average over all acceptable fits. Concerning the uncertainty, we quote the smallest error of the single fits included in the average, thus being quite conservative, as suggested in [58]. The final result is

$$\nu = 1.0000 \pm 0.0006 \quad (L_{\min} = 32), \tag{5.2}$$

which perfectly coincides with the analytically known value of $\nu = 1$. As a next step, making use of the relation (4.27) in combination with the pseudo-transition point sequences, the critical temperature β_c can be determined via infinite-volume extrapolation, where we fix $\nu = 1$. After averaging the individual β_c, we arrive at

$$\beta_c = 0.440688 \pm 0.000015 \quad (L_{\min} = 32), \tag{5.3}$$

where the reported uncertainty is the standard error of the average. This value is quite close to the exact critical temperature of $\beta_c = \ln(1 + \sqrt{2})/2 \approx 0.4406868$. The smallest lattice ($L = 16$) has again been discarded in all fits.

The exponent γ/ν is obtained from relation (4.24b). Here, we exclude all lattice sizes $L \leq 64$, since residual plots indicate (slight) systematic deviations up to that value. The weighted average of the three resulting fits with acceptable quality ($Q \geq 0.3$) yields $\gamma/\nu = 1.7516 \pm 0.0008$ ($L_{\min} = 80$) as the final result, which is compatible with the exact value of $7/4$. The residuals of all seven fits are shown in Figure 5.2a. The combinations $(1 - \beta)/\nu$ and β/ν are determined from fits to relations (4.24d) and (4.24a), respectively. For the former exponent, we find three fits with $Q \geq 0.2$, similar as for γ/ν, but the residual plots show no need to discard further data points. Our final value is thus given by the average $(1 - \beta)/\nu = 0.8747 \pm 0.0010$ ($L_{\min} = 64$), also compatible with the exact value of $7/8$. For β/ν, however, our data does not return a single acceptable fit – even when discarding half of the data points. A thorough analysis of the fit residuals shows no systematic corrections for $L > 32$, but reveals that the

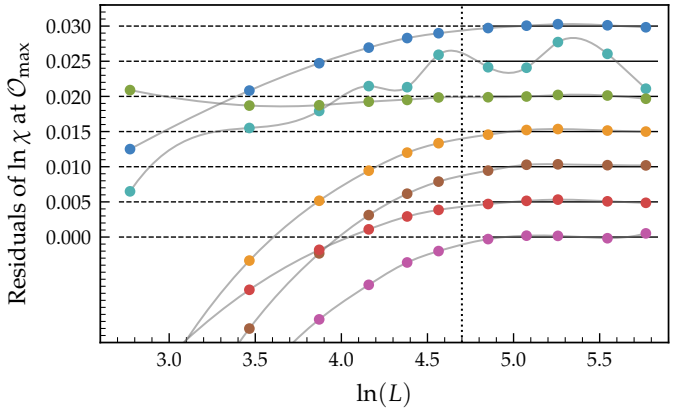

Figure 5.3 | Fit residuals for the exponent γ/ν (Ising, DT). The single lines correspond to observables (4.16c) to (4.17e) from top to bottom and are shifted for convenience. The dashed horizontal black lines show the region excluded in the fits. The grey curves are only guides to the eye. Error bars are smaller than the markers, except for the cyan curve (second from the top), where they are about three times as large as the marker. Only the green curve (third from the top) shows no systematic deviation and yields $\gamma/\nu = 1.7512(7)$, with a goodness-of-fit value $Q = 0.90$.

poor quality of the fits arises from the small uncertainties assigned to the values of $\langle m \rangle$. Indeed, the relative uncertainties are about half an order of magnitude smaller compared to, e. g. the last five observables of (4.24). If we increase the uncertainties of the data points by an *ad hoc* factor $f = 5$, then five out of seven fits turn out to be acceptable, with $Q \geq 0.01$, producing the reasonable final average of $\beta/\nu = 0.1261 \pm 0.0013$ ($L_{\min} = 48$). The full list of fits can be seen in Table 5.1 and the corresponding residual plot in Figure 5.2b. By calculating β/ν estimates for multiplication factors $f = 2$ to 8, we observe that the number of good fits increases with f, but the average β/ν fluctuates only in the last digit, consistently maintaining compatibility with the exact result $1/8$.

We note, regarding the fits for the three ratios γ/ν, $(1-\beta)/\nu$ and β/ν, that those fits which depend on the function values at the pseudo-critical points of either C, $\mathrm{d}\ln\langle m^2 \rangle/\mathrm{d}\beta$ or $\mathrm{d}U_4/\mathrm{d}\beta$ always present the lowest fit quality (i. e. large reduced χ^2). This is due to the fact that those three quantities have their maxima at a larger distance from the simulation temperature, compared to the remaining observables. Therefore, in order to obtain a larger number of acceptable fits and more accurate estimates for the critical exponents, multi-histogram reweighting methods (compare Section 4.1.5) would be necessary, which would however require at least a second set of simulations and therefore essentially double the computational effort.

Delaunay triangulation

As a second benchmark, and an analysis walkthrough for disordered models, we proceed with the Ising model on a two-dimensional Delaunay triangulation. Due to the spatial randomness, stronger corrections to scaling, compared to the regular case, are to be expected. For $L = 16$, $24, \ldots, 320$, we perform quenched replica averages over $N_r = 1000$ independent realizations of the DT construction. For the largest lattice considered, $L = 400$, only $N_r = 500$ realizations are simulated. Starting from a completely ordered configuration, we perform $4 \cdot 10^4$ EMCS to equilibrate the system, followed by $2 \cdot 10^6$ cluster updates. As for the regular case, one

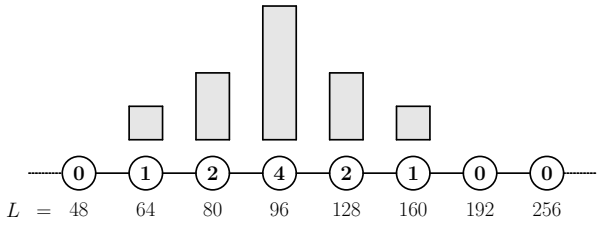

Figure 5.4 | Local fitting procedure. Schematic illustration for $L = 96$. Each circle symbolizes one lattice size L, whereas the numbers inside the circle are the corresponding weights.

EMCS consists of 25 cluster updates and one Metropolis sweep, independent of the lattice size. Physical observables are obtained by reweighting for each simulated replica individually – this amounts to one curve for each observable and each replica. After averaging the curves of the observables of all replicas, extremal points are determined using an iterative bisection method.

The statistical uncertainties of the replica-averaged observables are obtained from the standard error of the N_r different observable curves used to calculate the average. This error estimate contains both the uncertainty corresponding to the thermal fluctuations in each replica, as well as the fluctuations among different replicas, arising from the different disorder realizations. As the latter are effectively uncorrelated, standard and Jackknife error will give nearly identical results. Note however that we still use Jackknife resampling in order to reduce the bias of the individual curves. We perform linear fits to the scaling equations, as in the previous subsection, thereby ignoring any corrections to scaling. For each observable listed in Equations (4.24a) – (4.24h), we perform seven linear fits, each using a different estimate of the pseudo-critical temperature, as obtained from extremal points of the observables. Instead of adopting a fixed $L_{\min}$, as for the regular lattice, we employ a *local* fitting procedure in order to obtain an effective (i. e. running) exponent. More specifically, we perform the fitting over a window of five consecutive data points from the range $L \in \{16, 32, \ldots, 320, 400\}$, assigning weights that emphasize the central data point, as illustrated in Figure 5.4. This local fitting is necessary due to the rather strong systematic deviations from a pure power-law. The residuals of the fits for γ/ν, for instance, shown in Figure 5.3, clearly demonstrate that the data points systematically deviate from the horizontal.

The effective local exponents ν, γ/ν, $(1-\beta)/\nu$ and β/ν for the DT are shown in Figure 5.6 and listed in Table B.3, where we display the averages of the single fits in each individual fitting window. For the estimates of ν, we observe a very smooth curve, decreasing continuously as the fitting window is moved towards larger lattices. Therefore, we offer no final result for the exponent ν. Regarding the estimates at hand, we expect the effective exponent ν to tend to the exact value in the infinite-volume limit. For γ/ν, the situation is very similar. As in the case for ν, the individual estimates again exhibit a systematic downwards trend and we expect the exact value to be reached in the infinite-volume limit. For the critical exponent β, which can be estimated from the scaling of $[\langle m \rangle]_{\text{avg}}$ and $\mathrm{d}[\langle m \rangle]_{\text{avg}}/\mathrm{d}\beta$, the corresponding curves are also smooth and indicate a tendency towards the expected values in both cases. In particular, for β/ν the universal value of 0.125 is already reached within the error bars for smaller values of L.

Turning our attention to the critical temperature, linear fits according to Equation (4.27) reveal systematic deviations, even if many of the small lattice sizes are discarded, qualitatively similar to those observed for the exponents (compare Figure 5.3). Therefore, we decided to take into account higher order corrections in the finite-size scaling analysis in order to allow for a more precise estimate of β_c. Considering a first-order correction term, Equation (4.27) becomes

$$\beta_{c,i}^{L} = \beta_c + a_i L^{-\omega} + b_i L^{-\omega-1/\nu}, \tag{5.4}$$

where the indices indicate the dependence of the amplitudes on the chosen observable. As outlined in Section 2.4, on a square lattice with periodic boundary conditions, the leading correction-to-scaling exponent ω is expected to take on a value of exactly 2 due to the breaking of rotational invariance. For the strongly site-diluted Ising model, which is perhaps more directly comparable to the DT model, a value of $\omega = 0.63(20)$ has been found [333]. When fitting Equation (5.4) to our data, we can, in light of the results of Table B.3, set ν to unity, which reduces the number of fitting parameters to four. As the effects we are trying to detect are rather small, it is still challenging to obtain stable fits. For this reason, we perform a series of fits for different, fixed values of ω and hence obtain corresponding β_c estimates. We follow this procedure for the data for each of the seven observables, and then calculate the average as well as the standard deviation of β_c for each ω. In Figure 5.5, the estimate of β_c and its error (shaded region) is depicted together with the average reduced χ^2 as a function of fixed ω. It can be seen that the best fits are obtained for $\omega \lesssim 1$, coinciding with the most precise estimates of β_c as well. The best fit value is

$$\beta_c = 0.262904(9), \tag{5.5}$$

corresponding to $T_c = 3.80368(13)$, at a correction exponent of

$$\omega \approx 0.84. \tag{5.6}$$

To the best of our knowledge, this is so far the most precise value available for the critical coupling for the two-dimensional Ising model on a Delaunay lattice. Also our estimate for the correction exponent may be used for future reference, although we remark that the method we used does not allow to determine proper error bars for that quantity.

Constant Coordination lattice

We study CC lattices with coordination numbers $q = 4, 6$ and 10 (short: CC4, CC6, CC10), constructed from a Poissonian point cloud. For all three systems we use the same number of independent disorder realizations, measurements, equilibration steps and cluster updates as for the DT lattice. In this way, the results for the different models are of comparable precision. Also the estimates of the exponents are obtained following the same procedures described in the previous section. The results for the CC4, CC6 and CC10 models are presented in Figure 5.6, where we also added the DT exponents for comparison. A detailed list of the data points can also be found in Table B.3.

Recall that due to the nature of the CC construction, small isolated components may occur, in contrast to the DT, where the lattice always consists of one single component. In order to

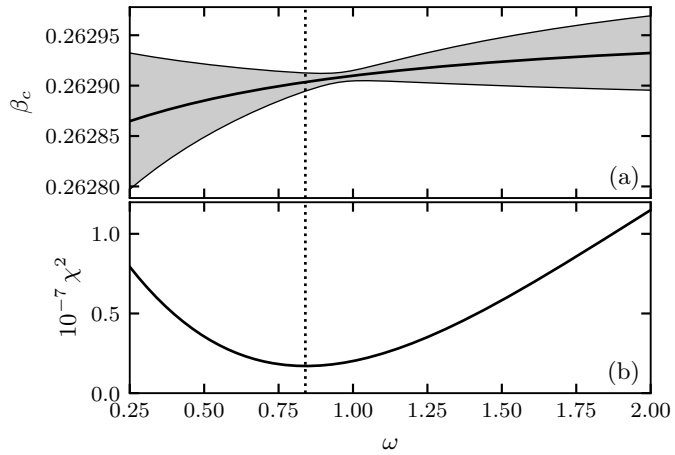

Figure 5.5 | Estimate of β_c and ω (Ising, VD). (a) Estimate of β_c and its error (shaded region) as a function of fixed ω. (b) Corresponding reduced χ^2-values, as described in the text. Employing different fitting algorithms generates qualitatively similar results, which are also insensitive to the choice of lattice size range.

properly update those islands, we employ an additional Metropolis step between measurements. Furthermore, we report results only for lattices of size $L = 16$ to $L = 320$, as for larger lattice sizes the construction already becomes as expensive as the actual Monte Carlo simulation.[35] Considering the fit results presented in Figure 5.6, we see similar tendencies as for the DT, however, with larger absolute deviations from the clean universal values. For the correlation length exponent ν, all CC models seem to show a systematic trend. However, the deviations become larger for smaller q. Compared to the DT, for $q = 10$ those deviations are roughly three times as large, and for $q = 6$ already about one order of magnitude larger. Considering also the fact that for $q = 6$ the error bars are only about twice as large as for DT, the results indicate that any possible convergence is significantly slower. A remarkably different situation arises for the susceptibility exponent γ/ν, where the effective exponents for all models seem to collapse. However, whereas the CC10 shows a clear trend of decreasing estimates, this behaviour becomes less distinct for $q = 6$, where the curves seem to saturate within the considered range of L. Eventually, for $q = 4$, almost all values are compatible with $7/4$, which may, however, be a consequence of the relatively large error bars.

As for ν, the exponent $(1 - \beta)/\nu$ is clearly different for CC and DT graphs. For the DT, a trend consistent with $(1 - \beta)/\nu = 0.875$ is evident. In contrast, the CC exponents are further away from the universal value and show no clear trend, with a possible exception of CC4, where the effective exponent appears to increase with L. Similar to ν, the absolute deviations for CC6 are already almost one order of magnitude larger than for the DT. Finally, the exponent β/ν shows a clear trend towards the universal value in the case of $q = 4$ and 6, with the last few data points being fully compatible with $1/8$. For $q = 10$, however, all estimates match the universal value, very similar to the DT model. For completeness, we state the critical temperatures for the constant coordination models which are roughly $\beta_c \approx 0.549$, 0.294 and 0.148 for CC4, CC6 and

[35] In this particular study, we used the original algorithm for constructing the CC lattice as presented in [P2], which, as pointed out in Appendix A.1, scales quadratically with the number of points and hence restricts the range of accessible lattice sizes heavily (compare also Section 3.3).

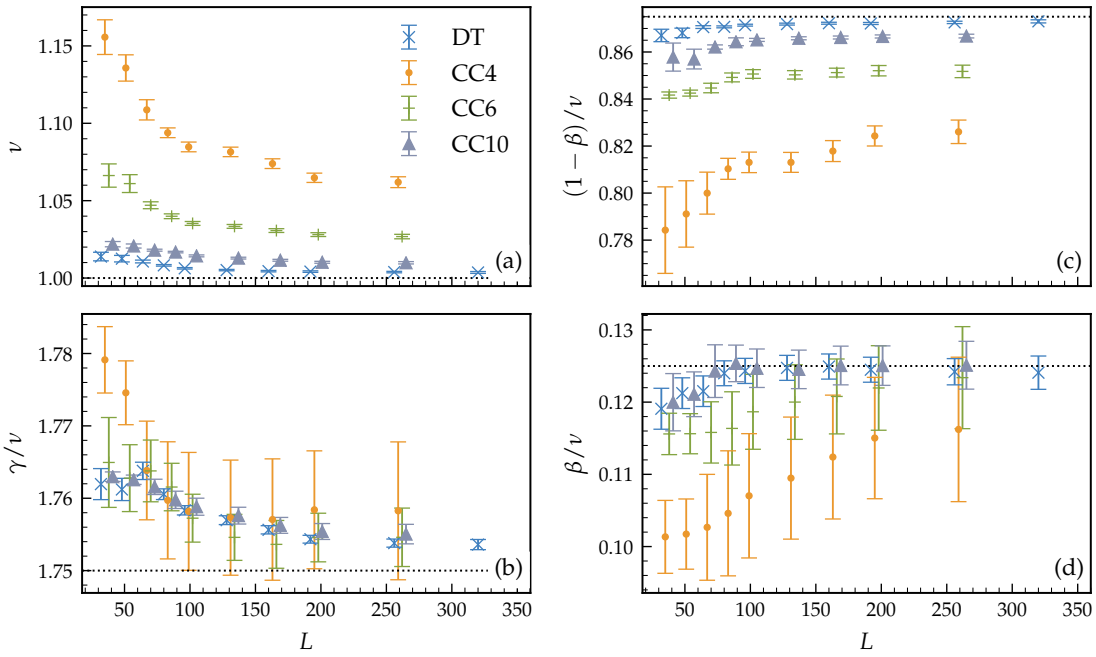

Figure 5.6 | Critical exponents (Ising, CC and DT). Comparison of critical exponent estimates for CC lattices with $q = 4, 6, 10$ and DT lattices, as a function of the lattice size, obtained through the local fitting procedure. Dashed horizontal lines indicate the clean universal values of the 2D Ising universality class.

CC10, respectively. A more precise determination is omitted, since these values depend on the fine-tuning of the CC algorithm and are therefore non-universal.

Discussion

In comparison with the Delaunay triangulation, the CC model for $q = 6$ has exponents ν and $(1-\beta)/\nu$ that show deviations from their respective universal values which are larger by about one order of magnitude (e. g. $\nu = 1.0042(5)$ for DT and $\nu = 1.0281(12)$ for CC6 at $L = 192$). Furthermore, for all CC models, the convergence of the effective exponents seems weaker or even doubtful, with the possible exception of β/ν, which has rather large relative errors. In the following, we want to understand our findings using a number of topological arguments. As pointed out in Section 2.5.4, for the DT lattice, the constrained total coordination number imposes strong anti-correlations in the local q fluctuations, which in turn are responsible for the fast decay of disorder under spatial renormalization-group-type blocking transformations (compared to, e. g. diluted lattices) and are thus asymptotically irrelevant. It was reasoned that this fast decay can be expressed in terms of a modified (so-called Harris-Barghathi-Vojta) criterion $a\nu > 1$ that explains the fact that, e. g. simulations of the contact process on those lattices show the clean universal exponents, although the classical Harris criterion $d\nu > 2$ is violated.

With the CC lattice, we constructed a lattice that provides random connectivity (and thus topological disorder)[36] and – as an obvious effect of the fixed local coordination number – no fluctuations in the original lattice or on any blocking level. Therefore, since the effective critical

[36] At this point, keep in mind that *random connectivity* does not imply a *random coordination number*.

Table 5.2 | Global geometric lattice properties. The disorder decay exponent a is defined by the relation $\sigma_Q \sim L_b^{-a}$, where σ_Q is defined according to Equation (2.94). The values marked with † have been calculated in Section 3.4, see Figure 3.11, the symbol ‡ refers to Figure 3.12 (upper panel). §: for the RGG and the symmetric qNN, no clear universal properties are expected, see text. $*$: negative correlations are present, but positive correlations are dominant, especially on the typical scale of one bond length, see Figure 3.12. We only consider two-dimensional structures in this table.

Geometry	a	Coordination number anti-correlation	Total coordination number constrained	Planar	Connected	clean 2D Ising universality	
DT	$3/2$	yes	yes	yes	yes	yes	[67]
VG	undef.	no	no	yes	yes	yes	[P4]
CC	undef.	no	yes	no	no	questionable	[P2]
GG	$1^\dagger$	no‡	no	yes	yes	yes	[260]
RNG	$1^\dagger$	yes‡	no	yes	yes	yes	[260]
BD	1	no	yes	yes	no	strong/weak	[185–200]
SD	$1^\dagger$	yes	no	yes	no	strong/weak	[185–200]
RGG	$1^\dagger$	no	no	no	no	unclear§	
qNNsym	$1^\dagger$	no*	no	no	no	unclear§	

exponents clearly deviate from the corresponding universal values, we are led to the conclusion that the scaling of coordination number fluctuations σ_Q under coarse-graining should not be the decisive property determining the nature of the phase transition. This conclusion is supported by recent results of Schawe et al. [260], where it is shown that the universality of the Ising model on two-dimensional Gabriel graphs (GG) and relative neighbourhood graphs (RNG) is unchanged and therefore belongs to the same class as the Ising model on a regular lattice. In Section 3.4, we performed the blocking analysis for these two types of proximity graphs and find that both of them unambiguously show a decay of $\sigma \propto L_b^{-1}$, hence $a = 1$. This means that disorder in these graphs decreases as slow as for generically disordered models. Hence, one would expect considerably strong (logarithmic) corrections to the clean scaling behaviour, which were not found by the authors in [260].

We collect several different disordered lattice models in Table 5.2, together with some relevant geometric properties and statements concerning the universality of the two-dimensional Ising model on each lattice. From the overview given in this table, we claim that the general statement of topological disorder being less relevant than generic disorder, as stated in [67], might be too general. However, the particular instances of lattices mentioned by the authors can indeed be expected to preserve the universal features of a transition, since they are all tilings. The key difference between tilings and lattices with bonds that may cross each other (like our CC model or the random geometric graph with fixed interaction radius) lies in the fact that for tilings, it is always ensured that there exists one single component containing all sites. We thus conclude that very clear universal properties (e. g. no strong logarithmic corrections) are obtained if the underlying lattice is both *planar and connected*. Note, in this context, that tilings are a special case of planar, connected graphs. Also, we remind that a graph is called planar if it *can be* embedded

in the plane such that there are no edge crossings. Whether a specific graph is planar or not can be checked according to Kuratowski's theorem [334], which can be implement efficiently on a computer [335]. Since RNG and GG possess these properties, this would explain the positive results observed in Reference [260].

Comparing the GG and the random geometric graph (RGG) in Table 5.2, it is clear that – apart from the RGG being neither planar nor connected – they show the same geometric characteristics. Following our line of argumentation, the Ising model on the RGG lattice is expected to have disorder dependent effective critical exponents, exactly as for the CC model. Some preliminary simulations with a short-ranged interaction radius of $R_{\langle q\rangle=6}$ (see Equation 3.4), not presented here, indeed seem to confirm this expectation. Similar holds for the symmetrized q-nearest neighbour graph, compare also Table 5.2. Moreover, a prominent and well-studied example of disordered lattices that are planar but not connected are the site- or bond-diluted regular lattices (compare Figure 3.3), also included in Table 5.2. They allow for isolated clusters and thus show a percolation transition, resulting in a multi-critical point in the temperature/dilution-strength phase diagram. The constant coordination model also allows for the occurrence of isolated islands. By employing a cluster counting procedure, we calculate the fraction $1 - p_{\mathrm{con}}$ of all sites on the CC lattices belonging to islands disconnected from the giant component.[37] For the CC4, we find $1 - p_{\mathrm{con}} \sim 10^{-3}$. As expected, this number decreases strongly as q is increased. For $q = 6$ we find $1 - p_{\mathrm{con}} \sim 10^{-6}$ and for $q = 10$ no small islands were detectable in all of the $N_r = 1000$ realizations of constant coordination lattices with $L = 320$, yielding $1 - p_{\mathrm{con}} < 10^{-7}$ as an upper bound.[38] Considering, in contrast, smaller values of q, say $q = 2$, the lattice would undergo a percolation transition, as in this case the formation of, e. g., triangles (3 sites, 3 links) is very likely and a giant component may not form at all in most realizations. It should be emphasized that the effect of the isolated islands on the measured observables might be negligible, since, even for CC4 lattices, such sites amount to only 0.1% of the total lattice sites. Furthermore, we ensured that isolated clusters are properly updated by local Metropolis updates, as explained above. By decreasing q below the percolation threshold, though, any collective long-range magnetic phase must inevitably be destroyed since the system is then decomposed into many disconnected finite clusters and no collective long-range behaviour can be maintained.

Reviewing the ample literature on the two-dimensional site- or bond-diluted Ising model, one indeed finds remarkable similarities to our results for the CC lattice. First of all, many numerical simulations seem to show exponents which are clearly non-universal and vary dramatically with dilution strength. Already in the 1990's, these numerical results, as well as field-theoretic calculations, led to a controversy that still persists, regarding the universal character of those models. According to the so-called *strong universality* hypothesis, disorder is marginally irrelevant, leading to clean exponents accompanied by logarithmic scaling corrections and, particularly remarkable, a specific heat diverging ultra-slowly in form of a double logarithm [185–189]. The *weak universality* scenario, in contrast, posits leading critical exponents that vary continuously with the strength of the dilution, but with some quotients of exponents,

[37] The following estimates again consider the original CC algorithm. For the improved algorithm, the occurrence of isolated components is even less likely, as pointed out in Section 3.3.5.

[38] Due to the constraint of fixed q, the smallest possible isolated component needs to contain at least 11 sites. Thus, if we had found one single realization in the 1000 lattice replicas, the fraction would have been calculated by $11/(1000 \cdot 320^2) \approx 10^{-7}$.

such as γ/ν and β/ν, remaining unchanged [190–195]. For a comprehensive historical review covering articles supporting either of the two scenarios, we refer the reader to [196]. Currently, the strong universality scenario is favoured, having been strengthened by recent numerical studies [197–199], with Zhu et al. effectively ruling out the weak scenario for their large-scale, high-accuracy results [200].

Comparing our results with those from the aforementioned studies of dilute models, we recognize a number of similarities. In particular, the effective exponents ν and $(1-\beta)/\nu$ change continuously with the lattice parameter q, whereas γ/ν varies only slightly among the models and β/ν is already compatible with the universal value for all choices of q. Given these similarities, the question arises whether topological disorder in the CC model is also marginally irrelevant and logarithmic corrections arise (i. e., strong universality) or whether one is facing continuously varying leading critical exponents (as proposed by the weak universality hypothesis). As both scenarios predict unchanged values for the ratios γ/ν and β/ν, they both can not be used for a distinction. The specific heat, in contrast, shows a different scaling behaviour already in the leading order. For the strong scenario, a double-logarithmic scaling

$$C = a\ln(b\ln(cL)), \tag{5.7}$$

with constants a, b, c, can be expected [336–338], whereas weak universality predicts a power-law scaling

$$C = C_0 + aL^{\alpha/\nu}, \tag{5.8}$$

with negative exponent and regular background C_0. In order to investigate the origin of the deviations from clean universality in our models, we fit the finite-size data of the specific heat to both ansätze (5.7) and (5.8), summing up to seven fits each (corresponding to the peak locations of the scaling functions). Remarkably, both scenarios fit the data equally well. Even when including the smallest lattice size, $L = 16$, we find reduced χ^2-values between 0.5 and 3 for all seven fits for both scenarios. However, as the leading scaling behaviour is only valid for large L, we discard the smallest lattice size which again significantly increases the quality of most fits. Specifically, for the strong universality scenario, we then find 5 out of 7 fits with χ^2/d.o.f in the range 0.1 to 0.2. Furthermore, if further lattice points are discarded, all fits appear very stable. For the power-law scenario, Equation (5.8), after discarding $L = 16$, we also find 5 out of 7 fits with very good quality (see Table 5.3). Moreover, the fits are again numerically very stable and their quality (in terms of χ^2) as well as the fitted parameters $\alpha/\nu, a$ and C_0 show no systematic trend if further lattices are discarded. As can be seen in Table 5.3, all seven fits consistently yield a small negative exponent α/ν. Performing a simple average with standard error, we obtain an exponent ratio of $\alpha/\nu = -0.048(12)$ for the CC6 model. Using the hyperscaling relation $2 - \alpha = d\nu$, this yields a correlation length exponent of $\nu = 1.025(6)$, which is, rather remarkably, compatible with the effective exponent ν we obtained earlier for the largest lattices available (see also top left panel of Figure 5.6). In light of these findings, one may speculate about whether the two-dimensional Ising model on the CC lattice is situated in a weakly universal scenario with q-dependent leading exponents. The exponents ν and $(1-\beta)/\nu$ in Figure 5.6 would thus not tend towards the respective clean universal value. However, it should be emphasized again that also the logarithmic corrections fit the data well. Therefore,

Table 5.3 | Single fits for the specific heat finite-size data to Equation (5.8) for the CC6 lattice with the linear lattice size ranging from 32 to 320 (10 data points).

α/ν	C_0	a	χ^2/d.o.f	at max of
-0.026	13.58	-13.21	0.11	χ
-0.040	9.78	-9.42	1.95	C
-0.052	8.00	-7.70	1.20	$\mathrm{d}m/\mathrm{d}\beta$
-0.059	7.20	-7.14	0.07	$\mathrm{d}\ln m/\mathrm{d}\beta$
-0.066	6.61	-6.66	0.10	$\mathrm{d}\ln m^2/\mathrm{d}\beta$
-0.043	9.06	-8.84	0.08	$\mathrm{d}U_2/\mathrm{d}\beta$
-0.050	8.07	-8.04	0.21	$\mathrm{d}U_4/\mathrm{d}\beta$

based on the data at hand, we can not ultimately decide on either scenario.

5.2 Continuous transitions on Voronoi graphs

The literature on critical phenomena under quenched topological disorder has so far neglected Voronoi graphs, focusing instead on lattices such as its dual, the Delaunay triangulation. In order to correct for this omission, we conduct large-scale numerical simulations of the classical Ising model, the contact process (CP) and the conserved stochastic sandpile model (CSSM) on two-dimensional VGs constructed from randomly distributed sites. In particular, we compute the critical points for all three models to considerable precision, allowing them to be used as reference values. For the Ising model, also the first correction-to-scaling exponent is obtained to considerable precision. The VG is introduced in Section 3.2 and features a constant coordination number of the nodes, $q_i = 3$. Hence due to the lack of coordination number fluctuations, it represents a valuable new puzzle piece for finding a complete criterion for the influence of topological disorder on continuous phase transitions.

Ising class

For the simulation and analysis of the Ising model on two-dimensional Voronoi graphs, we use the method of finite-size data collapses, which provides a convenient way of verifying the universality of a given model. Furthermore, in order to obtain the correction exponent ω, we employ the quotient method. Both techniques are described in Section 4.1.3. For the quotient method, we determine the crossing points of the correlation length in units of the system size, ξ/L, using histogram reweighting techniques to high precision. The reweighting procedure is performed for every disorder replica individually and the curves are averaged afterwards. Up to 10^5 disorder realizations are used for the smallest lattices and at least 4000 replicas for the largest ones. Every replica is initially prepared in a hot spin configuration and is thermalized using 1000 elementary Monte Carlo steps. We check for a proper thermalization by also performing simulations starting from a cold configuration, which gives identical results within numerical precision. In our update procedure, one EMCS consists of a full Metropolis lattice sweep and

Table 5.4 | Results of the simultaneous fits according to Equation (5.9).

$L_{\min}$	$(\xi/L)^*$	U_4^*	U_6^*	ω	χ^2/d.o.f
16	0.9078(2)	0.61067(2)	1.4563(2)	1.36(2)	12.6
18	0.9070(2)	0.61066(2)	1.4564(2)	1.43(2)	7.2
20	0.9066(3)	0.61066(2)	1.4564(2)	1.47(3)	5.8
24	0.9062(3)	0.61065(2)	1.4564(2)	1.53(4)	5.0
32	0.9058(3)	0.61065(3)	1.4563(2)	1.59(7)	4.7
40	0.9060(5)	0.61067(4)	1.4561(3)	1.50(12)	4.1
48	0.9063(7)	0.61069(5)	1.4559(4)	1.37(18)	4.5

several single-cluster updates. Since the average cluster size in a d-dimensional system at criticality scales as $L^{d-\gamma/\nu}$, we increase the number of cluster updates with lattice size according to $L^{0.25}$ in order to keep the fraction of flipped spins approximately independent of the lattice size [58]. A detailed list of replica configurations and cluster steps can be found in Table B.1.

In order to obtain the fixed point phenomenological couplings and the correction exponent, we perform simultaneous fits of the relation

$$R|_{Q_\xi = s} = R^* + a_R L^{-\omega}, \tag{5.9}$$

for all three phenomenological couplings $R \in \{\xi/L, U_4, U_6\}$ with joint ω and for different $L_{\min}$, i. e., discarding the smallest lattices in the fits. As the quotients $Q_O = O(sL, T)/O(L, T)$ are naturally correlated in pairs $(L, 2L)$, we implement a fitting procedure that optimizes a generalized χ^2, including the full self-covariance information, as described in Section 4.2. Uncertainties for the fit parameters are obtained by a comprehensive bootstrap resampling procedure of the full data set. The results are shown in Table 5.4. As $L_{\min}$ is increased, the fit results show slight systematic trends, caused by higher-order corrections. Above $L_{\min} \approx 24$ the values saturate and the χ^2/d.o.f of the fit does not improve further. We therefore use, as our final estimates, the averages for $L_{\min} = 24, 32, 40$ and adopt a rather conservative uncertainty which includes the fluctuations among the single estimates as well as their individual uncertainties. This yields, as our final results

$$\omega = 1.54(16) \tag{5.10}$$

and

$$(\xi/L)^* = 0.9060(5), \tag{5.11a}$$
$$U_4^* = 0.61066(3), \tag{5.11b}$$
$$U_6^* = 1.4563(5). \tag{5.11c}$$

Comparing our estimates for the critical couplings with reference values of the Ising model on a regular square lattice, which are known exactly, up to small uncertainties from numerical

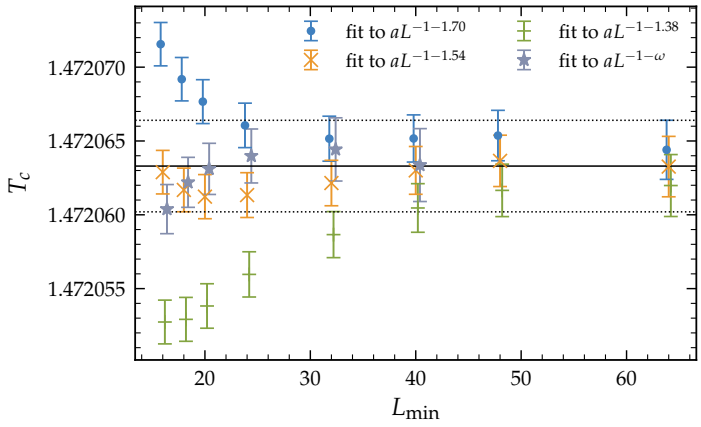

Figure 5.7 | Critical temperature (Ising, VG). Estimates for T_c from fits to Equation (5.12). Some results are slightly shifted along the x-axis to make them better visible. The horizontal lines correspond to the final estimate $T_c = 1.4720633(31)$.

integration, namely $(\xi/L)^* = 0.90505\ldots$, $U_4^* = 0.61069\ldots$, $U_6^* = 1.45565\ldots$ [154, 339], we find that even though these quantities are only considered universal in a limited sense (they weakly depend on certain geometrical characteristics of the system [310–312]) they compare remarkably well, giving a first indication that the Ising model on a VG stays in the universality class of the clean model. Also our result for the correction exponent is noticeably smaller than the reference value on a square lattice, $\omega = 2$ [340], though not particularly small in absolute numbers, which explains why corrections to scaling turn out to be relatively weak in the scaling collapses described below.

Essential for computing scaling collapses is a precise knowledge of the location of the critical point, which depends on the details of the lattice structure and is therefore in general not known in advance. In the framework of quotient-FSS, the critical temperature can be obtained using infinite-volume extrapolations, as the crossing points are expected to scale, according to [270], as

$$T|_{Q_\xi = s} = T_c + aL^{-\omega - 1/\nu}, \tag{5.12}$$

where higher-order terms have been neglected as in Equation (5.9), and we adopt the clean exponent $\nu = 1$. We perform four series of fits, where in the first three the correction exponent is fixed to our previous estimate (5.10), plus and minus its uncertainty, i. e., $\omega = 1.38, 1.54, 1.70$. In the last series of fits, ω is a treated as a free parameter. The results are displayed in Figure 5.7 and listed in detail in Appendix B, including χ^2/d.o.f values. It can be seen that for $L_{\text{min}} \gtrsim 40$ all four fits are compatible within their error bars. As our final estimate, we take the average of the fixed-ω fits for $L_{\text{min}} = 64$, obtaining

$$T_c = 1.4720633(31). \tag{5.13}$$

In the next step of the analysis we simulate the Ising model on Voronoi graphs of linear size $L = 24, 32, \ldots, 384$ for several temperatures in the vicinity of the critical point, using at least 1000 disorder replicas for every lattice size and temperature. Similar to the precision

simulations directly at criticality reported above, we start from cold configurations and perform 2500 measurements after a thermalization time of 500 EMCS. The number of cluster updates per EMCS is reduced by about a factor of five with respect to the values reported in Table B.1.

Finite-size scaling theory predicts that magnetization, susceptibility and Binder ratio scale according to

$$[\langle m \rangle]_{\text{avg}} = L^{-\beta/\nu} f_m(x)(1 + \cdots), \tag{5.14a}$$

$$\chi = L^{\gamma/\nu} f_\chi(x)(1 + \cdots), \tag{5.14b}$$

$$U_4 = f_{U_4}(x)(1 + \cdots), \tag{5.14c}$$

where β, γ and ν are critical exponents of the model and the universal scaling functions f have the argument

$$x = (T - T_c)L^{1/\nu}. \tag{5.15}$$

As detailed earlier, these equations describe the scaling behaviour to first order. Corrections of higher order are expected to become irrelevant for large system sizes. In Figure 5.8, we show the scaling collapse plots, fixing all critical exponents to their exactly known values ($\nu = 1$, $\beta = 1/8$, $\gamma = 7/4$) and T_c to the estimate (5.13). Evidently, a flawless collapse for all three scaling functions is obtained even for small lattices, which shows that the Ising model on a two-dimensional random Voronoi graphs belongs to the universality class of the clean Ising model.

Directed percolation

In order to show that the directed percolation universality class retains its clean universal behaviour on a Voronoi graph, we conduct numerical simulations of the contact process as described in Section 4.3. As a first step, from seed simulations, we determine the critical point, by rescaling the cluster size and survival probability according to their expected power law behaviour $N_a(t) \sim t^\theta$ and $P(t) \sim t^{-\delta}$, where θ and δ denote critical exponents. In total, we use 75 000 independent disorder realizations of linear size $L = 2048$ with periodic boundary conditions and perform 10 000 seed runs on each of them. Using reference values from Dickman [341], $\theta = 0.2293(4)$ and $\delta = 0.4523(10)$, we obtain the critical probability

$$p_c = 0.649788(1) \tag{5.16}$$

by determining the asymptotically constant curve, as shown in Figure 5.9. The uncertainty is obtained from curves which noticeably bend away from horizontal behaviour. Note that using larger lattices and longer simulation times would not significantly increase the precision of this estimate, as the analysis is limited by the uncertainties of the reference values.

Once the critical probability is known, we perform decay simulations starting from an initially fully occupied lattice for different system sizes precisely at criticality and monitor the density $\rho(t)$ of active sites until the system reaches the absorbing state. This allows us to obtain the

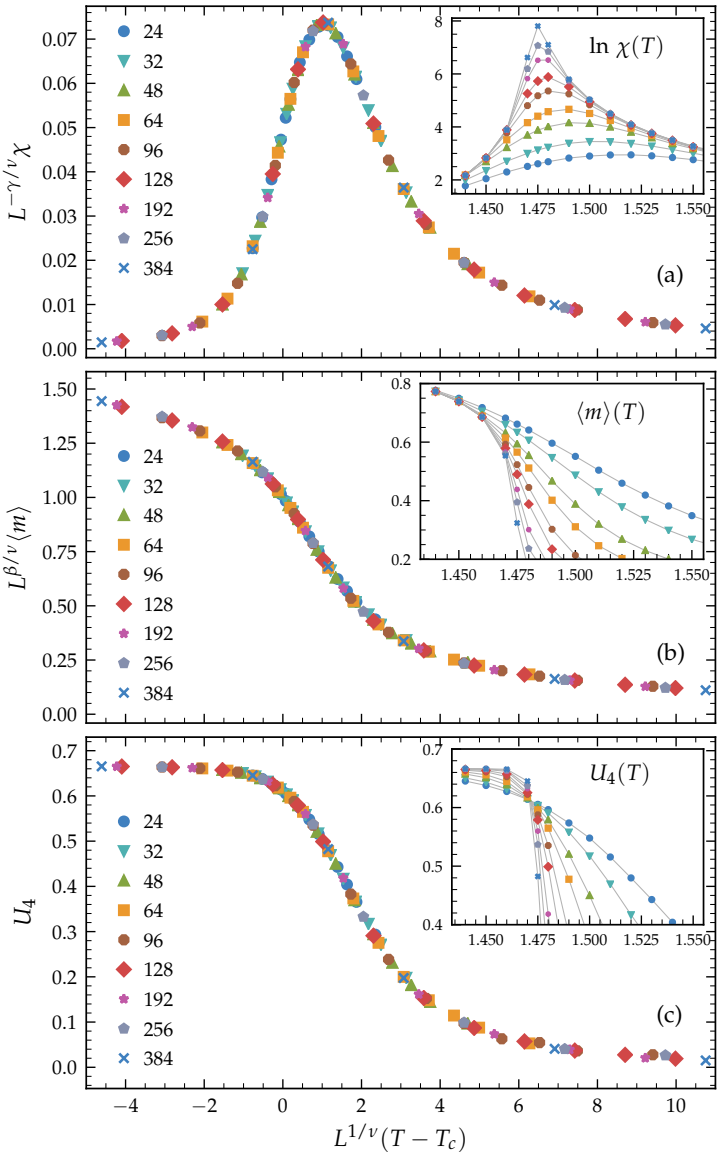

Figure 5.8 | Scaling collapse (Ising, VG). Shown are the scaling function of Equation (5.14). The insets display the non-rescaled observables. The gray lines are only guides to the eye. All three panels share the same x–axis.

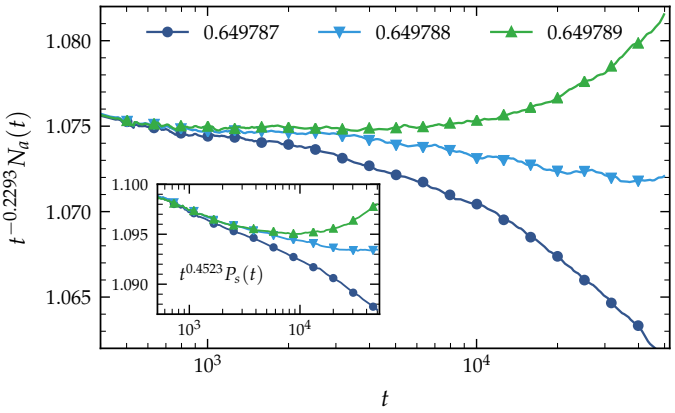

Figure 5.9 | Determination of the critical point (CP, VG). Size of the active cluster for different probabilities p in seed simulations of the CP close to the critical point, rescaled by the expected universal scaling law, $N_a(t) \sim t^{\theta}$. The inset shows the survival probability of the process, rescaled according to $P(t) \sim t^{-\delta}$. For the critical exponents, reference values from [341] were used.

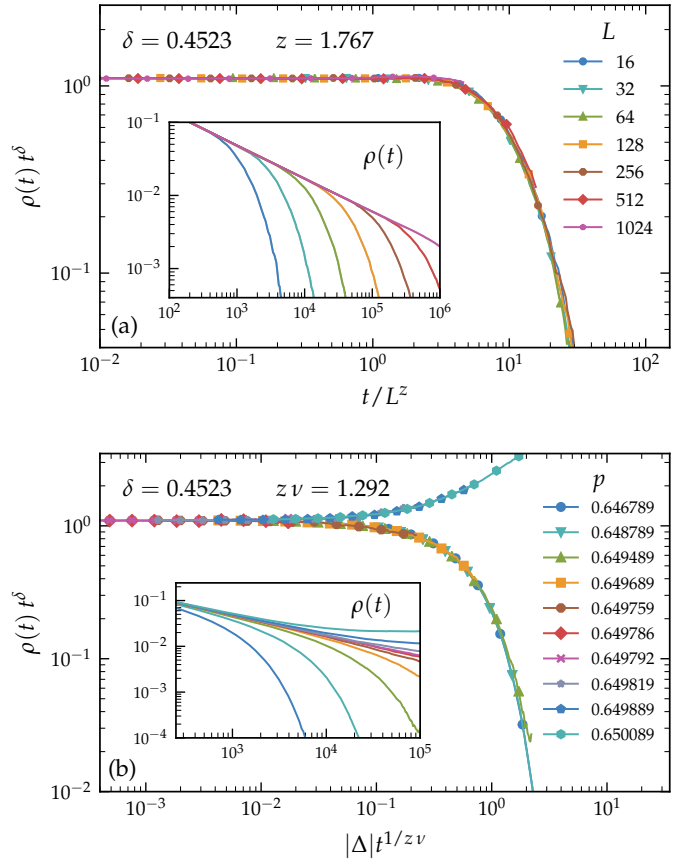

Figure 5.10 | Scaling collapses (CP, VG). (a) Finite-size collapse of simulations starting from a fully occupied lattice at the critical point $p_c = 0.649788$. (b) Data collapse in the off-critical region. The critical exponent estimates are given in the respective panels and the insets show the non-rescaled density as a function of time.

exponents δ and z via a data collapse according to

$$\rho(L,t) = t^{-\delta}\tilde{\rho}\left(t/L^{z}\right), \tag{5.17}$$

where $\tilde{\rho}$ denotes a universal scaling function. In a second set of simulations, we perform decay runs for lattices of fixed size $L = 1024$ in the vicinity of the critical point, which gives us the exponents δ and $\nu_{\parallel} = z\nu$ by means of the relation

$$\rho(\Delta,t) = t^{-\delta}\hat{\rho}\left(\Delta t^{1/\nu_{\parallel}}\right), \tag{5.18}$$

where we remind that $\Delta = p - p_c$ is the distance from criticality and $\hat{\rho}$ a scaling function. Both scaling collapses, which turn out flawless, are shown in Figure 5.10, where we used the reference values, $\delta = 0.4523(10)$, $z = 1.7674(6)$ and $\nu_{\parallel} = 1.292(4)$ from Reference [341]. In the top panel, all curves are averages over 1400 disorder realizations with 5 runs per realization, whereas in the bottom panel we used 250 disorder replicas and 5 runs per realization. The insets show the respective non-rescaled density as a function of time. This confirms the critical exponent values used and provides compelling evidence that CP on the random VG belongs to the clean DP universality class.

Manna class

In this section, we study the conserved stochastic sandpile model, belonging to the Manna universality class, on a two-dimensional Voronoi graph. In the CSSM, each site can contain an unlimited number of particles $n = 0, 1, 2, \ldots$. As long as n is below a threshold value of $N_c = 2$, the site is considered *inactive*, whereas it is *active* if $n \geq N_c$. The dynamics consists of toppling events where a random active site sends all of its particles to randomly chosen neighbouring sites. As detailed in Section 2.3, the CSSM exhibits a non-equilibrium phase transition into infinitely many absorbing states (in the infinite-volume limit), controlled by the density of particles $p = N_p/L^d$, where N_p denotes the total number of particles in the system. In the infinite-volume limit, if $p > p_c$, the system maintains a state of steady activity, whereas for $p < p_c$ an absorbing configuration is reached eventually.

For lattice models in the Manna universality class, it has been shown that the choice of initial conditions can have crucial influence on the critical behaviour. For instance, correct exponents for the conserved lattice gas (CLG) models are only obtained using so-called natural initial states (NIS), rather than random initial states (RIS) [342]. Furthermore, an argument raised in Reference [343], according to which the Manna critical behaviour would eventually cross over to DP universality for large times, was substantially weakened by Lee [344, 345] using MC simulations with carefully prepared initial states. The debate could finally be settled, as Dickman and da Cunha [346] showed that disorder fluctuations generated by the CSSM dynamics itself would in fact alter a DP transition, independent of the choice of initial conditions.

In this work, we perform quasi-stationary (QS) simulations of the CSSM, which should avoid ambiguities related to initial conditions altogether. For details on the method, see Section 4.3.1. We start from a RIS, where $N_p = pL^2$ particles are randomly distributed on the lattice sites. Note that in principle p can only be tuned in steps of $1/L^2$. However, we are able to realize intermediate values of p by employing a stochastic linear interpolation using the disorder

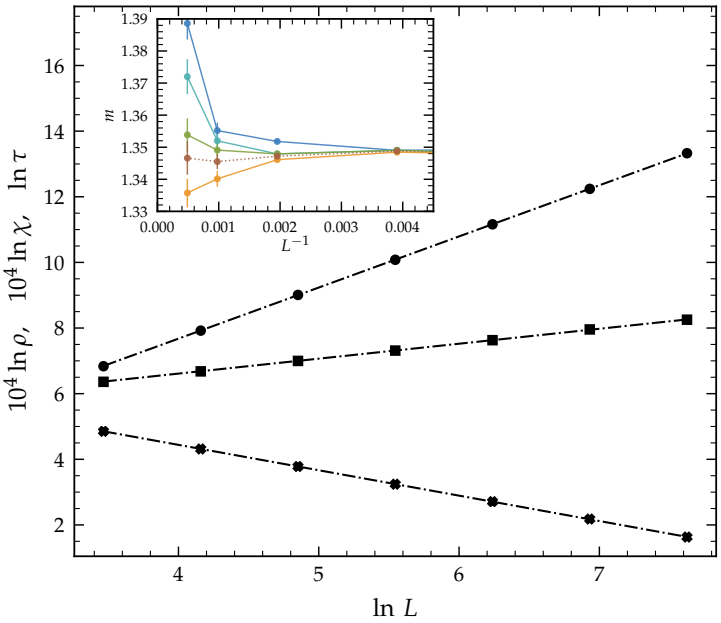

Figure 5.11 | Critical conserved Manna model on a VG. The curves represent fits of the lifetime (circles), susceptibility (squares) and density of active sites (stars). The inset shows the moment ratio against the inverse lattice size for $p = 0.721886$, 0.721889, 0.721892, 0.721893, 0.721895, from top to bottom. The curve for $p = 0.721893$ (dashed) represents our estimate of the critical point and is interpolated linearly from its two adjacent curves. The data points connected by solid lines represent actual measurements.

replicas.[39] In each time step, an active site is chosen and sends each of its particles to randomly selected neighbouring sites. The time is incremented by $1/N_a$, where N_a is the number of active sites prior to the update. During the run, a history, a list of M system configurations, is saved and periodically updated. Every time the process reaches an absorbing state, it is reset to a random configuration from its history. In order to ensure that the quasi-stationary state does not suffer from vestiges of the initial configuration, we run the evolution for a considerably long time of $T = 10^9$ units and take measurements after the first $6 \cdot 10^8$ time units. The measured quantities are the density of active sites ρ, and the lifetime of the QS state, τ. The latter is given by the average time between two successive visits to absorbing configurations. We employ large lattice sizes up to $L = 2048$ in order to reduce corrections due to sub-leading finite-size terms. For the history update probability per unit time, we use $p_r \approx 0.1/L^z$, where z is the dynamic exponent of the system. This ensures that the average residence time of a configuration in the history is larger than τ but much smaller than the total duration T of the run. Detailed simulation parameters are listed in Table 5.5.

In the framework of QS simulations, a reliable method to obtain an accurate estimate for the

[39] Consider a two-dimensional lattice of linear size $L = 10$. Due to the number of initially placed particles necessarily being integers, p can only be varied in steps of $\Delta p = 1/L^2 = 0.01$. Now say we want to realize a density given by $p = 0.7078$. First we distribute floor(pL^2) particles on the lattice. Then, a random number in the range $[0, 1)$ is drawn and compared to $\bar{p} \equiv \mod(pL^2, 1)$. If $p > \bar{p}$, one additional particle is added. Repeating this procedure for every disorder realization we end up with, on average, pL^2 particles.

Table 5.5 | QS simulation parameters for the CSSM model. N_r denotes the number of independent disorder realizations, M is the size of the history and p_r the associated update probability. For the QS lifetime we used a separate history list, containing 5000 slots, independent of L. During the first 10^8 time units a larger p_r (by a factor of ten) is adopted in order to efficiently erase initial states from the history.

L	N_r	M	$p_r \cdot 10^3$
32	400	4000	0.55
64	400	4000	0.20
128	400	2000	0.069
256	400	800	0.024
512	400	400	0.009
1024	192	100	0.003
2048	64	50	0.001

critical point is to consider the ratio

$$m = \left[\langle\rho^2\rangle / \langle\rho\rangle^2\right]_{\text{avg}}, \tag{5.19}$$

which is known to intersect at p_c for different L. In the inset of Figure 5.11, we show m for several probabilities close to criticality. Using linear interpolation in order to estimate the horizontal curve, we obtain

$$p_c = 0.721893(2) \tag{5.20}$$

for the critical point at an amplitude of $m_c = 1.35(1)$, which is compatible with the value on a square lattice $m_c = 1.348(7)$ [66]. Once the critical point is known, we are able to compute exponents from fits to the QS density

$$\rho_{\text{QS}} \equiv [\langle\rho\rangle]_{\text{avg}} \sim L^{-\beta/\nu}, \tag{5.21}$$

the average lifetime of the QS state

$$\tau \equiv [\langle\tau\rangle]_{\text{avg}} \sim L^{z}, \tag{5.22}$$

and the susceptibility

$$\chi \equiv L^d \left[\langle\rho^2\rangle - \langle\rho\rangle^2\right]_{\text{avg}} \sim L^{\gamma/\nu}, \tag{5.23}$$

directly at criticality. We perform fits for these three equations, shown in Figure 5.11, and present the corresponding results for the critical exponents in Table 5.6. The uncertainties of the estimates mostly stem from the uncertainty of the critical point, but also include the variation due to the exclusion of some of the data points. The latter variation turns out to be very small and, significantly, there is no systematic trend visible when discarding points corresponding to

Table 5.6 | Critical exponent estimates and reference values (Manna, VG). Estimates from numerical Monte-Carlo simulations of conserved lattice models belonging to the two-dimensional Manna universality class. The results of Lee correspond to the CSSM and the conserved lattice gas (CLG). Apart from Oliveira [66], which performed their simulations on a Delaunay triangulation, all simulations used a square lattice. When no direct measurement of γ was available, we employed the relation $\gamma = d\nu - 2\beta$ [5].

	β/ν	γ/ν	z
Dickman et al. [347]	0.774(3)	0.452(6)	1.572(7)
Lübeck et al. [317, 348]	0.80(3)	0.459(25)	1.533(24)
da Cunha et al. [349]	0.78(1)	0.44(2)	1.510(6)
Lee [342] (CSSM)	0.785(9)	0.430(18)	1.54(2)
Lee [342] (CLG)	0.781(8)	0.438(16)	1.53(1)
Oliveira et al. [66]	0.78(1)	0.44(2)	1.54(2)
this work	0.773(8)	0.456(3)	1.558(23)

even smaller lattices from the fits. Comparing our estimates with reference values from several authors also listed in Table 5.6, we find them to be clearly compatible, hence strongly indicating that the CSSM on the VG belongs to the clean Manna universality class.

Discussion

Summing up, critical phenomena on Voronoi graphs have, to the best of our knowledge, not yet been investigated, focusing instead on lattices such as its dual, the Delaunay triangulation. In order to correct for this omission, we conducted large-scale numerical simulations of the classical Ising model, the contact process and the conserved Manna sandpile model on two-dimensional VGs constructed from randomly distributed sites. We establish reference values for the critical points of the three models and, for the Ising model, also obtain the first correction-to-scaling exponent. Furthermore, using finite-size scaling techniques, we show that all systems display clean universal exponents at criticality, i. e., we reveal that the VG disorder is – in the sense of the RG – an irrelevant perturbation to their phase transitions. Although we only analysed three particular models, this result has implications for other classes of transitions as well. From the RG perspective, the correlation length exponent ν is directly related to the relevance of quenched disorder [46, 67–69, 175, 176]. Hence, the phase transition of, for instance, regular (isotropic) percolation can be predicted to also remain unchanged on a Voronoi graph, since its exponent, $\nu = 4/3$, is larger than for the models considered in this thesis. Moreover, our results are especially relevant for the search for a general disorder relevance criterion. The Voronoi graph has constant coordination number, similar to the CC lattice. In studies of both the Ising and DP phase transition on the CC lattice (also performed in this work), we find disorder to be probably marginal in the Ising case and clearly *relevant* for the DP universality class. The contrast of this result with the *irrelevance* of the VG disorder gives another indication that the absence of coordination number fluctuations is non-predictive of disorder relevance.

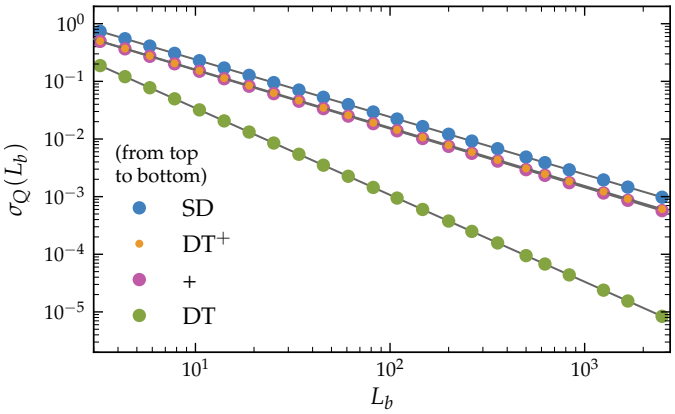

Figure 5.12 | Coordination number fluctuations on different length scales for DT$^+$, ordinary DT, the set of additional bonds that distinguishes both (+), and a site-diluted square lattice (SD). The curves are found to decay with a power of $a = 3/2$ for the DT, and with $a = 1$ for the other structures. For the analysis, 100 independent realizations of size $L = 5000$ have been used for each lattice. Note that the data points for DT$^+$ and (+) almost coincide.

5.3 Violation of the HBV criterion

In this section, we present a specific combination of a physical model and a randomly disordered lattice, which violates the Harris-Barghathi-Vojta (HBV) criterion, discussed in Section 2.5.4. Specifically, we use the DT$^+$ lattice[40], as introduced in Section 3.2: a Delaunay triangulation of a two-dimensional Poissonian point cloud, furnished with additional local bonds, compare Figure 3.2. This lattice is constructed from a Delaunay triangulation of N sites, to which kN bonds between next–nearest neighbours are randomly added (we select $k = 1$). Since from geometrical constraints, any triangular lattice with N vertices on a torus has exactly $6N$ bonds [67], this results in a lattice with a total coordination number of exactly $(6 + 2k)N$. This latter constraint is relevant for the applicability of the HBV criterion (compare Section 2.5.4).

We find the disorder decay exponent for the DT$^+$ to be $a = 1$, as can be seen in Figure 5.12. This naturally follows from the additional bonds being a source of uncorrelated disorder, which decays more slowly than the coordination number fluctuations of the original DT lattice (compare also Section 3.4). This interpretation is corroborated by the measurement of $\sigma_Q(L_b)$ for the additional bonds alone: as can be seen in Figure 5.12, both curves are almost identical, demonstrating the dominance of the additional bonds. The HBV criterion therefore predicts that our construction should not display clean universal behaviour for any universality class with spatial correlation length exponent $\nu < 1$, such as DP, where $\nu = 0.733\ldots$ [341]. In order to verify this prediction, we perform extensive numerical simulations of the two-dimensional contact process on the DT$^+$ lattice. However, as detailed in the following, we find strong indication of clean universal behaviour, thus contradicting the HBV prediction.

As a first step, the critical point p_c that separates the absorbing (subcritical) and active (supercritical) phase is determined. To this end, we conduct simulations starting from a single active seed on an otherwise empty DT$^+$ lattice of size $L = 6000$, allowing for times up to $T = 10^5$. Unwanted finite size effects are avoided by ensuring that cluster diameters remain

[40] In the original publication [P1], the structure was called VD$^+$.

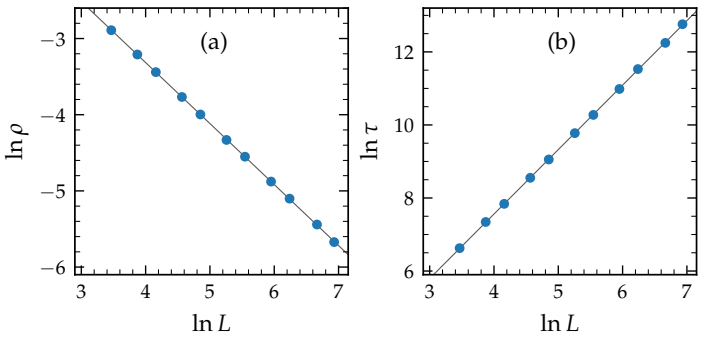

Figure 5.13 | Static exponents (CP, DT$^+$). Quasi-stationary density (a) and lifetime (b) as a function of the lattice size L, ranging from 32 to 1024. The slope of $\ln \rho$ yields β/ν, whereas $\ln \tau$ yields z. The dots represent averages over 320 independent disorder realizations. The error bars are smaller than the symbol sizes.

smaller than L. We use 2000 independent disorder realizations with 2000 runs each. For

$$p_c = 0.589775(3) \tag{5.24}$$

we find that the average cluster size follows a power-law behaviour, $N_a(t) \sim t^\theta$, as expected in the case of clean universality. The uncertainty of the critical point is estimated from simulations at probabilities close to the estimated critical point, such that the corresponding time evolution barely, but noticeably bends away from a straight line in a double-logarithmic plot. A linear fit in the region $10^3 < t < 10^5$ yields an exponent $\theta = 0.230(9)$, where the error stems from the uncertainty of the critical point, a result compatible with the reference value $\theta = 0.2293(4)$ of the clean DP class [341].

Once the critical point is known, we can obtain the quasi-stationary (QS) density ρ, as well as the average lifetime of the quasi-stationary state τ directly at p_c. For details on the method, see Section 4.3.1. As emphasized in [350], very long simulation times are required to reliably detect a deviation from the universal behaviour. We therefore use 320 independent realizations of the DT$^+$ lattice, ranging from $L = 32$ to 1024, and simulate the contact process for a time of 10^8 units. The measurements are taken after a generously sized relaxation period of $7 \cdot 10^7$ time units. The resulting data, shown in Figure 5.13, reveals that $\ln \rho$ and $\ln \tau$ follow straight lines, and linear fits yield the exponents

$$\beta/\nu = 0.800(5), \tag{5.25}$$

$$z = 1.758(14), \tag{5.26}$$

where the errors reflect both the uncertainty of the critical point and the fluctuations of the individual data points, with the latter accounting for roughly one third of the total uncertainties. Both exponents are compatible with reference values, $\beta/\nu = 0.797(3)$ and $z = 1.7674(6)$ [341]. In fact, the power law dependence displayed by τ is in itself an indication of clean universal behaviour, since an exponential scaling, $\ln \tau \sim L^\psi$, is expected for uncorrelated randomness, as pointed out in Section 4.3.3.

In a second set of simulations, we measure the density of particles $\rho(t)$, starting from a fully

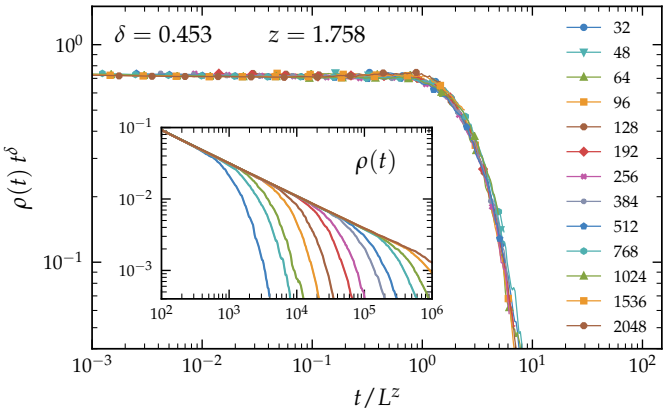

Figure 5.14 | Finite-size data collapse (CP, DT$^+$). Simulations starting from a fully occupied DT$^+$ lattice at the critical point $p_c = 0.589775$, using the critical exponent estimates stated in the figure. All curves are averages over 500 disorder realizations with 5 runs per realization. L denotes the linear system size. The inset shows the non-rescaled density as a function of time.

occupied lattice. For finite systems at the critical point, this density is expected to follow

$$\rho(L,t) = t^{-\delta}\tilde{\rho}\left(t/L^z\right), \tag{5.27}$$

where $\tilde{\rho}$ is a universal scaling function. Performing simulations on lattices from $L = 32$ to 2048, running for times up to 10^6 and using 500 disorder realizations with 5 runs on each realization, we obtain the data presented in Figure 5.14, which shows the finite-size data collapse, as well as the original measurement of $\rho(t)$ in the inset. The data collapse is performed by, using the estimate (5.26) for z, determining the value of δ for which the curves in Figure 5.14 superpose each other. We obtain as our final estimate

$$\delta = 0.453(5), \tag{5.28}$$

which is again compatible with the reference value $\delta = 0.4523(10)$ from Dickman [341].

We can obtain a further exponent, $\nu_\parallel = z\nu$, from off-critical simulations, using the relation

$$\rho(\Delta,t) = t^{-\delta}\hat{\rho}\left(\Delta t^{1/\nu_\parallel}\right), \tag{5.29}$$

where $\Delta = p - p_c$ denotes the distance from criticality and $\hat{\rho}$ is a scaling function. Taking the estimate for δ obtained above, we produce the curve collapse of Figure 5.15 when we set

$$\nu_\parallel = 1.31(2), \tag{5.30}$$

in accordance with the reference value $\nu_\parallel = 1.292(4)$ [341].

In summary, all the exponents we obtain for the two-dimensional DT$^+$ lattice in numerical simulations of the contact process turn out to be fully compatible with the ones of the corresponding clean universality class. In particular, the data collapse plots are flawless within numerical precision. This provides strong evidence that the phase transition on the DT$^+$ is in fact controlled by the clean universal behaviour of the DP class, hence indicating that this type

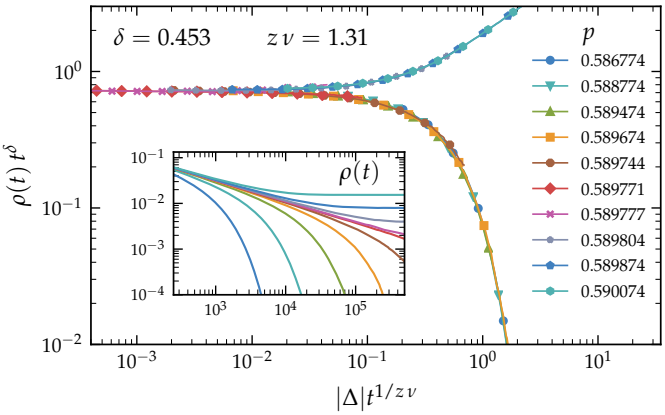

Figure 5.15 | Critical region collapse (CP, DT$^+$). Data collapse near criticality, starting from a fully occupied DT$^+$ lattice of linear size $L = 2048$ using the critical exponent estimates given in the figure. All curves are averages over 250 disorder realizations, with 5 runs per realization. The symbol Δ denotes the distance from the critical point $p_c = 0.589775$. The inset shows the non-rescaled density as a function of time.

of disorder violates the HBV criterion. Clearly, regardless of our extensive numerical effort, including large lattice sizes and long simulation times, the possibility of a crossover away from the clean universal behaviour for extremely long times can not be ruled out, though very large crossover times are unlikely for DT, as reasoned in Reference [67]. Moreover, it could be argued that the "canonical" constraint (i. e., fixed number of additional bonds) imposed in the DT$^+$ construction leads to spurious results. In particular, Aharony et al. [207] showed that although the canonical and its "grand-canonical" counterpart (i. e., without global constraints) belong to the same universality class, the approach to the asymptotic behaviour can be much slower in the former. We therefore also implemented a grand-canonical construction of the DT$^+$ lattice, DT$^+_{GC}$, where the additional bonds are now drawn independently with a certain probability for each node, resulting in a total coordination number which fluctuates around an average value of $(6+2)N$. When we repeat all simulations described above on the DT$^+_{GC}$, we again obtain results fully compatible with the clean universal behaviour of the DP class [41], revealing that the constraint has no influence on our conclusions. Corresponding plots are shown in Appendix B. Finally, since the DT$^+$ lattice is clearly not planar (triangulations are maximal sets of non-intersecting edges [238], thus added bonds necessarily cross existing ones), our results answer a question raised in Section 5.1, as planarity is shown *not* to be a necessary condition for stability of the phase transition against quenched spatial disorder.

5.4 CP on two-dimensional lattices

As mentioned earlier, there exist lattices inaccessible to the HBV criterion, namely, for instance, the VG and the CC lattice, where coordination number fluctuations are absent. However, numerical simulations of the two-dimensional Ising model on those two lattices with constant coordination number produce rather distinct results. Whereas for the VG, the system remains

[41] The location of the critical point of the DT$^+_{GC}$ is slightly lower (by about 0.2%) compared to the ordinary (canonical) DT$^+$.

in the clean Ising universality class (Section 5.2), the CC lattice shows varying exponents and hence no clear evidence of clean universal behaviour (Section 5.1). In fact, the latter results are qualitatively similar to those on diluted regular lattices, which, owing to the ambiguity of their universality character, received considerable attention through the last three decades. Specifically, deviations of the system's critical exponents from their clean values have been explained both as a disorder-dependent non-universal behaviour [190–195] (the so-called weakly universal scenario), and as resulting from strong logarithmic corrections due to the marginality of the model with respect to the Harris criterion (strong universality scenario) [185–189, 197–200]. This marginality makes it difficult to tell whether disorder of the CC type ultimately represents a relevant perturbation. In this section, we therefore turn our attention to the contact process, as it should allow for a clearer distinction between universal and non-universal behaviours, due to its smaller correlation length exponent, $\nu \approx 0.73$ in two spatial dimensions. We find that the CC lattice disorder constitutes a *relevant* perturbation, as the dynamics shifts from the conventional power-law scaling into the activated scaling regime. It turns out that the results are much like those for the contact process on Gabriel graph and relative neighbourhood graphs, also investigated in this section, for which the HBV criterion already predicts a failure of clean universal behaviour (compare Table 2.4). This raises the question of why disorder of the CC type is more relevant than that of the Voronoi type, even though both share the absence of the coordination number fluctuations.

Concretely, we perform simulations of the contact process on the CC lattice with four neighbours at each node (CC4), as well as on the GG and RNG, measuring the number of active sites N_a, the survival probability P_s and the radius of the active cluster R as a function of time. The critical points are determined using seed simulations where lattices of linear size $L = 12\,000$ with periodic boundary conditions are employed. This very large size allows simulation times at least up to $T = 10^6$, while avoiding any finite-size effects. We ensured this by monitoring the typical cluster diameter during the simulation. Even larger lattices could not be afforded due to the huge memory requirements. In total, we used up to 600 independent disorder realizations, with 10 000 spreading runs per probability on each realization. In the following we present the analysis for the CC4 lattice, whereas for the RNG and GG we proceeded completely analogous. For all three lattices, results are shown in Figure 5.16.

The first step in the analysis is to locate the critical point. According to the criterion of Moreira and Dickman [329], we search for the smallest p that results in a curve that asymptotically does not decay. In Figure 5.16(a), we therefore evaluate $N_a(t)$ for several probabilities. The curves corresponding to the smallest values decay quickly, while those for the largest p bend away from the critical region, providing us with a rough estimate of the critical value. In order to obtain a more precise estimate of p_c, we plot $N_a(t)$ against $P_s(t)$, as shown in the inset of Figure 5.16(b) and search for the curve best described by the power law, i. e. the one which is straight in the long-time limit in a double logarithmic plot. Note that this approach can be used independently of the scaling scenario, since in the case of activated logarithmic scaling, the non-universal time scale t_0 cancels out, which means that either way we are led to a power-law behaviour

$$N_a \sim P_s^{-\theta/\delta}. \tag{5.31}$$

We find $p_c = 0.644053(2)$, where the error is estimated from the nearby curves that show

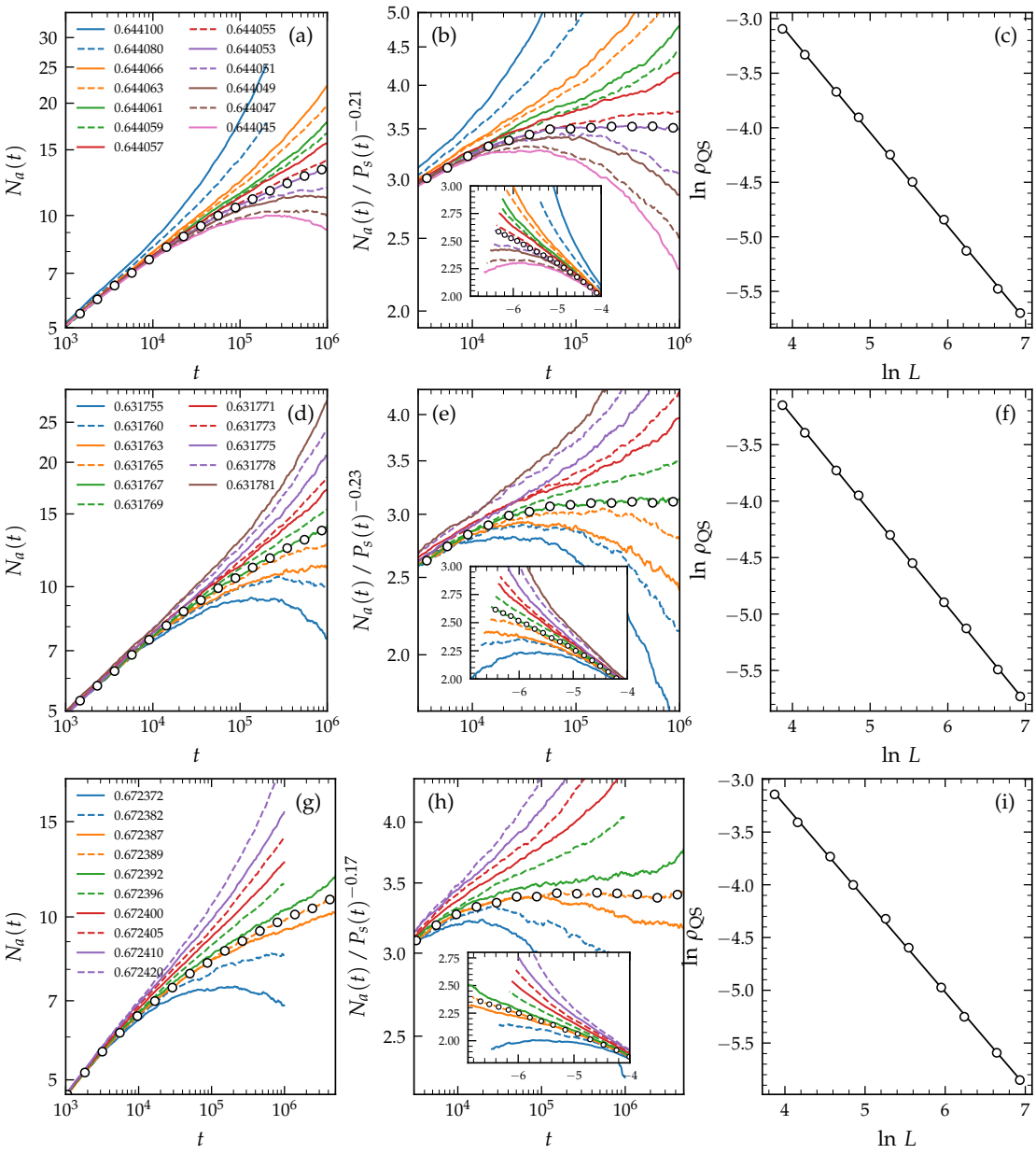

Figure 5.16 | Numerical results for the CC4 (top)**, GG** (middle) **and RNG** (bottom). Left column: Average cluster size as a function of time for spreading runs. The markers highlight the curve corresponding to the estimated critical point. Middle column: Verification of the exponent θ/δ. The insets show $\ln N_a(t)$ against $\ln P_s(t)$. Right column: Quasi-stationary density against the linear system size L. The solid line represents a linear fit to the data points, with slope β/ν (compare Table 5.7).

Table 5.7 | Critical exponent results (CP on 2D CC, RNG, GG). Errors stem from the uncertainty of the critical point and fluctuations of the individual data points. The latter are indicated in square brackets whenever comparably large to the former. The last two lines show the corresponding exponent combinations for the DP universality class [341] and for the random transverse-field Ising model [331] as reference values. Note that in the case of DP universality, $\delta z = \beta/\nu_\perp$ holds.

	θ/δ	$\theta\psi$	$\delta\psi$	$\beta/\nu_\perp$	p_c
CC	$0.21^{+0.03}_{-0.08}$	0.20(6)	1.06(6)	0.85(1)[1]	0.644053(2)
RNG	$0.17^{+0.05}_{-0.04}$	0.20(4)	1.08(4)	0.88(1)[1]	0.672389(3)
GG	$0.23^{+0.06}_{-0.10}$	0.24(8)	1.04(8)	0.84(1)[1]	0.631767(3)
DP reference [341]	0.507(1)	0.4051(7)	0.799(2)	0.799(2)	
RTFIM reference [331]	0.075(5)	0.078(4)	1.034(23)	0.964(2)	

noticeable deviations from a power law. Fitting Equation (5.31) to the asymptotic region (which spans about one order of magnitude in P_s), we obtain the exponent combination $\theta/\delta = 0.21^{+0.03}_{-0.08}$ where the error stems from the uncertainty of the critical point. We verified this estimate by also plotting the ratio $N_a(t)/P_s(t)^{-\theta/\delta}$, and found the expected results (asymptotically constant behaviour) to be fulfilled best at $\theta/\delta = 0.21$, as shown in Figure 5.16(b), confirming the former estimate. As a consistency check, we also tried to tune θ/δ such that the curves corresponding to $p_c = 0.644053 \pm 0.000002$ show horizontal behaviour for large times, however, they still exhibit slight systematic curvature, which confirms our estimate of the critical point. A similar analysis of N_a vs R and P_s vs R, yields the exponent combinations $\theta\psi = 0.20(6)$ and $\delta\psi = 0.106(6)$, if we use the relations

$$N_a \sim R^{\theta\psi}, \tag{5.32}$$

$$P_s \sim R^{-\delta\psi}. \tag{5.33}$$

Due to the very late onset of the non-algebraic behaviour we can estimate only exponent combinations rather than the explicit values of θ, δ and ψ. In principle, those could be computed by fitting Equations (4.84) to the respective curves under the constraint of $\ln(t_0)$ being the same for the three observables. However, as stable fits would require much longer simulation times and therefore enormous lattice sizes, this lies beyond present computational capabilities.

In addition to the dynamic exponents, we determine the static exponent of the order parameter. To this end, we perform QS simulations (compare Section 4.3.1), using lattice sizes up to $L = 1024$ and simulate the system for $2 \cdot 10^8$ time steps. For the largest lattices, we use at least 140 disorder realizations, for the smaller ones up to 1000 realizations. The quasi-stationary density is shown in Figure 5.16(c), revealing the expected straight behaviour of Equation (4.68). A linear fit yields the estimate $\beta/\nu_\perp = 0.85(1)[1]$, where the first error stems from the uncertainty of the critical point whereas the second one is due to the statistical fluctuations of the individual data points in the fit ($\chi^2/\text{d.o.f.} = 1.64$). The exponent estimates, also for the RNG and GG, are summarized in Table 5.7.

The critical exponent combinations we obtain for the topologically disordered lattices, com-

pared to those of the clean DP universality class (see Table 5.7), make it evident that, despite the relatively large error bars, it can be ruled out that the phase transitions belong to this class. This is already indicated by the behaviour of the dynamic observables, which show no straight lines in the double logarithmic plots (Figure 5.16, curves in the vicinity of the critical point). Furthermore, with the possible exception of $\delta\psi$, the exponents of all three models do not match those of the RTFIM either, which rules out this scenario as well. Strikingly, however, the exponents for the CC, RNG, and GG simulations coincide within their error bars, suggesting that the contact process on those three lattices might be determined by a yet undiscovered disorder fixed point and the three models belong to the same (potentially new) universality class. Whether or not that is the case remains open, especially since topological disorder has so far not been within the reach of analytical methods. From the numerical standpoint, more precise estimates of the exponent combinations can reveal whether they remain compatible with each other within smaller uncertainties or if there exists a weak dependence on the disorder strength that our simulations are not able to resolve. Given the already considerable computational effort demanded for obtaining the present results, these questions also remain open.

5.5 Ising model on the three-dimensional CC lattice

In the previous sections, we conducted simulations of the Ising model and the CP on two-dimensional constant coordination lattices. Although the CC lattice is particularly designed in a way which does not allow apply existing disorder relevance criteria (Harris-Luck or Harris-Barghathi-Vojta), the results of our simulations very much resembled those of traditional uncorrelated disorder. Specifically, for the Ising model indications of a marginal behaviour and strong corrections to scaling were found (Section 5.1) and for the CP an activated dynamical scaling and hence a clear departure from the universality of the clean model (Section 5.4), in accordance with simulations of the respective models on lattices with random bond or site dilution (compare Table 2.4). Hence, the results provide a consistent picture of the properties of the two-dimensional CC lattice.

In this section, we therefore turn our attention to the *three-dimensional* case and perform large-scale Monte Carlo simulations of the ferromagnetic Ising model on a 3D constant coordination lattice with coordination number $q = 4$ (CC4). For the construction of the CC4, we choose a number of $M_r = 8$ rewiring layers, a linear cell size of $\ell = 8$ and $s = 20\,000$ rewiring attempts per cell and layer at zero noise temperature. We use the definition of the Ising model in Equation (2.20) at zero external field, $h = 0$, considering nearest-neighbour interactions. All coupling strengths are fixed to unity.

As pointed out earlier, the first step in the analysis consists in locating the critical point. Although in previous sections a quite precise estimate of the critical point was obtained by a suitable infinite-volume extrapolation of the Binder ratio intersection points, here, we simply use the crossings without an infinite volume extrapolation. This already provides a sufficiently good estimate for the next steps of the analysis. In fact, since we are working in three dimensions, determining a more precise estimate would significantly increase the already large computational effort. In Section 5.2, this effort was justified as we were able to obtain a new reference value. However, for the CC, the precise location of the critical point is less meaningful,

since the lattice construction depends on choices of parameters, which influence the location of the critical point. We obtain the critical temperature estimate from the crossing points of the U_4 curves as

$$T_c = 2.4818(2), \tag{5.34}$$

where the error is evaluated, quite conservatively, from the width of the entire intersection region. The estimate from the crossing points of ξ/L turns out to be considerably less precise, though fully compatible. For the fixed point values of the phenomenological quantities, we obtain

$$(\xi/L)^* = 0.623(10), \tag{5.35}$$

$$U_4^* = 0.468(4), \tag{5.36}$$

again without using infinite volume extrapolations. These quantities are considered universal, at least in a limited sense, in that they depend weakly on certain geometrical characteristics of the system [310–312]. Taking as reference the most precise estimates available for the three-dimensional Ising model on a cubic lattice, $(\xi/L)^* = 0.6431(1)$ [351] and $U_4^* = 0.46548(5)$ [106], we see that our estimates present only small deviations, giving a first indication that the Ising model on a 3D CC4 lattice stays in the universality class of the clean model.[42]

In the next step, we simulate the Ising model on lattices of size $L = 16$, 24, 32, 48, 64, 96, and 128 for several temperatures in the vicinity of the critical point. A measurement is taken after EMCS, which, in this case, consists of one Metropolis sweep and L cluster updates, keeping the fraction of flipped sites approximately independent of the lattice size. Each disorder realization is initially prepared in a cold configuration and 500 EMCS are used for proper equilibration. Then another 1000 EMCS are performed, with a measurement being taken after each one of them. For the smaller lattices we use up to 10^4 disorder replicas for the disorder average, whereas for the two largest lattice, $L = 96$ and $L = 128$, we use at least 1500 replicas for every temperature. The time for constructing the lattices was below 1% of the total computing time.

Finite-size scaling theory (compare Sections 2.4 and 4.1.3) predicts that the susceptibility, the fourth-order magnetic cumulant and the correlation length scale according to

$$\chi = L^{\gamma/\nu} f_\chi(x)\,(1 + \ldots), \tag{5.37a}$$

$$U_4 = f_{U_4}(x)\,(1 + \ldots), \tag{5.37b}$$

$$\xi/L = f_\xi(x)\,(1 + \ldots), \tag{5.37c}$$

where γ and ν are critical exponents and f_χ, f_{U_4}, and f_ξ denote universal scaling functions, with the argument x given by

$$x = (T - T_c)L^{1/\nu}. \tag{5.38}$$

These equations describe the scaling behaviour to first order. Corrections of higher order are expected to become irrelevant for large system sizes. We compute the corresponding scaling collapse plots, assuming the best known values for the clean model critical exponents [106]

[42] Recall, that these quantities are only universal in a limited sense, as discussed in Section 5.2

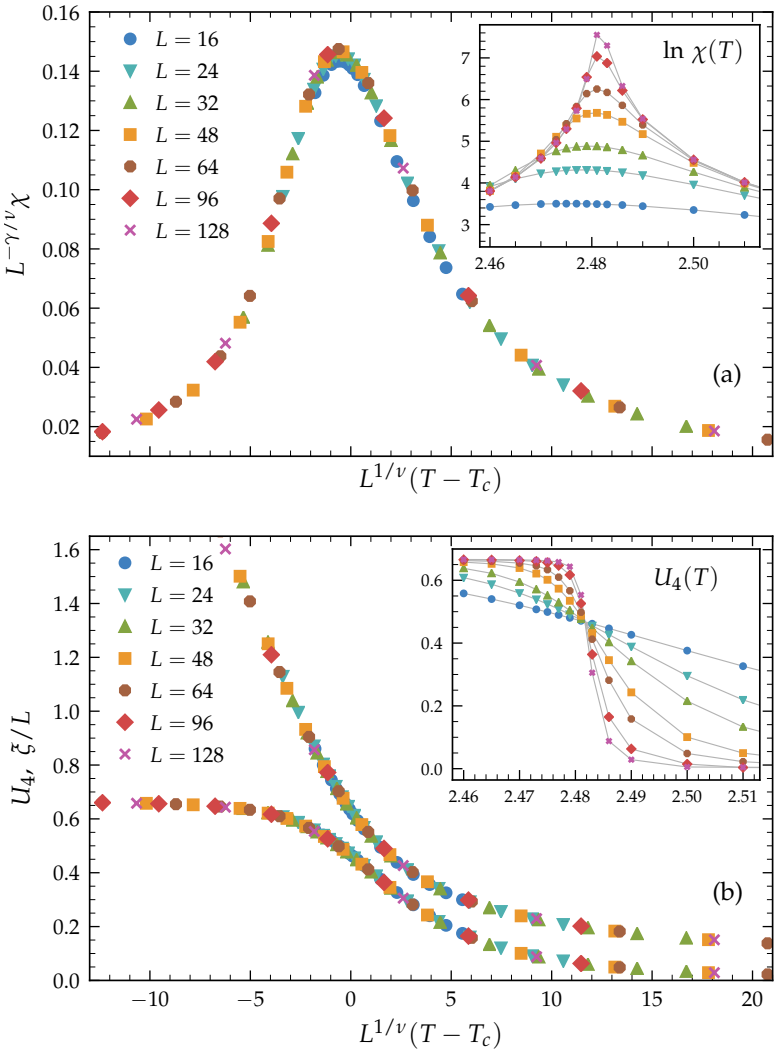

Figure 5.17 | Scaling collapse (Ising, 3D CC4). Finite-size data collapse for the Ising model on a 3D CC4 lattice, according to Equation (5.37c). (a) Magnetic susceptibility. (b) Fourth-order Binder cumulant (lower curve) and two-point finite-size correlation function (upper curve). Insets show the non-rescaled observables. The gray lines are guides to the eye.

and the value (5.34) for T_c. In the upper panel of Figure 5.17, we plot the scaling collapse for the susceptibility and, in its lower panel we plot both phenomenological couplings against the scaling variable. The nearly flawless collapse displayed by the curves, for lattice sizes $L \geq 32$ in the upper panel and for $L \geq 16$ in the lower panel, provides compelling evidence that the Ising model on a three-dimensional CC4 lattice belongs to the universality class of the clean 3D Ising model. This result is in fact surprising, since given the strong similarity of CC constructions compared to uncorrelated disorder in two-dimensions, one might have expected something similar in 3D as well. However, whereas the Ising model on 3D diluted random lattices is controlled by a new disorder fixed point (compare RG flow in Figure 2.10), for disorder of the CC type this is apparently not the case.

Chapter 6

Road towards a new relevance criterion

"An diesem Ort war ich noch niemals: Anders geht der Atem, blender als die Sonne strahlt neben ihr ein Stern."

– Franz Kafka (Aphorismen)

The numerical results of the previous chapter are reviewed and situated within the context of existing disorder relevance criteria. An immediate conclusion is that the randomness of coordination numbers alone provides an unsatisfactory description of topological disorder. We propose two novel approaches to characterizing topological randomness, potentially illuminating the path towards a more general relevance criterion for continuous phase transitions.

In Section 5, we performed a series of numerical simulations in order to explore the behaviour of prototypical systems with continuous phase transitions on topologically disordered graphs. Existing criteria for the relevance of disorder with respect to its effect on the character of the transition argue that spatial disorder fluctuations that decay too slowly are able to disrupt the clean collective behaviour at criticality, i. e. change the nature of the transition. For topological disorder in particular, the Harris-Luck and Harris-Barghathi-Vojta (HBV) criterion (compare Section 2.5) both focus on the local coordination numbers of the lattices nodes as the random variable whose fluctuations predominantly determine the stability of the transition.

Table 6.1 | Summary of numerical results with respect to whether the clean universal behaviour is present (✓) or not (✗) for the respective combination of model and geometry. The fourth row presents predictions of the HBV criterion, whenever applicable. List entries furnished with an asterisk are open to interpretation, as discussed in the text. Compare also Table 2.4.

Class	Dimension	Lattice	Prediction	Observation	Reference	Section
Ising	2	CC	n.a.	marginal*	[P2]	5.1
DP	2	CC	n.a.	✗	[P5]	5.4
DP	2	RNG, GG	✗	✗	[P5]	5.4
Ising, DP, Manna	2	VG	n.a.	✓	[P4]	5.2
DP	2	DT^+	✗	✓	[P1]	5.3
Ising	3	CC	n.a.	✓	[P3]	5.5
Heisenberg	3	RGG	✓	✓	[P6]	4.2

As can be seen from Table 6.1, our studies were revolved around specific random lattices where the above mentioned criteria are not applicable in the first place, as they feature a constant coordination number of the nodes. Aiming to investigate this scenario, we developed the CC lattice (Section 3.3), a topologically disordered lattice with a locally constant number of neighbours. On a two-dimensional realization of this graph, the spin-1/2 Ising model showed critical exponents slightly changing with the lattice size (Section 5.1), which could very well be attributed to strong finite-size corrections in an otherwise clean Ising scaling scenario. Similar behaviour has already been observed for the Ising model on diluted lattices, and is arguably associated to the marginality of the model with respect to the original Harris criterion (see Section 2.5 for details) on these structures. Also for the DP transition on the two-dimensional CC lattice, the results qualitatively resemble those from dilution-type disorder, as we were able to demonstrate in Section 5.4. Specifically, the transition appears to shift into the activated scaling regime with an infinite-order fixed point, accompanied by strong Griffiths effects. Irrespective of the precise classification of the phase transition, which can not be resolved in the present work, as even larger simulations would be needed, the fact that the transitions do not belong to the clean DP universality class means that the CC type disorder is relevant for these models.

For the two-dimensional Voronoi graph, however which features a constant coordination number of the nodes as well, the picture is entirely different. For both systems (Ising and DP) we find compelling numerical evidence that the respective regular (clean) universal behaviour is maintained (Section 5.2). Although this result could be expected – since the VG inherits its geometric structure and therefore presumably also its extraordinary stability from its dual, the DT (compare Section 2.5) – this indicates that coordination number correlations are not sufficient to draw a distinction between relevant and irrelevant types of disorder. Also summarized in Table 6.1 are our results for three-dimensional systems. In particular, we find clean universal behaviour for the Ising model on a CC lattice, which is quite remarkable, since on diluted lattices the transition is altered, as predicted by the Harris criterion, shifting towards a new disorder fixed point, independent of the dilution strength [273].

Besides those cases where the HBV criterion can not be applied, we also constructed an explicit violation for a combination of geometry and lattice model, i. e. a case where it makes incorrect predictions, see Section 5.3. In the so-called DT^+ lattice, we add a second layer of local bonds to a regular Delaunay triangulation, resulting in a slower decay of coordination number correlations. However, we were able to show that the transition does *not* shift into the activated scaling regime, even though both known criteria concerning topological disorder predict exactly that. This is a major result, as it reveals that existing criteria are not generically applicable.

In summary, we found that current disorder relevance criteria, although successful for a wide range of systems, are not general and can even produce false predictions. As a consequence, an area of research which seemed already settled, is effectively re-opened and the search for a general disorder relevance criterion for continuous phase transitions must continue. The aggregate of our results strongly suggests that coordination number fluctuations can be seen as a manifestation of a more general random variable that describes the spatial structure of the lattice. This evasive variable is still to be found, but in the following we believe to offer a few first steps towards a more general understanding.

6.1 Dual tessellation

In the case of the DT^+, where all connections remain local, slowly-decaying fluctuations caused by a surplus of edges will not deter the emergence of collective behaviour. Thus, the relevant inhomogeneities seem to be those that impair the propagation of information through the system. This leads us to the assumption that the key concept appears to be some form of *poor connectivity* of the lattice and how fast it decays. In order to characterize this poor connectivity, we turn our attention to *holes* in the lattice. A hole is understood as a region where nodes metrically close to each other are separated by large edge distances. Pictorially, holes are edgeless regions in the lattice where, were the edges between the nodes distributed more uniformly in space (such as in a triangulation), edges would be expected. In planar graphs, holes trivially correspond to faces, and a large hole is a face surrounded by a large number of nodes. The DT, for instance, has only triangular faces and, therefore, no proper holes, while GGs have moderately-sized holes and RNGs relatively large holes, compare Figures 3.2 and 3.3. For planar graphs, a convenient way to analyse the size of these holes (faces) is through the so-called *dual graphs*, where each site corresponds to a given face of the original lattice and bonds are placed between those sites whose associated faces share an edge [352]. Thus, dual lattice sites with high coordination numbers correspond to large holes in the original graph. In this way, by considering the coordination number fluctuations on their dual lattices, we can investigate the effect of hole-size fluctuations and their spatial decay and – in this way – characterize the stability of universal processes on the original lattices.

When considering *non-planar* graphs, such as the CC lattice, the concept of faces, and therefore dual graphs, is ill-defined and we need a new tool. Given that a face is delimited by the smallest path around it, we propose a generalization of a face, which is a *polygon* $\mathcal{P}$, defined by a closed path, and a *weight* w corresponding to the size of the face. These polygons can overlap with each other and, together, constitute a *dual tessellation* whose end-product is a function $W(x)$ attributing a weight to each point of space. A thorough description of this construction is

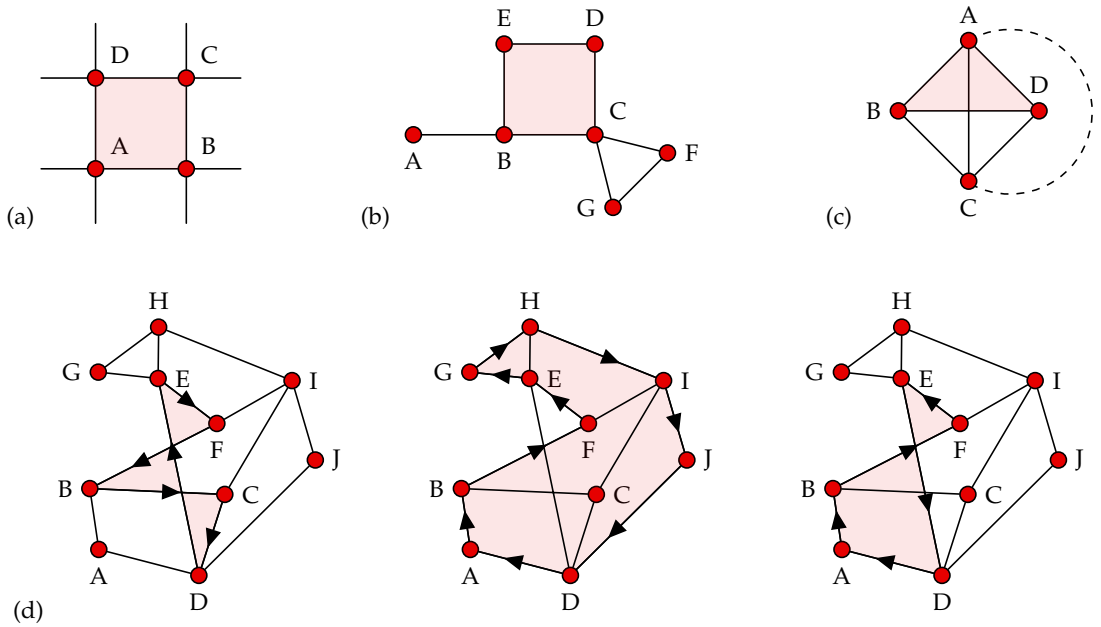

Figure 6.1 | Illustration of the cycle finding algorithm. (a) Section of a regular square lattice where the loop algorithm finds the usual face. (b) Illustration of the pruning process. (c) Simple example, where a bond, which breaks planarity, also breaks the symmetry between left- and right-turning walkers. (d) Non-unique contractions result in different loops.

presented in the following:

We introduce a generalization of the concept of duality to non-planar graphs, such as the CC lattice and the RGG (compare again Figures 3.2 and 3.3), for which dual graphs are not defined. Based on the fact that a face is delimited by the smallest path around it, we take as our starting point *cycles* $\mathcal{C}$, which reduce, in graphs with no bond crossings, to usual faces. Note that, by focusing on paths, this generalization might be only appropriate for weakly non-planar graphs, like the ones we consider in this work, rather than non-local lattices, such as small-world networks. The algorithm for finding the cycles $\mathcal{C}$ works as follows: Consider a walker which starts from a given site, say i, in the lattice and travels along a given bond, ending at site j; from j it continues along the rightmost (alternatively leftmost) bond with respect to the incoming bond, i. e. it chooses the next site k such that the angle between $i - j$ and $j - k$ in clockwise (anti-clockwise) direction is smallest. This rule is iterated until the walker closes a cycle, i. e. returns to i, which is guaranteed by the finiteness of the lattice. The cycle obtained as just described is what we call a generalized face. A schematic visualization is shown in Figure 6.1a, where a left-turning walker starting from A to B finds the cycle ABCDA.

In this procedure, the walker may close an intermediate loop before ultimately returning to its origin. In order to avoid inflating the cycle length and over-counting these loops (already found for different initial conditions) those intermediate, or *stray* loops are pruned from the cycle. An example is shown in Figure 6.1b: A left-turning walker starting from E towards D travels along the path

$$\overbrace{\text{EDCFGCB}}\overbrace{\text{ABE}} = \text{EDCBE}, \tag{6.1}$$

where the contraction symbols mark the pruned intermediate loops, namely the triangle CFGC and the leaf A. Note that a right-turning walker starting from E towards D returns the quadrilateral path EDCBE directly. In less trivial graphs the pruning process may be non-unique, in which case all possible pruned cycles are collected. An example can be seen in Figure 6.1d for a left-turning walker starting from F to E, where three different, overlapping intermediate loops are present, resulting in three possible pruned cycles:

$$\text{FEDCBADEGHIJDABF} = \begin{cases} \text{FEGHIJDABF} \\ \text{FEDABF} \\ \text{FEDCBF.} \end{cases} \tag{6.2}$$

Furthermore, closed paths are invariant under cyclic permutations, thus, we define equivalence classes, such as for example

$$[\mathcal{C}_{ABCD}] \equiv \{x \in \Omega \mid \mathcal{C}_{ABCD} \sim x\} = \{\mathcal{C}_{ABCD}, \mathcal{C}_{BCDA}, \mathcal{C}_{CDAB}, \mathcal{C}_{DABC}\}, \tag{6.3}$$

where Ω denotes the set of all cycles found in the graph by the algorithm. In the planar case the number of permutations (i. e. the cardinality or *multiplicity* of $[\mathcal{C}_i]$) exactly coincides with the number of edges in the cycle $\mathcal{C}_i$ for every i. Every class of equivalent cycles defines a *polygon* $\mathcal{P}([\mathcal{C}])$ that has the cycle's sites on its vertices (corners). To the polygon a *weight* w_i is attributed, which is given by

$$w_i \equiv |[\mathcal{C}_i]| \leq |\mathcal{C}_i|, \tag{6.4}$$

where the equality always holds for the planar case. In the above example, the polygon $\mathcal{P}_{ABCD} \equiv \mathcal{P}([\mathcal{C}_{ABCD}])$ consists of four vertices and therefore carries the weight $w_{ABCD} \equiv |[\mathcal{C}_{ABCD}]| = |\mathcal{C}_{ABCD}| = 4$.

For non-planar graphs, not necessarily every possible permutation is found by the walker, hence in general $|[\mathcal{C}_i]| \leq |\mathcal{C}_i|$ holds. Furthermore, when the pruning process is non-unique, we attribute fractional weights to the pruned paths. In Equation (6.2), each of the three pruned paths contributes to a different set of equivalent cycles with weight $1/3$. Consider the following example, where the overtext shows how often each cycle was found by the algorithm:

$$[\mathcal{C}_{DCBEF}] = \{x \in \Omega \mid \mathcal{C}_{DCBEF} \sim x\} = \{\overset{1}{\mathcal{C}}_{DCBEF}, \overset{1}{\mathcal{C}}_{CBEFD}, \overset{1/3}{\mathcal{C}}_{FEDCB}\}. \tag{6.5}$$

Here, the first two loops were found once, whereas the third cycle, $\mathcal{C}_{FEDCB}$, was only found "1/3-times", meaning that it was one of three valid contractions of a given path (such as in the example of Figure 6.1d). The cycles $\mathcal{C}_{EFDCB}$ and $\mathcal{C}_{BEFDC}$, which are also equivalent to $\mathcal{C}_{DCBEF}$, are not found at all by the walker. In this more general case, the multiplicity of the equivalence class and therefore the weight of the associated polygon $\mathcal{P}_{DCBEF}$ is given by the sum of the overnumbers, in this case $w_{DCBEF} \equiv |[\mathcal{C}_{ABCD}]| = 1 + 1 + 1/3 = 7/3 < |\mathcal{C}_{DCBEF}| = 5$. The polygons $\mathcal{P}_i$ and corresponding weights w_i can be seen as the generalization of faces and their size in the planar case.

Due to symmetry reasons, we always consider both right- and left-turning walkers. For

graphs with no bond crossings this results in a double-counting which is accounted for by dividing all face weights by two. Note that for this reason we do not include inversions in the equivalence class definition (compare Equation 6.3). However, as soon as bonds cross, as for non-planar graphs, the left/right symmetry can be broken, as illustrated in Figure 6.1c. There, a right-turning walker starting from A to D finds the cycle ADBA, whereas the reverse search (a left-turning walker starting from D to A) finds the cycle DACD. Were the bond A-D instead outside the quadrilateral (denoted by the dashed circle segment), the symmetry would be retained, with both walkers traversing the cycle ADBA, and, respectively DABD, which are the same path.

Finally, note that the examples of Figure 6.1 are only meant to clarify the concepts introduced. For such small graphs the infinite face (i. e., external to all bonds) needs to be taken into account as well – and the algorithm fails to do so properly when a site is present more than once in the path along the graph boundary (such as site C in Figure 6.1b), since the path is then pruned, misrepresenting the infinite face. For the large lattices under periodic boundary conditions we consider, though, a "bulk" algorithm is fully adequate.

We perform the search procedure using both right and left walkers, starting from every site and direction. The resulting set of polygons and corresponding weights is what defines our generalised dual tessellation

$$\mathcal{T} \equiv \{(\mathcal{P}_i, w_i), (\mathcal{P}_j, w_j), \ldots\}. \tag{6.6}$$

Every polygon covers a certain area of the spatial domain, as exemplified in Figure 6.1d. The weight of the polygon is attributed to this area, as shown in Figure 6.2. For planar graphs (Figure 6.2b), the weights exactly represent the coordination numbers of the dual lattice sites, i. e. w are the number of vertices of the corresponding face. For dual tessellations of non-planar graphs (Figure 6.2a) different cycles often overlap. The weights attributed to those regions are the sums of the weights of the individual overlapping polygons. Note that irrespective of the overlap and the in general fractional final weights, the total weight of an area still can be interpreted very similarly compared to the planar case. More precisely, the total weight W of a point x in space is defined by

$$W(x) \equiv \sum_i w_i \quad | \quad x \text{ inside } \mathcal{P}([\mathcal{C}_i]), \tag{6.7}$$

i. e. the sum of the weights of polygons inside of which x can be found.

We calculate the dual tessellation for the VG, GG, CC4 and DT$^+$ lattices and show them (more precisely their weight fields $W(x)$) in the top row of Figure 6.3. In planar graphs, (ordinary) faces present no overlaps and the weights are simply the coordination numbers of the corresponding sites of the dual lattice. Hence, the VG's dual tessellation shows the coordination number fluctuations of the corresponding DT lattice, its dual. As can be seen, the weight amplitudes vary considerably between the different lattices considered. For instance, VG cells with $W > 10$ are rare, whereas the CC features a few large holes with $W \approx 30$. In order to make the weight fluctuations comparable, we rescale the dual tessellations according to $W_{\text{rescaled}} = (W - \mu_W)/\sigma_W$, where μ_W and σ_W represent the weight mean and standard deviation.

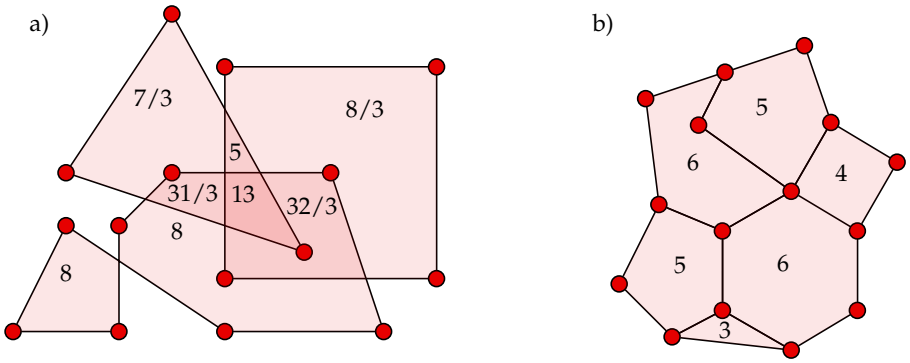

Figure 6.2 | Schematic visualization of the dual tessellation. The numbers denote the corresponding weights of the polygons $\mathcal{P}$ (generalized faces). In the example of a non-planar lattice (a) the polygons intersect and the weights are added in the overlapping regions. In the planar case (b) no overlaps exist and the weights reduce to the number of sites in the polygon.

The rescaled dual tessellations for the four lattices displayed in the second row of Figure 6.3 are quite distinct: the VG is characterized by regions of very high and very low weights found close together, giving it a relatively homogeneous, well-mixed appearance – a visual consequence of the coordination number anti-correlation present in the DT lattice [67]; the GG's dual tessellation, on the other hand, appears less homogeneous, with high-weight regions standing out more clearly, as a consequence of the lack of such anti-correlations; even less homogeneous is the CC4, whose dual tessellation displays large swaths of high-W regions against a relatively featureless background; and the DT^+ is marked by randomly distributed peaks of very high weights. More decisive still than the magnitude of the fluctuations, is how fast they decay under a block coarse-graining analysis [67], i. e. how fast homogeneity increases as the weights are averaged over increasingly larger square blocks of the spacial domain. The lower two rows of Figure 6.3 show two steps of this analysis. In the case of the VG, significant homogeneity sets in already after a weak coarse-graining step, due to the inherent anti-correlations mentioned above. This fast decay of the fluctuations indicates that the disorder should be less relevant. In contrast, the GG has no such anti-correlations [P2] and regions of high weight survive large coarse-graining steps, keeping the tessellation less homogeneous through the procedure. For the CC lattice – an important motivation for the introduction of the generalized dual tessellation – we find that the fluctuations are indeed as pronounced, and decrease equally slowly as those of the GG. Finally, we see that the prominent peaks of the dual tessellation of the DT^+ quickly disappear under coarse-graining, leaving only fluctuations that decay about as fast as those of the VG.

Just as the behaviour of coordination number fluctuations under coarse graining of the original (i. e. non-dual) lattice is used to establish the HBV criterion, we propose to apply the same reasoning to the *dual* tessellation. This means taking a slow decay in the dual tessellation weights to imply a stronger relevance of disorder in the original lattice. Hence, the slow decay of fluctuations in the CC4 dual tessellation indicates that the disorder is as relevant as for the GG, agreeing with the results of our simulations (Table 5.7), where both lattices show very similar behaviour. Therefore, we argue that the relevance of the disorder present in the contact process on the CC4 (see Section 5) is reflected by the persistent fluctuations in its dual tessellation.

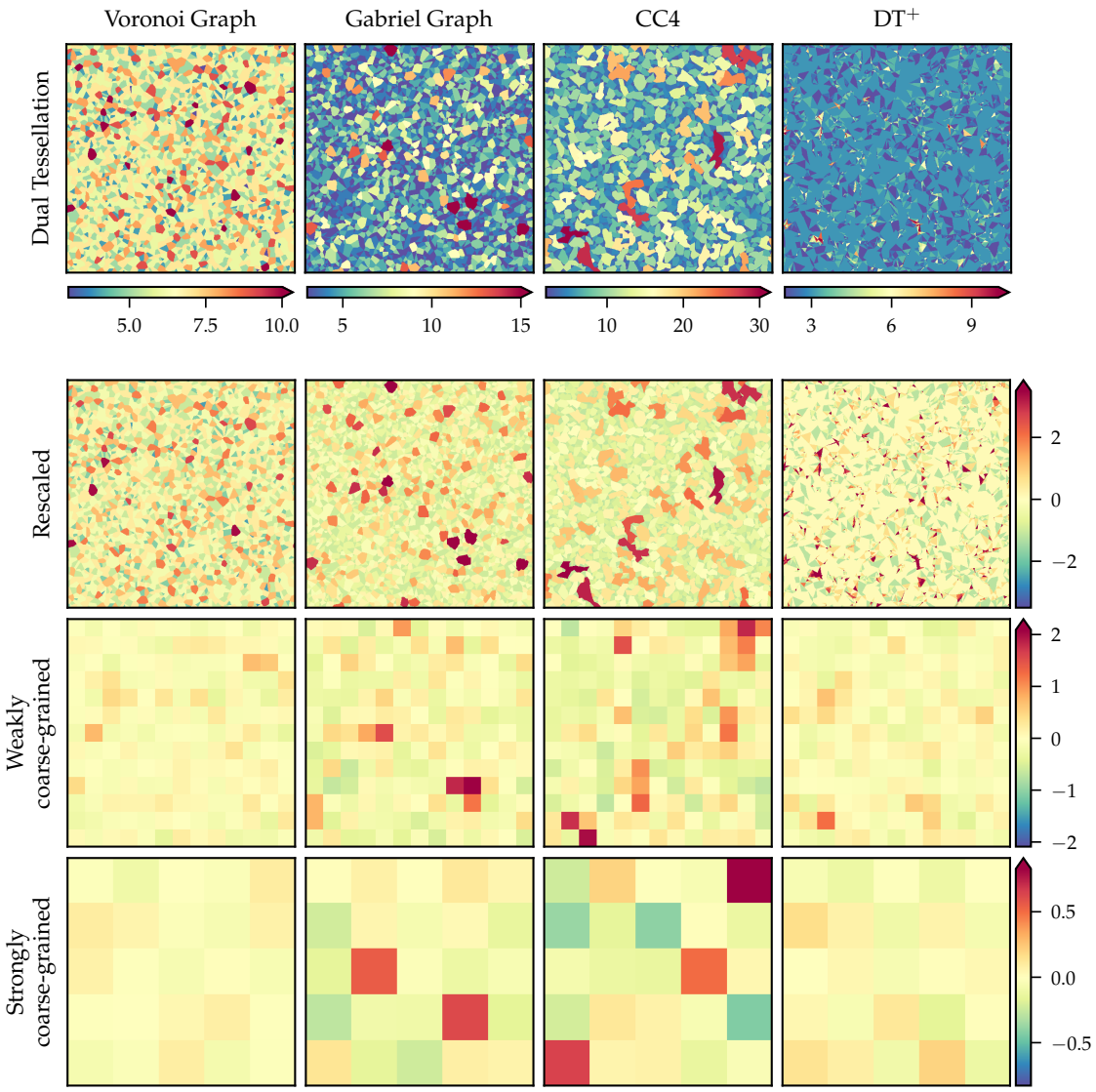

Figure 6.3 | Dual tessellation samples for the lattices VG, GG, CC4, and DT$^+$. In the second row, the dual tessellation weights are rescaled as described in the text. Hence, the colours denote the fluctuations of the weights around their respective spatial averages. Except for the top row, the colour ranges are the same in every row. The two bottom rows show coarse graining steps.

Conversely, the fast decay of dual-tessellation fluctuations for the DT^+ would indicate its disorder to be less relevant. Hence, it might successfully explain the universal character of the CP, which could not be explained by a coordination number analysis performed directly on the DT^+ lattice [P1].

6.2 Elastic relaxation

In a different approach, we perform a relaxation process with respect to tensions imposed along bonds in the graph. This results in a new spatial distribution of the nodes, which should reflect the topology of the lattice. Specifically, we let one site at a time move, under a decreasing heat bath, according to the total force the site is subjected to when we take its bonds to be stretched Hookean springs. Lattice sites are therefore attracted to sites they are connected to, and bond-poor regions tend to expand – highlighting the poor connectivity we believe to characterize relevant topological disorder. In this way, the topology of the lattice becomes accessible to *geometrical* tools, besides the established tools from graph theory. This approach also greatly facilitates visual inspection in two-dimensional lattices, since any holes present become more pronounced, as can be seen in Figure 6.4, and it can trivially be generalized to higher dimensions.

Sites in periodic and quasiperiodic structures find themselves in equilibrium or near equilibrium with respect to bond tension and wiggle about slightly due to the heat bath, but otherwise remain unchanged under elastic relaxation. As soon as dilution is introduced into the lattice, however (e. g. by randomly eliminating a fraction of its sites), the picture changes: even at low dilution rates, the lattice's connectivity is affected and relaxation makes a number of significant holes evident. Similar and even more numerous holes can be seen in the relaxed versions of the proximity graphs, such as the RNG. The CC lattice also presents significant holes and a remarkable resemblance to the RNG after relaxation. Among the considered lattices, the most dramatic change brought about by elastic relaxation is found in the RGG, which is reduced to threads by the procedure. Triangulations of random clouds, on the other hand, contain maximal sets of non-crossing bonds and, akin to periodic tessellations, are little affected by relaxation, as can be seen in the Delaunay triangulation. The introduction of a number of additional random local bonds to a DT (resulting in the DT^+ lattice, not shown) promotes a moderate degree of agglutination, but does not otherwise change the scenario. Also the VG remains mostly unaffected by the relaxation.

The results described above show that the elastic relaxation procedure provides a tool which clearly distinguishes, to the unaided eye, between lattices with and without significant holes. Every lattice belonging to the latter group (no holes: DT, DT^+, and VG) is found to present an irrelevant perturbation to the DP universality class, while those with significant holes do not. These results provide strong, if qualitative evidence for our claim that the decisive factor for the relevance of topological disorder is how strongly the disorder affects the connectivity properties of a lattice.

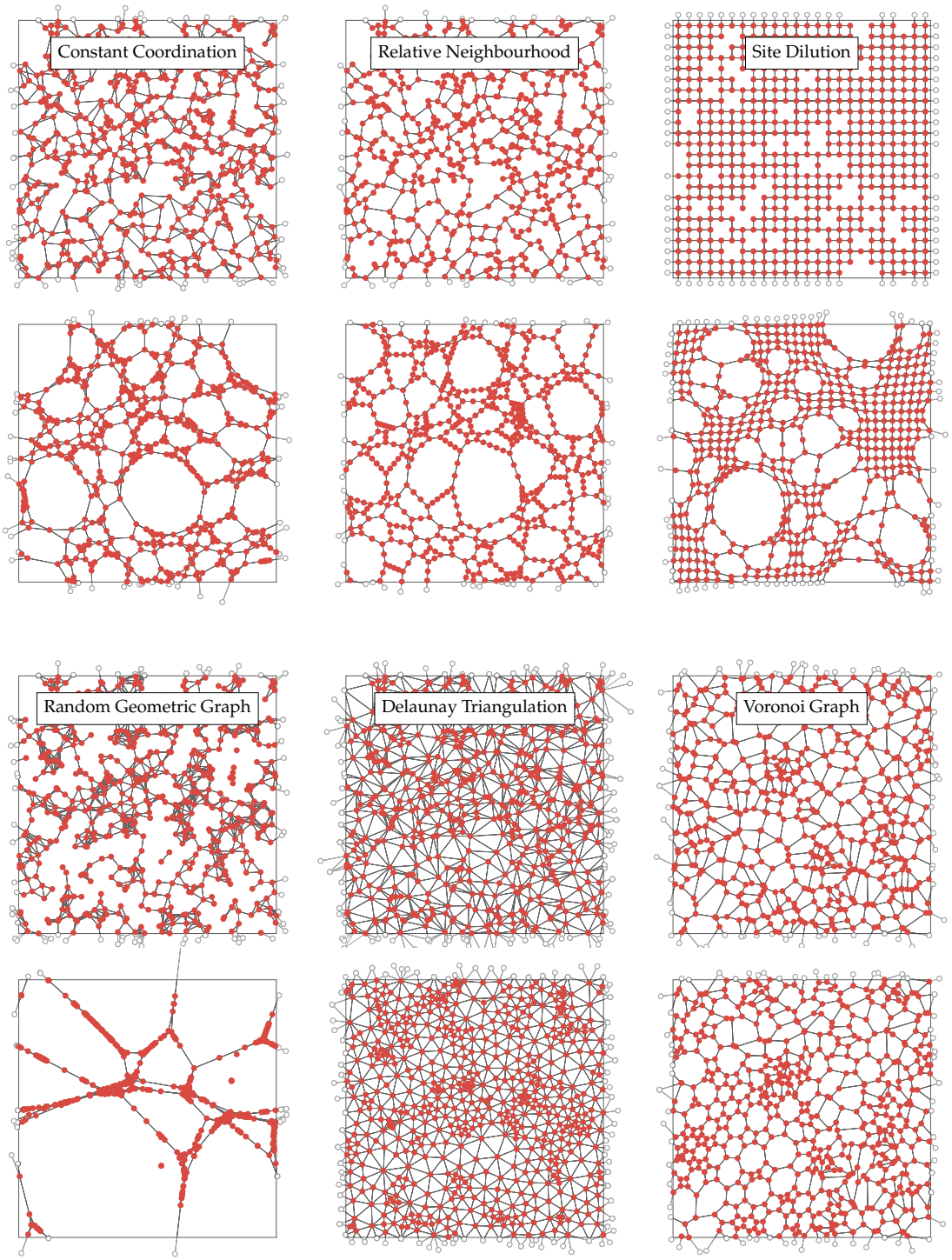

Figure 6.4 | Random lattices before and after elastic relaxation. Pulled by tensions attributed to the bonds, sites tend to agglutinate, accentuating any holes present. CC, RNG, RGG and DT are generated from the same set of points.

Chapter 7

Conclusion

"I think it's much more interesting to live not knowing than to have answers which might be wrong."

– Richard Feynman

In this work we explored the influence of quenched topological disorder on critical phenomena. This was realized mainly through large-scale numerical Monte Carlo simulations, covering the most common classes of continuous phase transitions. At criticality, they all develop collective behaviour over long distances, even though the individual, microscopic components are only locally coupled. We discussed how, according to the concept of universality, the critical behaviour is in fact independent of the underlying mechanisms driving the system at the microscopic level and – as a consequence – is governed by the dimensionality and the symmetries of the system alone.

Convincingly demonstrated in numerous experiments and well established theoretically through the renormalization group framework, the notion of universality has become one of the most intriguing concepts in modern physics. But how robust are critical systems with respect to quenched spatial disorder? When spatial randomness is introduced, can we predict whether the universal character of a transition is preserved? Can we predict when it will be broken instead, allowing for a qualitatively new behaviour to emerge? Even though Harris in 1974 provided a convenient heuristic criterion [46], it has a very limited applicability, namely to cases where the disorder does not feature any significant spatial correlations. Since uncorrelated randomness also considerably simplifies analytical calculations, corresponding systems become

tractable by standard renormalization group methods and have already been extensively studied analytically. In contrast, the investigation of disordes endowed with more complex spatial structures has considerably shorter history, dating back to the seminal work by Luck in the 1990's [68]. Typically, the local number of interacting neighbours is given the role of the primary variable encoding the spatial structure of the disorder. By comparing the decay rate of coordination number fluctuations under spatial coarse-graining to the critical exponent of the correlation length, Barghathi and Vojta were able to derive a generalization of the Harris criterion applicable to more general types of quenched disorder [67]. This refined criterion provided a clear picture of the interplay between scales of geometric and physical fluctuations and was able to explain the existing numerical results, suggesting that the role of quenched disorder had been essentially understood.

In this work we revealed that this is not the case. Specifically, we examined the robustness of both established criteria for the relevance of topological disorder on critical phenomena (i. e. Harris-Luck [68], Harris-Barghathi-Vojta [67]) and constructed an explicit violation. Moreover, we explored lattices where fluctuations of coordination numbers are absent by construction – in particular the so-called Voronoi graph, as well as the newly developed constant coordination (CC) lattice – providing evidence that fluctuations in the number of interacting neighbours are not a key measure for predicting the impact of disorder on continuous phase transitions. In what follows we go through our results in more detail. A systematic summary of the simulations that support our conclusions is found in Table 6.1.

As already pointed out above, a large part of our work has been devoted to structures to which existing disorder relevance criteria can not be applied, which is the case when the number of interacting neighbours is locally constant. Specifically, we investigated three prominent critical systems – the Ising model, the non-equilibrium contact process, and the conserved stochastic sandpile model – on two-dimensional Voronoi graphs (VG), which arise naturally when considering regions of influence and are hence frequently encountered across the natural sciences and engineering. We found that all three models remain in their respective clean universality classes – a result which can be motivated by the graph-theoretical dual of the VG, the Delaunay triangulation, showing analogous behaviour. Therefore, we developed a second structure, the so-called CC lattice – a topologically disordered lattice with constant local coordination number, bearing only short-ranged interactions. We devised a very efficient algorithm for constructing the CC lattice, which is in fact significantly faster to build than traditional proximity graphs. This is achieved by a multi-layer dynamical simulated annealing procedure, operating only in spatially local blocks. Concretely, nodes are distributed at random, such as for any proximity graph. The domain is then decomposed into spatial blocks and random connections among the points inside the respective boxes are introduced. That is followed by a relaxation of link distances by a dynamical pairwise rewiring scheme, which is based on a simulated annealing technique. In both stages, multiple, staggered grids of blocks are used in order to guarantee a homogeneously connected graph. We demonstrated that the lattice is perfectly suitable for finite-size scaling studies and generalizes straightforwardly to higher dimensions. However, due to combinatorial restrictions, the algorithm can only construct lattices of even coordination number.

Similar to our investigation of the VG, we performed numerical simulations of a number of systems on the CC lattice. For the two-dimensional Ising model we found critical exponents

varying with the strength of the disorder. From the lattice sizes available we were not able to conclude whether they eventually converge to the universal Ising ones in the infinite-volume limit. The character of the phase transition hence remains unclear, although we speculate that the deviations can be explained by strong logarithmic corrections. Overall, the situation looks somewhat similar to the case of the randomly site- or bond-diluted Ising model, which represent exactly the borderline scenario in terms of Harris' original criterion. In order to shed more light on this situation, we also simulated the two-dimensional contact process on the CC lattice, since for this model the Harris criterion predicts an unusual "activated" scaling scenario on diluted structures. On the CC lattice, we found strong indications for this type of scaling scenario as well, although it shapes up only at significantly longer times, making a numerical detection particularly challenging. Both results, the two-dimensional Ising model and contact process, suggest that the CC lattice behaves similarly to traditional lattices with uncorrelated disorder. Therefore, as another test, we conducted simulations of the Ising model on a three-dimensional CC lattice, where due to the positive specific heat exponent, a failure of clean universal behaviour should follow. In particular, the Ising model on a randomly diluted three-dimensional lattice is known to cross over to a new universality class. Surprisingly, however, we obtained a striking finite-size data collapse using the *clean* critical exponent, hence providing compelling evidence that the model in fact remains in the clean 3D Ising universality class.

In a further study, we designed another novel type of lattice, which is based on the well-known Delaunay triangulation but where – in a random fashion – links to next-nearest neighbours are added, the DT^+ lattice. The additional bonds are short-ranged and spatially uncorrelated, which we were able to demonstrate using a numerical block-coarse-graining scheme [67]. In fact, the coordination number fluctuations due to the additional bonds dominate the overall decay of disorder correlations and, as a result, the lattice presents a geometric decay exponent of $a = 1$. According to the criterion by Barghathi and Vojta, this should result in a changed critical behaviour for all universality classes with correlation length exponent $\nu < 1$, such as it is the case for the directed percolation (DP) class. We therefore simulated the non-equilibrium contact process on the DT^+ lattice, in order to verify this prediction, and, strikingly, determined the transition to be controlled by the *clean* universal DP exponents. In particular, we could not find any indications of exotic or unusual scaling behaviour. Instead, the temporal decay of the density of active particles from a fully occupied configuration resulted in excellent data collapses, both in the off-critical regime as well as in a finite-size study. Moreover, through simulations of the quasi-stationary state, we were also able to verify the static exponents to be compatible with the ones of clean DP as well. These results combined provide convincing evidence that the two-dimensional DP class is unaffected by the disorder present in the DT^+ lattice, which represents an explicit violation of existing disorder relevance criteria.

In summary, our results raise considerable doubt about the current understanding of the influence of topological disorder (or disorder with complex spatial structure in general) being in fact sufficient. In particular, we revealed that although coordination number fluctuations in some cases capture the structure of the disorder sufficiently well in order to draw qualitative conclusions, they must be regarded as non-predictive in general.

Comparing the lattices we considered in this work on a qualitative level, one notices that those which are in some sense more strongly connected turn out to be less effective in altering

critical behaviour. Hence, based on the assumption that a yet-to-be-precisely-defined poor connectivity may lead to relevant perturbations, we devised two tools: the dual tessellation and the elastic relaxation. The dual tessellation generalizes the concept of duality to non-planar graphs. Using a deterministic walker-based cycle-detection algorithm, we are able to reveal large topological holes in the lattice, which can then be subjected to a quantitative coarse-graining analysis. We find that for the CC lattice, these disorder fluctuations decay comparably slow, possibly explaining their strong effect in altering the DP phase transition. The dual tessellation fluctuations of the VG and DT^{+}, however, decay noticeably faster under the coarse graining – consistent with the clean DP phase transition on those lattices being retained. In the elastic relaxation approach, we consider the lattices subjected to mechanical tension along their bonds and allow the sites to move according to the resulting forces. This leads poorly connected regions to expand, clearly revealing graphs that are loosely connected, in contrast to tightly connected ones, such as DTs, which are stable against the relaxation. As expected, poor connectivity corresponds to the contact process leaving the clean DP universality class. In summary, both geometric approaches are able to qualitatively distinguish which perturbations are relevant against the two-dimensional DP phase transition. In this way, they provide a visual indication, acting as a road sign towards a more general relevance criterion – a sign that indicates that a measure of the degree of connectivity may provide the additional property required to obtain a more general relevance criterion.

Chapter 8

Outlook

"Modern science has been a voyage into the unknown, with a lesson in humility waiting at every stop."

– Carl Sagan (Pale Blue Dot)

Our results raise a number of questions. First, if the local fluctuations in the number of interacting neighbours do not sufficiently capture the spatial structure of the disorder, which quantity can be used instead? In our topological analysis we found that connectivity might play an important role, however there is no general, established way for encoding this property in a locally defined measure. The dual tessellation approach we introduced offers some insight, but is restricted to two-dimensional graphs and can therefore only hint at the needed connectivity characterization we look for. Second, the general mechanism underlying the interplay of quenched disorder and critical behaviour remains to be found. Right now, there is a number of different criteria, namely, Harris' original one for short-ranged correlations and the generalizations discussed in Table 2.5, such as Halperin and Weinrib's criterion for very specific long range correlations and Barghathi and Vojta's for lattices which are dominantly anti-correlated. However, the complete picture is still missing. Third, how can topological disorder be made accessible to analytical methods? This question is in fact directly related to the previous ones. As detailed earlier in this work, handling general types of disorder would require to pinpoint the relevant properties which establish the connectivity behaviour and re-formulate them as a random variable with a suitable distribution – an undertaking which is certainly highly non-trivial. As long as analytical descriptions are out of reach, it becomes

clear that numerical simulations are the go-to method for studying the influence of spatially correlated quenched disorder on critical phenomena – the additional puzzle pieces that these simulations gradually reveal should allow a helpful, increasingly clear glimpse at the complete picture. Looking forward, a number of lines of inquiry suggest themselves, which we will briefly discuss in the following.

8.1 Random fields

A promising approach for studying topological disorder might be to take one step back and construct *regular* lattices with random interactions that obey a pre-defined correlation structure. This can, for instance, be realized by interactions strengths which are modelled according to so-called random fields [353]. A random field is a random function $z : \Omega \to \mathbb{R}$, where $\Omega \in \mathbb{R}^d$ such that for any position $x_i \in \Omega$ the quantity $z(x_i)$ is a random variable. If z follows a multi-variate normal distribution, we have a Gaussian random field (GRF). In this case, the field is only characterized by its mean $\mu(x) = \mathbb{E}[z(x)]$ and covariance $C(x_1, x_2) = \mathbb{E}[z(x_1)z(x_2)]$, where $\mathbb{E}$ denotes the expectation value. Without loss of generality we can take $\mu = 0$. Furthermore, let us assume the field to be homogenous, i. e. the covariance is invariant under translations, $C(x_1, x_2) = C(|x_1 - x_2|) \equiv \zeta(r)$. A couple of realizations of random fields with given correlation structure are shown in Figure 8.1. They have been generated by a spectral decomposition of the covariance matrix using Fast Fourier transforms (FFT). The randomness is introduced as a white noise in Fourier space and the field is finally transformed back to real coordinates. If the power spectrum $\gamma(k)$, which essentially represents the Fourier transform of the correlation function ζ, can be computed analytically, the generation of a GRF can be carried out with less sampling and discretization errors, as only a single FFT is necessary. Other methods to generate Gaussian random fields include Cholesky decompositions of the covariance matrix or more sophisticated spectral methods, such as circulant embedding techniques [354]. Our goal is to use the height of the random field $z(x)$ as bond strengths in, for instance, ferromagnetic models. Therefore, it makes sense to transform the Gaussian distribution to a finite non-negative one, naturally resulting in a so-called non-Gaussian random field. In the examples of Figure 8.1, the fields have been transformed to uniformly distributed values in a closed, finite interval. While transformations like this are technically simple, they will in general alter the correlation structure. Even though there exists some literature pointing out how this can be circumvented [355–357], the corresponding techniques turn out to be quite involved.

In a preliminary study, we simulated the two-dimensional Ising model on a lattice where interactions strengths were modelled according to a random field with power spectrum

$$\gamma(k) \propto \frac{1}{k^2 + \xi^{-2}},$$

which transforms to interaction correlations that decay exponentially with real-space distance. The characteristic spatial scale is given by ξ. As a result, disorder can be regarded as effectively uncorrelated and the system should show no clear universal behaviour to due to the marginality of the problem with respect to the Harris criterion, which was indeed found in our simulations. The next step would be to expand this study to random-bond lattices with other than exponentially decaying correlation structure (compare, e. g. Figure 8.1) and to resort to

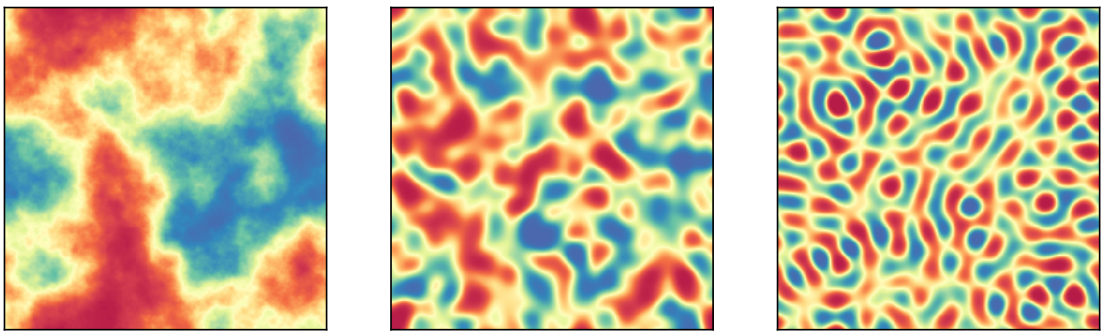

(a) (b) (c)

Figure 8.1 | Random fields. Realizations of random fields with different correlation structure, sampled on 512×512 points. All fields have initially been constructed as Gaussian random fields using spectral methods and were transformed to uniform distributions afterwards. Colours encode the height of the field in the interval [0,1]. (a) Scale-free fractal random field, constructed from a power spectrum $\gamma(k) = |k|^{-1}$. (b) Gaussian correlation structure $\zeta(x) = \exp(-|x|^2/\xi^2)$ with reference scale $\xi = 20$. (c) Damped wave correlations $\zeta(x) = \exp(-|x|/\tau)\cos(2\pi|x|/\xi)$ with decay scale $\tau = 20$ and wavelength $\xi = 50$.

a physical model other then Ising model (i. e. one which does not represent a borderline case in terms of the Harris criterion). Eventually, the goal would be to map topological structures to a regular lattice with varying interactions strengths, hence fulfilling the original ambition of answering the question as to which is the relevant measure or observable that captures the structure of the randomness.

8.2 More topological disorder

In addition to the study of correlated regular lattices, one might also continue to investigate further random graphs. Particularly interesting are those structures which in a certain limit become regular. For instance, applying a neighbour search with appropriate radius to a square grid of regularly spaced points will result in a regular lattice. Similarly, constructing the Delaunay triangulation of a triangular point grid will yield a regular triangular lattice. Therefore, jittered regular point clouds can provide a natural passage from ordered to topologically disordered structures, with the jittering amplitude acting as the control parameter. In principle this should also work for our CC lattice algorithm. As however the dynamic rewiring process is stochastic, a fully regular topology is not guaranteed although after a sufficiently long relaxation, the lattice can certainly be regarded as quasi-regular. A smooth passage from a regular topology to a random one has the particular advantage that the scaling functions can be monitored as the disorder is increased. As demonstrated e. g. in Reference [260] this allows to reliably detect the presence or absence of clean universal behaviour and hence avoids potential ambiguities related to strong scaling corrections in other standard FSS methods.

Also the CC lattice itself might inspire a number of further studies. Although the Harris criterion is commonly applied to both equilibrium and non-equilibrium transitions, recent studies of models in the Manna class raised doubt about whether the criterion is generally applicable in the latter case. Namely, in a series of articles [344, 358, 359], it was revealed

that both discrete and continuum realizations of the Manna class display unchanged critical behaviour when strong disorder in the form of random impurities is present. Since, due to a correlation length exponent of $\nu \approx 0.8$, Harris' inequality predicts disorder to be relevant in this case, these unexpected results remain to be explained. In this work we have demonstrated that in two dimensions the CC lattice behaves somewhat similar to "traditional" uncorrelated randomness. One might therefore ask whether this unexpectedly stable behaviour of the Manna class persists in the CC construction as well. Note that our study of the conserved Manna sandpile model on the VG can not contribute to resolving the "Manna anomaly", since on this structure, it should obey the generalized criterion by Barghathi and Vojta rather than the original Harris criterion.

Still with regard to the CC construction, also the study of the three-dimensional Ising model could be extended. As detailed earlier, the clean universal behaviour found in our simulations comes as a surprise. As the CC lattice is particularly designed in a way to be inaccessible to existing disorder relevance criteria, obviously no predictions are available and the results remain unexplained. To shed more light on this situation, one might for instance think of realizing a variation of the CC lattice where on half of the points has four neighbours and the other half has six. This construction should therefore have exactly five neighbours on average. Moreover, although not a CC lattice in the strict sense, the morphology should presumably be very similar to a pure CC4 or CC6. This, in turn, makes a strong case for a still clean universal behaviour of the 3D Ising model also being present on this structure. However, since in this case coordination number fluctuations do exist, the criterion by Barghathi & Vojta can be applied and the decay exponent should present a slow decay, if the distribution of 4-nodes and 6-nodes is sufficiently mixed, and therefore predict the universal character to be changed, hence possibly resulting in a further violation of the HBV criterion.

Finally, the unexpectedly stable behaviour of the CC lattice in three dimensions should be further explored by considering other physical systems. Particularly, as we found the Ising transition with a clean correlation length exponent of $\nu_{\text{Ising}}^{\text{3D}} \approx 0.630$ to be unaffected by the disorder, this demands considering a transitions with smaller exponents, as they should be less stable. Natural candidates are again the DP and Manna class, with their exponents $\nu_{\text{DP}}^{\text{3D}} \approx 0.584$ and $\nu_{\text{Manna}}^{\text{3D}} \approx 0.594$, respectively. For instance, one may ask whether the character of the DP transition will change, namely to being controlled by an infinite-random fixed point with activated scaling, accompanied by strong Griffiths effects, as it is the case for conventional disorder in three dimension [330]. If the DP transitions instead turns out to be stable as well, i. e. unaffected by the disorder, the Manna universality class should be considered. In this case, if the Manna class were revealed to be unstable on the CC lattice, this would present another strong indication that equilibrium and non-equilibrium phenomena should not be treated on the same footing in terms of the relevance of quenched disorder (compare above discussion).

8.3 Curved manifolds

To conclude this thesis, let us discuss an application of topological randomness which might not be obvious at a first glance: *curved manifolds*, i. e. spaces with non-Euclidean geometry. Even though cosmological phase transitions (such as it is believed to have taken place in the early universe) may come to mind as obvious examples of critical behaviour in curved spaces, there are in fact many more situations where physical phenomena are crucially altered by the effects of the supporting geometry, ranging from magnetic properties of artificially fabricated nano-devices [360–362], soft materials [363], aspects of complex networks [364, 365] such as information infrastructure [366], quantum gravity [367–369], bio-membranes [370], glass transitions [371, 372], up to adsorption and coating phenomena on non-flat surfaces [372]. From the theoretical point of view, due to the introduction of additional control parameters (e. g. the curvature radius), curved spaces represent a very intuitive extension of the usual *flat* geometry. Induced by the non-trivial geometry, established physical systems might behave substantially different or even produce entirely new effects. This, in turn, can help to gain a deeper insight into the physics of the corresponding flat models, whenever the corresponding limit is available.

Even though it is a rather simple and well-understood concept, ordinary diffusion – due to its importance as a substantial biophysical mechanism – has been addressed in curved environments [370, 373, 374]. In particular, it was found that on a manifold with constant negative curvature (a so-called *hyperbolic* space) diffusive motion is accelerated [375] but slowed down on *spherical* geometries, where the curvature is positive [376]. Regarding critical phenomena, the Ising model has been investigated on sphere-like lattices and other compact topologies (see e. g. [377–380]). It was revealed that in the thermodynamic limit, such systems feature the same universality class as the flat Ising model. The arguably more interesting case, however, concerns hyperbolic manifolds, which are, unlike spheres, non-compact spaces. There, one has found strong indications that the critical exponents take on their corresponding mean-field values as the hyperbolic grid (compare Figure 8.2) can be regarded as effectively infinite-dimensional [381–383]. Moreover, even at temperatures much larger than T_c, small-sized ferromagnetic domains can be observed [384]. Despite the mean-field properties on hyperlattices, the correlation length does not diverge at criticality, rather it stays finite, thus indicating the existence of an inherent length scale linked to the curvature radius which destroys the usual concept of scale invariance at criticality [385, 386]. Also other equilibrium critical phenomena have been examined on hyperbolic lattices, including the q-state Potts model and the XY model [371, 387, 388]. For the latter, it turned out that the hyperbolic surface induces a zero-temperature glass transition even in systems without disorder. This is due to the non-commutativity of parallel transport of spin vectors which causes a breakdown of their perfect orientational order and consequently gives rise to local frustration. Even more striking novel effects were found in *percolation* systems on hyperbolic lattices [389–394]. Specifically, an intermediate phase associated with two critical thresholds arises. At the lower critical probability, infinitely many unbounded clusters emerge. At the upper critical point, these clusters join into one unique unbounded cluster, spanning the entire system. In the flat Euclidean limit, these two thresholds coincide and the intermediate phase vanishes. It was found that this behaviour is due to the non-vanishing surface-volume ratio of these lattices in the infinite-volume limit. Percolation on hyperlattices was also studied quantitatively by means of finite-size scaling methods [395], where the authors suggested that

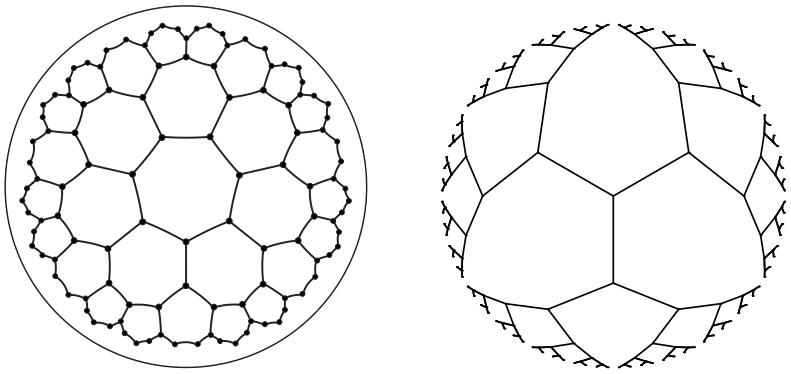

Figure 8.2 | Hyperlattices. Left: Innermost three levels of a regular tiling of the hyperbolic plane by congruent heptagons. Since three heptagons meet at each vertex, the tessellation shown here is denoted by $\{7,3\}$. In this representation, the hyperbolic plane is projected onto the Poincaré disk. Note that the circumference of the disk corresponds to an infinite distance from the centre of the disk. Right: Cayley tree $\{\infty,3\}$ with seven layers projected onto the Poincaré disk. Algorithm from [258].

hyperbolic percolation may form a universality class on its own.

Turning from the Euclidean space to geometries with constant curvature, as they arguably represent the simplest curved manifolds, one faces a number of crucial implications concerning spatial discretizations. Due to the inherent length scale, regular tilings, such as depicted in Figure 8.2 are restricted to very specific polygons and corresponding dimensions,[43] which severely limits the applicability of traditional FSS methods. Moreover, these geometric peculiarities essentially forbid the construction of periodic boundaries which appear to be indispensable when studying bulk systems due to the generically *large* boundary of hyperbolic spaces.

A clever way to circumvent most of these issues can be random lattices, where (as it was defined in Section 3), nodes are distributed in a homogeneous and isotropic fashion and are then locally linked according to a given set of rules. When dealing with curved geometries, the approach of non-regular positions of sites has the great advantage that the shape of the underlying space can be varied continuously, which appears to be a very cumbersome task for e. g. regular hyperbolic lattices [386]. As another consequence, the Euclidean limit of vanishing curvature is directly available and may thus be used as benchmark. For the hyperbolic space of constant negative curvature, random lattices allow one to use periodic boundary conditions, although their implementations is somewhat technical [259]. Besides the special cases of constant curvature, spatial discretizations in arbitrary manifolds where a proper metric tensor can be written down, should be feasible through random graphs.

In summary, random lattices have the potential to significantly enhance the study of critical phenomena on curved geometries, as they provide a convenient way to discretize these spaces, therefore making them tractable for standard numerical methods. In fact, this yields another motivation for this work. Before applying topological disorder to manifolds more complex than the flat Euclidean space, one needs to make sure that the effects of the randomness itself are properly understood.

[43] Scaling (i. e. shrinking or enlarging) a regular polygon in a hyperbolic/spherical space will also influence its shape (for instance the angles at the corners) and the regular tessellation will in general no longer cover the space without voids or overlappings. Technically speaking, there is no concept of *similarity* in curved spaces.

Appendix A

This appendix collects and presents the technical details of several numerical methods and concepts used throughout this work.

A.1 Drawbacks of the original CC algorithm

In the original algorithm of the constant coordination lattice, which was proposed in [P2], every rewiring step takes, at random, two bonds of the *full* set of bonds. Hence, the time complexity scales as $\mathcal{O}(sqN^2)$, where N is the number of sites in the lattice, q the coordination number and s the number of rewiring attempts. Even though q and s are constant parameters, the $\mathcal{O}(N^2)$ dependence alone renders the algorithm prohibitively expensive for large lattices. Besides, as the typical bond length becomes small with respect to L, random rewirings grow increasingly unlikely to satisfy condition (3.8) and the majority of update attempts is rejected, resulting in a slow convergence which demands a very large number of steps s.

The need for a large number of rewiring steps can be mitigated by starting the rewiring procedure from a configuration that already has a certain degree of locality, instead of being fully random. Such an initial configuration can be obtained simply by, considering only sites with fewer than q bonds, randomly linking those sites to their nearest neighbours until each site has exactly q bonds. This requires the full distance matrix of the sites to be known, which can be calculated in $\mathcal{O}(N \ln N)$ using spatial tree techniques [396]. In practice, this initial step allows the parameter s to be reduced by about two orders of magnitude.

However, the use of an optimized initial configuration also comes with a drawback of its own: the occasional failure to produce a so-called simple graph, due to unlucky configurations, or *pathological* motifs. One such configuration arises, e. g. when the last site in the initial construction loop is left to connect to itself (all the other sites already having q bonds). Figure A.1 shows the most frequently encountered pathological or "degenerate" motifs. In the case labelled by (2), for instance, every site except for one is already fully connected. This site, however, still has two dangling connectors, which clearly would lead to a self-connection, which is illegal. Another example is the case $(1,1)^*$, where eventually two sites remain with one dangling bond each. As they, however, are already connected, this would result in a double-connection, which is also illegal. These occasional failures must be dealt with using either some involved iterative

procedure or a complete restart. In the improved CC algorithm, presented in this paper, these issues do not arise in the first place, as fully random initial connections are sufficient, as pointed out in Section 3.3.3.

Finally, the original algorithm does not fulfil micro-scale equivalence strictly. Even though the initial connection step connects most of the sites locally, typically a few larger bonds spanning a significant part of the system can not be avoided, hence introducing a dependence on the lattice size. Therefore, in order to achieve micro-scale equivalence, larger lattices must be subjected to longer SA procedures, i.e., instead of a constant parameter s, we have a function $s = s(L)$, which is an undesirable additional parameter and a possible source of error.

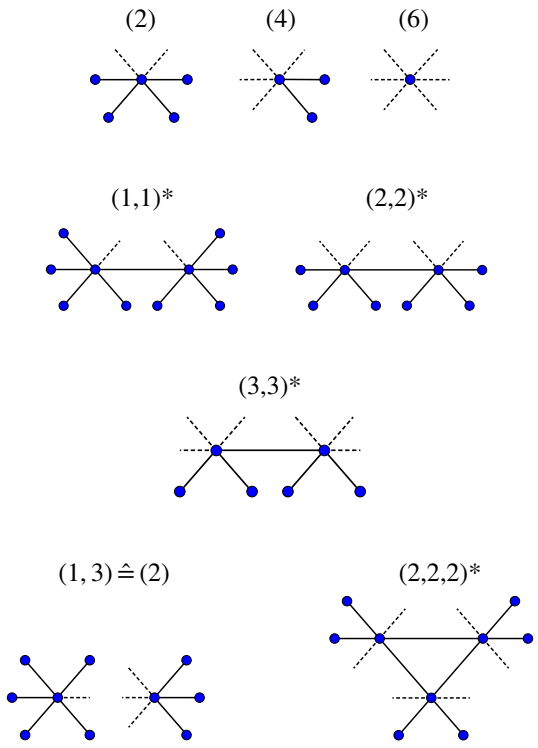

Figure A.1 | Pathological motifs of the originally proposed CC lattice algorithm. Dashed lines symbolize open connectors (which form a bond when two are closed/connected) at the end of the initial construction step, whereas the peripheral blue dots represent sites that are already fully connected.

A.2 Statistical bias

This appendix provides a detailed explanation of how systematic bias arises when a non-linear combination of physical observables is estimated from a finite sample size. It is based on Reference [273], however, for the sake of clarity, the notation was slightly adjusted and a couple of intermediate steps were added in the calculations.

In this work we usually consider two averages, the *thermal average* of an observable on one disorder realization (replica) of the system, as well as the average over disorder realizations, the *replica average*. For the disorder realizations we assume them to be drawn from a state space $R = \{r_1, r_2, \ldots\}$ which is huge although finite, since even for topological disorder the number of possible bond configuration is bound. The probability of drawing a specific sample is $p(r)$. As soon as the disorder replica is drawn, we have another state space of spin configurations $S = \{\sigma_1, \sigma_2, \ldots\}$ with probability distribution $\pi(\sigma; r)$ being a Boltzmann distribution. Note, that π depends on r. We use the notation $\langle \ldots \rangle$ for *thermal expectation values*, i.e.

$$\langle A \rangle_r \equiv \sum_{\sigma \in S} \pi(\sigma; r) A(\sigma, r) \tag{A.1}$$

where the subscript r denotes the specific replica which is considered. In case the calculations holds for any r the subscript is omitted.

In practice, our goal is to calculate an observable, given by

$$\mathcal{O}_n \equiv \overline{\langle A \rangle^n} = \sum_{r \in R} p(r) \langle A \rangle_r^n = \sum_{r \in R} p(r) \left[\sum_{\sigma \in S} \pi(\sigma; r) A(\sigma, r) \right]^n \tag{A.2}$$

where we introduced the overline notation for the *replica expectation value*. In a simulation we draw N_r disorder samples denoted by $r_1, r_2, \ldots, r_{N_r}$ from R and N_m samples (measurements) $\sigma_1, \sigma_2, \ldots \sigma_{N_m}$ from S on every replica r. Hence we can write down an *estimator* for $\mathcal{O}$ as [273]

$$\mathcal{O}_n^{\text{est}} \equiv \frac{1}{N_r} \sum_{i=1}^{N_r} [A]_{r_i}^n \equiv \frac{1}{N_r} \sum_{i=1}^{N_r} \left(\frac{1}{N_m} \sum_{j=1}^{N_m} A(\sigma_j, r_i) \right)^n \tag{A.3}$$

At this point it is important to emphasize the conceptual distinction between expectation values and averages. Whereas the former, Equation (A.2), represent the exact, but of course unknown result, the average, Equation (A.3) represent an approximation, which due to the finite sample size, fluctuate around the respective expectation value. For *thermal average* we use square brackets with subscript as defined in Equation (A.3).

The central question is now whether $\mathcal{O}_n^{\text{est}} \to \mathcal{O}_n$ for $N_r \to \infty$ at fixed N_m. As we will see, for $n = 1$ this is in fact the case, whereas for $n = 2$ a correction term (bias) arises.

The estimator Equation (A.3) can be recast as

$$\mathcal{O}_n^{\text{est}} = \frac{1}{N_r} \sum_{r \in R} \sum_{i=1}^{N(r)} [A]_{r_i}^n \tag{A.4}$$

where $N(r)$ denotes the number of r_i such that $r_i = r$, since in general the same configuration

can be drawn multiple times. We multiply by a factor $N(r)/N(r)$ and perform the limit $N_r \to \infty$

$$\lim_{N_r\to\infty} \sum_{r\in R} \frac{N(r)}{N_r} \left(\frac{1}{N(r)} \sum_{i=1}^{N_r} [A]_{r_i}^n \right) = \sum_{r\in R} p(r) \langle [A]_r^n \rangle_r = \overline{\langle [A]^n \rangle} \tag{A.5}$$

where we used that $N(r)/N_r \to p(r)$ according to the law of large numbers and the average converges to the corresponding thermal expectation value due to ergodicity. The last equality holds per definition of the replica expectation value.

We now consider the case $n = 1$ for one specific replica r and obtain

$$\langle [A] \rangle_r = \langle \frac{1}{N_m} \sum_{j=1}^{N_m} A(\sigma_j, r) \rangle_r = \frac{1}{N_m} \sum_{j=1}^{N_m} \langle A(\sigma_j, r) \rangle_r = \langle A \rangle_r \tag{A.6}$$

where we used the linearity of the expectation value. Hence,

$$\mathcal{O}_1^{\text{est}} \to \overline{\langle [A] \rangle_r} = \overline{\langle A \rangle_r} = \mathcal{O}_1 \qquad \text{for} \quad N_r \to \infty \tag{A.7}$$

i. e. the estimator $\mathcal{O}_1^{\text{est}}$ converges to $\mathcal{O}_1$ for any fixed (i. e. even for very small) N_m.

Let us now consider the case $n = 2$. We obtain

$$\begin{aligned} \langle [A]^2 \rangle_r =& \langle \frac{1}{N_m^2} \sum_{j_1=1}^{N_m} \sum_{j_2=1}^{N_m} A(\sigma_{j_1}, r) A(\sigma_{j_2}, r) \rangle_r \\ =& \frac{1}{N_m^2} \sum_{j_1=1}^{N_m} \sum_{j_2=1}^{N_m} \langle A(\sigma_{j_1}, r) A(\sigma_{j_2}, r) \rangle_r \\ =& \frac{1}{N_m^2} \left[N_m (N_m - 1) \langle A \rangle_r^2 + N_m \langle A^2 \rangle_r \right] \\ =& \langle A \rangle_r^2 - \frac{1}{N_m} \left(\langle A \rangle_r^2 - \langle A^2 \rangle_r \right) \end{aligned} \tag{A.8}$$

and therefore

$$\mathcal{O}_2^{\text{est}} \to \overline{\langle [A]^2 \rangle_r} = \mathcal{O}_2 + \frac{1}{N_m} \left(\overline{\langle A^2 \rangle_r} - \overline{\langle A \rangle_r^2} \right) \neq \mathcal{O}_2 \qquad \text{for} \quad N_r \to \infty. \tag{A.9}$$

Hence the estimator systematically underestimates the true value of $\mathcal{O}_2$ by a factor proportional to $1/N_m$. The correction term is what we call *bias* of the estimator.

A.3 Bootstrap and Jackknife

A powerful set of techniques, which allows to estimate parameter uncertainties, covariances and reduce the statistical bias arising in non-linear combinations of averages, is given by so-called *resampling methods*. In the following we give a brief introduction of this concept, based on the standard textbooks [288, 289], which are here the implicit references. Specifically for the application in Monte Carlo simulations of equilibrium spin systems, a compact summary is provided in Reference [397]. The key idea of resampling is to generate new samples from the original data pool by drawing combinations of subsamples and analyse the correlation structure among them. To be specific, suppose we have a set of n data points, for instance independent measurements of a physical quantity, denoted by

$$\mathbf{X} = \{X_1, X_2, \dots X_n\}. \tag{A.10}$$

In Monte Carlo simulations, the samples X_i are typically generated by dividing the time series of N_m measurements into n blocks, with the their size being chosen large enough to render consecutive blocks effectively uncorrelated.

We seek to calculate a quantity $f(\mathbf{X})$ from the data set, which for now is some function of the average of $\mathbf{X}$. Later in this section, we will generalize the procedure to non-parametric objects, such as parameters of a fit.

In the *delete-1-Jackknife* method, we define a Jackknife replica $X_{(j)}$ as the set which includes all samples *except* X_j, i. e.

$$\mathbf{X}_{(j)} \equiv \{X_1, X_2, \dots X_{i-1}, X_{i+1}, \dots, X_n\}. \tag{A.11}$$

The estimator of $f(\cdot)$ for the j-th Jackknife sample is formally denoted as

$$\hat{\theta}_{(j)} \equiv f(\mathbf{X}_{(j)}) \tag{A.12}$$

and we write the average over the individual Jackknife replicas as

$$\hat{\theta}_{(\cdot)} = \frac{1}{n} \sum_{k=1}^{n} \hat{\theta}_{(k)}. \tag{A.13}$$

The variance of the estimator is now defined as

$$\mathrm{Var}(\hat{\theta}) \equiv \frac{n-1}{n} \sum_{k=1}^{n} \left(\hat{\theta}_{(k)} - \hat{\theta}_{(\cdot)} \right)^2, \tag{A.14}$$

where the factor $n-1$ in the numerator compensates for the reduction of variance due to repeatedly using almost identical samples. An important feature of resampling techniques is that they allow for the construction of unbiased estimators (compare the general discussion in Section 4.1.4). Specifically for Jackknife, it can be shown that for

$$\hat{\theta}^{\mathrm{Jack}}_{\mathrm{unb}} = n\hat{\theta} - (n-1)\hat{\theta}_{(\cdot)} \tag{A.15}$$

the leading bias correction vanishes. Here, $\hat{\theta} = f(\mathbf{X})$.

A related resampling technique is the *Bootstrap* method, where one also generates a number n_B of new sets of samples from $\mathbf{X}$, but in this case by drawing n measurements X_i at *random*, i. e.

$$\mathbf{X}_{(j)} \equiv \{X_1^*, X_2^*, \ldots, X_n^*\}. \tag{A.16}$$

where $j = 1, \ldots, n_B$ and $X_i^* \in \mathbf{X}$ (random). Note that an individual sample may be drawn multiple times (sampling with replacement). Similar to the Jackknife method, we define the estimator of $f(\cdot)$ for the j-th Bootstrap replica as

$$\hat{\theta}_{(j)} \equiv f(\mathbf{X}_{(j)}) \tag{A.17}$$

and the average over the individual Bootstrap replicas is denoted by

$$\hat{\theta}_{(\cdot)} = \frac{1}{n_B} \sum_{k=1}^{n_B} \hat{\theta}_{(k)}, \tag{A.18}$$

where the number of Bootstrap samples n_B can be chosen as a free parameter. As a rule of thumb, however, a number of 100–500 replicas is usually a good choice, depending on the quality of the data set [397]. The variance of the estimator is now defined as

$$\mathrm{Var}(\hat{\theta}) \equiv \frac{1}{n_B - 1} \sum_{k=1}^{n_B} \left(\hat{\theta}_{(k)} - \hat{\theta}_{(\cdot)} \right)^2. \tag{A.19}$$

One particular strength of resampling methods is that they allow us to compute uncertainties and correlations of problems which do not rely on a parametric formulation of an underlying theoretical model. In order to illustrate how this can be implemented, suppose that we have an *ordered* data sample

$$\mathbf{Y} = \{Y_1, Y_2, \ldots Y_n\}, \tag{A.20}$$

which could, for instance, represent the mean values of some observables for different lattice sizes. We want to perform a fit, which is symbolically denoted by

$$\hat{\theta} = S(\mathbf{Y}), \tag{A.21}$$

resulting in a vector of fit parameters $\hat{\theta}$. How can we calculate uncertainties for these fit parameters? Propagating the uncertainties of the original data pool through a fit (or a non-parametric object in general), effectively results in a vectorized Bootstrap resampling. This requires to measure each Y_i several times, i. e. strictly speaking, $\mathbf{Y}$ represents a set of sets

$$\mathbf{Y} = \{\mathbf{Y}_1, \mathbf{Y}_2, \ldots, \mathbf{Y}_m\} \tag{A.22}$$

$$= \{\{Y_{1,1}, \ldots Y_{1,n}\}, \{Y_{2,1}, \ldots Y_{2,n}\}, \ldots, \{Y_{m,1}, \ldots Y_{m,n}\}\}, \tag{A.23}$$

where, in general, $m \neq n$. We are now able to construct n_B bootstrap replicas $\mathbf{Y}_{(k)}$ by drawing randomly from each respective subset, i. e.

$$\mathbf{Y}_{(k)} = \{\mathbf{Y}_1^*, \mathbf{Y}_2^*, \ldots, \mathbf{Y}_m^*\} \tag{A.24}$$

$$= \{\{Y^*_{1,1}, \dots Y^*_{1,n}\}, \{Y^*_{2,1}, \dots Y^*_{2,n}\}, \dots, \{Y^*_{m,1}, \dots Y^*_{m,n}\}\}, \tag{A.25}$$

where $Y^*_{i,j} \in \mathbf{Y_i}$ (random) for $i = 1, \dots, m$, $j = 1, \dots, n$ and $k = 1, \dots, n_B$. For each replica $\mathbf{Y}_{(k)}$, we compute the averages of the individual resampled data points, i. e.

$$\overline{\mathbf{Y}}_{(k)} = \{Y^*_1, Y^*_2, \dots, Y^*_m\}, \tag{A.26}$$

where

$$Y^*_i = \frac{1}{n} \sum_{j=1}^{n} Y^*_{i,j} \tag{A.27}$$

and use these to compute

$$\hat{\theta}_{(k)} = S(\overline{\mathbf{Y}}_{(k)}), \tag{A.28}$$

resulting in a number of n_B fit parameter vectors, from which the final estimates, as well as their corresponding uncertainties can be computed straightforwardly, using Equations (A.18) and (A.19). Furthermore, the covariance matrix is given by

$$\Gamma_{\alpha\beta}(\hat{\theta}) \equiv \frac{1}{n_B - 1} \sum_{k=1}^{n_B} \left(\hat{\theta}_{\alpha(k)} - \hat{\theta}_{\alpha(\cdot)}\right) \left(\hat{\theta}_{\beta(k)} - \hat{\theta}_{\beta(\cdot)}\right) \tag{A.29}$$

where, $\hat{\theta}_{\alpha(k)}$ represent the results for the α-th fit parameter in the Bootstrap replica with index k and $(\cdot)$ denotes the corresponding average

$$\hat{\theta}_{\alpha(\cdot)} = \frac{1}{n_B} \sum_{k=1}^{n_B} \hat{\theta}_{\alpha(k)}. \tag{A.30}$$

Finally, by means of the Bootstrap analysis, we are also able to compute cross-correlations among the data points. The corresponding covariance matrix is given by

$$\mathrm{C}_{ij}(Y) \equiv \frac{1}{n_B - 1} \sum_{k=1}^{n_B} \left(Y^*_{i(k)} - Y^*_{i(\cdot)}\right) \left(Y^*_{j(k)} - Y^*_{j(\cdot)}\right) \qquad i, j = 1, \dots, m \tag{A.31}$$

where $Y^*_{i(k)}$ denotes the i-th (averaged) data point of the k-th Bootstrap replica and $Y^*_{i(\cdot)}$ is the average of the corresponding data point over all replicas, as before.

A.4 Covariance matrix

We seek to perform fits which minimize a general χ^2, given in terms of an inverse covariance matrix, which accounts for cross-correlations among the data points by

$$\chi^2 = \sum_{l=1}^{N} \sum_{m=1}^{N} (x_l - \text{fit})\, C_{lm}^{-1}\, (x_m - \text{fit}), \tag{A.32}$$

where N denotes the length of the data set. The covariance matrix can readily be computed from bootstrap methods [288, 289], using the formula

$$C_{lm} = \frac{1}{n_B} \sum_{i=1}^{n_B} (\tilde{x}_{l,i} - \langle x_l \rangle)(\tilde{x}_{m,i} - \langle x_m \rangle), \tag{A.33}$$

where n_B denotes the number of bootstrap samples. Moreover, $\tilde{x}_{l,i}$ denotes the l-th out of N data points in the bootstrap sample with index i and $\langle x \rangle$ is the corresponding average over all bootstrap samples.

A sufficient condition for the covariance matrix to be invertible is that the matrix is positive definite, which should apply by construction. However, numerically it turns out that this is not the case, even if, in our Python implementation, we use `math.fsum` (rather than `numpy.sum`) for carrying out the summations in Equation (A.33). Since, especially in joint fits consisting of several observables, huge differences in the orders of magnitudes of the individual entries can be expected, `math.fsum` is more robust against numerical rounding errors.

As a consequence of the covariance matrix being non-symmetric due to numerical uncertainties, we need to "repair" it, which is done in multiple steps. First, we symmetrize C by computing

$$C_{\text{sym}} = \frac{1}{2}(C + C^T). \tag{A.34}$$

For joint fits such as performed in this work one now typically faces the problem that the covariance matrix is rank deficient due to the strongly correlated blocks it is build of. In order to circumvent this problem, we compute the spectral decomposition and neglect contributions from some of the smallest eigenvalues. Specifically,

$$C_{\text{sym}} = Q \Lambda Q^{-1} \tag{A.35}$$

where Q is a square matrix which contains the eigenvectors of C_{sym} as columns and Λ is the diagonal matrix built from the corresponding eigenvalues. Numerically, it turns out that the eigenvalues and eigenvectors depend noticeably on the algorithm used for the decomposition. In particular, we compared `numpy.linalg.eig` which can be regarded as the generic implementation for that purpose and `numpy.linalg.eigh` which exploits the fact that C_{sym} is symmetric by using appropriately specialised routines. Eventually, we found that in our case both routines tend to behave numerically unstable due to large differences in numerical values mentioned already and therefore resorted to a *singular value decomposition*

$$C_{\text{sym}} = U \Sigma V^T \tag{A.36}$$

by using `numpy.linalg.svd` instead, which turns out to be considerably more robust. For details on the singular value decomposition, we refer the reader to standard textbooks, such as [398]. Since, in our case, C_{sym} is a square matrix, also U, Σ and V are. Furthermore, Σ is diagonal and contains the singular values s_i, i. e.

$$\Sigma = \text{diag}(s_1, s_2, \ldots, s_N). \tag{A.37}$$

We reconstruct the covariance matrix by means of a *principal component analysis* [399],

$$C_{\text{PCA}} \equiv U\tilde{\Sigma}V^T, \tag{A.38}$$

where

$$\tilde{\Sigma} = \text{diag}(s_1, s_2, \ldots, s_M, 0, \ldots, 0), \qquad M < N \tag{A.39}$$

and where we assume that the singular values are ordered according to their size, $s_1 \geq s_2 \geq \ldots \geq s_M$. Hence, any contributions from the smallest $N - M$ singular values are neglected. According to [400], the optimal threshold for square matrices is given by 2.858 times the median of the s_i. The reconstructed matrix is still rank deficient. In order to obtain a full rank matrix, we add a so-called isotropic noise [401]

$$C_{\text{SPD}} = C_{\text{PCA}} + \beta I, \tag{A.40}$$

where I denotes the identity and β is given by

$$\beta = \text{tr}(C_{\text{sym}}) - \text{tr}(C_{\text{PCA}}). \tag{A.41}$$

This procedure conserves the trace of the covariance. In summary, we found a symmetric positive semi-definite reconstruction of the original covariance matrix, given by Equation (A.40), which can be used in the fitting procedure.

Appendix B

Supplementary Material

Table B.1 provides detailed simulation settings for the Ising model on the DT, performed in Section 5.2, and Table B.2 lists fit results for the critical temperature of this simulations, according to Equation (5.12). Moreover, in Figures B.1 and B.2, we present data collapses for the contact process on the grand-canonical DT^+ lattice, mentioned in Section 5.3. Finally, Table B.3 presents the detailed fit results for the running critical exponents of the Ising model on CC and DT lattices, investigated in Section 5.1.

L	N_r	n_{Wolff}
16, 18, 20, 24	100 000	10
32, 36, 40, 48	100 000	12
64, 80, 96	100 000	15
128, 192, 256	35 000	17
384, 512	15 000	23
768	5000	27
1024	4000	29

Table B.1 | Number of disorder replicas and cluster updates (Ising, VG). Number of disorder replicas and cluster updates per EMCS for simulations of the Ising model on two-dimensional Voronoi graphs at criticality. All systems were simulated at $T = 1.47205$.

Table B.2 | Critical temperature (Ising, VG). Results of the fits according to Equation (5.12) with fixed $\nu = 1$. The results are graphically displayed in Figure 5.7.

	ω =1.70		ω =1.54		ω =1.38				
L_{min}	T_c	χ^2/d.o.f	T_c	χ^2/d.o.f	T_c	χ^2/d.o.f	T_c	ω	χ^2/d.o.f
16	1.472009(15)	32.9	1.472031(15)	8.8	1.472040(15)	16.8	1.4720607(17)	1.495(12)	7.5
18	1.472686(15)	13.2	1.472619(15)	4.0	1.472541(15)	18.4	1.4720624(17)	1.552(15)	3.9
20	1.472673(15)	7.9	1.472615(15)	3.9	1.472548(15)	18.6	1.4720631(17)	1.582(21)	3.3
24	1.472659(15)	4.0	1.472616(15)	4.4	1.472566(15)	14.7	1.4720639(18)	1.626(32)	3.2
32	1.472650(16)	3.2	1.472622(16)	4.1	1.472590(16)	8.1	1.4720645(20)	1.668(55)	3.8
40	1.472651(16)	3.8	1.472631(16)	3.5	1.472608(16)	4.5	1.4720636(24)	1.582(98)	7.3
48	1.472653(17)	4.6	1.472637(17)	3.6	1.472619(17)	3.2			
64	1.472645(19)	5.0	1.472635(20)	4.3	1.472623(20)	3.8			

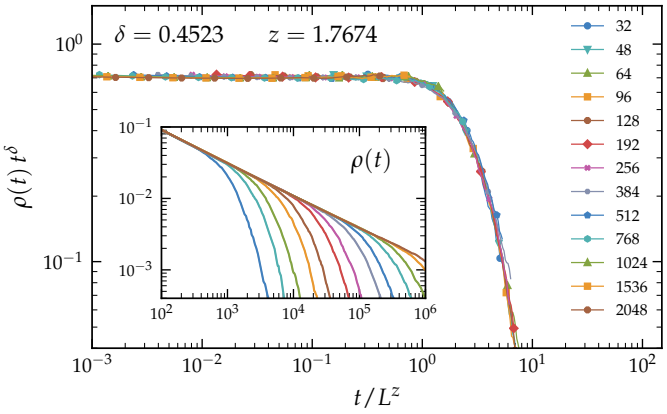

Figure B.1 | Finite-size data collapse (CP, DT^{+}_{GC}). Simulations starting from a fully occupied grand-canonical DT^{+} lattice at the critical point $p_c = 0.588311$, using the critical exponent estimates stated in the figure. All curves are averages over 800 disorder realizations with 5 runs per realization. L denotes the linear system size. The inset shows the non-rescaled density as a function of time.

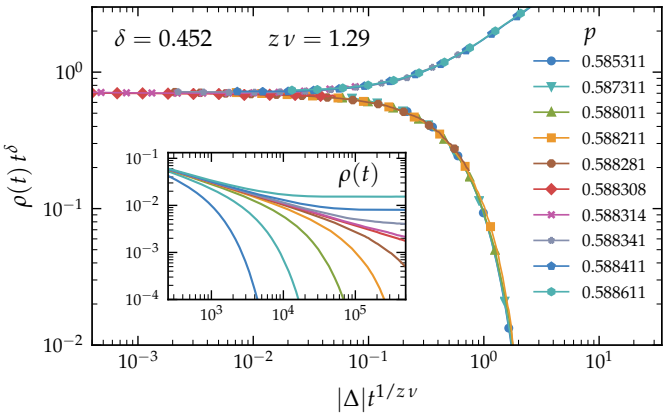

Figure B.2 | Critical region collapse (CP, DT^{+}_{GC}). Data collapse near criticality, starting from a fully occupied grand-canonical DT^{+} lattice of linear size $L = 2048$ using the critical exponent estimates given in the figure. All curves are averages over 250 disorder realizations, with 5 runs per realization. The symbol Δ denotes the distance from the critical point $p_c = 0.588311$. The inset shows the non-rescaled density as a function of time.

	L	N_{fits}	ν	N_{fits}	γ/ν	N_{fits}	$(1-\beta)/\nu$	N_{fits}	β/ν
DT		$Q > 0.2$		$Q > 0.2$		$Q > 0.2$		$Q > 0.8$	
	32	4	1.0139(28)	3	1.7620(23)	2	0.8670(28)	2	0.1191(28)
	48	4	1.0125(2)	3	1.7612(16)	2	0.8681(20)	3	0.1212(22)
	64	16	1.0107(9)	5	1.7638(12)	6	0.8706(6)	5	0.1215(21)
	80	25	1.0082(5)	6	1.7606(7)	7	0.8707(4)	6	0.1240(17)
	96	28	1.0063(5)	7	1.7583(6)	7	0.8714(4)	6	0.1243(17)
	128	28	1.0051(4)	7	1.7570(6)	7	0.8719(4)	6	0.1247(17)
	160	28	1.0045(5)	7	1.7556(6)	7	0.8722(4)	6	0.1249(17)
	192	28	1.0042(5)	7	1.7543(5)	6	0.8721(4)	5	0.1245(17)
	256	28	1.0038(5)	7	1.7538(6)	7	0.8726(5)	5	0.1242(18)
	320	27	1.0036(6)	6	1.7536(7)	6	0.8730(7)	4	0.1241(23)
CC4		$Q > 0.01$		$Q > 0.2$		$Q > 0.3$		$Q > 0.6$	
	32	7	1.156(11)	7	1.779(5)	3	0.784(19)	7	0.101(5)
	48	3	1.136(8)	7	1.775(4)	3	0.791(14)	7	0.102(5)
	64	19	1.109(6)	7	1.764(7)	5	0.800(9)	7	0.103(7)
	80	28	1.0939(32)	7	1.760(8)	7	0.810(5)	7	0.105(9)
	96	28	1.0847(31)	7	1.758(8)	7	0.813(4)	7	0.107(9)
	128	28	1.0815(31)	7	1.757(8)	7	0.813(4)	7	0.110(8)
	160	28	1.0739(31)	7	1.757(8)	7	0.818(5)	7	0.112(9)
	192	28	1.0648(30)	7	1.758(8)	7	0.824(4)	7	0.115(8)
	256	28	1.0619(35)	7	1.758(10)	7	0.826(5)	7	0.116(10)
CC6		$Q > 0.05$		$Q > 0.1$		$Q > 0.3$		$Q > 0.6$	
	32	5	1.066(8)	4	1.765(6)	6	0.8417(13)	4	0.1156(29)
	48	5	1.061(6)	4	1.763(5)	6	0.8425(13)	7	0.1156(28)
	64	18	1.0470(23)	7	1.764(4)	6	0.8447(20)	7	0.119(4)
	80	24	1.0399(16)	7	1.7615(33)	7	0.8492(19)	7	0.116(5)
	96	28	1.0353(13)	7	1.7572(33)	7	0.8506(19)	7	0.1190(5)
	128	28	1.0334(12)	7	1.7546(32)	7	0.8503(18)	7	0.120(5)
	160	28	1.0307(12)	7	1.7536(33)	7	0.8512(19)	7	0.121(5)
	192	28	1.0281(12)	6	1.7546(34)	6	0.8520(22)	6	0.122(6)
	256	28	1.0268(14)	6	1.755(4)	6	0.8517(27)	6	0.123(7)

CC10		$Q > 0.1$		$Q > 0.3$		$Q > 0.3$		$Q > 0.8$	
	32	5	1.0219(18)	5	1.7630(7)	1	0.858(6)	1	0.1200(40)
	48	6	1.0207(14)	5	1.7626(6)	3	0.857(4)	3	0.1211(30)
	64	25	1.0180(6)	7	1.7616(11)	7	0.8621(9)	6	0.1243(36)
	80	28	1.0168(5)	7	1.7598(12)	6	0.8643(17)	7	0.1254(25)
	96	26	1.0143(6)	7	1.7588(12)	7	0.8651(6)	7	0.1247(27)
	128	27	1.0129(6)	7	1.7576(12)	7	0.8658(6)	7	0.1245(27)
	160	27	1.0115(6)	7	1.7563(11)	7	0.8662(6)	7	0.1251(27)
	192	28	1.0102(6)	7	1.7554(11)	7	0.8666(7)	6	0.1251(27)
	256	28	1.0099(7)	7	1.7550(13)	7	0.8668(8)	6	0.1251(33)

Table B.3 | Effective critical exponents for the DT, CC4, CC6 and CC10 lattices. Columns N_{fits} denote the number of fits with a goodness-of-fit parameter Q larger than the value indicated out of $4 \cdot 7 = 28$ fits for ν and 7 for all other exponents. L denotes the centre of the respective fitting window, compare Figure 5.4. The data is displayed in Figure 5.6.

Own Publications

P1. Schrauth, M., Portela, J. S. E. & Goth, F. Violation of the Harris-Barghathi-Vojta Criterion. *Physical Review Letters* **121,** 100601 (2018).

P2. Schrauth, M., Richter, J. A. J. & Portela, J. S. E. Two-dimensional Ising model on random lattices with constant coordination number. *Physical Review E* **97,** 022144 (2018).

P3. Schrauth, M. & Portela, J. S. E. Fast algorithm for topologically disordered lattices with constant coordination number. *Physical Review Research* **1,** 033061 (2019).

P4. Schrauth, M. & Portela, J. S. E. Universality of continuous phase transitions on random Voronoi graphs. *Physical Review E* **100,** 062118 (2019).

P5. Schrauth, M., Portela, J. S. E. & Goth, F. Relevance of topological disorder on the directed percolation phase transition. *arXiv:1907.05809* (2019).

P6. Schrauth, M. Universality of the three-dimensional Heisenberg model in disordered media with fixed interaction radius. *to be published.*

Bibliography

1. Lenz, W. Beitrag zum Verständnis der magnetischen Erscheinungen in festen Körpern. *Zeitschrift für Physik* **21,** 613–615 (1920).
2. Ising, E. Beitrag zur Theorie des Ferromagnetismus. *Zeitschrift für Physik A Hadrons and Nuclei* **31,** 253–258 (1925).
3. Kadanoff, L. P. Relating theories via renormalization. *Studies in History and Philosophy of Science Part B: Studies in History and Philosophy of Modern Physics* **44,** 22–39 (2013).
4. Curie, P. Propriétés magnétiques des corps a diverses températures. *Annales de Chimie* **5,** 289 (1895).
5. Henkel, M., Hinrichsen, H. & Lübeck, S. *Non-Equilibrium Phase Transitions - Volume 1: Absorbing Phase Transitions* (Springer Netherlands, 2008).
6. Brush, S. G. History of the Lenz-Ising model. *Reviews of Modern Physics* **39,** 883 (1967).
7. Back, C. *et al.* Experimental confirmation of universality for a phase transition in two dimensions. *Nature* **378,** 597–600 (1995).
8. Pestak, M. & Chan, M. H.-W. Equation of state of N_2 and Ne near their critical points. Scaling, corrections to scaling, and amplitude ratios. *Physical Review B* **30,** 274 (1984).
9. Abdulagatov, I., Polikhronidi, N. & Batyrova, R. Measurements of the isochoric heat capacities C_v of carbon dioxide in the critical region. *The Journal of Chemical Thermodynamics* **26,** 1031–1045 (1994).
10. Sullivan, D., Neilson, G., Fischer, H. & Rennie, A. Small angle neutron scattering from D_2O in the critical region. *Journal of Physics: Condensed Matter* **12,** 3531 (2000).
11. Guggenheim, E. A. The principle of corresponding states. *The Journal of Chemical Physics* **13,** 253–261 (1945).
12. Landau, L. D. On the theory of phase transitions. *Zhurnal Éksperimental'noĭ i Teoreticheskoĭ Fiziki* **7,** 19–32 (1937).
13. Fisher, M. E. Renormalization group theory: Its basis and formulation in statistical physics. *Reviews of Modern Physics* **70,** 653 (1998).
14. Kadanoff, L. P. Scaling laws for Ising models near T_c. *Physics Physique Fizika* **2,** 263 (1966).
15. Wilson, K. G. Renormalization group and critical phenomena. I. Renormalization group and the Kadanoff scaling picture. *Physical Review B* **4,** 3174 (1971).

16. Wilson, K. G. Renormalization group and critical phenomena. II. Phase-space cell analysis of critical behavior. *Physical Review B* **4,** 3184 (1971).
17. Stanley, H. E. Scaling, universality, and renormalization: Three pillars of modern critical phenomena. *Reviews of Modern Physics* **71,** S358 (1999).
18. Hurst, C. A. & Green, H. S. New solution of the Ising problem for a rectangular lattice. *The Journal of Chemical Physics* **33,** 1059–1062 (1960).
19. Schultz, T. D., Mattis, D. C. & Lieb, E. H. Two-dimensional Ising model as a soluble problem of many fermions. *Reviews of Modern Physics* **36,** 856 (1964).
20. Baxter, R. J. & Wu, F. Y. Exact Solution of an Ising Model with Three-Spin Interactions on a Triangular Lattice. *Physical Review Letters* **31,** 1294–1297 (1973).
21. Baxter, R. J. & Enting, I. G. 399th solution of the Ising model. *Journal of Physics A: Mathematical and General* **11,** 2463 (1978).
22. Baxter, R. *Exactly Solved Models in Statistical Mechanics* (Dover Publications, 2007).
23. Yang, C.-N. & Lee, T.-D. Statistical theory of equations of state and phase transitions. I. Theory of condensation. *Physical Review* **87,** 404 (1952).
24. Lee, T.-D. & Yang, C.-N. Statistical theory of equations of state and phase transitions. II. Lattice gas and Ising model. *Physical Review* **87,** 410 (1952).
25. Pelissetto, A. & Vicari, E. Critical phenomena and renormalization-group theory. *Physics Reports* **368,** 549–727 (2002).
26. Suzuki, H., Imura, J.-i. & Aihara, K. Chaotic Ising-like dynamics in traffic signals. *Scientific Reports* **3,** 1127 (2013).
27. Noble, A. E., Rosenstock, T. S., Brown, P. H., Machta, J. & Hastings, A. Spatial patterns of tree yield explained by endogenous forces through a correspondence between the Ising model and ecology. *Proceedings of the National Academy of Sciences* **115,** 1825–1830. eprint: `https://www.pnas.org/content/115/8/1825.full.pdf` (2018).
28. Zhou, W.-X. & Sornette, D. Self-organizing Ising model of financial markets. *The European Physical Journal B* **55,** 175–181 (2007).
29. Broadbent, S. R. & Hammersley, J. M. *Percolation processes: I. Crystals and mazes* in *Mathematical Proceedings of the Cambridge Philosophical Society* **53** (1957), 629–641.
30. Harris, T. E. Contact Interactions on a Lattice. *Annals of Probability* **2,** 969–988 (1974).
31. Von Niessen, W. & Blumen, A. Dynamics of forest fires as a directed percolation model. *Journal of Physics A: Mathematical and General* **19,** L289 (1986).
32. Hinrichsen, H. On possible experimental realizations of directed percolation. *Brazilian Journal of Physics* **30,** 69–82 (2000).
33. Takeuchi, K. A., Kuroda, M., Chaté, H. & Sano, M. Directed percolation criticality in turbulent liquid crystals. *Physical Review Letters* **99,** 234503 (2007).
34. Takeuchi, K. A., Kuroda, M., Chaté, H. & Sano, M. Experimental realization of directed percolation criticality in turbulent liquid crystals. *Physical Review E* **80,** 051116 (2009).
35. Bak, P., Tang, C. & Wiesenfeld, K. Self-organized criticality: An explanation of the 1/f noise. *Physical Review Letters* **59,** 381–384 (1987).

36. Bak, P., Tang, C. & Wiesenfeld, K. Self-organized criticality. *Physical Review A* **38,** 364–374 (1988).

37. Pruessner, G. *Self-organised criticality: theory, models and characterisation* (Cambridge University Press, 2012).

38. Manna, S. Two-state model of self-organized criticality. *Journal of Physics A: Mathematical and General* **24,** L363 (1991).

39. Bollmann, W. *Crystal defects and crystalline interfaces* (Springer Science & Business Media, 2012).

40. Crawford, J. H. & Slifkin, L. M. *Point Defects in Solids: General and ionic crystals* (Springer Science & Business Media, 2013).

41. Hull, D. & Bacon, D. *Introduction to Dislocations* Fifth Edition (Butterworth-Heinemann, Oxford, 2011).

42. Elliott, S. R. *Physics of amorphous materials* (Longman Scientific & Technical, Harlow, Essex, England, 1990).

43. Greer, A. L. Metallic glasses. *Science* **267,** 1947–1953 (1995).

44. Johnson, W. L. Bulk glass-forming metallic alloys: Science and technology. *MRS Bulletin* **24,** 42–56 (1999).

45. O'handley, R. Physics of ferromagnetic amorphous alloys. *Journal of Applied Physics* **62,** R15–R49 (1987).

46. Harris, A. B. Effect of random defects on the critical behaviour of Ising models. *Journal of Physics C: Solid State Phys* **7,** 1671 (1974).

47. Harris, A. B. The Harris Criterion lives on. *Journal of Physics: Condensed Matter* **28,** 421006 (2016).

48. Edwards, S. F. & Anderson, P. W. Theory of spin glasses. *Journal of Physics F: Metal Physics* **5,** 965 (1975).

49. Sherrington, D. & Kirkpatrick, S. Solvable model of a spin-glass. *Physical Review Letters* **35,** 1792 (1975).

50. Janke, W., Katoot, M. & Villanova, R. Ising model universality for two-dimensional lattices. *Physics Letters B* **315,** 412–416 (1993).

51. Janke, W., Katoot, M. & Villanova, R. Single-cluster Monte Carlo study of the Ising model on two-dimensional random lattices. *Physical Review B* **49,** 9644–9657 (1994).

52. Swendsen, R. H. & Wang, J.-S. Nonuniversal critical dynamics in Monte Carlo simulations. *Physical Review Letters* **58,** 86 (1987).

53. Ferrenberg, A. M. & Swendsen, R. H. New Monte Carlo technique for studying phase transitions. *Physical Review Letters* **61,** 2635–2638 (1988).

54. Ferrenberg, A. M. & Swendsen, R. H. Optimized Monte Carlo data analysis. *Physical Review Letters* **63,** 1195–1198 (1989).

55. Ferrenberg, A. M. & Swendsen, R. H. Optimized Monte Carlo data analysis. *Computers in Physics* **3,** 101–104 (1989).

56. Wolff, U. Collective Monte Carlo updating for spin systems. *Physical Review Letters* **62,** 361 (1989).

57. Janke, W. & Villanova, R. Two-dimensional eight-state Potts model on random lattices: A Monte Carlo study. *Physics Letters A* **209,** 179–183 (1995).

58. Janke, W. & Villanova, R. Ising model on three-dimensional random lattices: A Monte Carlo study. *Physical Review B* **66,** 134208 (2002).

59. Lima, F., Moreira, J., Andrade, J. & Costa, U. The ferromagnetic Ising model on a Voronoi-Delaunay lattice. *Physica A: Statistical Mechanics and its Applications* **283,** 100–106 (2000).

60. Lima, F., Costa, U., Almeida, M. & Andrade Jr, J. Critical behavior of a three-state Potts model on a Voronoi lattice. *The European Physical Journal B* **17,** 111–114 (2000).

61. Oliveira-Neto, N., Alves, S., Silva, R., Pereira, A. & Moura-Melo, W. On the topological phase transition of the two-dimensional XY-model on the Voronoi–Delaunay lattice. *Journal of Physics A: Mathematical and Theoretical* **42,** 385002 (2009).

62. Lima, F. Potts model with $q = 4, 6$, and 8 states on Voronoi–Delaunay random lattice. *Physica A: Statistical Mechanics and its Applications* **389,** 3039–3047 (2010).

63. Lima, F. W. S. & Plascak, J. A. Magnetic models on various topologies. *Journal of Physics: Conference Series* **487,** 012011 (2014).

64. Weigel, M. & Johnston, D. Frustration effects in antiferromagnets on planar random graphs. *Physical Review B* **76,** 054408 (2007).

65. De Oliveira, M. M., Alves, S. G., Ferreira, S. C. & Dickman, R. Contact process on a Voronoi triangulation. *Physical Review E* **78,** 031133 (2008).

66. De Oliveira, M. M., Alves, S. G. & Ferreira, S. C. Continuous and discontinuous absorbing-state phase transitions on Voronoi-Delaunay random lattices. *Physical Review E* **93,** 012110 (2016).

67. Barghathi, H. & Vojta, T. Phase transitions on random lattices: How random is topological disorder? *Physical Review Letters* **113,** 120602 (2014).

68. Luck, J. A classification of critical phenomena on quasi-crystals and other aperiodic structures. *EPL (Europhysics Letters)* **24,** 359 (1993).

69. Janke, W. & Weigel, M. Harris-Luck criterion for random lattices. *Physical Review B* **69,** 144208 (2004).

70. Binney, J. J., Dowrick, N. J., Fisher, A. J. & Newman, M. E. *The theory of critical phenomena: an introduction to the renormalization group* (Oxford University Press, 1992).

71. Cardy, J. *Scaling and Renormalization in Statistical Physics* (Cambridge University Press, 1996).

72. Goldenfeld, N. *Lectures on phase transitions and the renormalization group* (Westview Press, 1992).

73. Herbut, I. *A modern approach to critical phenomena* (Cambridge University Press, 2007).

74. Nishimori, H. & Ortiz, G. *Elements of Phase Transitions and Critical Phenomena* (Oxford University Press, 2010).

75. Täuber, U. C. *Critical Dynamics: A Field Theory Approach to Equilibrium and Non-Equilibrium Scaling Behavior* (Cambridge University Press, 2014).

76. Wolf, D. E., Schreckenberg, M. & Bachem, A. *Traffic and granular flow* in *Traffic and Granular Flow* (1996), 1–394.

77. Vojta, T. Quantum phase transitions in electronic systems. *Annalen der Physik* **9,** 403–440 (2000).

78. Vojta, M. Quantum phase transitions. *Reports on Progress in Physics* **66,** 2069 (2003).

79. Ehrenfest, P. Phasenumwandlungen im ueblichen und erweiterten Sinn, classifiziert nach den entsprechenden Singularitaeten des thermodynamischen Potentiales. *Proceedings of the Royal Academy of Sciences at Amsterdam* **36,** 153–157 (1933).

80. Kosterlitz, J. The critical properties of the two-dimensional XY model. *Journal of Physics C: Solid State Physics* **7,** 1046 (1974).

81. Müller, K. & Berlinger, W. Static critical exponents at structural phase transitions. *Physical Review Letters* **26,** 13 (1971).

82. Lipa, J., Nissen, J., Stricker, D., Swanson, D. & Chui, T. Specific heat of liquid helium in zero gravity very near the lambda point. *Physical Review B* **68,** 174518 (2003).

83. Barmatz, M., Hahn, I., Lipa, J. & Duncan, R. Critical phenomena in microgravity: Past, present, and future. *Reviews of Modern Physics* **79,** 1 (2007).

84. Campostrini, M., Hasenbusch, M., Pelissetto, A., Rossi, P. & Vicari, E. Critical behavior of the three-dimensional XY universality class. *Physical Review B* **63,** 214503 (2001).

85. Campostrini, M., Hasenbusch, M., Pelissetto, A. & Vicari, E. Theoretical estimates of the critical exponents of the superfluid transition in He4 by lattice methods. *Physical Review B* **74,** 144506 (2006).

86. Kos, F., Poland, D., Simmons-Duffin, D. & Vichi, A. Bootstrapping the O(N) archipelago. *Journal of High Energy Physics* **2015,** 106 (2015).

87. Kos, F., Poland, D., Simmons-Duffin, D. & Vichi, A. Precision islands in the Ising and O(N) models. *Journal of High Energy Physics* **2016,** 36 (2016).

88. Widom, B. Surface tension and molecular correlations near the critical point. *The Journal of Chemical Physics* **43,** 3892–3897 (1965).

89. Widom, B. Equation of state in the neighborhood of the critical point. *The Journal of Chemical Physics* **43,** 3898–3905 (1965).

90. Essam, J. W. & Fisher, M. E. Padé approximant studies of the lattice gas and Ising ferromagnet below the critical point. *The Journal of Chemical Physics* **38,** 802–812 (1963).

91. Rushbrooke, G. On the thermodynamics of the critical region for the Ising problem. *The Journal of Chemical Physics* **39,** 842–843 (1963).

92. Domb, C. & Hunter, D. On the critical behaviour of ferromagnets. *Proceedings of the Physical Society* **86,** 1147 (1965).

93. Griffiths, R. B. Thermodynamic functions for fluids and ferromagnets near the critical point. *Physical Review* **158,** 176 (1967).

94. Wannier, G. H. Antiferromagnetism. The triangular Ising net. *Physical Review* **79,** 357–364 (1950).

95. Vannimenus, J. & Toulouse, G. Theory of the frustration effect. II. Ising spins on a square lattice. *Journal of Physics C: Solid State Physics* **10,** L537 (1977).

96. Binder, K. & Young, A. P. Spin glasses: Experimental facts, theoretical concepts, and open questions. *Reviews of Modern Physics* **58,** 801 (1986).

97. Parola, A. & Reatto, L. Liquid state theories and critical phenomena. *Advances in Physics* **44,** 211–298 (1995).

98. Fisher, M. E. The story of coulombic critiality. *Journal of Statistical Physics* **75,** 1–36 (1994).

99. Dornic, I., Chaté, H., Chave, J. & Hinrichsen, H. Critical coarsening without surface tension: The universality class of the voter model. *Physical Review Letters* **87,** 045701 (2001).

100. Schneidman, E., Berry II, M. J., Segev, R. & Bialek, W. Weak pairwise correlations imply strongly correlated network states in a neural population. *Nature* **440,** 1007 (2006).

101. Onsager, L. Crystal statistics. I. A two-dimensional model with an order-disorder transition. *Physical Review* **65,** 117 (1944).

102. Kramers, H. A. & Wannier, G. H. Statistics of the two-dimensional ferromagnet. Part I. *Physical Review* **60,** 252 (1941).

103. Kramers, H. A. & Wannier, G. H. Statistics of the two-dimensional ferromagnet. Part II. *Physical Review* **60,** 263 (1941).

104. Newell, G. F. & Montroll, E. W. On the theory of the Ising model of ferromagnetism. *Reviews of Modern Physics* **25,** 353 (1953).

105. McCoy, B. M. & Wu, T. T. *The Two-Dimensional Ising Model* 2nd ed. (Dover Publications, Inc, Mineola, New York, 2014).

106. Ferrenberg, A. M., Xu, J. & Landau, D. P. Pushing the limits of Monte Carlo simulations for the three-dimensional Ising model. *Physical Review E* **97,** 043301 (2018).

107. Landau, L. & Lifshitz, E. *Statistical Physics* (Pergamon, New York, 1980).

108. Van Hove, L. Sur l'intégrale de configuration pour les systèmes de particules à une dimension. *Physica* **16,** 137–143 (1950).

109. Cuesta, J. A. & Sánchez, A. General non-existence theorem for phase transitions in one-dimensional systems with short range interactions, and physical examples of such transitions. *Journal of Statistical Physics* **115,** 869–893 (2004).

110. Hubbard, J. Calculation of partition functions. *Physical Review Letters* **3,** 77 (1959).

111. Stratonovich, R. L. *A method for the computation of quantum distribution functions* in *Doklady Akademii Nauk* **115** (1957), 1097–1100.

112. Wilson, K. G. & Fisher, M. E. Critical exponents in 3.99 dimensions. *Physical Review Letters* **28,** 240 (1972).

113. Seeger, M., Kaul, S., Kronmüller, H. & Reisser, R. Asymptotic critical behavior of Ni. *Physical Review B* **51,** 12585 (1995).

114. Zhao, J., Kunkel, H., Zhou, X., Williams, G. & Subramanian, M. Critical behavior of the magnetoresistive pyrochlore Tl2Mn2O7. *Physical Review Letters* **83,** 219 (1999).

115. Zhao, J. *et al.* La0.95Mg0.05MnO3: an ideal ferromagnetic system? *Journal of Physics: Condensed Matter* **12,** 6903 (2000).

116. Yang, F., Chien, C., Li, X., Xiao, G. & Gupta, A. Critical behavior of epitaxial half-metallic ferromagnetic CrO_2 films. *Physical Review B* **63,** 092403 (2001).

117. Kaul, S. & Rao, M. S. Asymptotic critical behaviour of quenched random-exchange Heisenberg ferromagnets. *Journal of Physics: Condensed Matter* **6,** 7403 (1994).

118. Rao, M. S. & Kaul, S. Determination of asymptotic critical exponents and amplitudes for amorphous 3D ferromagnets from bulk magnetization measurements. *Journal of Magnetism and Magnetic Materials* **147,** 149–159 (1995).

119. Babu, P. & Kaul, S. Scaling behaviour of magnetization for temperatures in the vicinity of, and far from, the ferromagnetic-paramagnetic phase transition in amorphous and alloys. *Journal of Physics: Condensed Matter* **9,** 7189 (1997).

120. Said, M., Hamam, Y., Abu-Aljarayesh, I. & Mahmood, S. Critical exponents of $(Fe, Mn)_3Si$. *Journal of Magnetism and Magnetic Materials* **195,** 679–686 (1999).

121. Tsurkan, V., Baran, M., Szewczyk, A., Szymczak, R. & Szymczak, H. Magnetic phase transition in MnCr2-2xIn2xS4 crystals. *Journal of Physics: Condensed Matter* **11,** 7907 (1999).

122. Campostrini, M., Hasenbusch, M., Pelissetto, A., Rossi, P. & Vicari, E. Critical exponents and equation of state of the three-dimensional Heisenberg universality class. *Physical Review B* **65,** 144520 (2002).

123. Guida, R. & Zinn-Justin, J. Critical exponents of the N-vector model. *Journal of Physics A: Mathematical and General* **31,** 8103 (1998).

124. Mermin, N. D. & Wagner, H. Absence of ferromagnetism or antiferromagnetism in one-or two-dimensional isotropic Heisenberg models. *Physical Review Letters* **17,** 1133 (1966).

125. Heisenberg, W. Zur Theorie des Ferromagnetismus. *Zeitschrift für Physik* **49,** 619–636 (1928).

126. Hasenbusch, M. Eliminating leading corrections to scaling in the three-dimensional O(N)-symmetric ϕ^4 model: $N = 3$ and 4. *Journal of Physics A: Mathematical and General* **34,** 8221 (2001).

127. Wu, F.-Y. The potts model. *Reviews of Modern Physics* **54,** 235 (1982).

128. Janssen, H.-K. On the nonequilibrium phase transition in reaction-diffusion systems with an absorbing stationary state. *Zeitschrift für Physik B Condensed Matter* **42,** 151–154 (1981).

129. Hinrichsen, H. Non-equilibrium critical phenomena and phase transitions into absorbing states. *Advances in Physics* **49,** 815–958 (2000).

130. Ziff, R. M., Gulari, E. & Barshad, Y. Kinetic phase transitions in an irreversible surface-reaction model. *Physical Review Letters* **56,** 2553 (1986).

131. Tang, L.-H. & Leschhorn, H. Pinning by directed percolation. *Physical Review A* **45,** R8309 (1992).

132. Pomeau, Y. Front motion, metastability and subcritical bifurcations in hydrodynamics. *Physica D: Nonlinear Phenomena* **23,** 3–11 (1986).

133. Grassberger, P. On phase transitions in Schlögl's second model. *Zeitschrift für Physik B Condensed Matter* **47,** 365–374 (1982).

134. Janssen, H.-K. & Täuber, U. C. The field theory approach to percolation processes. *Annals of Physics* **315,** 147–192 (2005).

135. Täuber, U. C., Howard, M. & Vollmayr-Lee, B. P. Applications of field-theoretic renormalization group methods to reaction–diffusion problems. *Journal of Physics A: Mathematical and General* **38,** R79 (2005).

136. Jensen, H. J. *Self-organized criticality: emergent complex behavior in physical and biological systems* (Cambridge University Press, 1998).

137. Olami, Z., Feder, H. J. S. & Christensen, K. Self-organized criticality in a continuous, nonconservative cellular automaton modeling earthquakes. *Physical Review Letters* **68,** 1244 (1992).

138. Drossel, B. & Schwabl, F. Self-organized critical forest-fire model. *Physical Review Letters* **69,** 1629 (1992).

139. Bak, P. & Sneppen, K. Punctuated equilibrium and criticality in a simple model of evolution. *Physical Review Letters* **71,** 4083 (1993).

140. Ben-Hur, A. & Biham, O. Universality in sandpile models. *Physical Review E* **53,** R1317 (1996).

141. Milshtein, E., Biham, O. & Solomon, S. Universality classes in isotropic, Abelian, and non-Abelian sandpile models. *Physical Review E* **58,** 303 (1998).

142. Huynh, H. N., Pruessner, G. & Chew, L. Y. The Abelian Manna model on various lattices in one and two dimensions. *Journal of Statistical Mechanics: Theory and Experiment* **2011,** P09024 (2011).

143. Janssen, H., Schaub, B. & Schmittmann, B. The effects of surfaces on directed percolation and related stochastic evolution processes. *Zeitschrift für Physik B Condensed Matter* **72,** 111–114 (1988).

144. Lauritsen, K. B., Fröjdh, P. & Howard, M. Surface critical behavior in systems with absorbing states. *Physical Review Letters* **81,** 2104 (1998).

145. Fröjdh, P., Howard, M. & Lauritsen, K. B. Directed percolation with a wall or edge. *Journal of Physics A: Mathematical and General* **31,** 2311 (1998).

146. Fröjdh, P., Howard, M. & Lauritsen, K. B. Directed percolation and other systems with absorbing states: Impact of boundaries. *International Journal of Modern Physics B* **15,** 1761–1797 (2001).

147. Mendes, J., Dickman, R., Henkel, M. & Marques, M. C. Generalized scaling for models with multiple absorbing states. *Journal of Physics A: Mathematical and General* **27,** 3019 (1994).

148. Jensen, H. J. Lattice gas as a model of 1/f noise. *Physical Review Letters* **64,** 3103 (1990).

149. Rossi, M., Pastor-Satorras, R. & Vespignani, A. Universality class of absorbing phase transitions with a conserved field. *Physical Review Letters* **85,** 1803 (2000).

150. Cardy, J. *Finite-Size Scaling* (Elsevier, 2012).

151. Newman, M. & Barkema, G. *Monte Carlo Methods in Statistical Physics* (Clarendon Press, 1999).

152. Brézin, E. An investigation of finite size scaling. *Journal de Physique* **43,** 15–22 (1982).

153. Aharony, A. & Fisher, M. E. Nonlinear scaling fields and corrections to scaling near criticality. *Physical Review B* **27,** 4394 (1983).

154. Salas, J. & Sokal, A. D. Universal amplitude ratios in the critical two-dimensional Ising model on a torus. *Journal of Statistical Physics* **98,** 551–588 (2000).

155. Wegner, F. J. Corrections to scaling laws. *Physical Review B* **5,** 4529 (1972).

156. Privman, V., Hohenberg, P. & Aharony, A. in (eds Domb, C. & JL, L.) chap. Universal critical-point amplitude relations (Academic Press, 1991).

157. Salas, J. Exact finite-size-scaling corrections to the critical two-dimensional Ising model on a torus. *Journal of Physics A: Mathematical and General* **34,** 1311 (2001).

158. Campostrini, M., Pelissetto, A., Rossi, P. & Vicari, E. Two-point correlation function of three-dimensional O(N) models: The critical limit and anisotropy. *Physical Review E* **57,** 184 (1998).

159. Caselle, M., Hasenbusch, M., Pelissetto, A. & Vicari, E. Irrelevant operators in the two-dimensional Ising model. *Journal of Physics A: Mathematical and General* **35,** 4861 (2002).

160. Campostrini, M., Pelissetto, A., Rossi, P. & Vicari, E. 25th-order high-temperature expansion results for three-dimensional Ising-like systems on the simple-cubic lattice. *Physical Review E* **65,** 066127 (2002).

161. El-Showk, S. *et al.* Solving the 3D Ising model with the conformal bootstrap. *Physical Review D* **86,** 025022 (2012).

162. El-Showk, S. *et al.* Solving the 3D Ising model with the conformal bootstrap II. c-Minimization and precise critical exponents. *Journal of Statistical Physics* **157,** 869–914 (2014).

163. Anderson, P. W. Absence of diffusion in certain random lattices. *Physical Review* **109,** 1492 (1958).

164. Castellani, T. & Cavagna, A. Spin-glass theory for pedestrians. *Journal of Statistical Mechanics: Theory and Experiment* **2005,** P05012 (2005).

165. Nattermann, T. in *Spin Glasses and Random Fields* 277–298 (World Scientific, 1998).

166. Mezard, M., Parisi, G. & Virasoro, M. *Spin Glass Theory and Beyond* (World Scientific, 1986).

167. Fischer, K. & Hertz, J. *Spin Glasses* (Cambridge University Press, 1993).

168. Calabrese, P., Parruccini, P., Pelissetto, A. & Vicari, E. Crossover behavior in three-dimensional dilute spin systems. *Physical Review E* **69,** 036120 (2004).

169. Grinstein, G. & Luther, A. Application of the renormalization group to phase transitions in disordered systems. *Physical Review B* **13,** 1329 (1976).

170. Vojta, T. *Phases and phase transitions in disordered quantum systems* in *AIP Conference Proceedings* **1550** (2013), 188–247.

171. Vojta, T. Rare region effects at classical, quantum and nonequilibrium phase transitions. *Journal of Physics A: Mathematical and General* **39,** R143 (2006).

172. Griffiths, R. B. Nonanalytic behavior above the critical point in a random Ising ferromagnet. *Physical Review Letters* **23,** 17–19 (1969).

173. Randeria, M., Sethna, J. P. & Palmer, R. G. Low-Frequency Relaxation in Ising Spin-Glasses. *Physical Review Letters* **54,** 1321–1324 (1985).

174. Vojta, T. & Schmalian, J. Quantum Griffiths effects in itinerant Heisenberg magnets. *Physical Review B* **72,** 045438 (2005).

175. Weinrib, A. & Halperin, B. I. Critical phenomena in systems with long-range-correlated quenched disorder. *Physical Review B* **27,** 413 (1983).

176. Kinzel, W. Phase transitions of cellular automata. *Zeitschrift für Physik B Condensed Matter* **58,** 229–244 (1985).

177. Chayes, J., Chayes, L., Fisher, D. S. & Spencer, T. Correlation length bounds for disordered Ising ferromagnets. *Communications in Mathematical Physics* **120,** 501–523 (1989).

178. Espriu, D., Gross, M., Rakow, P. E. L. & Wheater, J. F. Random lattices versus regular lattices. *Progress of Theoretical Physics Supplements* **86,** 304 (1986).

179. Vojta, T. & Dickison, M. Critical behavior and Griffiths effects in the disordered contact process. *Physical Review E* **72,** 036126 (2005).

180. Vojta, T. & Lee, M. Y. Nonequilibrium Phase Transition on a Randomly Diluted Lattice. *Physical Review Letters* **96,** 035701 (2006).

181. Vojta, T., Farquhar, A. & Mast, J. Infinite-randomness critical point in the two-dimensional disordered contact process. *Physical Review E* **79,** 011111 (2009).

182. Hooyberghs, J., Iglói, F. & Vanderzande, C. Strong Disorder Fixed Point in Absorbing-State Phase Transitions. *Physical Review Letters* **90,** 100601 (2003).

183. Hooyberghs, J., Iglói, F. & Vanderzande, C. Absorbing state phase transitions with quenched disorder. *Physical Review E* **69,** 066140 (2004).

184. Lima, F., Costa, U. & Costa Filho, R. Critical behavior of the 3D Ising model on a poissonian random lattice. *Physica A: Statistical Mechanics and its Applications* **387,** 1545–1550 (2008).

185. Dotsenko, V. S. & Dotsenko, V. Phase transition in the 2D Ising model with impurity bonds. *JETP Letters* **33,** 37–40 (1981).

186. Jug, G. Critical singularities of the random two-dimensional Ising model. *Physical Review B* **27,** 4518–4521 (1983).

187. Shankar, R. Exact critical behavior of a random bond two-dimensional Ising model. *Physical Review Letters* **58,** 2466–2469 (1987).

188. Shalaev, B. Critical behavior of the two-dimensional Ising model with random bonds. *Physical Review E* **237,** 129–188 (1994).

189. Ludwig, A. W. Critical behavior of the two-dimensional random q-state Potts model by expansion in (q- 2). *Nuclear Physics B* **285,** 97–142 (1987).

190. Kim, J.-K. & Patrascioiu, A. Critical behavior of the two-dimensional site-diluted Ising system. *Physical Review B* **49,** 15764–15770 (1994).

191. Kim, J.-K. & Patrascioiu, A. Critical behavior of the specific heat in the two dimensional site diluted Ising system. *Physical Review Letters* **72,** 2785–2788 (1994).

192. Selke, W. Comment on "Critical Behavior of the Specific Heat in the Two Dimensional Site Diluted Ising System". *Physical Review Letters* **73,** 3487–3487 (1994).

193. Ziegler, K. Comment on ´´Critical behavior of the specific heat in the two dimensional site diluted Ising system". *Physical Review Letters* **73,** 3488–3488 (1994).

194. Kühn, R. Critical Behavior of the Randomly Spin Diluted 2D Ising Model: A Grand Ensemble Approach. *Physical Review Letters* **73,** 2268–2271 (1994).

195. Kim, J.-K. Scaling and finite-size scaling in the two-dimensional randomly coupled Ising ferromagnet. *Physical Review B* **61,** 1246–1250 (2000).

196. Gordillo-Guerrero, A., Kenna, R. & Ruiz Lorenzo, J. *The quenched-disordered Ising model in two and four dimensions* in *AIP Conference Proceedings* **1198** (2009), 42–54.

197. Martins, P. H. L. & Plascak, J. A. Universality class of the two-dimensional site-diluted Ising model. *Physical Review E* **76,** 012102 (2007).

198. Fytas, N. G. & Malakis, A. Critical behavior of the pure and random-bond two-dimensional triangular Ising ferromagnet. *Physical Review E* **81,** 041109 (2010).

199. Fytas, N. G. & Theodorakis, P. E. Universality aspects of the 2d random-bond Ising and 3d Blume-Capel models. *European Physical Journal A: Hadrons and Nuclei* **86,** 30 (2013).

200. Zhu, Q., Wan, X., Narayanan, R., Hoyos, J. A. & Vojta, T. Emerging criticality in the disordered three-color Ashkin-Teller model. *Physical Review B* **91,** 224201 (2015).

201. Kim, J.-K. Weak universality in the two-dimensional randomly disordered three-state Potts ferromagnet. *Physical Review B* **53,** 3388 (1996).

202. Picco, M. Numerical results for the two-dimensional random-bond three-state Potts model. *Physical Review B* **54,** 14930 (1996).

203. Novotny, M. & Landau, D. Critical behavior of the Baxter-Wu model with quenched impurities. *Physical Review B* **24,** 1468 (1981).

204. Schwenger, L., Budde, K., Voges, C. & Pfnür, H. Effect of random quenched impurities on the critical behavior of a four-state Potts system in two dimensions: An experimental study. *Physical Review Letters* **73,** 296 (1994).

205. Wiseman, S. & Domany, E. Critical behavior of the random-bond Ashkin-Teller model: A Monte Carlo study. *Physical Review E* **51,** 3074 (1995).

206. Schreiber, N. & Adler, J. Monte Carlo study of the pure and dilute Baxter–Wu model. *Journal of Physics A: Mathematical and General* **38,** 7253 (2005).

207. Aharony, A., Harris, A. B. & Wiseman, S. Critical disordered systems with constraints and the inequality $\nu > 2/d$. *Physical Review Letters* **81,** 252 (1998).

208. Vojta, T. & Dickman, R. Spatiotemporal generalization of the Harris criterion and its application to diffusive disorder. *Physical Review E* **93,** 032143 (2016).

209. Senechal, M. *Quasicrystals and Geometry* (Cambridge University Press, 1996).

210. Baddeley, A., Rubak, E. & Turner, R. *Spatial Point Patterns: Methodology and Applications with R* (CRC Press, 2015).

211. Aurenhammer, F. Voronoi diagrams – A survey of a fundamental geometric data structure. *ACM Computing Surveys (CSUR)* **23,** 345–405 (1991).

212. Jaromczyk, J. W. & Toussaint, G. T. Relative neighborhood graphs and their relatives. *Proceedings of the IEEE* **80,** 1502–1517 (1992).

213. Weatherill, N. Delaunay triangulation in computational fluid dynamics. *Computers & Mathematics with Applications* **24,** 129–150 (1992).

214. Bebis, G., Deaconu, T. & Georgiopoulos, M. *Fingerprint identification using Delaunay triangulation* in *Proceedings 1999 International Conference on Information Intelligence and Systems* (1999), 452–459.

215. Gopi, M., Krishnan, S. & Silva, C. T. *Surface reconstruction based on lower dimensional localized Delaunay triangulation* in *Computer Graphics Forum* **19** (2000), 467–478.

216. Ramella, M., Boschin, W., Fadda, D. & Nonino, M. Finding galaxy clusters using Voronoi tessellations. *Astronomy and Astrophysics* **368,** 776–786 (2001).

217. Wu, C.-H., Lee, K.-C. & Chung, Y.-C. A Delaunay Triangulation based method for wireless sensor network deployment. *Computer Communications* **30,** 2744–2752 (2007).

218. Barthélemy, M. Spatial networks. *Physics Reports* **499,** 1–101 (2011).

219. Watts, D. J. & Strogatz, S. H. Collective dynamics of 'small-world' networks. *Nature* **393,** 440 (1998).

220. Cohen, R. & Havlin, S. Scale-free networks are ultrasmall. *Physical Review Letters* **90,** 058701 (2003).

221. Herrero, C. P. Ising model in scale-free networks: A monte carlo simulation. *Physical Review E* **69,** 067109 (2004).

222. Ringler, T., Ju, L. & Gunzburger, M. A multiresolution method for climate system modeling: application of spherical centroidal Voronoi tessellations. *Ocean Dynam.* **58,** 475–498 (2008).

223. Ju, L., Ringler, T. & Gunzburger, M. in *Numerical techniques for global atmospheric models* 313–342 (Springer, 2011).

224. Wigner, E. & Seitz, F. On the constitution of metallic sodium. *Physical Review* **43,** 804 (1933).

225. Weygaert, R., Icke, V., *et al.* Fragmenting the universe. II – Voronoi vertices as Abell clusters. *Astronomy and Astrophysics* **213,** 1 (1989).

226. Poupon, A. Voronoi and Voronoi-related tessellations in studies of protein structure and interaction. *Current Opinion in Structural Biology* **14,** 233–241 (2004).

227. William, J. & Mehl, R. Reaction kinetics in processes of nucleation and growth. *Transactions of the Metallurgical Society of AIME* **135,** 416–442 (1939).

228. Okabe, A. & Suzuki, A. Locational optimization problems solved through Voronoi diagrams. *European Journal of Operational Research* **98,** 445–456 (1997).

229. Ahn, H.-K., Cheng, S.-W., Cheong, O., Golin, M. & Van Oostrum, R. Competitive facility location: the Voronoi game. *Theoretical Computer Science* **310,** 457–467 (2004).

230. Cheong, O., Har-Peled, S., Linial, N. & Matousek, J. The one-round Voronoi game. *Discrete & Computational Geometry* **31,** 125–138 (2004).

231. Dürr, C. & Thang, N. K. *Nash equilibria in Voronoi games on graphs* in *European Symposium on Algorithms* (2007), 17–28.

232. Forbus, K. D., Mahoney, J. V. & Dill, K. How qualitative spatial reasoning can improve strategy game AIs. *IEEE Intelligent Systems* **17,** 25–30 (2002).

233. Gavrilova, M. *Generalized Voronoi Diagram: A Geometry-Based Approach to Computational Intelligence* (Springer Berlin Heidelberg, 2008).

234. Ward, L. *et al.* Including crystal structure attributes in machine learning models of formation energies via Voronoi tessellations. *Physical Review B* **96,** 024104 (2017).

235. Na, H.-S., Lee, C.-N. & Cheong, O. Voronoi diagrams on the sphere. *Computational Geometry* **23,** 183–194 (2002).

236. Boissonnat, J.-D., Wormser, C. & Yvinec, M. in *Effective Computational Geometry for Curves and Surfaces* 67–116 (Springer, 2006).

237. Jooyandeh, M., Mohades, A. & Mirzakhah, M. Uncertain voronoi diagram. *Information Processing Letters* **109,** 709–712 (2009).

238. Okabe, A., Boots, B., Sugiharaa, K. & Chiu, S. N. *Spatial Tessellations: Concepts and Applications of Voronoi Diagrams* 2nd ed. (Wiley, Chichester, 2000).

239. Kruithof, N. in *CGAL User and Reference Manual* 4.11 (CGAL Editorial Board, 2017).

240. Keblinski, P., Bazant, M., Dash, R. & Treacy, M. Thermodynamic behavior of a model covalent material described by the environment-dependent interatomic potential. *Physical Review B* **66,** 064104 (2002).

241. Büchner, C. & Heyde, M. Two-dimensional silica opens new perspectives. *Progress in Surface Science* **92,** 341–374 (2017).

242. Gaspard, J. Space filling models of amorphous structures. *Journal de Physique Colloques* **46,** C8–21 (1985).

243. Godrèche, C. & Bray, A. J. Nonequilibrium stationary states and phase transitions in directed Ising models. *Journal of Statistical Mechanics: Theory and Experiment* **2009,** P12016 (2009).

244. Lima, F. & Stauffer, D. Ising model simulation in directed lattices and networks. *Physica A: Statistical Mechanics and its Applications* **359,** 423–429 (2006).

245. Lima, F., Luz, E. M. & Costa Filho, R. Critical behavior Ising model $S = 1, 3/2$ and 2 on directed networks. *Multidiscipline Modeling in Materials and Structures* **5,** 223–228 (2009).

246. Fernandes, F., Lima, F. & Plascak, J. Blume–Capel model on directed and undirected small-world Voronoi–Delaunay random lattices. *Computer Physics Communications* **181,** 1218–1223 (2010).

247. Lima, F. & Plascak, J. Critical behavior of the Ising and Blume-Capel models on directed two-dimensional small-world networks. *European Physical Journal B: Condensed Matter Physics* **86,** 300 (2013).

248. Sánchez, A. D., López, J. M. & Rodriguez, M. A. Nonequilibrium phase transitions in directed small-world networks. *Physical Review Letters* **88,** 048701 (2002).

249. Herrero, C. P. Ising model in small-world networks. *Physical Review E* **65,** 066110 (2002).

250. Lima, F. & Sumour, M. Ising model with spins $S = 1/2$ and 1 on directed and undirected Erdös–Rényi random graphs. *Physica A: Statistical Mechanics and its Applications* **391,** 948–953 (2012).

251. Kirkpatrick, S., Gelatt, C. D. & Vecchi, M. P. Optimization by simulated annealing. *Science* **220,** 671–680 (1983).

252. Euler, L. Solutio problematis ad geometriam situs pertinentis. *Commentarii academiae scientiarum Petropolitanae,* 128–140 (1741).

253. Su, P. & Drysdale, R. L. S. A comparison of sequential Delaunay triangulation algorithms. *Computational Geometry* **7,** 361–385 (1997).

254. Supowit, K. J. The relative neighborhood graph, with an application to minimum spanning trees. *Journal of the ACM* **30,** 428–448 (1983).

255. Vaidya, P. M. An O(nlogn) algorithm for the all-nearest-neighbors Problem. *Discrete & Computational Geometry* **4,** 101–115 (1989).

256. Dwyer, R. A. A faster divide-and-conquer algorithm for constructing Delaunay triangulations. *Algorithmica* **2,** 137–151 (1987).

257. Agarwal, P. K. & Mataušek, J. *Relative neighborhood graphs in three dimensions* in *Proceedings of the third annual ACM-SIAM symposium on Discrete algorithms* (1992), 58–65.

258. Dunham, D. in *Symmetry* 139–153 (Pergamon, 1986).

259. Sausset, F. & Tarjus, G. Periodic boundary conditions on the pseudosphere. *Journal of Physics A: Mathematical and Theoretical* **40,** 12873 (2007).

260. Schawe, H., Norrenbrock, C. & Hartmann, A. K. Ising ferromagnets on proximity graphs with varying disorder of the node placement. *Scientific Reports* **7,** 8040 (2017).

261. Hammersley, J. & Handscomb, D. *Monte-Carlo Methods* (Springer Netherlands, 1964).

262. Metropolis, N., Rosenbluth, A. W., Rosenbluth, M. N., Teller, A. H. & Teller, E. Equation of state calculations by fast computing machines. *Journal of Chemical Physics* **21,** 1087–1092 (1953).

263. Janke, W. in *Computational Many-Particle Physics* (eds Fehske, H., Schneider, R. & Weiße, A.) 79–140 (Springer Berlin Heidelberg, Berlin, Heidelberg, 2008).

264. Krauth, W. *Statistical mechanics: algorithms and computations* (Oxford University Press, 2006).

265. Machta, J., Choi, Y., Lucke, A., Schweizer, T. & Chayes, L. Invaded cluster algorithm for equilibrium critical points. *Physical Review Letters* **75,** 2792 (1995).

266. Machta, J., Choi, Y., Lucke, A., Schweizer, T. & Chayes, L. Invaded cluster algorithm for Potts models. *Physical Review E* **54,** 1332 (1996).

267. Dukovski, I., Machta, J. & Chayes, L. Invaded cluster simulations of the XY model in two and three dimensions. *Physical Review E* **65,** 026702 (2002).

268. Prokof'ev, N. & Svistunov, B. Worm algorithms for classical statistical models. *Physical Review Letters* **87,** 160601 (2001).

269. Kandel, D., Domany, E. & Brandt, A. Simulations without critical slowing down: Ising and three-state Potts models. *Physical Review B* **40,** 330 (1989).

270. Binder, K. Finite size scaling analysis of Ising model block distribution functions. *Zeitschrift für Physik B Condensed Matter* **43,** 119–140 (1981).

271. Cooper, F., Freedman, B. & Preston, D. Solving $\phi^4_{1,2}$ field theory with Monte Carlo. *Nuclear Physics B* **210,** 210–228 (1982).

272. Ballesteros, H. G. *et al.* Critical behavior of the three-dimensional Ising spin glass. *Physical Review B* **62,** 14237–14245 (2000).

273. Hasenbusch, M., Toldin, F. P., Pelissetto, A. & Vicari, E. The universality class of 3D site-diluted and bond-diluted Ising systems. *Journal of Statistical Mechanics: Theory and Experiment* **2007,** P02016 (2007).

274. Katzgraber, H. G., Körner, M. & Young, A. Universality in three-dimensional Ising spin glasses: A Monte Carlo study. *Physical Review B* **73,** 224432 (2006).

275. Press, W. H., Teukolsky, S. A., Vetterling, W. T. & Flannery, B. P. *Numerical Recipes - The Art of Scientific Computing* 3rd (Cambridge University Press, 2007).

276. Ballesteros, H., Fernandez, L., Martin-Mayor, V. & Sudupe, A. M. Finite size effects on measures of critical exponents in $d = 3$ O(N) models. *Physics Letters B* **387,** 125–131 (1996).

277. Ballesteros, H., Fernández, L., Martin-Mayor, V. & Sudupe, A. M. New universality class in three dimensions?: the antiferromagnetic RP_2 model. *Physics Letters B* **378,** 207–212 (1996).

278. Caracciolo, S., Edwards, R. G., Ferreira, S. J., Pelissetto, A. & Sokal, A. D. Extrapolating Monte Carlo simulations to infinite volume: Finite-size scaling at $\xi/L \gg 1$. *Physical Review Letters* **74,** 2969–2972 (1995).

279. Nightingale, M. P. Scaling theory and finite systems. *Physica A: Statistical Mechanics and its Applications* **83,** 561–572 (1976).

280. Amit, D. J. & Martin-Mayor, V. *Field Theory, the Renormalization Group, and Critical Phenomena: Graphs to Computers Third Edition* (World Scientific Publishing Company, 2005).

281. Landau, D. P. & Binder, K. *A Guide to Monte Carlo Simulations in Statistical Physics* 4th ed. (Cambridge University Press, 2014).

282. Brandt, S. *Data Analysis: Statistical and Computational Methods for Scientists and Engineers* (Springer International Publishing, 2014).

283. Priestley, M. B. *Spectral analysis and time series* (Academic Press London, 1981).

284. Sokal, A. D. & Thomas, L. E. Exponential convergence to equilibrium for a class of random-walk models. *Journal of Statistical Physics* **54,** 797–828 (1989).

285. Janke, W. Statistical analysis of simulations: Data correlations and error estimation. *Quantum Simulations of Complex Many-Body Systems: From Theory to Algorithms* **10,** 423–445 (2002).

286. Madras, N. & Sokal, A. D. The pivot algorithm: a highly efficient Monte Carlo method for the self-avoiding walk. *Journal of Statistical Physics* **50,** 109–186 (1988).

287. Flyvbjerg, H. & Petersen, H. G. Error estimates on averages of correlated data. *Journal of Chemical Physics* **91,** 461–466 (1989).

288. Efron, B. *The jackknife, the bootstrap, and other resampling plans* (Siam, 1982).

289. Efron, B. & Tibshirani, R. J. *An Introduction to the Bootstrap* (Chapman and Hall, Boca Raton, 1994).

290. Miller, R. G. The Jackknife – A review. *Biometrika* **61,** 1–15 (1974).

291. Quenouille, M. H. Approximate Tests of Correlation in Time-Series. *Journal of the Royal Statistical Society* **11,** 68–84 (1949).

292. Ballesteros, H. *et al.* Ising exponents in the two-dimensional site-diluted Ising model. *Journal of Physics A: Mathematical and General* **30,** 8379 (1997).

293. Ballesteros, H. G. *et al.* Critical exponents of the three-dimensional diluted Ising model. *Physical Review B* **58,** 2740–2747 (1998).

294. Gordillo-Guerrero, A., Kenna, R. & Ruiz-Lorenzo, J. J. Scaling behavior of the Heisenberg model in three dimensions. *Physical Review E* **88,** 062117 (2013).

295. Ballesteros, H. *et al.* The four-dimensional site-diluted Ising model: A finite-size scaling study. *Nuclear Physics B* **512,** 681–701 (1998).

296. Kumar, S., Rosenberg, J. M., Bouzida, D., Swendsen, R. H. & Kollman, P. A. The weighted histogram analysis method for free-energy calculations on biomolecules. I. The method. *Journal of Computational Chemistry* **13,** 1011–1021 (1992).

297. Kumar, S., Rosenberg, J. M., Bouzida, D., Swendsen, R. H. & Kollman, P. A. Multidimensional free-energy calculations using the weighted histogram analysis method. *Journal of Computational Chemistry* **16,** 1339–1350 (1995).

298. Souaille, M. & Roux, B. Extension to the weighted histogram analysis method: combining umbrella sampling with free energy calculations. *Computer Physics Communications* **135,** 40–57 (2001).

299. Zhang, C., Lai, C.-L. & Pettitt, B. M. Accelerating the weighted histogram analysis method by direct inversion in the iterative subspace. *Molecular Simulation* **42,** 1079–1089 (2016).

300. Kajantie, K., Kärkkäinen, L. & Rummukainen, K. Tension of the interface between two ordered phases in lattice SU(3) gauge theory. *Nuclear Physics B* **357,** 693–712 (1991).

301. Kärkkäinen, L., Lacaze, R., Lacock, P. & Petersson, B. Critical behaviour of the three-dimensional Gross-Neveu and Higgs-Yukawa models. *Nuclear Physics B* **415,** 781–796 (1994).

302. Bereau, T. & Swendsen, R. H. Optimized convergence for multiple histogram analysis. *Journal of Computational Physics* **228,** 6119–6129 (2009).

303. Bae, S., Ko, S.-H. & Coddington, P. D. Parallel Wolff cluster algorithms. *International Journal of Modern Physics C: Computational Physics and Physical Computation* **6,** 197–210 (1995).

304. Kaupužs, J., Rimšāns, J. & Melnik, R. V. Parallelization of the Wolff single-cluster algorithm. *Physical Review E* **81,** 026701 (2010).

305. Ziff, R. M. Four-tap shift-register-sequence random-number generators. *Computers in Physics* **12,** 385–392 (1998).

306. Dall, J. & Christensen, M. Random geometric graphs. *Physical Review E* **66,** 016121 (2002).

307. Hasenbusch, M. & Vicari, E. Anisotropic perturbations in three-dimensional O(N)-symmetric vector models. *Physical Review B* **84,** 125136 (2011).

308. Dudka, M., Folk, R., Holovatch, Y. & Ivaneiko, D. Effective critical behaviour of diluted Heisenberg-like magnets. *Journal of Magnetism and Magnetic Materials* **256,** 243–251 (2003).

309. Gordillo-Guerrero, A. & Ruiz-Lorenzo, J. J. Self-averaging in the three-dimensional site diluted Heisenberg model at the critical point. *Journal of Statistical Mechanics: Theory and Experiment* **2007,** P06014 (2007).

310. Selke, W. & Shchur, L. Critical Binder cumulant in two-dimensional anisotropic Ising models. *Journal of Physics A: Mathematical and General* **38,** L739 (2005).

311. Selke, W. & Shchur, L. Critical Binder cumulant in a two-dimensional anisotropic Ising model with competing interactions. *Physical Review E* **80,** 042104 (2009).

312. Malakis, A., Fytas, N. G. & Gülpinar, G. Critical Binder cumulant and universality: Fortuin-Kasteleyn clusters and order-parameter fluctuations. *Physical Review E* **89,** 042103 (2014).

313. Privman, V. *Finite size scaling and numerical simulation of statistical systems* (World Scientific Singapore, 1990).

314. Marro, J. & Dickman, R. *Nonequilibrium phase transitions in lattice models* (Cambridge University Press, 2005).

315. Dickman, R. *Nonequilibrium statistical mechanics in one dimension* (ed Privman, V.) (Cambridge University Press, 1997).

316. Jensen, I. & Dickman, R. Nonequilibrium phase transitions in systems with infinitely many absorbing states. *Physical Review E* **48,** 1710–1725 (1993).

317. Lübeck, S. & Heger, P. Universal finite-size scaling behavior and universal dynamical scaling behavior of absorbing phase transitions with a conserved field. *Physical Review E* **68,** 056102 (2003).

318. Pruessner, G. Equivalence of conditional and external field ensembles in absorbing-state phase transitions. *Physical Review E* **76,** 061103 (2007).

319. De Oliveira, M. M. & Dickman, R. How to simulate the quasistationary state. *Physical Review E* **71,** 016129 (2005).

320. Dickman, R. & de Oliveira, M. M. Quasi-stationary simulation of the contact process. *Physica A: Statistical Mechanics and its Applications* **357,** 134–141 (2005).

321. Dickman, R. Absorbing-state phase transitions: Exact solutions of small systems. *Physical Review E* **77,** 030102 (2008).

322. Grassberger, P. & De La Torre, A. Reggeon field theory (Schlögl's first model) on a lattice: Monte Carlo calculations of critical behaviour. *Annals of Physics* **122,** 373–396 (1979).

323. Dahmen, S. R., Sittler, L. & Hinrichsen, H. Multicritical behaviour of the diluted contact process. *Journal of Statistical Mechanics: Theory and Experiment* **2007,** P01011 (2007).

324. Fisher, D. S. Random transverse field Ising spin chains. *Physical Review Letters* **69,** 534–537 (1992).

325. Fisher, D. S. Critical behavior of random transverse-field Ising spin chains. *Physical Review B* **51,** 6411–6461 (1995).

326. Motrunich, O., Mau, S.-C., Huse, D. A. & Fisher, D. S. Infinite-randomness quantum Ising critical fixed points. *Physical Review B* **61,** 1160–1172 (2000).

327. Janssen, H. K. Renormalized field theory of the Gribov process with quenched disorder. *Physical Review E* **55,** 6253–6256 (1997).

328. Hoyos, J. A. Weakly disordered absorbing-state phase transitions. *Physical Review E* **78,** 032101 (2008).

329. Moreira, A. G. & Dickman, R. Critical dynamics of the contact process with quenched disorder. *Physical Review E* **54,** R3090 (1996).

330. Vojta, T. Monte Carlo simulations of the clean and disordered contact process in three dimensions. *Physical Review E* **86,** 051137 (2012).

331. Wada, A. H. & de Oliveira, M. J. Critical properties of the contact process with quenched dilution. *Journal of Statistical Mechanics: Theory and Experiment* **2017,** 043209 (2017).

332. Kaupužs, J., Melnik, R. & Rimšāns, J. Corrections to finite-size scaling in the ϕ^4 model on square lattices. *International Journal of Modern Physics C: Computational Physics and Physical Computation* **27,** 1650108 (2016).

333. Tomita, Y. & Okabe, Y. Crossover and self-averaging in the two-dimensional site-diluted Ising model: Application of probability-changing cluster algorithm. *Physical Review E* **64,** 036114 (2001).

334. Kuratowski, C. Sur le probleme des courbes gauches en topologie. *Fundamenta mathematicae* **15,** 271–283 (1930).

335. Williamson, S. Depth-first search and Kuratowski subgraphs. *Journal of the ACM* **31,** 681–693 (1984).

336. Hasenbusch, M., Toldin, F. P., Pelissetto, A. & Vicari, E. Universal dependence on disorder of two-dimensional randomly diluted and random-bond $\pm J$ Ising models. *Physical Review E* **78,** 011110 (2008).

337. Mazzeo, G. & Kühn, R. Critical behavior of the two-dimensional spin-diluted Ising model via the equilibrium ensemble approach. *Physical Review E* **60,** 3823–3836 (1999).

338. Kenna, R. & Ruiz-Lorenzo, J. Scaling analysis of the site-diluted Ising model in two dimensions. *Physical Review E* **78,** 031134 (2008).

339. Kamieniarz, G. & Blote, H. Universal ratio of magnetization moments in two-dimensional Ising models. *Journal of Physics A: Mathematical and General* **26,** 201 (1993).

340. Blöte, H. W. & den Nijs, M. P. Corrections to scaling at two-dimensional Ising transitions. *Physical Review B* **37,** 1766 (1988).

341. Dickman, R. Reweighting in nonequilibrium simulations. *Physical Review E* **60,** R2441 (1999).

342. Lee, S. B. Critical behavior of absorbing phase transitions for models in the Manna class with natural initial states. *Physical Review E* **89,** 062133 (2014).

343. Basu, M., Basu, U., Bondyopadhyay, S., Mohanty, P. & Hinrichsen, H. Fixed-energy sandpiles belong generically to directed percolation. *Physical Review Letters* **109,** 015702 (2012).

344. Lee, S. B. Comment on "Fixed-energy sandpiles belong generically to directed percolation". *Physical Review Letters* **110,** 159601 (2013).

345. Lee, S. B. Universality class of the conserved Manna model in one dimension. *Physical Review E* **89,** 060101 (2014).

346. Dickman, R. & da Cunha, S. Particle-density fluctuations and universality in the conserved stochastic sandpile. *Physical Review E* **92,** 020104 (2015).

347. Dickman, R., Tomé, T. & De Oliveira, M. J. Sandpiles with height restrictions. *Physical Review E* **66,** 016111 (2002).

348. Lübeck, S. Scaling behavior of the conserved transfer threshold process. *Physical Review E* **66,** 046114 (2002).

349. Da Cunha, S. D., da Silva, L. R., Viswanathan, G. M. & Dickman, R. Activity, diffusion, and correlations in a two-dimensional conserved stochastic sandpile. *Journal of Statistical Mechanics: Theory and Experiment* **2014,** P08003 (2014).

350. De Oliveira, M. M. & Ferreira, S. C. Universality of the contact process with random dilution. *Journal of Statistical Mechanics: Theory and Experiment* **2008,** P11001 (2008).

351. Hasenbusch, M. Finite size scaling study of lattice models in the three-dimensional Ising universality class. *Physical Review B* **82,** 174433 (2010).

352. Harary, F. *Graph Theory* (Addison-Wesley, 1969).

353. Vanmarcke, E. *Random fields: analysis and synthesis* (World Scientific, 2010).

354. Dietrich, C. R. & Newsam, G. N. Fast and exact simulation of stationary Gaussian processes through circulant embedding of the covariance matrix. *SIAM Journal on Scientific Computing* **18,** 1088–1107 (1997).

355. Vio, R., Andreani, P. & Wamsteker, W. Numerical Simulation of Non-Gaussian Random Fields with Prescribed Correlation Structure. *Publications of the Astronomical Society of the Pacific* **113,** 1009 (2001).

356. Vio, R., Andreani, P., Tenorio, L. & Wamsteker, W. Numerical Simulation of Non-Gaussian Random Fields with Prescribed Marginal Distributions and Cross-Correlation Structure. II. Multivariate Random Fields. *Publications of the Astronomical Society of the Pacific* **114,** 1281 (2002).

357. Ma, C. Construction of non-Gaussian random fields with any given correlation structure. *Journal of Statistical Planning and Inference* **139,** 780–787 (2009).

358. Lee, S. B. & Kim, J. S. Absorbing phase transitions in diluted conserved threshold transfer process. *Physical Review E* **87,** 032117 (2013).

359. Lee, S. B. Hyperuniformity and absorbing phase transition in continuous media with a conserved field. *Journal of Statistical Mechanics: Theory and Experiment* **2019,** 053201 (2019).

360. Himpsel, F., Ortega, J., Mankey, G. & Willis, R. Magnetic nanostructures. *Advances in physics* **47,** 511–597 (1998).

361. Martın, J., Nogues, J., Liu, K., Vicent, J. & Schuller, I. K. Ordered magnetic nanostructures: fabrication and properties. *Journal of Magnetism and Magnetic Materials* **256,** 449–501 (2003).

362. Park, N. *et al.* Magnetism in all-carbon nanostructures with negative Gaussian curvature. *Physical Review Letters* **91,** 237204 (2003).

363. Moura-Melo, W., Pereira, A., Mól, L. & Pires, A. Geometrical pinning of magnetic vortices induced by a deficit angle on a surface: Anisotropic spins on a conic space background. *Physics Letters A* **360,** 472–480 (2007).

364. Krioukov, D., Papadopoulos, F., Vahdat, A. & Boguñá, M. Curvature and temperature of complex networks. *Physical Review E* **80,** 035101 (2009).

365. Krioukov, D., Papadopoulos, F., Kitsak, M., Vahdat, A. & Boguná, M. Hyperbolic geometry of complex networks. *Physical Review E* **82,** 036106 (2010).

366. Boguná, M., Papadopoulos, F. & Krioukov, D. Sustaining the Internet with hyperbolic mapping. *Nature Communications* **1,** 62 (2010).

367. Crnkovic, C., Ginsparg, P. & Moore, G. The Ising model, the Yang-Lee edge singularity, and 2D quantum gravity. *Physical Review B* **237,** 196–201 (1990).

368. Gross, M. & Hamber, H. W. Critical properties of two-dimensional simplicial quantum gravity. *Nuclear Physics B* **364,** 703–733 (1991).

369. Di Francesco, P., Ginsparg, P. & Zinn-Justin, J. 2D gravity and random matrices. *Physics Reports* **254,** 1–133 (1995).

370. Faraudo, J. Diffusion equation on curved surfaces. I. Theory and application to biological membranes. *The Journal of Chemical Physics* **116,** 5831–5841 (2002).

371. Baek, S. K., Shima, H. & Kim, B. J. Curvature-induced frustration in the XY model on hyperbolic surfaces. *Physical Review E* **79,** 060106 (2009).

372. Tarjus, G., Sausset, F. & Viot, P. in *Advances in Chemical Physics* 251–310 (John Wiley & Sons, Inc., 2011).

373. Balakrishnan, J. Spatial curvature effects on molecular transport by diffusion. *Physical Review E* **61,** 4648 (2000).

374. Ghosh, A., Samuel, J. & Sinha, S. A Gaussian for diffusion on the sphere. *EPL (Europhysics Letters)* **98,** 30003 (2012).

375. Sausset, F. & Tarjus, G. Self-diffusion in a monatomic glass-forming liquid embedded in the hyperbolic plane. *Philosophical Magazine* **88,** 4025–4031 (2008).

376. Castro-Villarreal, P. Brownian motion meets Riemann curvature. *Journal of Statistical Mechanics: Theory and Experiment* **2010,** P08006 (2010).

377. Diego, O., González, J. & Salas, J. The Ising model on tetrahedron-like lattices: a finite-size analysis. *Journal of Physics A: Mathematical and General* **27,** 2965 (1994).

378. Hoelbling, C. & Lang, C. Universality of the Ising model on spherelike lattices. *Physical Review B* **54,** 3434 (1996).

379. Weigel, M. & Janke, W. Universal amplitude-exponent relation for the Ising model on sphere-like lattices. *EPL (Europhysics Letters)* **51,** 578 (2000).

380. Costa-Santos, R. The Ising model on curved lattices. *Acta Physica Polonica B* **34,** 4777–4794. 19 p (2003).

381. Rietman, R., Nienhuis, B. & Oitmaa, J. The Ising model on hyperlattices. *Journal of Physics A: Mathematical and General* **25,** 6577 (1992).

382. Shima, H. & Sakaniwa, Y. The dynamic exponent of the Ising model on negatively curved surfaces. *Journal of Statistical Mechanics: Theory and Experiment* **2006,** P08017 (2006).

383. Shima, H. & Sakaniwa, Y. Geometric effects on critical behaviours of the Ising model. *Journal of Physics A: Mathematical and General* **39,** 4921 (2006).

384. Sakaniwa, Y. & Shima, H. Survival of short-range order in the Ising model on negatively curved surfaces. *Physical Review E* **80,** 021103 (2009).

385. Iharagi, T., Gendiar, A., Ueda, H. & Nishino, T. Phase transition of the Ising model on a hyperbolic lattice. *Journal of the Physical Society of Japan* **79,** 104001 (2010).

386. Gendiar, A., Daniška, M., Krčmár, R. & Nishino, T. Mean-field universality class induced by weak hyperbolic curvatures. *Physical Review E* **90,** 012122 (2014).

387. Baek, S. K., Minnhagen, P. & Kim, B. J. Phase transition of XY model in heptagonal lattice. *EPL (Europhysics Letters)* **79,** 26002 (2007).

388. Baek, S. K., Minnhagen, P., Shima, H. & Kim, B. J. Phase transition of q-state clock models on heptagonal lattices. *Physical Review E* **80,** 011133 (2009).

389. Benjamini, I. & Schramm, O. Percolation in the hyperbolic plane. *Journal of the American Mathematical Society* **14,** 487–507 (2001).

390. Lyons, R. Phase transitions on nonamenable graphs. *Journal of Mathematical Physics* **41,** 1099–1126 (2000).

391. Nogawa, T., Hasegawa, T. & Nemoto, K. Local cluster-size statistics in the critical phase of bond percolation on the Cayley tree. *Journal of Statistical Mechanics: Theory and Experiment* **2016,** 053202 (2016).

392. Baek, S. K., Minnhagen, P. & Kim, B. J. Surface and bulk criticality in midpoint percolation. *Physical Review E* **81,** 041108 (2010).

393. Sausset, F., Toninelli, C., Biroli, G. & Tarjus, G. Bootstrap percolation and kinetically constrained models on hyperbolic lattices. *Journal of Statistical Physics* **138,** 411–430 (2010).

394. Lopez, J. H. & Schwarz, J. M. Constraint percolation on hyperbolic lattices. *Physical Review E* **96,** 052108 (2017).

395. Baek, S. K., Minnhagen, P. & Kim, B. J. Percolation on hyperbolic lattices. *Physical Review E* **79,** 011124 (2009).

396. Bentley, J. L. Multidimensional binary search trees used for associative searching. *Communications of the ACM* **18,** 509–517 (1975).

397. Weigel, M. & Janke, W. Error estimation and reduction with cross correlations. *Physical Review E* **81,** 066701 (2010).

398. Wall, M. E., Rechtsteiner, A. & Rocha, L. M. in *A practical approach to microarray data analysis* 91–109 (Springer, 2003).

399. Jolliffe, I. T. Principal components in regression analysis. *Principal component analysis,* 167–198 (2002).

400. Gavish, M. & Donoho, D. L. The Optimal Hard Threshold for Singular Values is $4/\sqrt{3}$. *IEEE Transactions on Information Theory* **60,** 5040–5053 (2014).

401. Bartz, D. *Advances in high-dimensional covariance matrix estimation* PhD thesis (Technische Universität Berlin, 2016).

Acknowledgements

First and foremost, I would like to thank my doctoral supervisor, **Prof. Dr. Haye Hinrichsen**. Not only did he, through several of his lectures I attended during my master's, spark my interest in the field of statistical physics in the first place – he also gave me the opportunity to join his group and to become a part of this exciting area of research myself. I would like to thank him particularly for giving me the freedom to pursue my own research direction and shape this project according to my own ideas. Finally, I sincerely appreciate the amount of time he spent in numerous scientific discussions and his invaluable expertise in the field.

I would also like to thank **Prof. Dr. Jefferson S. E. Portela**, with whom I collaborated closely for the most part of this project. I really enjoyed the many long discussions with him, where we, although both of us came from different fields, dove deeper and deeper into the realm of critical systems, geometry, graph theory, numerical algorithms and many other topics. It was an unbelievable journey and I found a friend.

Moreover, I would like to thank **Dr. Florian Goth**, who also contributed to this work. His knowledge and expertise in all matters of computing infrastructure as well as software development and optimization were invaluable. Personally, I learned a ton from him – about efficient coding and high-performance computing in general. Without Florian, numerical simulations on scales as large as they had turned out in the end, would certainly not have been possible.

During the course of my project I had the honour to supervise a number of master projects at our group, in particular those of **Christoph Türk**, **Julian Richter**, **Konstantin Weisenberger**, **Maximilian Schneider** and **Maximilian Döring**. It is fair to say, that our understanding of critical phenomena and geometry mutually benefited from the interesting problems we worked on. I would also like to thank my fellow PhD students, **Christian Northe**, **Ignacio Reyes**, **Nina Miekley**, **Raimond Abt**, **Pascal Fries** and **Yiqiang Du**. Although our projects were quite different, I deeply appreciated the pleasant working environment and the lively discussions, as well as our numerous activities beyond academia, such as the weekly basketball group we had in the summer of 2016 and 2017, which also involved a number of former master students in our group, **Ilja Rausch**, **Maximilian Wagner**, **Maximilian Weber**, **Oliver Niggemann**, **Roman Engelhardt** and **Theresa Christ**. Participating at the city-wide tournament with you guys was a blast!

I am grateful to all those at the Theoretical Physics institute that I have not mentioned so far, and that made my stay an unforgettable experience. This includes **Emma Loos**, **Ioannis Matthaiakakis**, **Marius Gerbershagen**, **Dr. Rene Meyer**, **Prof. Dr. Wolfgang Kinzel** and the head of our chair, **Prof. Dr. Johanna Erdmenger**. In particular, I would like to thank our secretary, **Nelly Meyer**, for always providing advice and support in all daily matters at the university.

I am particularly indebted to the **Studienstiftung des deutschen Volkes** (National German Scholarship Foundation) for granting me a three-year doctoral research fellowship. I deeply appreciate their financial support and the intellectual exchange with many outstanding people during this time.

Moreover, I want to thank all the people who took on the burden to carefully proofread parts of this thesis, including **Christian Northe**, **Christoph Hartmann**, **Dominik Heps**, **Joshua Orth**, **Julian Schrauth**, **Laura Lauerbach** and **Lisa Schrauth**. These people were extraordinarily important and I appreciate the time they spent.

I owe a deep gratitude to my parents, **Andrea** and **Elmar Schrauth**. Their education and steady support has made me who I am today. This work would not have been possible without them.

Finally, from the bottom of my heart, I thank **Laura** for her love, support and encouragement over the past years.